Coherent manipulation of Andreev Bound States in an atomic contact

Camille Janvier

NNT : 2016SACLS217

THESE DE DOCTORAT
DE
L'UNIVERSITE PARIS-SACLAY
PREPAREE A
L'UNIVERSITE PARIS-SUD

ECOLE DOCTORALE N° 564
Physique en Ile-de-France
Spécialité de doctorat : Physique

Par

M. Camille Janvier

au sein du groupe Quantronique, SPEC, CEA-Saclay & CNRS

Coherent manipulation of Andreev bound states in a superconducting atomic contact

Thèse soutenue au CEA-Saclay le 22 septembre 2016

Composition du Jury :

Dr. Hélène Bouchiat, Université Paris-Sud	Présidente du jury
Dr. Jean-Philippe Brantut, ETH Zürich	Examinateur
Dr. Gianluigi Catelani, Forschungszentrum Jülich	Examinateur
Prof. Per Delsing, Chalmers University of Technology	Rapporteur
Prof. Alfredo Levy Yeyati, Universidad Autónoma de Madrid	Rapporteur
Dr. Hugues Pothier, CEA Saclay	Directeur de thèse

“ Je veux rendre toute puissante l’influence du clergé, parce que je compte sur lui pour propager cette bonne philosophie qui apprend à l’homme qu’il est ici-bas pour souffrir et non cette autre philosophie qui dit au contraire à l’homme : « Jouis ».”
Adolphe Thiers

“The Total Perspective Vortex derives its picture of the whole Universe on the principle of extrapolated matter analyses. To explain : since every piece of matter in the Universe is in some way affected by every other piece of matter in the Universe, it is in theory possible to extrapolate the whole of creation, every sun, every planet, their orbits, their composition and their economic and social history from, say, one small piece of fairy cake. [...] The man who invented the Total Perspective Vortex did so basically in order to annoy his wife.”
The hitchiker guide to the galaxy : The Restaurant at the End of the Universe . **Douglas Adams**

“ N’ayez jamais peur de la vie, n’ayez jamais peur de l’aventure, faites confiance au hasard, à la chance, à la destinée. Partez, allez conquérir d’autres espaces, d’autres espérances. Le reste vous sera donné de surcroît.”
Henry de Monfreid

Remerciements

« Et maintenant appelons les protagonistes... Puisque c'est la nuit du 24 avril et que nous sommes sur "l'escalier des rencontres". »
Corto Maltèse, Fable de Venise. **Hugo Pratt**.

Le travail de thèse présenté ici est le résultat de trois ans de travail au sein du groupe Quantronique. Le résultat scientifique de ce travail est l'objet du reste de ce manuscrit, ces quelques pages en revanche sont l'endroit où je me penche sur l'aspect humain de cette thèse et où je remercie toutes les personnes qui ont contribué, de près ou de loin, à la réussite de cette thèse.

En premier lieu je souhaiterais remercier Hugues et Cristián, mes deux « papas » de thèse, comme ils se sont eux-mêmes désignés lors d'une de nos premières rencontres. Avec vous j'ai appris de la physique bien-sûr, mais surtout j'ai appris à faire de la physique, à faire de la science de qualité. Vous m'avez appris (à mon corps défendant!) à ne pas tomber dans les écueils de la facilité, et que dans le plus petit signal se trouve souvent une vraie information. Merci aussi pour m'avoir apporté votre soutien dans les moments difficiles que j'ai pu traverser durant cette thèse. Cela a compté.

Hugues, tu m'as supporté en première ligne pendant trois années, merci. Merci aussi de m'avoir inculqué un peu de ton sens de la perfection. J'espère qu'un jour tu trouveras un remplaçant digne de Testpoint !

Cristián, « viejo diablo », en plus de m'avoir appris d'excellents proverbes, tu m'as appris beaucoup sur la physique, la communication, et la vie en général. Merci de ta patience. Merci aussi d'être venu si souvent faire le plein du frigo à ma place !

De grands mercis aussi à Marcelo, pour son immense contribution aux

expériences présentées dans cette thèse, pour sa bonne humeur permanente, et surtout pour ses talents de chanteur sous hélium.

Je vous souhaite à tous les trois une bonne continuation, puissent les nanofils et les modèles de Markov cachés vous porter chance, et vous aider à faire de la belle physique.

Merci au groupe Quantronique dans son ensemble qui entretient une qualité scientifique impressionnante, tout en ne négligeant pas ses qualités humaines. Les discussions sont passionnées sur tous les sujets, la politique, la culture, le sport ... et bien évidemment la physique qui n'est jamais loin ! Les réunions de groupe aussi resteront gravées dans ma mémoire : écouter une présentation scientifique tout en dégustant un bon fromage avec un verre de raisin fermenté est un plaisir tout à fait raffiné. Au sein du groupe je souhaite en particulier remercier :

- Daniel pour m'avoir appris de « ne pas me contenter d'un seul échec », et pour tout le travail qu'il fournit pour faire vivre ce groupe scientifiquement et même administrativement.
- Denis pour ses explications toujours claires, et d'avoir partagé ses connaissances physiques et techniques. Merci d'avoir, avec Michaël et Vivien, mis en place en temps record la chaîne micro-onde nécessaire à la première manipulation des états d'Andreev.
- Pief pour être quelqu'un exceptionnel, tout simplement.
- Pascal, qui a conçu une grande partie des pièces mécaniques de l'expérience. Merci aussi de m'avoir appris à me servir d'un tour et d'une fraiseuse, ce qui manquait clairement à ma formation technique.

Je veux aussi remercier tous les étudiants et post-docs du groupe (élargi) que j'ai pu côtoyer : Vivien, Olivier (un jour nous reparleront de ce fameux spectacle de danse malaisienne!), Benoît (qui n'est pas le fils caché de Patrice), Sebastian avec qui j'ai pu partager ma passion de la voile et qui m'a fait découvrir d'excellentes bières allemandes. Du côté de l'Allemagne toujours, merci à Marc pour sa bonne humeur et les discussions sur les sujets relativement pointus que sont les détecteurs supraconducteurs pour la radioastronomie, et l'administration française. Un grand merci aussi à Leandro qui a réalisé le premier échantillon sur lequel j'ai pu travailler, et

dont le dynamisme m'a toujours impressionné, et aussi parce que c'est un bon camarade. Thanks to Simon, you fucking twat for the fun of discussing with you. Merci à Maelle, François et Ramiro d'avoir rempli ma playlist de rédaction avec de l'excellente musique.

Parmi les étudiants je souhaiterais remercier spécialement Audrey, Chloé, Kiddy, Matthieu et Pierre qui sont en quelque sorte mes frères et sœurs de thèse. Les derniers mois de rédaction notamment, sont passé beaucoup plus facilement grâce à vous. Je vous souhaite beaucoup de bonheur pour la suite de vos carrières. Une dédicace spéciale à Audrey pour m'avoir si souvent ramené sur Paris après une longue journée de rédaction avec sa 106 Benny Collinet, mais aussi pour sa gentillesse, et pour son talent pour la physique. Merci à Chloé qui a réussi à garder le sourire alors même que son frigo fuyait, ou qu'elle trouvait encore une poussière sur son résonateur. Matthieu, nous avons fait notre formation de nouveaux arrivants ensemble, cela créé des liens, c'est indéniable. Les quelques poulets du dimanche midi aussi. Merci d'avoir été là quand ça n'allait vraiment pas. Thanks Kiddy for your friendship and your outsider views on French society. Quant à Pierre ce fut un plaisir de partager mon bureau avec toi lors de ces derniers mois et de déconner quand le besoin s'en faisait sentir.

Merci à Çağlar, pour les discussions scientifiques et de m'avoir hébergé à maintes reprises au Collège de France.

Je souhaite remercier Yannick Dappe pour les simulations qu'il a réalisées et qui m'ont donné une meilleure intuition de ce qu'il se passait dans nos contacts atomiques.

Je voudrais rendre hommage à tous les professeurs de physique qui m'ont permis d'arriver jusqu'ici. Que ce soit par leurs cours mais aussi par leurs conseils et leur écoute. Parmi eux je remercie en particulier Ségolène Callard et Göran Johansson.

Au sein du laboratoire je souhaite remercier le chef du SPEC : François Daviaud ; le personnel administratif : Martine, Nathalie, Corinne, pour le travail qu'elles font et qui facilite vraiment la vie. Merci aussi aux compagnons de l'atelier, Dominique, Vincent, et Jean-Claude sans qui les expériences marcheraient beaucoup moins bien ou même pas du tout. Mon frigo ayant relativement bien fonctionné durant ces trois années, je n'ai que peu eu recourt aux services de P.P. , Philippe et Matthieu, mais je les remercie de leurs bons conseils. Merci aussi à Pierre Janvier, au magasin, pour avoir toujours réussi à nous dégoter une bouteille d'hélium quand on s'y

prenait au dernier moment. Merci à tout le reste du SPEC, qui a contribué de près ou de loin à cette thèse.

Hors du laboratoire je remercie les sponsors officiels de cette thèse Maxime et les grumeaux (Elise et Clément), pour m'avoir offert des bières, des repas, pour m'avoir soutenu dans les moments les plus durs, et m'avoir fait sortir de chez moi. Merci aux amis de toujours, Henri, Valentin, Antoine, Quentin et les autres. Merci à Emmanuel pour avoir apporté une certaine fraîcheur dans le groupe au moment où tous les thésards se mettaient à rédiger. Merci à S.A. et A.R. pour l'aide précieuse qu'elles m'ont apporté. Merci à Camilla, Anil, Pierre, Adèle, Jean, Indranil, Matthias, pour m'avoir rappelé que, non, je ne suis pas le seul à faire une thèse. Merci à Raphaëlle pour les discussions et les parties de squash. Merci à tous les amis qui de près ou de loin ont participé à cette aventure de trois ans.

Enfin merci à ma famille qui a organisé un pot mémorable et surtout pour être encore là malgré les épreuves de ces dernières années. Merci de m'avoir soutenu jusqu'au bout.

Contents

Acronyms

2DEG:	Two-Dimensional Electron Gas
ABS:	Andreev Bound States
ADC:	Analog to Digital Converter
AFG:	Arbitrary Function Generator
CPMG:	Carr-Purcell-Meiboom-Gill
CPR:	Current Phase Relation
CPW:	Coplanar Waveguide
CQED:	Cavity Quantum Electrodynamics
cQED:	circuit Quantum Electrodynamics
CW:	Continuous Wave
DOS:	Density Of States
FWHM:	Full Width at Half Maximum
HMM:	Hidden Markov Model
I,Q:	In phase quadrature (I) and out of phase quadrature (Q)
MCBJ:	Mechanically Controllable Break Junction
PID:	Proportional–Integral–Derivative controller
PSD:	Power Spectral Density
RWA:	Rotating Wave Approximation
VNA:	Vector Network Analyzer

Chapter 1

Introduction

1.1 The internal degree of freedom of Josephson junctions

Superconducting electronic devices - like the well-known SQUID - are nowadays used in a variety of fields, ranging from astrophysics to medical applications, which exploit their extreme sensitivity to magnetic fields and microwave fields. Future technologies may use rapid single-flux quantum circuits for low-energy or high speed computation [1], and superconducting qubits for quantum processors [2] or quantum simulators [3]. All superconducting circuits, with the notable exceptions of kinetic inductance detectors [4] and superconducting single-photon detectors [5], rely on a fundamental phenomenon: the Josephson effect.

The first theory of this effect was established by Brian Josephson in 1962 [6]. He predicted that a non-dissipative current of Cooper pairs could flow through an insulating barrier between two superconducting electrodes, when a superconducting phase difference is applied between them. Moreover, he predicted that under a voltage bias, the supercurrent oscillates in time. These subtle and rich phenomena are surprisingly described with just two simple equations, the famous Josephson equations.

In fact, Josephson supercurrents arise not only through insulating tunnel barriers but also through any weak link between superconductors —like semiconducting and normal metal nanowires, or magnetic layers —provided it is short enough for the electrons to keep their quantum coherence all

along. The mesoscopic theory of the Josephson effect [7, 8], developed in the nineties, provided a unified description treating all weak links on the same footing, and showed that there is more to the Josephson effect than the Josephson equations. In this framework the supercurrent is carried through a set of discrete quasiparticle states localized at the weak link. The energy of these "Andreev states" is within the superconducting energy gap of the bulk, and is governed by the superconducting phase difference and by the electron transmission probability through the weak link. In the simplest case of a single-conduction-channel weak link, short with respect to the superconducting coherence length, the Andreev set reduces to a two-level system. The link between Andreev states and supercurrent has already been explored with experiments on atomic contacts [9, 10, 11, 12].

The Andreev two-level system can be viewed as an internal degree of freedom of the Josephson weak link, and it has been proposed as a new kind of superconducting qubit [13, 14, 15]. This internal degree of freedom has been probed through spectroscopy, which has been achieved in atomic contacts [16] and in carbon nanotubes [17, 18]. Moreover, measurements of the AC-response of a superconducting ring hosting a normal metal weak link showed that its susceptibility at high frequencies could be understood in terms of the dynamics of Andreev states [19, 20].

The goal of my thesis work was to observe and quantify the coherence of Andreev two-level systems. In this aim, two experimental requirements had to be fulfilled. On the one hand, one needed a simple system hosting only a few, and preferably just one, conduction channels: this was achieved by creating atomic contacts between two superconducting electrodes [21] using the microfabricated mechanically controllable break junction technique (MCBJ) [21]. On the other hand, one needed means to manipulate and read-out the state of the Andreev two-level system. This was achieved by coupling the Andreev system to a microwave resonator (or cavity), and using the well-developed techniques of cavity [22] and circuit [23] quantum electrodynamics (cQED). Essentially, the state of the system is probed by detecting a shift in the resonance frequency of the resonator. This basic principle has by now been successfully applied to probe many different systems: superconducting qubit [24, 25], spins [26, 27, 28], quantum dots [29], nano-mechanical oscillators [30]. It was therefore natural to turn ourselves to cQED and to combine it with the MCBJ technique to achieve the coherent manipulation of Andrev bound states.

1.2 From the Andreev dot to the Andreev qubit

When a phase bias is applied to a Josephson weak link, superconductivity is locally frustrated. As a response, localized energy levels appear within the superconducting gap in the excitation spectrum. When the junction is constituted by a short, single conduction channel weak link of normal state transmission probability τ, a single energy level appears at an energy $E_A < \Delta_{sc}$, the Andreev energy:

$$E_A = \Delta_{sc}\sqrt{1 - \tau \sin^2(\delta/2)}, \tag{1.1}$$

with Δ_{sc} the superconducting gap energy of the electrodes and δ the phase difference across the weak link. Because this energy level lies within the superconducting gap, the corresponding states cannot propagate into the electrodes and are localized at the weak link. By analogy with semi-conducting circuits where electrons are localized with electrostatic barriers in "quantum dots", the weak link can be seen as an "Andreev dot" [31]. This picture accounts for the physics at subgap energies, but it should be kept in mind that the propagating states at energies larger than the gap are delocalized across the weak link. The phase gradient across the weak link only localizes subgap states, which spatially overlap with higher energy states. The Andreev level in the Andreev dot can be occupied by 0, 1 or 2 quasiparticles, which corresponds, taking into account the 2 spin directions, to 4 states, see Fig. 1.1:

- The ground state $|g\rangle$ with no quasiparticle in the Andreev level;
- The two "odd states" $|o\uparrow\rangle$ and $|o\downarrow\rangle$ with a single quasiparticle of either spin in the Andreev level;
- The even excited state $|e\rangle$ with two quasiparticles with opposite spin in the Andreev level.

The two-level system constituted by the even states $|g\rangle$ and $|e\rangle$ was proposed as a qubit by Zazunov *et al.* [13]. This qubit is markedly different from the other superconducting qubits in two respects:

- It is of microscopic nature. All other superconducting qubits (historically classified into charge, flux or phase qubits [33]) rely on electromagnetic modes of a circuit containing one or a few tunnel Josephson junctions, the Josephson junction acting as a non-linear inductor.

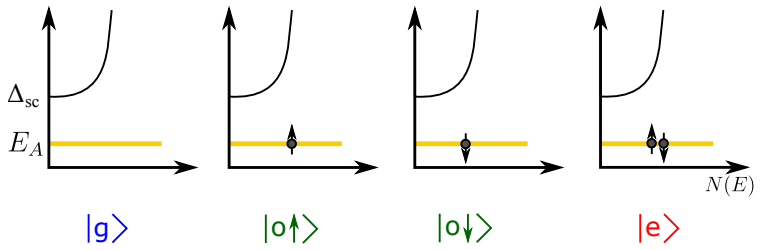

Figure 1.1: Low-energy excitation spectrum of an Andreev dot in a short weak link. In blue and red are the even states, which correspond to the states of a single superconducting pair localized at the weak link. They constitute a two-level system, the "Andreev qubit". The two odd states (green) correspond to the single occupancy of the spin-degenerate Andreev level. Note that in presence of subgap Andreev states, the DOS $N(E)$ is also modified at $E > \Delta_{sc}$ [32].

- It is a "true" two-level system. In other superconducting qubits, which are anharmonic oscillators, the Josephson junction is responsible for unevenly spaced energy levels, which allows to address separately the two lowest ones. Depending on the anharmonicity introduced by the junction, higher energy levels can also be accessed. In the Andreev qubit, the closest excitation above the Andreev level is either that of another Andreev level (if several channels are present), or the superconducting gap, typically at an energy ten times larger than the Andreev energy in our experiments.

1.3 Obtaining Andreev dots

In order to implement experimentally the model described above, we used single atom contacts between two superconducting electrodes made of aluminium. Such atomic contacts have been shown [34] to support a few conduction channels with transmission that can be higher 0.99. Several techniques exist to produce such contacts [35, 36]. The one used on the experiments presented in this thesis is the microfabricated mechanically controllable break junction (MCBJ) technique [37, 38, 21]. It makes use of

a suspended bridge microfabricated on a flexible substrate (see Fig. 1.2). When the substrate is bent, the bridge elongates and ultimately breaks. Subsequent fine tuning enables achieving a single-atom contact. Moreover, it has been shown [34] that the strain on the contact modulates its transmission. Different Andreev qubits with various transition energies can therefore be explored by adjusting the bending of the substrate.

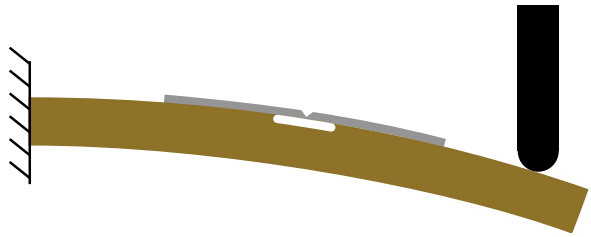

Figure 1.2: Side view of a mechanically controllable break junction. The substrate of the chip (in brown) is firmly clamped on its left end and in contact with a pushing rod on its right end. The pushing rod can moves up and down to adjust the bending of the substrate. On top of the substrate is a microfabricated bridge with a constriction. As the substrate is bent, the bridge elongates, the strain being concentrated at the constriction. The bridge ultimately breaks but can be reformed (under high vacuum conditions) for fine tuning.

1.4 Andreev dots in a cQED architecture

The circuit QED (cQED) architecture is now widely used to measure superconducting qubits. It consists in coupling a qubit to a microwave resonator. The resonance frequency of the resonator —which is easily detected— depends on the state of the qubit. The theoretical description of this architecture for superconducting qubits is due to Blais *et al.* [23]. It was later adapted to Andreev dots by Romero *et al.* [39], who considered a half-wavelength microwave resonator galvanically coupled to the qubit. In our experiments, we use a quarter-wavelength resonator inductively coupled to the Andreev dot. The whole circuit is realized on a plastic substrate because of the mechanically controllable break junction technique used to

obtain weak links. A micrograph of a sample is shown in Fig. 1.3.

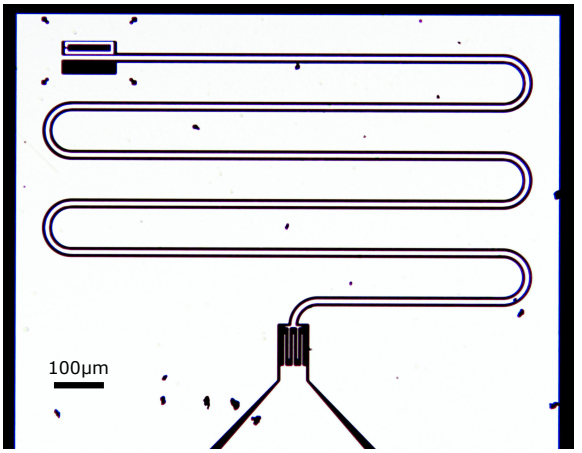

Figure 1.3: Micrograph of one of the samples used in this work (BR3). Dark regions are insulating, clear regions are superconducting. The resonator is constituted by a superconducting (Nb) quarter-wavelength meander line at the end of which is placed a superconducting loop (Al) in which the break junction is embedded (top left). The resonator is coupled to the measurement line through an interdigitated capacitor visible at the bottom of the picture.

The coupling between the resonator and the qubit is characterized using single-tone spectroscopy. The reflection coefficient S_{11} of microwaves with a frequency close to that of the uncoupled ("bare") resonator frequency is measured as a function of the superconducting phase difference δ across the weak link. The qubit and resonator frequencies coincide, an avoided crossing is observed, see Fig. 1.5. The fit of this avoided crossing gives access to the coupling between the qubit and the resonator, here ≈ 80 MHz. The resonance of the uncoupled resonator is also faintly observed at all phases. This is a first indication that the Andreev dot is often found in one of the odd states.

When the qubit is detuned from the resonator, the state of the qubit is inferred from the shift of the resonator frequency. In practice, one sends microwave pulses at the frequency of the bare resonator. The in-phase (I) and in-quadrature (Q) amplitudes of the reflected signal are represented,

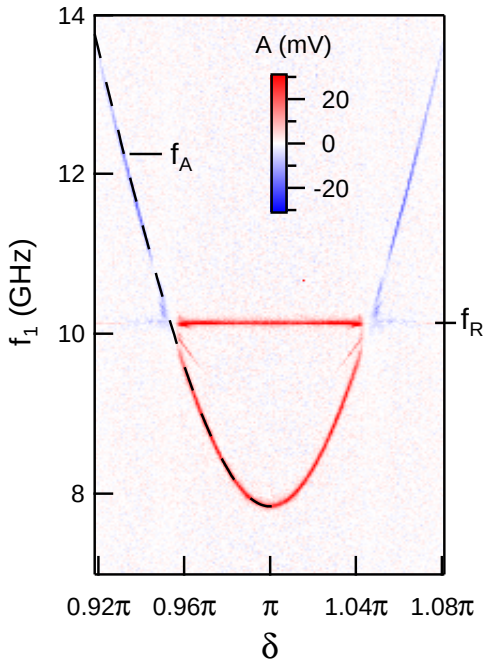

Figure 1.4: Two-tone spectroscopy of the Andreev transition. The dashed line is a fit using Eq. 1.1 obtained for a transmission of the conduction channel $\tau = 0.99217$.

for each pulse, by a point in the (I,Q) plane. A histogram of the results of $\approx 10^4$ pulses is shown in Fig. 1.6.

The data gather in three clusters of points that correspond to the dot being in one of its three states $|g\rangle$, $|e\rangle$ and $|o\rangle$. The large separation between clusters is remarkable because it was achieved without a quantum-limited amplifier as it is normally required for other superconducting qubits. The number of points in each cluster normalized by the number of measurements, corresponds to the population of the states of the Andreev dot, revealing in particular the fact that the Andreev dot is about half of the time in an odd state.

The first application of this pulsed measurement procedure is the spectroscopy of the Andreev transition. Figure 1.4 shows the amplitude of the in-phase quadrature as a function of the superconducting phase difference

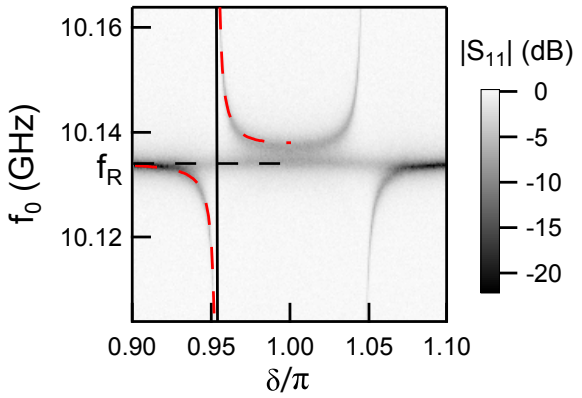

Figure 1.5: Amplitude of the reflection coefficient S_{11} of the resonator as a function of the phase difference δ across the contact and the microwave frequency f_0. The Andreev transition frequency is represented with the thick black line, which at this scales appears vertical. An avoided crossing is observed, fitted with dashed red line. The bare resonance is also observed at all phases, which shows that the Andreev dot spends a significant fraction of time in an odd state, in which the resonator is unaffected by the qubit.

across the weak link and the frequency of a microwave pump pulse applied just before the resonator is probed. The superconducting phase dependence of the Andreev transition is fitted with the theoretical prediction $f_A = 2E_A/h$, with E_A given by Eq. 1.1. At $\delta = \pi$, the spectroscopy line has linewidth of 16 MHz, which is 2 orders of magnitude smaller than what was previously reported [16].

1.5 Probing the coherence of Andreev qubits

The main contribution of this thesis is the experimental demonstration and characterization of the coherence of Andreev qubits. Figure 1.7 shows results obtained on one of the the Andreev qubits that we have measured. Rabi oscillations (panel A) are obtained by measuring the populations of the qubit after a driving pulse of varying length. The observation of these oscillations constitutes the first signature of the quantum coherence of the

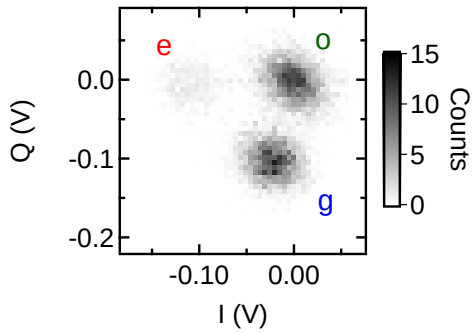

Figure 1.6: Histogram in the (I,Q) plane of the signal reflected by the resonator. I and Q are the in-phase and in-quadrature amplitudes of a microwave pulse reflected by the resonator. The data gather in three well separated clusters that can be identified as corresponding to the different states of the Andreev dot.

Andreev qubit. The decay of the amplitude of these oscillations is linked to the lifetime of the excited state T_1 and to the dephasing time of the qubit T_2^*. In order to quantify these two quantities independently, two other experiments are performed. In the first one, populations of $|g\rangle$ and $|e\rangle$ are inverted using a "π-pulse", and the relaxation to equilibrium is observed by measuring the populations after a delay. An exponential decay is observed with a characteristic time T_1 of the order of a few microseconds (here 1.3 µs). This time is comparable to other superconducting qubits but is significantly smaller than predicted theoretically, as it will be discussed in chapter 4. The dephasing time is measured using a Ramsey sequence; a first a "$\pi/2$" microwave pulse sets the qubit in an equal superposition of ground and excited state. After a varying delay a second $\pi/2$-pulse is applied and the populations are measured. From the Gaussian envelope of the population oscillations, one deduces the dephasing time T_2^* which is typically between 10 ns and 200 ns (here 188 ns). This time is small compared to other superconducting qubits [40, 41]. More information on the source of dephasing of the Andreev qubit is provided by a Hahn-echo sequence. It consists in a Ramsey sequence with a π-pulse applied midway between the $\pi/2$-pulses. This sequence filters-out the low frequency noise

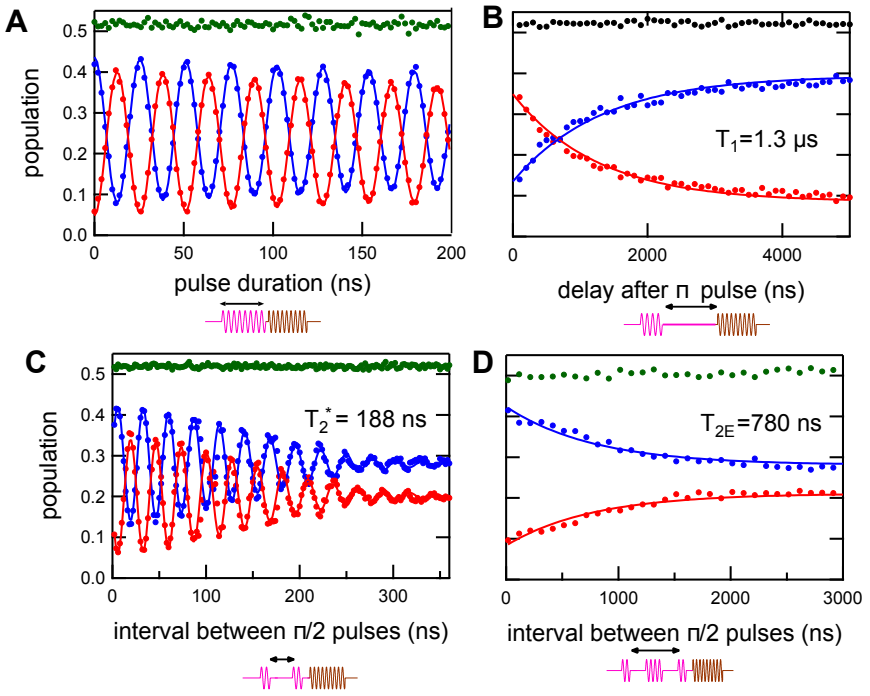

Figure 1.7: Characterization of the Andreev qubit obtained for a contact with a transmission $\tau = 0.99806$. Green dots represent the population of the odd states, blue dots the population of the ground state and red dots population of the excited state. The pulse sequence associated to each experiment is represented below with the qubit driving pulse represented in magenta and measurement pulse in brown. (A) Rabi oscillations; (B) Relaxation of the excited state; (C) Ramsey fringes (note the gaussian decay of the oscillations); (D) Hahn-echo. This dataset shows the longest ramsey decay time observed during this thesis.

to which the Ramsey sequence is mainly sensitive to. A much larger decay time is observed, here T_{2E} =780 ns, which suggests that low frequency (lower than $T_{2E}^{-1} \approx 2$ MHz) noise is the main source of decoherence for the

Andreev qubit. As discussed in chapter 4, the decoherence results mainly from transmission fluctuations of the weak link, although the source of these fluctuations remains to be determined.

1.6 Probing the resonator using the Andreev qubit

Estimating the number of photons in the resonator for a given microwave power at the input of the microwave lines is important to quantify the measurement strength [42]. This relation can be estimated from a calibration of the attenuation of the microwave lines in the refrigerator, at room temperature. Because this attenuation varies when cooling down to low temperatures, *in situ* calibration techniques are to be preferred. Experiments that exploit the dispersive coupling between the qubit and the resonator can be used to access the photon population of the resonator [43]. However these experiments have stringent requirements in terms of dephasing time of the qubit. Here, we found that the number of photons in the resonator could be accessed through the spectroscopy of the Andreev qubit performed in presence of a second microwave tone at a frequency close to the resonator frequency. The spectroscopy line of the Andreev qubit is strongly affected by the frequency and power of this microwave tone, as shown in Fig. 1.8. Steady state population inversions and cooling of the qubit are observed. By comparing the result of these experiments with simulations, we showed that the frequency at which they are observed gives access to the photon population in the resonator (see chapter 5).

1.7 Observation of quantum and parity jumps in an Andreev dot

The dynamics of quasiparticles in an Andreev dot was already accessed in a previous work by using the switching current measurements of an atomic contact [44]. However, the even excited state of the Andreev dot could not be observed in these experiments. The effects of single [45, 46, 47], or a few [48, 49] quasiparticles were detected in other superconducting devices. Moreover it has been observed that out-of-equilibrium quasiparticles are present below 100 mK in aluminium [50, 51, 52].

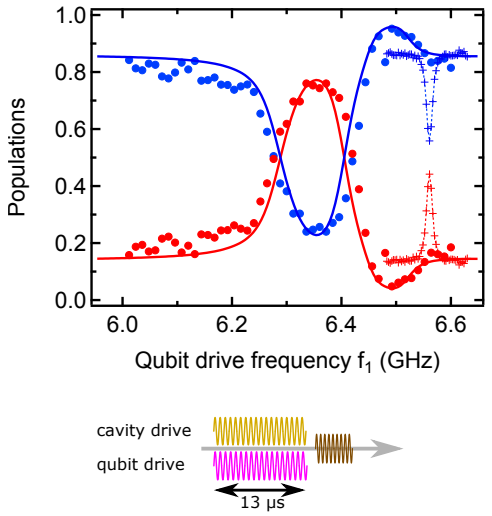

Figure 1.8: Three-tone spectroscopy in presence of a cavity drive at the frequency of the resonator when the qubit is in the ground state. Dots are experimental data and full lines the result of simulations. The blue (red) dots represent the renormalized population of the ground (excited) state so the population of the odd states is not taken into account. The qubit is cooled down when the qubit driving frequency is close to the natural Andreev transition frequency (crosses); at a lower frequency that depends on the photon number, the population of the qubit is inverted.

In experiments where the state of the Andreev dot was continuously monitored, quantum jumps between the ground and excited states as well as parity jumps due to the trapping or un-trapping of a single quasiparticle in the dot were observed. This was performed by measuring continuously the signal reflected by the resonator for durations much longer than the characteristic lifetimes of the different configurations of the Andreev states. This signal was then reconstructed using a Bayesian statistics model known has a hidden Markov model (HMM) [53, 54]. Figure 1.9 shows the result of such a continuous measurement along with the evolution of the state of the dot inferred by the HMM algorithm. The rates extracted from this reconstruction provide information on the influence of the measurement power and the phase difference on the dynamics of the Andreev dot.

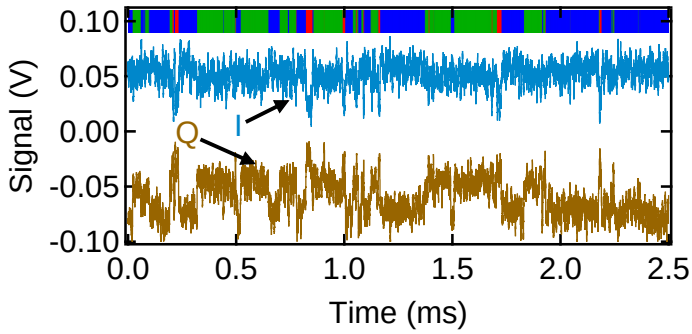

Figure 1.9: Variations during 2.5 ms of the in-phase (I) and out-of-phase (Q) amplitudes of the signal reflected by the resonator. Jumps are observed and analysed using a hidden Markov model algorithm. The top bar shows the color-coded state of the qubit deduced from this analysis: blue when the qubit is in $|g\rangle$, green when it is in $|o\rangle$, red when it is in $|e\rangle$.

Chapter 2

The Andreev dot

In all generality a Josephson junction is constituted by two superconducting electrodes separated by a weak link. The mesoscopic description of the Josephson effect was provided by Beenakker [8]. It relies on the description of the weak link in terms of conduction channels and the apparition of subgap states in each channel: the Andreev bound states (ABS). Because these states are localized by Andreev reflection, one cites of an "Andreev dot" [31].

In this chapter, we give a short theoretical description of the Andreev bound states, and an overview of their experimental manifestations. We then show how these states can be used to define a qubit, the Andreev qubit. Finally the Andreev qubit is compared with the other types of superconducting qubits.

2.1 Andreev bound states

2.1.1 Foreword on representations

In the following discussion two representations are used to describe the energy spectrum superconducting structures. The first one is the one most commonly used in mesoscopic superconductivity papers and is called the "one-particle picture" or semiconductor picture. It is particularly convenient to describe transport experiments. The second one, the "excitation picture", is more adapted to discuss the Andreev qubit. In order to facilitate the understanding for readers used to the semiconductor picture, both

representations are used in parallel in the following discussion. However, only the excitation picture is used in the rest of the thesis. In a nutshell, the one-particle picture represents states that are, in the ground state, all filled up to the Fermi energy and excitations either with empty states below E_F or occupied states above E_F. In contrast, the excitation picture only represents quasiparticle excitations [16].

2.1.2 A weak-link between two superconductors

Bulk superconductors The ground state of a bulk superconducting electrode is a BCS condensate of delocalized pairs characterized by a complex superconducting order parameter $\Delta = \Delta_{sc} e^{i\phi}$. If no current or magnetic field is applied the phase ϕ is homogeneous in the electrode. In the semiconductor picture, the density of states (DOS) consists in two bands symmetric with respect to the Fermi energy and separated by an energy $2\Delta_{sc}$. The excitation spectrum is shown in Fig. 2.1. The lowest energy excitation consists in adding a single quasiparticle (either a quasielectron in the empty, positive energy band, or a quasihole in the filled, negative energy band), which requires at least an energy Δ_{sc}. This excitation having an odd number of quasiparticles, it has a parity different from that of the ground state. In contrast, excitations can be obtained without parity change, for example by absorption of photons. The lowest energy excitation of even parity results in the breaking of a pair into 2 quasiparticles. This excitation requires a photon with an energy $h\nu \geq 2\Delta_{sc}$.

Two electrodes separated by a single conduction channel When two electrodes are coupled through a weak-link a phase difference $\delta = \phi_L - \phi_R$ can be sustained by the system, see Fig. 2.2. This phase difference frustrates superconductivity at the weak link. The condensate accommodates this frustration by the apparition of pairs of subgap states localized at the weak link, the Andreev bound states.

Here, we consider the case of a short weak link with a single conduction channel. We adopt a mesoscopic description of electrical transport through this channel, the sole parameter being τ, the normal state transmission probability of electrons through the channel (see Fig 2.2). In this situation,

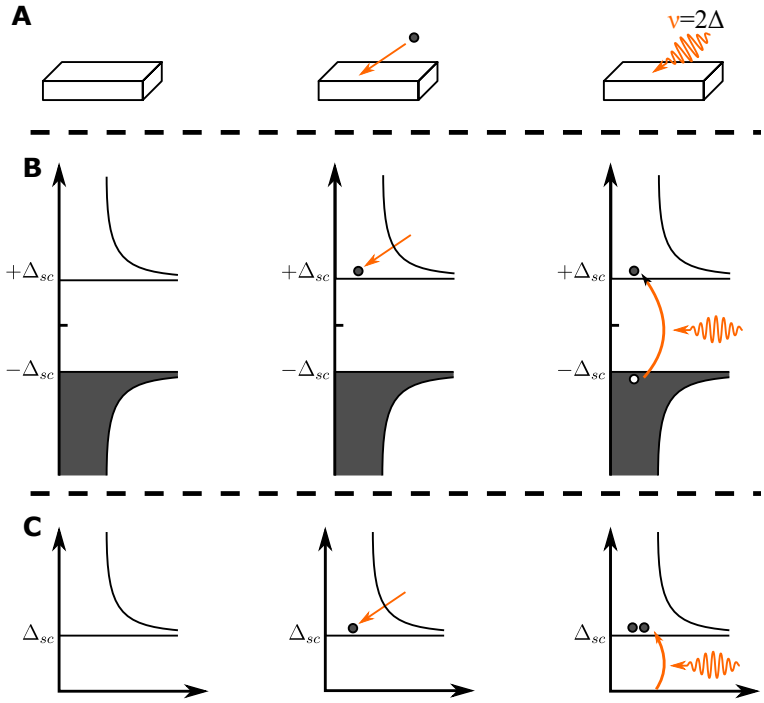

Figure 2.1: Ground state and lowest energy excitations of a superconducting electrode. A: Illustration of the electrode. B: Lowest energy excitations in the single-particle representation. C: Lowest energy excitations in the excitation picture. Vertical axis is the energy, horizontal axis is the DOS. From left to right: ground state, lowest energy odd excitation, lowest energy even excitation.

a single pair of energy levels appear within the gap at energies given by [8]:

$$E_A = \pm\Delta_{sc}\sqrt{1-\tau\sin\left(\delta/2\right)}. \tag{2.1}$$

The ground state $|g\rangle$ of this system is still a condensate of pairs, all of them being delocalized but one, which is localized at the contact and has an energy $-E_A$. The semiconductor representation illustrates best the phase dependence of the energy of the ground state ($-E_A$), which is at the origin of the Josephson supercurrent. Note that in the absence of frustration (*i.e.*

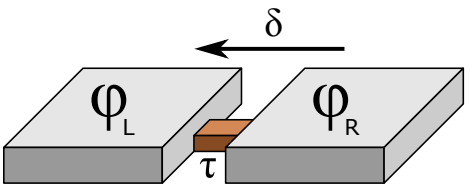

Figure 2.2: Two superconducting electrodes separated by a short weak link accommodating a single channel of transmission τ.

when $\delta = 0$), $E_A(0, \tau) = \Delta$ and the state of the dot is the same as in the single electrode case with a modified density of states in the continuum.

The excitations are of the same nature as in the single electrode case. The lowest energy excitations with odd parity, $|o\uparrow\rangle$, and $|o\downarrow\rangle$ have a single quasiparticle. In the semiconducting picture, they are represented as an electron-like quasiparticle in the level at energy $+E_A$ or a hole-like quasiparticle in the level at energy $-E_A$. The ground state energy being $-E_A$, $|o\uparrow\rangle$ and $|o\downarrow\rangle$ have zero energy. In the excitation picture, they correspond to the presence of a quasiparticle of either spin in the level at energy $+E_A$, as shown in Fig. 2.3. The lowest energy excitation with even parity, $|e\rangle$, consists in exciting a Cooper pair. In the semiconducting picture, this is represented as a transition from levels $-E_A$ to $+E_A$, and requires a photon of energy $h\nu = 2E_A$. In the excitation representation, the Andreev level gets occupied with two quasiparticles (one of each spin). Since this double excitation has a subgap energy, it cannot decay as easily as two quasiparticles in the continuum, and it remains localized at the weak link. In this particular situation, the photon has not "broken" a pair, it has only excited it.

The Andreev qubit [13] is the two-level system constituted by the ground state $|g\rangle$ of the Andreev dot and its lowest energy even excitation $|e\rangle$.

The energy of the states of the Andreev dot as a function of the phase difference δ across the weak link is shown in Fig. 2.4. The transition energy between $|e\rangle$ and $|g\rangle$ reaches its minimum value $2\Delta_{sc}\sqrt{1-\tau}$ at $\delta = \pi$. The supercurrent carried by the states $|g\rangle$ and $|e\rangle$, shown in Fig. 2.5, is proportional to the first derivative of the Andreev energy and is given by

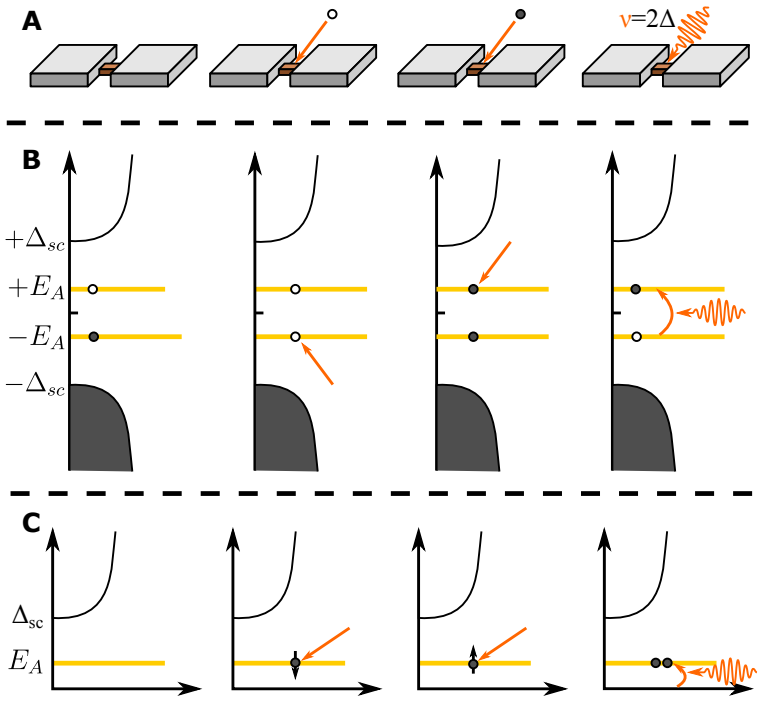

Figure 2.3: Lowest energy excitations of the Andreev dot. A: illustration of the weak link. B: single-particle representation. C: excitation representation. The ground state is still a condensate of pairs. The single-particle representation illustrates that its energy is $-E_A$. The lowest energy excitations of odd parity result from the addition of a single quasi-particle. The lowest energy excitation with even parity has two quasiparticles in the Andreev levels. It can be seen as the excitation of a Cooper pair localized at the contact, with an energy $2E_A$.

[8]:

$$I_A(\delta,\tau) = \pm\frac{\Delta_{sc}}{4\phi_0}\frac{\tau\sin(\delta)}{\sqrt{1-\tau\sin^2(\delta/2)}}. \tag{2.2}$$

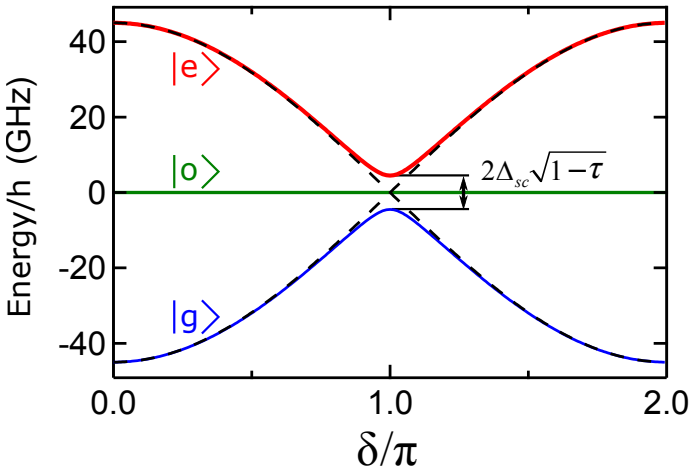

Figure 2.4: Energy of the states of the Andreev dot (in frequency units) as a function of the phase difference δ across the contact, taking for Δ_{sc} the gap of aluminum $h \times 45$ GHz, and a transmission $\tau = 0.99$. Dashed lines: $\tau = 1$.

2.1.3 Experimental evidences of the Andreev bound states

Since the microscopic description of the Josephson effect relies on the Andreev bound states, one could argue that any observation of the Josephson effect is an evidence of Andreev bound states. Nevertheless the supercurrent in tunnel junctions can also be described using perturbative theories (as Josephson did), and ABS do not need to be invoked. We focus here on the most direct and quantitative evidences before this work without the pretension of exhaustiveness.

Evidences for the phase-dependent energy of the ground state

At equilibrium, Andreev bound states are revealed by the current-phase relation (CPR) of weak links (see Fig. 2.5), in particular when the weak link contains few conduction channels. The first measurement of the CPR of few-channel weak links was performed by Koops *et al.* [55] but the weak links

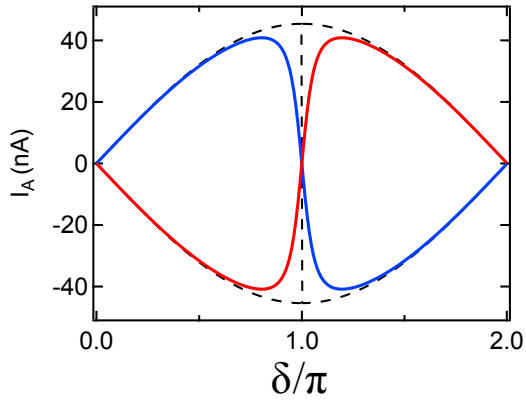

Figure 2.5: Current carried by the even state $|g\rangle$ (blue) and $|e\rangle$ (red) as a function of the phase difference δ across the contact. Thick lines : aluminium weak link with $\Delta_{sc}/h = 45$ GHz, and transmission $\tau = 0.99$. Dashed lines: aluminium weak link, $\tau = 1$.

could not be characterized independently. In order to characterize the weak links, Della Rocca *et al.* [56] placed an atomic contact in a superconducting loop in parallel with a Josephson junction having large critical current. From a fit of the I-V characteristic of the circuit with the theory of Multiple Andreev Reflections (MAR), the number of conduction channels and their transmissions could be determined precisely. The CPR of the weak link was revealed by the modulation of the switching current of the circuit. Quantitative agreement between measurements and theory was found.

Refined SQUID geometries were used to access the current-phase relations of carbon nanotubes weak links [57]. The results were consistent with a model in which two degenerate channels contribute to the supercurrent. Competition between superconductivity and Kondo effect was investigated by measuring the CPR on a similar setup [58]. Recently, similar measurements were performed on bismuth nanowires [59] in which the interplay between the Andreev bound states with spin-orbit interaction is expected to alter significantly the CPR [60].

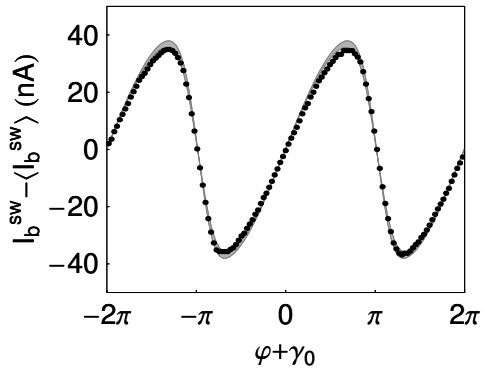

Figure 2.6: Current-phase relation of an atomic contact (from [11]). Dots: measured switching current as a function of the phase difference across the weak link. Gray line: Theoretical prediction at finite temperature for two conduction channels of transmissions $\tau_1 = 0.95$ and $\tau_2 = 0.185$.

Probing the excited state

Multiple Andreev Reflection The first phenomenon that reveals transitions between the ground and excited Andreev states is related to the finite-voltage current in a weak link. At subgap voltages, it is well established that the current is due to multiple Andreev reflections (MAR), which correspond to electron- or hole-like quasiparticles bouncing back and forth between the two electrodes [61]. MAR were used in Scheer *et al.* [34] to characterize the transmissions of channels in atomic contacts. The picture of Andreev bound states revealed powerful to describe the low-voltage regime, at the transition between the supercurrent and MAR. When the voltage is very small, a weak link can be described with Andreev levels, the phase δ increasing linearly with time: $\dot{\delta} = \frac{V_{bias}}{\phi_0}$. An AC current is associated with the corresponding variations of the supercurrent. A finite DC current is associated to Landau-Zener [62, 63] transitions (see Fig. 2.7) from the ground state to the excited state near $\delta = \pi$, as described in Ref. [64].

Quasiparticle injection spectroscopy In recent years, several experiments performed Andreev states spectroscopy by tunneling: on carbon nanotubes [17] (see Fig. 2.8), nanowires [65], graphene [66], or quantum dots [67]. Tunneling spectroscopy relies on the fact that the differential

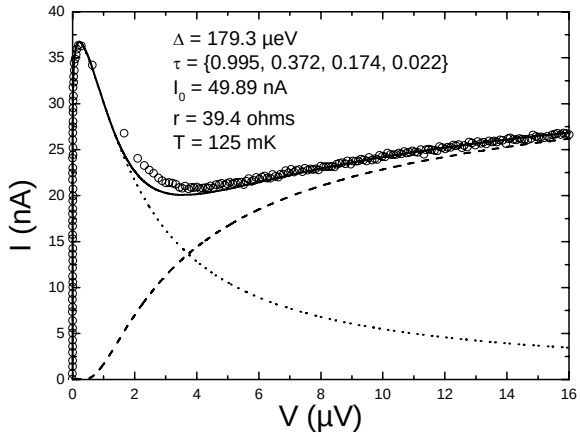

Figure 2.7: Supercurrent peak of a contact containing a high transmission channel. Open circles are experimental data. Dashed lines represent the MAR current, dotted line the current due to Landau-Zener transitions at 125 mK, and the thick line the result of the combination of the two. Taken from [10].

conductance between a normal electrode and a system of interest is proportional to the density of states of the latter. Since quasiparticles are injected by tunneling, this type of spectroscopy probes transitions between odd and even states.

Josephson spectrometer The first photon spectroscopy of ABS was performed by Bretheau *et al.* [68] using a Josephson spectrometer [69]. The method relies on dynamical Coulomb blockade [70], which in this case corresponds to inelastic tunneling of Cooper pairs. When a Josephson junction is biased at a voltage V such that $eV_{bias} < 2\Delta_{sc}$, Cooper pairs can tunnel inelastically through the junction only if a photon at an energy $2eV_{bias}$ can be absorbed by the environment of the junction. This gives rise to a net subgap current in the I-V characteristic of the junction. In the case of the experiments performed by Bretheau *et al.*, Andreev bound states localized a single-atom contact containing a few conduction channels were part of the

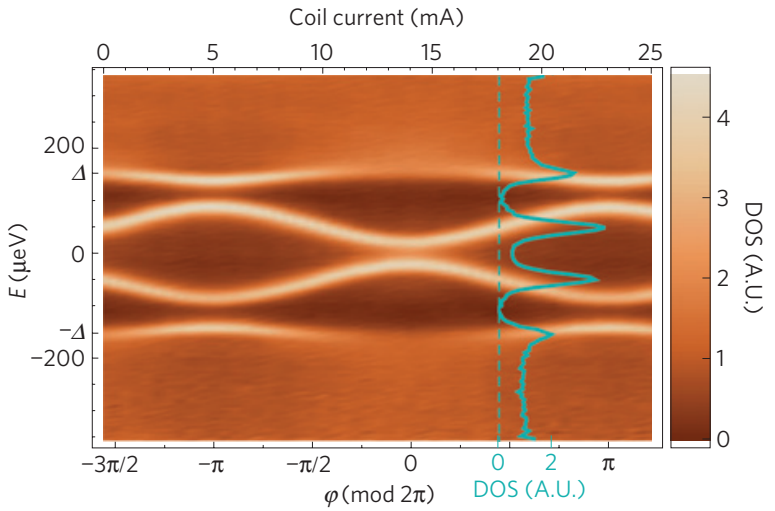

Figure 2.8: Tunnel spectroscopy of a carbon nanotube connected to aluminium contacts. The differential conductance of the tunnel probe as a function of the phase difference ϕ across the weak link and the bias voltage of the probe. The ABS are clearly visible as bright 2π-periodic lines. Taken from Ref. [17]

environment of the junction and were revealed as current peaks at voltages corresponding the Andreev transition frequency, see Fig. 2.9. Such a spectroscopy gives access to energies as high as $4\Delta_{sc}$. A difficulty is that the requirement to measure the I-V characteristic of the junction coupled to the Andreev levels gives rise in practice to an electromagnetic environment hard to control, which results in a poor lifetime of the excited state and to decoherence. As a result, the linewidth of the spectroscopy lines was large, about 1 GHz.

Very recent experiments used the same setup to perform the spectroscopy of ABS in semiconductor nanowires that exhibit spin-orbit interaction effects [71].

Experiments of diffusive wires Signatures of the dynamics of ABS in diffusive weak links with a large number of channels were observed by Dassoneville *et al.* [20]. The weak links consisted in short metallic gold

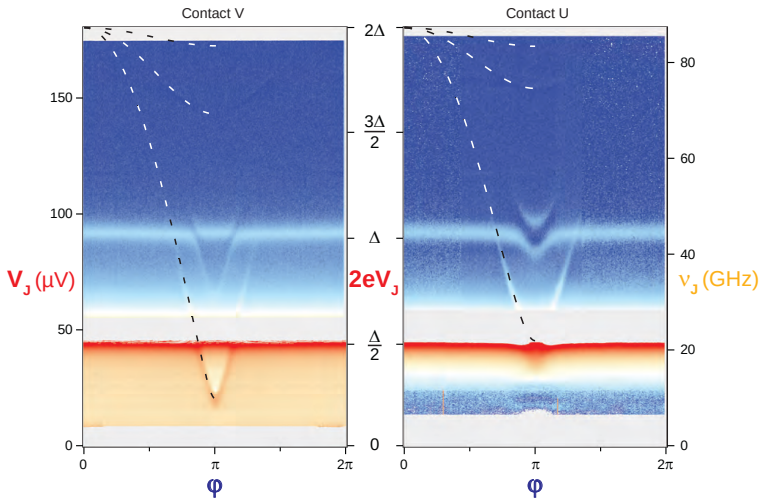

Figure 2.9: Spectrum of Andreev bound states for two different contacts. The current of the Josephson spectrometer is plotted as a function of the phase difference across the contact φ and the voltage V_J across the spectrometer junction. Andreev transitions are clearly observed. Dotted lines are fits (other lines correspond to excitation of a plasma mode of the parallel Joesphson junction and to combined excitations). Taken from Ref. [16].

wires contacted at both ends to a superconducting electrode forming a loop, which was connected to a multimode superconducting resonator. The flux modulation of the frequency and quality factor of the different harmonics of this resonator give access to the real and imaginary part of the susceptibility $\chi(\omega) = \delta I/\delta\Phi = \chi' + i\chi''$ where $\delta\Phi$ is the oscillating flux in the loop generated by the resonator. This susceptibility was measured at various frequencies ranging from 0.2 to 2 GHz. These results are interpreted in terms of transitions between states and relaxation of the states' populations.

2.1.4 Odd states

Direct evidence for quasiparticle trapping in Andreev bound states ("quasiparticle poisoning") have been provided by only few experiments. The most detailed results were obtained with switching current measurements of SQUIDs formed by an atomic contact and a large critical current Josephson

junction [44]. The switching current of the SQUID being dependent on the current through the atomic contact, poisoning could be observed and the rate of poisoning deduced from time-resolved measurements. The poisoning rates where found to be phase-dependent, and reach values as low as 5 kHz. A theoretical modeling [72] is in qualitative agreement with the data.

Quasiparticle trapping in Andreev bound states was also observed in an aluminium nanowire used as the inductor of a lumped element resonator [73]. The high quality factor of the resonator made it possible to detect the shift of the resonance frequency of the device associated with the poisoning of a single conduction channel out of the ≈ 1000 channels of the nanowire.

More recently, quasiparticle trapping was investigated in semiconducting nano-wires [74]. In these experiments, a nanowire probed by tunneling from normal electrodes is partly covered with a thin superconducting island. The rate of poisoning was found to be in the 1-Hz range. This low rate was attributed to the geometry of the device which presumably limits quasiparticle production in the superconducting electrode.

2.2 The Andreev qubit

2.2.1 The Andreev Hamiltonian

The effective Andreev Hamiltonian describing the Andreev qubit is due to Zazunov *et al.* [14]. It is given in the basis of the ballistic states by:

$$H_A = \Delta_{sc} e^{-i\sigma_x \sqrt{1-\tau}\delta/2} (\cos(\delta/2)\sigma_z + \sqrt{1-\tau}\sin(\delta/2)\sigma_y), \tag{2.3}$$

where σ_x, σ_y and σ_z are the Pauli matrices:

$$\sigma_x = \begin{pmatrix} 0 & 1 \\ 1 & 0 \end{pmatrix}, \quad \sigma_y = \begin{pmatrix} 0 & -i \\ i & 0 \end{pmatrix}, \quad \sigma_x = \begin{pmatrix} 1 & 0 \\ 0 & -1 \end{pmatrix}. \tag{2.4}$$

This Hamiltonian can be diagonalized in the phase-dependent basis of Andreev states $\{|g\rangle\,;|e\rangle\}$ and is equivalent to that of a spin 1/2 in a magnetic field:

$$H_A = -E_A(\delta,\tau)\sigma_z, \tag{2.5}$$

with a transition energy given by:

$$hf_A = 2E_A \tag{2.6}$$

As mentioned earlier, the Andreev states carry a supercurrent through the weak link, and one can define a current operator [14]. Importantly, this operator is not diagonal in the Andreev states basis and is given by:

$$\hat{I}_A(\delta,\tau) = I_A(\delta,\tau)[\sigma_z + \sqrt{1-\tau}\tan(\delta/2)\sigma_x]. \tag{2.7}$$

Non diagonal terms in I_A allow for transitions between $|g\rangle$ and $|e\rangle$. As shown in Chapter 3, the current operator enters in the description of the coupling between the resonator used to measure the state of the Andreev qubit and the qubit itself.

2.2.2 A word on the odd states

The Andreev qubit Hamiltonian only considers the even states $|g\rangle$ and $|e\rangle$. The states with odd parity $|o\uparrow\rangle$ and $|o\downarrow\rangle$ are the basis states of another Hilbert space, and do not interact with the even states. Since they have a different parity, they can only be accessed if a quasiparticle enters or leaves the Andreev dot. Moreover these states do not carry any supercurrent. As a consequence, they constitute dark states for our experiments and do not affect coherence as long as the parity jump rate is small compared to the coherence time. The dynamics of this poisoning by single quasiparticle probed by switching experiments [44] showed that the characteristic poisoning time was of a few hundreds of µs when the Andreev energy was much smaller than the gap. As it will be shown, this time is much larger than the relaxation and coherence times of the Andreev qubits.

2.2.3 Phase biasing a superconducting weak link: the atomic rf SQUID

Experimentally the phase biasing of a weak link is realized by inserting it in a superconducting loop and applying a perpendicular magnetic field. We now discuss phase biasing of weak links in this rf SQUID geometry [75, 76].

The rf SQUID

We consider the situation sketched in Fig. 2.10. A superconducting loop containing a weak link is placed in a magnetic field that threads a flux Φ_{ext} in the loop. The junction length is assumed to be very short compared to

the loop circumference $\mathcal{C}$ and we define two close points P and Q on each side of the contact.

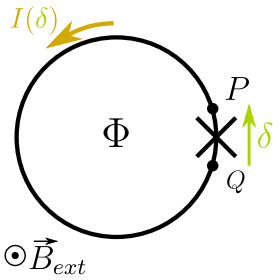

Figure 2.10: rf SQUID: a superconducting loop containing a weak link is placed in a magnetic field B_{ext} that threads a flux Φ_{ext} in the loop. A current I is circulating in the loop, so that the total flux in the loop is $\Phi \neq \Phi_{ext}$. The phase difference δ across the break junction is taken between points P and Q.

The gauge-invariant phase difference across the contact is:

$$\delta = \varphi_P - \varphi_Q - \frac{2e}{\hbar}\int_Q^P \overrightarrow{A}d\overrightarrow{s}, \tag{2.8}$$

where φ_P and φ_Q are the superconducting phases at P and Q, respectively. $\overrightarrow{A}$ is the vector potential, and $\overrightarrow{s}$ the curvilinear coordinate along the circumference of the loop. In the diffusive superconductive wire forming the loop, the supercurrent density $\overrightarrow{j}$ is related to the gauge-invariant phase φ by [77] $\overrightarrow{j} = \frac{\pi}{2}\frac{\sigma\Delta_{sc}}{e}\left(\overrightarrow{\nabla}\varphi - \frac{2e}{\hbar}\overrightarrow{A}\right)$, where σ is the normal state conductivity. Integrating from P to Q around the loop, one obtains:

$$\frac{2e}{\pi\sigma S\Delta_{sc}}\int_P^Q I(\delta)ds = \varphi_Q - \varphi_P - \frac{2e}{\hbar}\int_P^Q \overrightarrow{A}d\overrightarrow{s} \tag{2.9}$$

with S the section of the wire constituting the loop. Since the loop current $I(\delta)$ is the same everywhere and since P and Q are very close one to another, $\int_P^Q I(\delta)ds \approx I(\delta)\mathcal{C}$. Summing Eq.(2.8) and Eq.(2.9), one obtains:

$$\delta + \frac{2\pi}{\Phi_0}L_K I(\delta) = \frac{2e}{\hbar}\oint \overrightarrow{A}d\overrightarrow{s} = 2\pi\frac{\Phi}{\Phi_0}, \tag{2.10}$$

where $\Phi_0 = h/2e$ is the magnetic flux quantum, $L_K = \frac{\hbar R}{\pi \Delta_{sc}}$ is the kinetic inductance of the loop, expressed as a function of the normal state resistance of the loop $R = \frac{\mathcal{C}}{\sigma S}$. The total flux Φ being partially screened by the loop current $\Phi = \Phi_{ext} - L_g I(\delta)$, with $L_g \approx \mu_0 \mathcal{C}$ the geometrical inductance of the loop, one finaly obtains:

$$\delta = \frac{\Phi_{ext}}{\Phi_0} - \pi \beta_m \frac{I(\delta)}{I_0}, \tag{2.11}$$

where $\beta_m = \frac{2(L_K + L_g) I_0}{\Phi_0}$ is the "screening parameter" [76], with I_0 the critical current of the weak link, *i.e.* the maximum value of $I(\delta)$. Note that in our case, the contribution of the kinetic inductance can be neglected: the ratio of the kinetic and geometric inductances depends on the sheet resistance $R_\square$ and on the width w of the film forming the loop: $\frac{L_K}{L_g} = \frac{\hbar R_\square}{\mu_0 w \Delta_{sc}} \ll 1$. Equation (2.11) can be solved graphically, see Fig. 2.11.

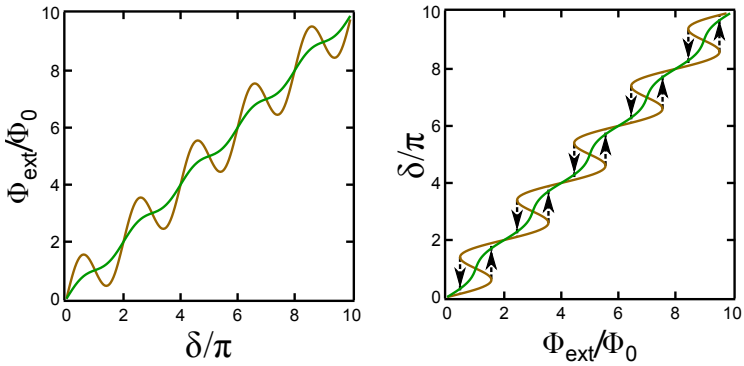

Figure 2.11: Left: Φ_{ext} as a function of the phase δ across the contact, using Eq. (2.11) and assuming for simplicity $I(\delta)/I_0 = \sin\delta$. Right: reversed plot: δ as a function of the experimental parameter Φ_{ext}. Brown: $\beta_m = \frac{1}{\pi}$. Green: $\beta_m = \frac{0.2}{\pi}$. Note the hysteresis for the largest β_m and the remaining non-linearity for the smallest one.

- If $\beta_m \ll 1$, the phase across the contact is proportional to Φ_{ext}.
- If the $\beta_m \approx 1$, the flux generated by the current in the loop has a significant influence on the the phase difference across the weak link.

This leads to a strongly non-linear relation between the phase and the applied flux.

In order to have a linear phase bias across the contact and to be able to reach $\delta = \pi$, β_m should be kept much smaller than 1 when a one-atom contact is formed. For aluminum contacts with a transmission close to 1, $I_0 \approx 50$ nA. This leads to the constraint $L_g \ll 5$ nH, or $\mathcal{C} \ll 5$ mm.

In our samples, the loop inductance was 110 pH. This is small enough to obtain a good phase biasing for single-atom contacts. But in the process of getting such contacts, weak links that accommodate many conduction channels are formed and an hysteretic response is observed, see Section 3.5.2.

2.3 Comparison of the Andreev qubit with other superconducting qubits

In the previous section we chose to present the Andreev two-level system as the "Andreev qubit", following the proposal by Zazunov *et al.* [13]. How far is the Andreev qubit more than one more superconducting qubit?

Two types of superconducting qubits are nowadays[1] used in quantum information experiments: charge qubits [79, 80, 25], and flux qubits [81, 82, 41].

The prototype of the charge qubit is the Cooper-pair box. It relies on the quantization of the charge in a superconducting island connected to a superconducting reservoir through a Josephson junction. The electrostatic potential of the island is tuned through a capacitor. This was the first superconducting qubit, demonstrated by Nakamura *et al.* in 1999 [79]. The dimension of the states space is not bounded to two levels: the circuit can be used as a qubit only if the anharmonicity[2] is sufficiently large, so that the two lowest energy states can be addressed separately from the others. In its original configuration, the charge qubit was very sensitive to charge

[1] Another type of qubit was developed in the early days: the phase qubit [78]. However it seems abandoned today.

[2] The difference in transition energy between the two lowest pairs of levels.

noise. The charge sensitivity was significantly reduced in the Quantronium [80], which can be seen as a split Cooper pair box, and the readout method was more efficient leading to improved lifetime and coherence. A further increase in the ratio of the Josephson energy to the charging energy lead to an exponentially reduced [83] charge sensitivity at the price of a smaller anharmonicity of a few 100 MHz. This new device, integrated in a circuit QED architecture, was called the transmon. It has proven very successful in the last years [40, 84, 85], with coherence times and lifetimes close to 100 µs.

The prototype of the flux qubit is an rf SQUID. As shown in the previous section, if the geometrical inductance of the rf SQUID becomes too large, the flux bias of the SQUID becomes hysteretic. In the hysteresis zone, for a given applied flux Φ_{ext}, the flux in the SQUID can have two values depending on the current direction. These two states of current constitute the ground and excited state of the qubit. The main source of decoherence of this type of qubit is flux noise. In order to reduce the size of the biasing loop, and therefore the sensitivity to magnetic noise, a three-junctions configuration was developed [81]. Yet, this type of qubit must be operated at its sweetspot where its transition energy is insensitive to first order to flux noise. Like the charge qubit, the state space of the qubit is not bounded to two levels. However the anharmonicity is much larger, exceeding 10 GHz [82]. The coherence times in flux qubits have reached 10 µs and lifetimes 18 µs [41].

These superconducting qubits are all based on Josephson junctions. Most of the realizations have used tunnel junctions; a few recent experiments have used more weak links made of semiconducting nanowires [86, 87]. All these realisations have in common the fact that they only exploit the non-linear inductance associated to the weak link. Microscopically, this inductance is related to the phase dependence of the energy of the ground state of each Andreev dot associated to the weak link channels. As a result, they all rely on the quantization of an electromagnetic, macroscopic variable in an anharmonic potential.

The Andreev qubit is markedly different. First, it relies on a localized microscopic excitation of the BCS condensate and not a collective excitation of the circuit in which the condensate remains in its ground state. Second, its state space is bounded to two levels, making it a true two-level system.

Chapter 3

Measuring the state of an Andreev dot

This chapter presents the theoretical and practical backgrounds needed to realize the experiments presented in this thesis.

As mentioned in the introduction, we measure the state of the qubit by coupling it to microwave resonator (or cavity). After presenting the classical treatment of a transmission line resonator, we show how the state of the qubit affects the resonance frequency of the resonator and how this can be detected.

In our experiments, the Andreev dot is obtained with a single-atom contact between superconducting electrodes. The mechanically controllable break junction (MCBJ) technique is used to obtain such a contact. The technique and its implementation in our experiments is presented in Section 2.

Section 3 presents the samples design and fabrication. A first estimation of the coupling between the Andreev qubit and the resonator is also presented. The microwave setup is described in Section 4.

In previous works, I-V characteristics were used to characterize atomic contacts. In our experiments, all the DC-lines used to measure these characteristics were removed in order to simplify the electromagnetic environment to which the Andreev dot is sensitive. New techniques were developed to characterize atomic contacts. They are presented in section 5.

3.1 Circuit QED

3.1.1 Measuring the state of a qubit with a cavity

During the last decade circuit QED techniques have proven to be well adapted to the measurement of the quantum state of solid-state qubits [88, 89, 28]. At the origin of these techniques is the proposal by Blais *et al.* [23] to use high-quality factor resonators/cavities as probes for the quantum state of qubits in a similar way to what had been done in the Cavity-QED field [90]. In the following section we describe the tools taken from the circuit QED toolbox that have been used in the present work to probe the Andreev bound states.

3.1.2 The classical quarter-wavelength transmission line resonator

At the heart of a circuit-QED setup is a resonator, in our case a quarter-wavelength transmission line resonator. In order to derive its classical response, we first consider an isolated lossy resonator, then a resonator capacitively coupled to a 50 Ω measurement line. The complex[1] reflection coefficient is calculated, the internal and external quality factors are introduced with estimations of their values for resonators fabricated on a kapton substrate.

Uncoupled case

As a first approach to a transmission line resonator, we consider the uncoupled case as sketched on Fig. 3.1. The input impedance of a lossy short-circuited transmission line with characteristic impedance Z_R is given by [91]:

$$Z_{in}(l) = Z_R \frac{1 - j \tanh(\alpha l) \cot(\beta l)}{\tanh(\alpha l) - j \cot(\beta l)}, \tag{3.1}$$

[1] A microwave signal is described in terms of amplitude and phase (with respect to a reference signal). The phase and amplitude can be treated together by using complex amplitudes of the form: $A = |A|e^{i\phi}$

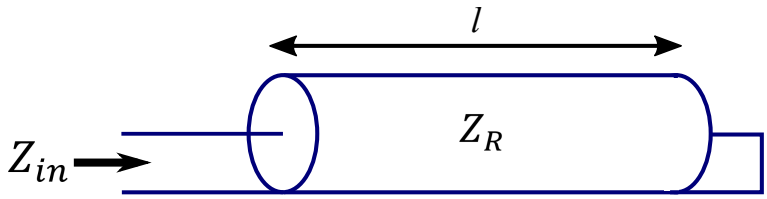

Figure 3.1: A quarter wavelength transmission line resonator is composed by a shunted transmission line of characteristic impedance Z_R and length l.

where $\beta = \frac{2\pi}{\lambda(\omega)}$ is the wavenumber of the microwave with wavelength $\lambda(\omega)$, l is the length of the transmission line, and α the attenuation. We are here interested in the case where $\omega \approx \omega_0$ such that $l = \lambda(\omega_0)/4$. Introducing the reduced frequency $x' = \frac{\omega-\omega_0}{\omega_0}$, we have:

$$\beta l = \frac{\pi}{2}(1 + x'). \tag{3.2}$$

Replacing in Eq. (3.1):

$$Z_{in} = Z_R \frac{1 + j \tanh(\alpha l) \tan(\frac{\pi}{2}x')}{\tanh(\alpha l) + j \tan(\frac{\pi}{2}x')}. \tag{3.3}$$

Assuming low losses ($\alpha l \ll 1$) and considering only small detuning ($x' \ll 1$):

$$Z_{in} = \frac{Z_R}{\alpha l + j\frac{\pi}{2}x'} \tag{3.4}$$

$$= \frac{2}{\pi} \frac{Z_R}{\frac{1}{2Q_{int}} + jx'}, \tag{3.5}$$

with $Q_{int} = \frac{\pi}{4\alpha l}$ the internal quality factor. The attenuation α can be decomposed as:

$$\alpha = \alpha_c + \alpha_d, \tag{3.6}$$

where α_c and α_d are the resistive and dielectric contribution of the losses respectively. The dielectric losses are given by:

$$\alpha_d = \frac{\beta}{2} \tan(\delta), \tag{3.7}$$

where $\tan(\delta)$ is the loss tangent[2] of the dielectric. The loss tangent[3] for kapton at 4 K is 2.10^{-4} which would give, alone, an internal quality factor $Q_{int} = 5000$. Since quality factors of several millions [92] have been achieved with aluminum resonators on low dielectric-losses substrates, we will assume that resistive losses are negligible compared to the dielectric losses for a resonator on kapton.

Therefore, using Eq. 3.7, a simple expression for the internal quality factor is found:

$$Q_{int} = \frac{1}{\tan\delta}. \tag{3.8}$$

Coupled case

We consider now the case of a resonator coupled through a capacitor of capacitance C to a measurement line of impedance Z_0, as shown on Fig. 3.2.

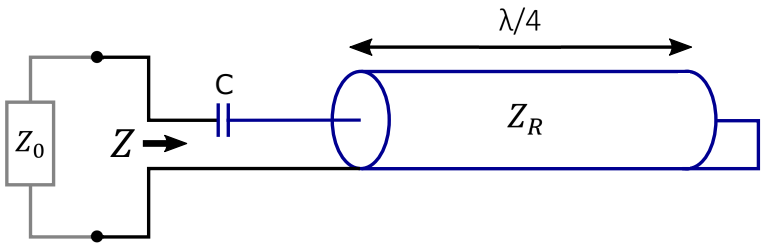

Figure 3.2: Resonator coupled through a capacitor C to a measurement line of impedance Z_0

Resonance condition The first step is to find the resonance condition in this new configuration. We introduce the normalized impedance $z(x') =$

[2]The dielectric permittivity ϵ is complex in lossy materials. The loss tangent is defined as $\tan(\delta) = \frac{Im(\epsilon)}{Re(\epsilon)}$

[3]This value for the dielectric losses was obtained from two different measurements: measuring the losses of a transmission line fabricated on a kapton substrate, or measuring the losses of a 3D-cavity containing a kapton foil

$\frac{Z(x')}{Z_0}$. Seen from the input line:

$$z(x') = \frac{-j}{b(1+x')} + \frac{\frac{2\gamma}{\pi}}{\frac{1}{2Q_{int}} + jx'}, \tag{3.9}$$

with $\gamma = \frac{Z_R}{Z_0}$, and $b = Z_0 C\omega_0$. The resonance condition[4] is found from the complex solution of $z(x_R) = 0$. $\mathrm{Re}\{x_R\}$ gives the position of the resonance, whereas $\frac{\mathrm{Re}[x_R]}{2\,\mathrm{Im}[x_R]}$ is the internal quality factor. Recalling that $x' \ll 1$, one gets:

$$x_R = -\frac{2\gamma}{\pi}b + \frac{j}{2Q_{int}}. \tag{3.10}$$

Compared to the uncoupled case where $\mathrm{Re}\{x'_R\} = 0$, the resonance has been shifted by $\frac{2\gamma}{\pi}b$. This can be understood with an analogy with a RLC circuit in which the total capacitance of the circuit would be modified by the series coupling capacitor. The normalized impedance can now be written using a Taylor expansion:

$$z(x') = (x' - x_R)\frac{dz}{dx'}\Big|_{x'=x_R} \tag{3.11}$$

Introducing $Q_{ext} = \frac{\pi}{4\gamma b^2}$, recalling again $x' \ll 1$ and using the resonance condition:

$$\frac{dz}{dx'}\Big|_{x'=x_R} = \frac{-j\pi}{2\gamma}Z_{in}^2 \tag{3.12}$$

$$= \frac{-j\pi}{2\gamma}\left(\frac{j}{b}\right)^2 \tag{3.13}$$

$$= 2jQ_{ext}, \tag{3.14}$$

yielding:

$$z(x) = \frac{2jx + \frac{1}{Q_{int}}}{\frac{1}{Q_{ext}}}, \tag{3.15}$$

where x is the reduced frequency centered on the shifted reduced resonance frequency, $x = x' + \frac{2\gamma}{\pi}b$.

[4]The resonance condition for a circuit is found for either $Z(\omega_R) = 0$ or $Y(\omega_R) = 0$ [93]

In order to give a first estimation of the coupling capacitor needed for the experiments, its capacitance can be written using Q_{ext}

$$C = \sqrt{\frac{\pi}{Z_0 Z_R Q_{ext}}} \frac{1}{2\omega_0} \tag{3.16}$$

For the uncoupled case according to Eq. (3.8), the internal quality factor for a resonator on kapton is $Q_{int} = 5000$. Assuming a resonance frequency of 10 GHz, a resonator impedance Z_R =70 Ω, critical coupling ($Q_{int} = Q_{ext}$, see below) is obtained for a coupling capacitor of 3.4 fF.

Reflected signal The reflection coefficient is given by [91] :

$$S_{11}(x) = \frac{z(x) - 1}{z(x) + 1}. \tag{3.17}$$

Using Eq. (3.15), and introducing the total quality factor : $\frac{1}{Q_{tot}} = \frac{1}{Q_{ext}} + \frac{1}{Q_{int}}$ and the differential quality factor $\frac{1}{Q^*} = \frac{1}{Q_{ext}} - \frac{1}{Q_{int}}$:

$$S_{11}(x) = \frac{2jx - \frac{1}{Q^*}}{2jx + \frac{1}{Q_{tot}}}. \tag{3.18}$$

In this expression, Q_{int} and Q_{ext} contribute in a similar way, which justifies *a posteriori* the definition for Q_{ext}. The full width at half minimum of $|S_{11}|^2$ gives $\Delta x = \frac{1}{Q_{tot}}$. The expression Eq. 3.18 can be re-written:

$$S_{11}(\theta) = 1 - \frac{1}{1 + \frac{Q_{ext}}{Q_{int}}}(1 + e^{i\theta}), \tag{3.19}$$

with $\theta = -2 \arctan(2Q_{tot}x)$. One recognizes in Eq. (3.19) the equation of a circle of radius $\frac{1}{1+\frac{Q_{ext}}{Q_{int}}}$ in the complex plane[5].

It is plotted on Fig. 3.3 (left panel) along with the reflection amplitude in dB and phase in degrees, as a function of the reduced frequency x. Three

[5]Also called IQ-plane. This term originates from a homodyne demodulation technique in which a microwave signal is decomposed into its "In-phase" and "Quadrature" components. The "In-phase" ("Quadrature") component is the real (imaginary) part of the complex amplitude of the demodulated signal.

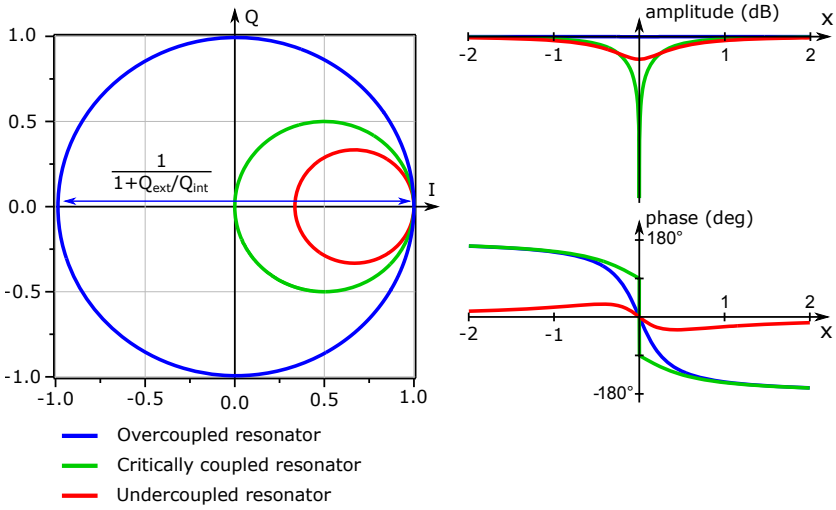

Figure 3.3: Reflection coefficient $S_{11}(x)$ for different quality factors. Left panel: S_{11} represented in the complex plane. The transition from the undercoupled regime to the overcoupled regime occurs when the origin is in the circle. Right panel: amplitude in dB and the phase in degrees of S_{11} as it would be displayed by a vectorial network analyser. Note that the phase origin is different for the undercoupled case compared to the two others in order to emphasize the fact that the phase undergoes no discontinuity at resonance.

cases are considered: undercoupled ($Q_{ext} > Q_{int}$), critically coupled ($Q_{int} = Q_{ext}$) and overcoupled ($Q_{ext} < Q_{int}$). In the undercoupled case most of the microwave is reflected by the input capacitor, the drop in phase and dip in amplitude are small. In the overcoupled regime, the amplitude of the reflected signal is almost not affected but the drop in phase is maximal. At critical coupling, the phase jumps by π at resonance.

3.1.3 Coupling a resonator to the Andreev qubit

Experimentally we measure the state of the qubit by probing the resonator to which it has been coupled to. In this section we describe the quantum

treatment of the qubit-resonator coupling.

General description

The description of a two-level system coupled to a electromagnetic field is due to Jaynes and Cummings [94]. It was first applied to the case of qubits coupled to superconducting resonators by Blais *et al.* [23]. The Hamiltonian of an Andreev qubit galvanically coupled to a resonator was derived by Romero *et al.* [39]. Here we consider the case of an inductive coupling between a microwave resonator and a superconducting loop containing a quantum point contact supporting a single conduction channel of transmission τ, see Fig. 3.4. The inductance of the loop itself is assumed to be negligible compared to that of the contact.

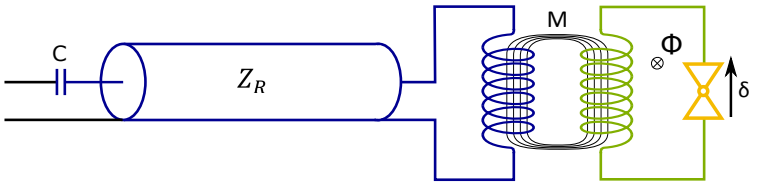

Figure 3.4: The Andreev qubit consists in a superconducting quantum point contact placed in a superconducting loop. This loop is used to phase bias the quantum point contact with a flux Φ and couples inductively the contact to the resonator with a mutual inductance M.

The Hamiltonian of the system is decomposed in three parts:

$$H = H_R + H_A + H_g, \tag{3.20}$$

where

$$H_R = \hbar\omega_R \left(a^\dagger a + \frac{1}{2}\right), \tag{3.21}$$

is the Hamiltonian of the resonator with resonance frequency $\omega_R/2\pi$. It is here described as a harmonic oscillator, with a and $a^\dagger$ the annihilation and creation operator, respectively. The second part is:

$$H_A = -E_A(\delta,\tau)\sigma_z = -\frac{\hbar\omega_A(\delta,\tau)}{2}\sigma_z, \tag{3.22}$$

and describes the isolated Andreev two-level system in the instantaneous Andreev states basis ($|g\rangle$,$|e\rangle$) [13], with $E_A(\delta,\tau)$ is the Andreev energy, and σ_z the z-axis Pauli matrix. Finally,

$$H_g = M\hat{I}_R\hat{I}_A \tag{3.23}$$

describes the coupling between the Andreev qubit and the resonator. Here, $\hat{I}_A$ and $\hat{I_R}$ are the current operators for the Andreev system and the resonator respectively. M is the mutual inductance between the resonator and the superconducting loop containing the superconducting quantum point contact.

We now focus on the coupling part of the Hamiltonian. The resonator current operator can be written [95]:

$$\hat{I_R} = \sqrt{\frac{\hbar\omega_R^2}{2Z_R}}(a^\dagger + a), \tag{3.24}$$

where Z_R is the characteristic impedance of the resonator. The current operator of the Andreev system is given by [14]:

$$\hat{I}_A = I_A(\delta,\tau)(\sigma_z + \sqrt{1-\tau}\tan(\delta/2)\sigma_x), \tag{3.25}$$

where $I_A(\delta,\tau)$ is given by:

$$I_A(\delta,\tau) = \frac{\Delta_{sc}}{4\phi_0}\frac{\tau\sin(\delta)}{\sqrt{1-\tau\sin^2(\delta/2)}}, \tag{3.26}$$

with $\phi_0 = \hbar/2e$ the reduced flux quantum, Δ_{sc} the superconducting gap energy, τ the transmission of the conduction channel, and δ the phase difference applied on the channel. The coupling Hamiltonian can then be written:

$$H_g = g(a^\dagger + a)(\frac{1}{\sqrt{1-\tau}\tan(\delta/2)}\sigma_z + \sigma_x), \tag{3.27}$$

where the coupling factor g can be expressed using Eq. (3.24) and Eq. (3.25):

$$g(\delta,\tau) = \sqrt{z}\frac{E_A(\pi)}{2}\Big(\frac{\Delta_{sc}}{E_A(\delta,\tau)} - \frac{E_A(\delta,\tau)}{\Delta_{sc}}\Big). \tag{3.28}$$

The prefactor z is given by:

$$z = \pi \frac{M^2 Z_R}{L^2 R_Q} = \pi \frac{M^2 \omega_R^2}{Z_R R_Q}, \tag{3.29}$$

where Z_R is the characteristic impedance of the resonator, and $R_Q = \frac{h}{4e^2}$. The coupling factor g is plotted in Fig. 3.5 as a function of the phase difference across the contact for different values of the transmission τ of the conduction channel. The coupling factor is highly peaked at a phase difference of π across the contact. The higher the transmission, the narrower the peak.

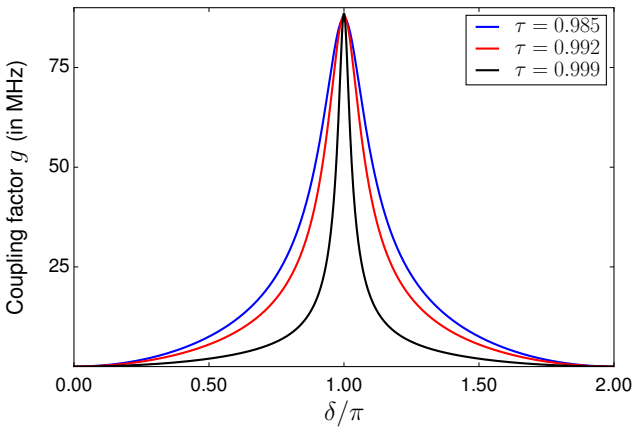

Figure 3.5: Coupling factor g as a function of the phase difference across the contact, for different transmission coefficients. The parameters chosen for this calculation are $M = 0.02L$, Z_R=80 Ω, and Δ_{sc}/h =45 GHz.

Finally the Jaynes-Cummings Hamiltonian is obtained from Eq. (3.27), Eq. (3.21) and Eq. (3.22) by going to the rotating frame (see Appendix A) and neglecting fast rotating terms, assuming that $|\omega_A - \omega_R| \ll \omega_A + \omega_R$ and $|\omega_A - \omega_R| \ll \omega_A$. This procedure is called the rotating wave approximation and is discussed in appendix A.

$$H = \hbar\omega_R(a^\dagger a + \frac{1}{2}) - E_A\sigma_z + \hbar g(a\sigma^+ + a^\dagger\sigma^-), \tag{3.30}$$

where $\sigma^+ = |e\rangle\langle g|$ and $\sigma^- = |g\rangle\langle e|$. The coupling term can be understood as the transfer of a single excitation from the two-level system to the oscillator ($a^\dagger\sigma^-$) or from the oscillator to the two-level system ($a\sigma^+$).

The coupling between the resonator and the Andreev qubit gives rise to an avoided crossing between the Andreev two-level system and the resonator, as shown in Fig. 3.6. It has been calculated both by diagonalizing numerically the full Hamiltonian Eq. (3.20), and by using the energies found with the exact diagonalization [23] of the Jaynes-Cummings Hamiltonian given by:

$$E_{\pm,n} = \hbar\omega_R(n+1) \pm \frac{\hbar}{2}\sqrt{4(n+1)g^2 + \Delta^2}, \tag{3.31}$$

with $\Delta = \omega_A - \omega_R$, and n the number of photons in the resonator. When the qubit and the resonator are in their respective ground states, there is no coupling. Therefore the ground state energy is given by:

$$E_{-,0} = -\frac{\hbar\Delta}{2} \tag{3.32}$$

The results of the two models are in good agreement when the Andreev transition energy is higher than the bare-resonator transition energy, but slightly disagree when the Andreev transition energy is lower. This is due both to the breakdown of the rotating wave approximation (when $\omega_A \ll \omega_R$ or $\omega_A \gg \omega_R$ it is no longer possible to assume $|\omega_R - \omega_A| \ll \omega_R + \omega_A$) and to the fact that the coupling factor g is peaked at $\delta = \pi$. Nonetheless the Jaynes-Cummings Hamiltonian still gives a good insight to understand the coupling between the qubit and the resonator, and therefore we are going to push further the description of our system using this Hamiltonian.

Since we want to use the cavity as a non-demolition[6] detection device, the exchange of energy between the cavity and the Andreev qubit should be as small as possible. With this aim, the transition energy of the qubit and the cavity are strongly detuned ($|\omega_R - \omega_A| \gg g$. This condition is called the dispersive limit and is the subject of the next section.

[6] That is to say that the measurement projects qubit to one of its eigen state but does not destruct this state. In other words, two measurements performed one just after the other should give the same results.

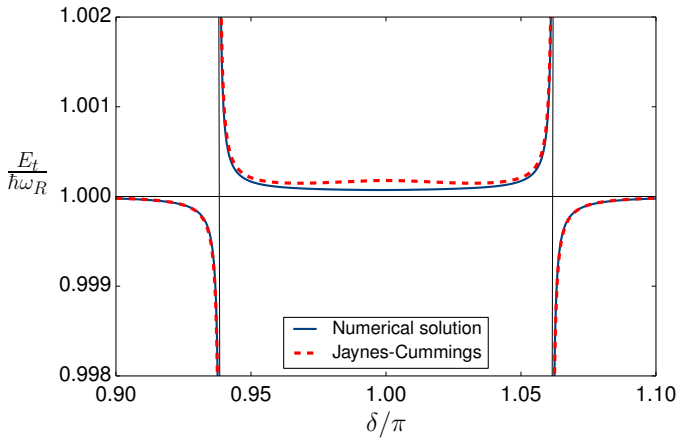

Figure 3.6: Transition energies as a function of the phase difference of the Andreev qubit-resonator system close to the resonance frequency of the resonator. The transition energies are plotted using the exact diagonalization of the Jaynes-Cummings model (dashed red) and the numerical diagonalization of the full Hamiltonian using 25 modes for the resonator (full blue line). The black thin lines represent the energies of the uncoupled resonator and qubit. The differencies between the two calculations close to π reveal the breakdown of the rotating wave approximation. Parameters used for these calculations: $\tau = 0.997$ ($f_A(\pi) = 4.92$ GHz), $f_R = 10$ GHz, others like in Fig. 3.5

Dispersive limit

The dispersive limit corresponds to the situation when

$$\frac{g\sqrt{n}}{|\Delta|} \ll 1. \tag{3.33}$$

The dispersive Hamiltonian is obtained from the Jaynes-Cummings Hamiltonian (3.30), using the unitary transformation:

$$U = e^{\frac{g}{\Delta}(a\sigma^+ - a^\dagger\sigma^-)}, \tag{3.34}$$

and developing the result to second order in $\frac{g}{\Delta}$ [23]. Using again the Baker–Campbell–Hausdorff relation[7], the result is:

$$\frac{H_{disp}}{\hbar} = \Big(\omega_R - \chi\sigma_z\Big)a^\dagger a - \frac{1}{2}\Big(\omega_A - \chi\Big)\sigma_z, \tag{3.35}$$

where $\chi = \frac{g^2}{\Delta}$. This Hamiltonian can be seen as creating an AC-Stark shift of the Andreev two-level system and a cavity shift of the resonator by the Andreev levels which depends on the state of the latter. This is shown in Fig. 3.7 where we have represented the energy states of the bare resonator and the ones of the dispersively coupled resonator when the qubit is the ground or excited state. The "ladder" spacing is shifted by $-\chi$ with respect to the uncoupled resonator when the qubit is its ground state and by $+\chi$ when the qubit is the excited state.

This dispersive shift is used to measure the state of the qubit. It should be noted that the odd configuration of the Andreev states carry no current and therefore does not couple to the resonator, leaving it in its bare state.

Effect of the dispersive shift in the IQ-plane

In order to apprehend how the measurement of the qubit is performed in our experiments, we now describe the effect of the dispersive shift on the resonator reflected signal in the IQ-plane and establish a few design constraints for realistic parameters. As expressed by Eq. (3.35), the shift in frequency of the resonator compared to its bare frequency is:

- $-\chi$ when the Andreev dot is in the ground state.
- $+\chi$ when the Andreev dot is in the exited state.

Using Eq. (3.19), the dispersive shift corresponds in the IQ-plane to a rotation of S_{11} a x by an angle:

$$\theta_\chi = \pm \arctan\left(2Q_{tot}\frac{\chi}{\omega_R}\right). \tag{3.36}$$

Moreover, there is no shift when the Andreev dot is in the odd states since they do not couple to the resonator.

[7] See the appendix B for more details.

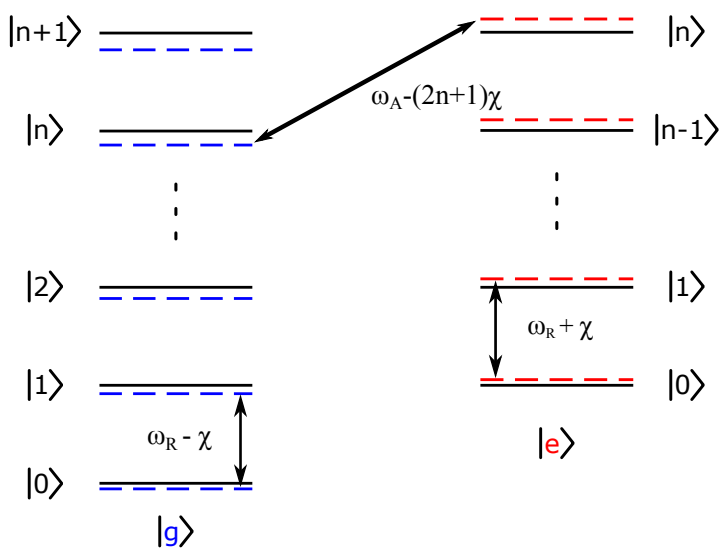

Figure 3.7: Energy levels of the system in the dispersive regime (dashed lines) compared to the uncoupled case (thick lines). On the left the Andreev dot is in its ground state, the resonator transition energy is shifted by $-\chi$. On the right the Andreev dot is in its excited state, the resonator transition energy is shifted by $+\chi$.

Effect of the measurement amplitude In an experimental situation, what is actually measured is not S_{11} but the reflected signal which is :

$$A_{out} = S_{11}(\theta)A_{in}, \tag{3.37}$$

where A_{in} is the amplitude of the signal send to the resonator. In a (hypotethical as we shall see) noiseless system probed at a given frequency, one would get three possible points in the IQ-plane corresponding to each one of the states. This situation is represented by the arrows in Fig. 3.8. However, the reflected signal A_{out} has to be amplified. This amplification adds noise which can be averaged by reducing the bandwidth of the acquisition. However for the measurement to be relevant this bandwidth must be larger than the relaxation rate of the qubit, which sets an intrinsic limit to the averaged noise. The effect of this noise in the IQ-plane is to scatter the measurements around the noiseless positions. For many measurements one

obtain three clusters of points represented as circles in Fig. 3.8.

Two measurement amplitudes A_{in} are shown in Fig. 3.8, the first one is too small to reliably discriminate the three states (the uncertainty circles overlap), the second amplitude is on the other hand large enough to resolve the three states (no overlap). In this last situation thresholds can be implemented to determine the state of the system in a single measurement. When a single measurement allows to discriminate between states, it is said to be a "single shot measurement" [96, 85].

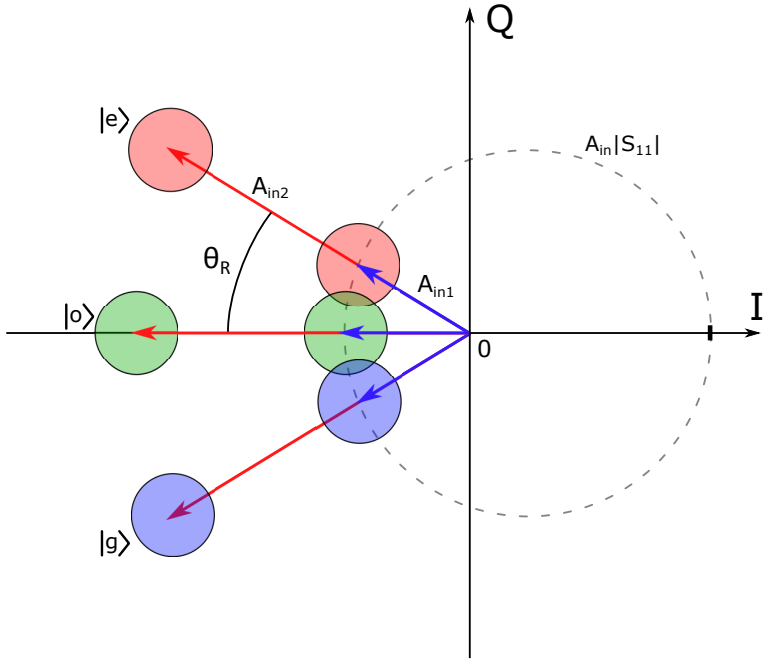

Figure 3.8: Measured signal in the IQ-plane when performed at the frequency of the bare resonator $f_{meas} = f_R$ for two different measurement amplitudes. The blue (red) arrows represent the signal that would be measured at low (high) measurement power, for the qubit being in one of its three state without measurement noise. The circles represent the dispersion of the measured points due to the averaged noise. At high power the circles do not overlap and it is possible to implement thresholds to achieve single shot measurements.

Effect of the external quality factor This discussion suggests that in order to reduce the impact of noise on the measurement a solution is to increase the measurement power. However this strategy is limited since a large number of photons in the resonator can significantly affect the state of the qubit. To take this constraint into account, one has to optimize the separation in the IQ-plane of the three states for a given number of photons in the resonator[8]. Since the internal quality factor is fixed and the cavity shift is confined to a narrow range, the only parameter left for this optimisation is the external quality factor Q_{ext}. Namely, one needs to maximize the distance between the pairs of points corresponding to the different states with respect to Q_{ext}:

$$\Delta A_{ge}(\theta_\chi, Q_{ext}, Q_{int}) = |S_{11}(-\theta_\chi, Q_{ext}, Q_{int}) - S_{11}(\theta_\chi, Q_{ext}, Q_{int})|A_{in}, \tag{3.38}$$

for the distance between the ground and excited states, and between the even and odd states:

$$\Delta A_{go}(\theta_\chi, Q_{ext}, Q_{int}) = |S_{11}(0, Q_{ext}, Q_{int}) - S_{11}(\theta_\chi, Q_{ext}, Q_{int})|A_{in}, \tag{3.39}$$

where $\theta_\chi = -2\arctan(2Q_{tot}x_\chi)$ and $x_\chi = \chi/\omega_R$. In this discussion Q_{int}, g, and Δ are fixed. The number of photons in the resonator is given by [97]:

$$\bar{n} = \frac{4Q_{ext}}{\hbar\omega_R(1+\frac{Q_{ext}}{Q_{int}})^2}P_{in}, \tag{3.40}$$

where $P_{in} = |A_{in}|^2/50\ \Omega$ is the power of the input signal delivered through a 50 Ω line. Using, Eq. (3.40),Eq. (3.19) and Eq. (3.38) or Eq. (3.39), one obtain respectively:

$$\Delta A_{ge}(\theta_\chi, Q_{ext}, Q_{int}) = A_0\frac{4Q_{tot}|x_\chi|}{\sqrt{Q_{ext}}(1+4Q_{tot}^2x_\chi^2)}, \tag{3.41}$$

and:

$$\Delta A_{go}(\theta_\chi, Q_{ext}, Q_{int}) = A_0\frac{2Q_{tot}|x_\chi|}{\sqrt{Q_{ext}(1+4Q_{tot}^2x_\chi^2)}}, \tag{3.42}$$

where $A_0 = \sqrt{\bar{n}\hbar\omega_R 50\ \Omega}$.

[8]Similar calculations were performed by Gambetta *et al.* but for a two-level system coupled to a resonator [42]

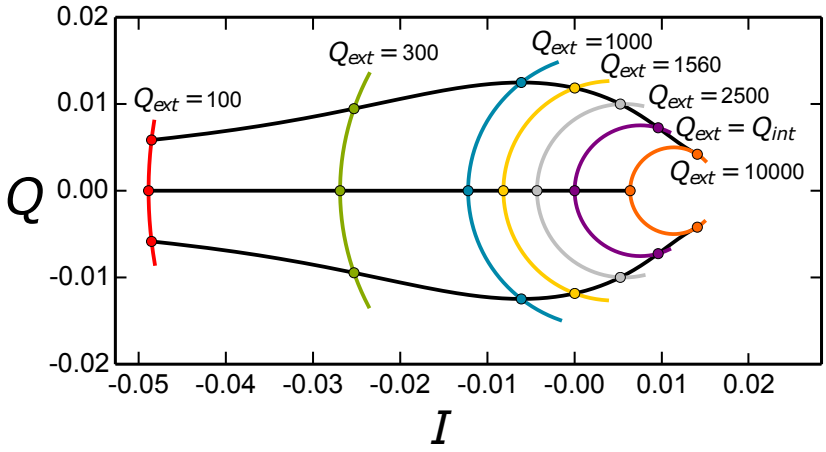

Figure 3.9: Position in the IQ-plane of the reflected signal for each state (black lines) as a function of Q_{ext} and with a constant number of photons in the resonator. The a cavity shift is $x_\chi = 0.0003$ and $Q_{int} = 4400$. The arcs represent the resonator response for different values of Q_{ext}. The maximum distance between states is obtained for Q_{ext} =1560. I and Q are in units of $\sqrt{\bar{n}\omega_R\ 50\ \Omega}$

Figure 3.9 shows the position of center of the three clusters of points in the IQ-plane as defined in Fig. 3.8 when Q_{ext} varies and for a constant number of photons in the resonator. This figure is done for a relative cavity shift $x_\chi = 0.0003$, and for $Q_{int} = 4400$, which are relevant for our experiments. Moreover the reflected signal of the bare resonator as a function of the frequency is shown for different values of Q_{ext}. For high Q_{ext} the input amplitude has to be small (see Fig. 3.10a) and the resonator is undercoupled, the three clusters are very close. At critical coupling the input power is the smallest (see Fig. 3.10a) but the resonance is also the finest. For lower Q_{ext} the input power increases again (see Fig. 3.10a) and the clusters are more separated up to an optimal point where $Q_{ext} \approx 1560$. When Q_{ext} is further reduced the linewidth of the resonator becomes large and the increasing power can't compensate the smaller separation in phase. Note that the distance between the centers of the clusters presents a rather soft

maximum as shown in Fig. 3.10b.

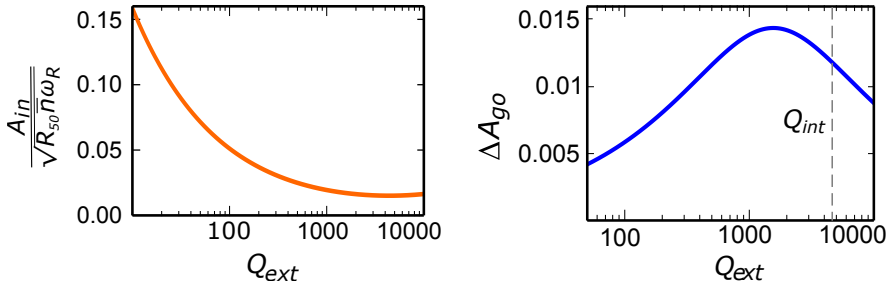

(a) (b)

Figure 3.10: Left: optimal Q_{ext} for a given cavity pull and an internal quality factor of 4400. For low cavity pull, it is preferable to have $Q_{int} = Q_{ext}$ and for large cavity pulls it is preferable to increase the external coupling of the resonator. Right: distance in the IQ-plane between the ground-state cluster and the odd-states cluster as a function of Q_{ext} in log scale. The maximum is found for Q_{ext} =1560

The optimization is performed numerically, and the result as a function of the cavity shift is shown Fig. 3.11 for parameters relevant to our experiments. For small shifts it is preferable to have a resonator close to the critical coupling ($Q_{ext} = Q_{int}$) since it results in a more peaked resonance even though the measurement amplitude has to stay low. As the cavity pull increases, it becomes preferable to decrease the external quality factor (*i.e.* to increase the external coupling of the resonator), which enables increasing the measurement power without increasing the actual number of photons in the resonator. This is done at the cost of a larger width of the resonance.

This results shows that it is preferable to design the resonator as overcoupled in order to obtain the best separation between the clusters and therefore a better signal-to-noise ratio.

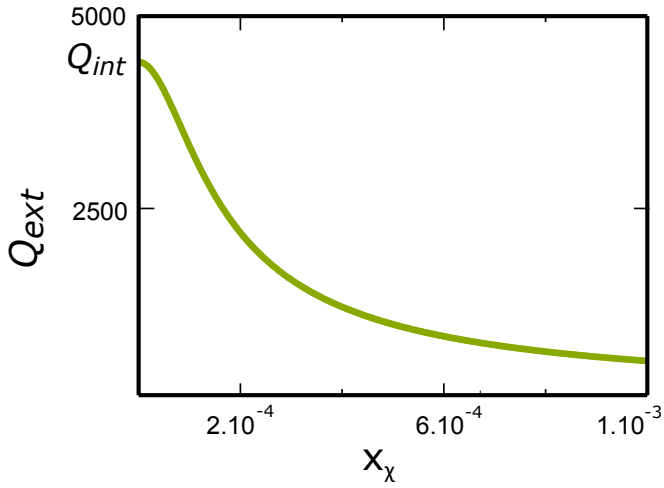

Figure 3.11: Optimal external quality factor as a function of the relative cavity shift x_χ. For low cavity shift, it is better to take advantage of the small linewidth ob tained at critical coupling. As x_χ becomes larger, Q_{ext} can be decreased to obtain a larger reflected signal.

3.2 Mechanically controllable break junctions

3.2.1 General presentation

The single-atom contacts used in our experiments are obtained using the mechanically controllable break junctions (MCBJ). Such a junction is constituted of a wire suspended on top of a flexible substrate, see Fig. 3.12. When the substrate is bent, the suspended region of the wire elogates, and ultimately breaks. subsequent fine tuning enables to obtain single-atoms contacts [21].

The technique is originally due to Moreland and Ekin [98] who used it to measure I-V characteristics of tunnel junctions made of Nb-Sn wire. It was later used in many mesoscopic physics experiments that have been reviewed by Agrait *et al.* [21].

Although the principle of the MCBJ has remained the same, several evolutions or configurations have been used. The first realisations were using glass or phosphore-bronze as a substrate, notched wires connected using

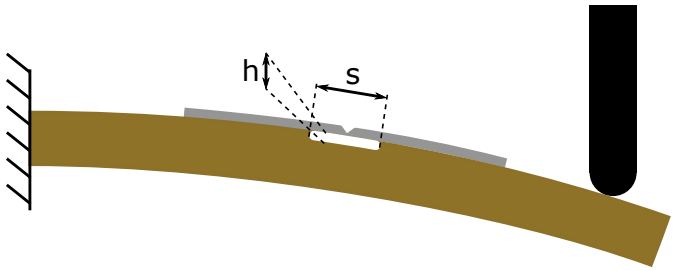

Figure 3.12: A MCBJ in a two-point configuration. The flexible substrate is clamped on the left and a deformation is imposed on the right by a pusher. On top of the substrate is a metallic wire suspended at a height h over a length s. A constriction has been made at one point of this suspended part.

silver paint, and piezo-electric actuators [21]. Later, the use of microfabricated junctions enabled an even greater stability and their integration in on-chip circuits. This is the technique used in the experiments presented in this thesis.

3.2.2 The microfabricated MCBJ

Microfabricated MCBJ [37, 38] take advantage of microfabrication techniques in order to increase even more the demultiplication factor of the technique (see next section). The wire is patterned using e-beam lithography, which enables to reduce the width and the thickness of the constriction to a few hundreds of nanometers. The suspension of the wire is done with plasma etching (see Section 3.3.3), which enables to reduce the suspended length to about one micrometer. The use of microfabrication techniques not only improves the reproducibility compared to hand-made samples, but also allows the integration of single-atom contacts in more complex circuits and a better controlled environment (see [99] and references therein).

3.2.3 Reduction factor

The principal asset of the MCBJ technique is that it enables to produce sub-nanometric displacements from micrometric ones. We now derive the reduction factor for a two-point bending mechanism, which is the geometry used in our experiments. The chip is modelled as a cantilever of thickness $2t$

clamped at one end, and with a vertical displacement d imposed at the other end, see Fig. 3.13. The wire is suspended at height h above the surface of the cantilever and over a length s, see Fig. 3.12. All the elongation concentrates at a constriction in the suspended part of the wire.

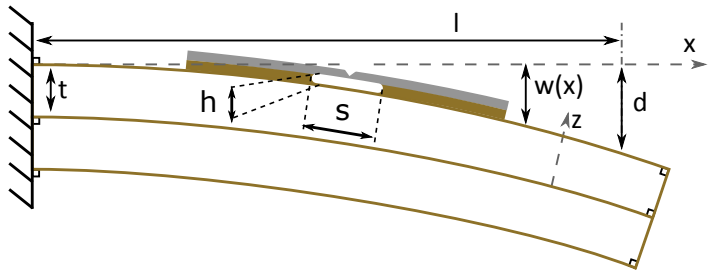

Figure 3.13: The clamped cantilever model used to calculate the reduction factor factor of a MCBJ. A displacement d is imposed on the substrate at a distance l from the clamp, the vertical displacement of the cantilever along the x-axis is $w(x)$ and the thickness of the cantilever is $2t$.

The vertical displacement $w(x)$ of the cantilever along x, is given in the Euler-Bernouilly theory by [100]:

$$w(x) = \frac{d}{2}\frac{x^2}{l^2}(3 - \frac{x}{l}). \tag{3.43}$$

Still in the Euler-Bernouilli limit, the strain can be found by taking a small element of undeformed length dx. Since the sections of the cantilever remain perpendicular to the neutral axis, the deformation of the small element can be reduced to a circle, see Fig. 3.14. The length $dx'(z)$ of the element at a position z along one of its section is given by :

$$dx'(z) = (r + z)d\theta, \tag{3.44}$$

where $r = \frac{d^2w}{dx^2}$ is the curvature radius. Therefore, the strain along the beam at position z is given by :

$$\epsilon_{xx} = z\frac{d^2w}{dx^2}. \tag{3.45}$$

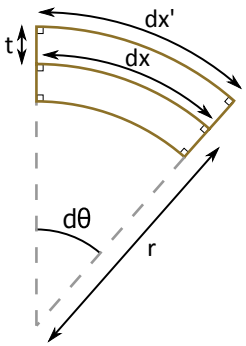

Figure 3.14: A small element dx of the deformed cantilever. The neutral axis is not elongated and the sections of the cantilever are perpendicular to this axis, by hypothesis of the Euler-Bernouilly theory. The curvature radius is r and the length of the surface of the element is dx'

We can now calculate the strain on the wire :

$$\epsilon_{xx}(x) = \frac{3d}{l^2}(h+t)(1-\frac{x}{l}) \approx \frac{3td}{l^2}(1-\frac{x}{l}) \tag{3.46}$$

From Eq. (3.46) one obtains the reduction factor:

$$u(x) = \frac{\epsilon_{xx}s}{d} \approx \frac{3ts}{l^2}(1-\frac{x}{l}). \tag{3.47}$$

Since the strain is maximal at the clamp, an upper bound for the reduction factor[9] is given by $u(0)$. For a suspended length s =2 µm, a thickness $2t$ ≈450 µm and a beam length l =15 mm, which are common parameters for microfabricated MCBJs, one find $u(0) \approx 7.10^{-6}$. This shows the high reduction factor of this technique. An elongation of the junction by 1 Å can be achieved by displacing the free-end of the cantilever by 15 µm. Displacements at this scale can be finely controlled using a micrometer screw.

[9]We want here to have a reduction factor as small as possible in order to be able to tune the contact as finely as possible. Therefore this upper bound constitute a worse case scenario.

3.2.4 Implementation of the MCBJ technique in a dilution fridge

The chips in the experiments presented in this thesis are $15 - 17$ mm long, 8.5 mm wide, and $400 - 500$ µm thick. They are made on a kapton substrate which has a room temperature young modulus of 2.5 GPa, and remains flexible at cryogenic temperatures. Another valuable characteristic of kapton is that its thermal coefficient of expansion is close to the one of aluminium [101], which prevents from differential contraction effects. Two bending mechanisms have been used in our experiments:

- For the experiments presented in Chapters 4 and 5 (unless mentionned differently), the pusher was a copper plate actuated by a micrometer screw (see Fig. 3.15) with a thread of 250 µm per turn.
- For the experiments presented in chapter 6, the mechanical setup has been stiffened, in order to improve mechanical stability. This has been done by replacing the pusher with a solid copper piece sliding on two brass columns and actuated by a differential screw (see Fig. 3.16) with a thread of 300 µm per turn. The screw was actuated by a prismatic joint.

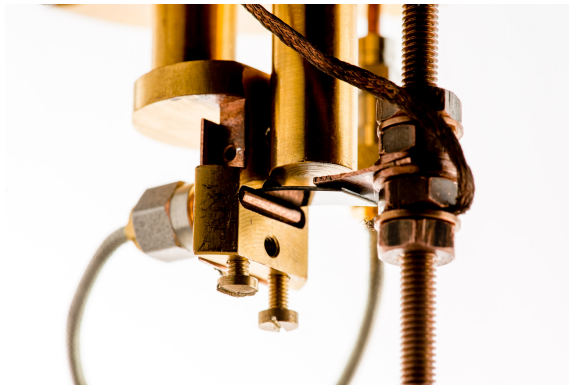

Figure 3.15: Mechanical setup used for the runs before BR3e. The chip is clamped against a SMA-launcher on the left using a small copper plate and two screws. On the right the chip is in contact with the "pusher" made of a thin copper plate and a copper rod connected to a micrometer screw.

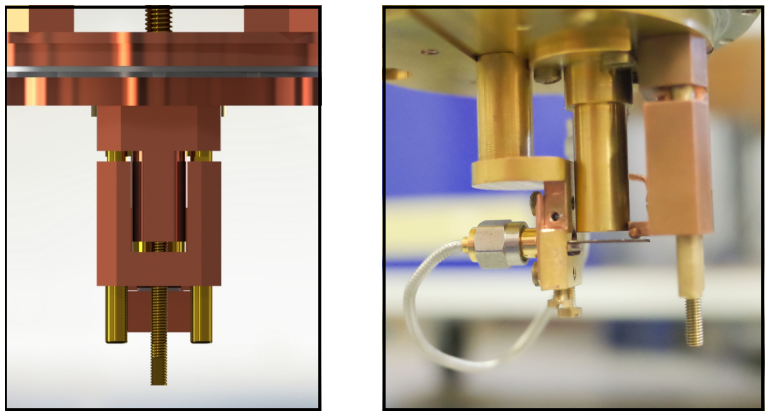

Figure 3.16: Second mechanical setup implemented for the run BR3f in order to improve mechanical stability. Left: Front view of the setup (CAD rendering). Right: sideview of the setup. The chip holder is the same but the "pusher" is now made of a solid copper piece actioned by a differential screw and guided by two brass rods.

In both cases, the actuation was performed by a DC-motor placed at room temperature through the following elements (see Fig. 3.17):

- A planetary gear-box with a reduction factor of 97;
- A vacuum rotating feedthrough;
- A second planetary gear reducer with a reduction factor of 9.3, thermalized at the 1 K pot of the dilution refrigerator. This reducer has been carefully degreased in order to avoid jamming due to frozen lubricant;
- A fiberglass axle connected to the gear-box at its top end and the micrometer screw, or the sliding joint at its bottom end. Fiberglass was used for its thermal insulation properties since the axle connects directly the 1K-pot and the mixing chamber of the refrigerator. It is connected to the gear box through a universal joint, and to the micrometer screw through an helical coupling. This joint reduce the effects of differential contraction.

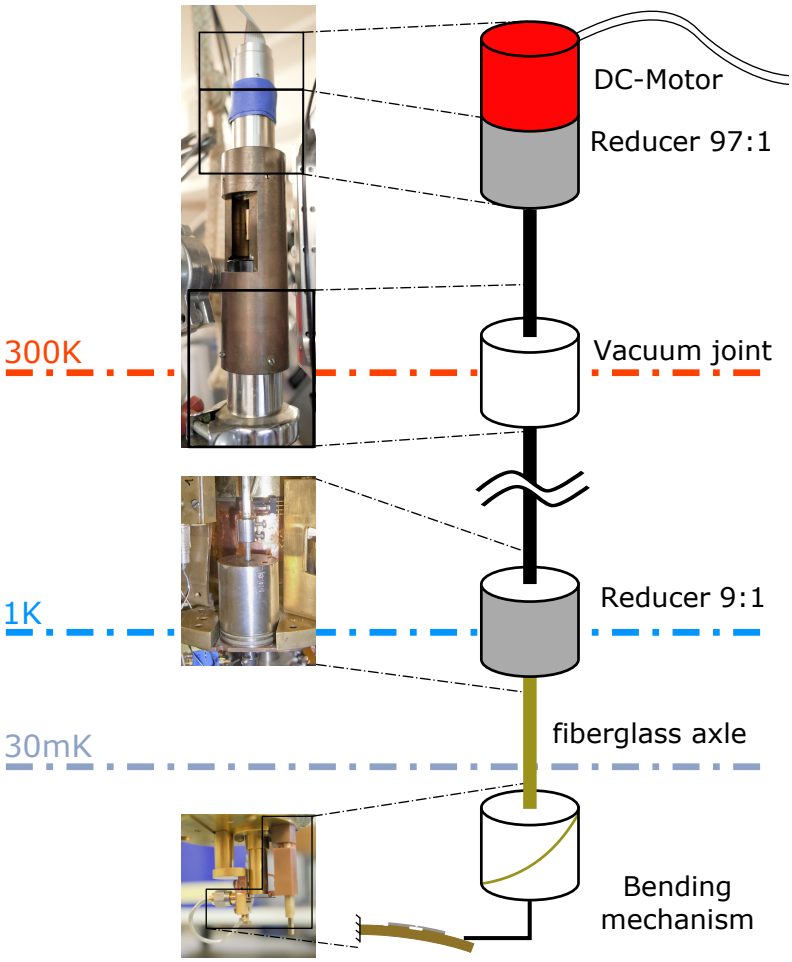

Figure 3.17: Overview of the mechanical setup. The DC-motor is placed at room temperature along with a first stage of reduction. A vacuum feedthrough transmits the rotation. A second stage of reduction is placed at 1 K, finally the bending mechanism is placed at 30 mK

3.3 Chip design and fabrication

3.3.1 Designing a microwave resonator

Design of the chip

As explained in section 3.1, a convenient implementation of a microwave resonator for circuit-QED is the transmission line resonator. Among the different implementations of planar transmission lines, the coplanar waveguide (CPW) has been chosen for this work. As a first approximation, the CPW can be seen as a planar version of a coaxial cable. It is composed of three parallel conductors on top of a dielectric (see Fig. 3.18). The mode supported by the CPW is a quasi-TEM mode [102] and can therefore be easily coupled to the TEM mode of the coaxial cables used to carry the microwave signal to the chip. The impedance of the mode is determined by the relative dielectric constant of the substrate ϵ_R and the aspect-ratio a/b (see Fig. 3.18)

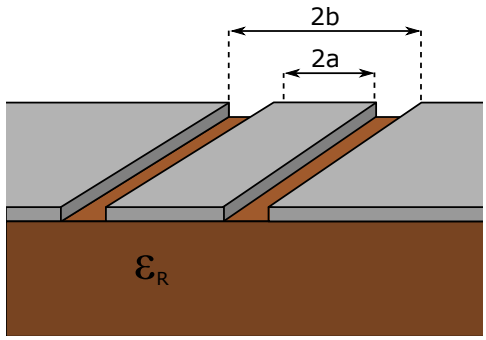

Figure 3.18: Schematics of a CPW. In grey are the conducting part of the waveguide and in brown the insulating substrate of relative permeability ϵ_R. The width of the center line is $2a$ and the width of the line is $2b$.

The field generated by the CPW is confined over distances $\ll \lambda$, which avoids radiative losses and the coupling with the surrounding electromagnetic environment. The characteristics mentioned above make the CPW transmission line suitable for making high-Q resonators (confined field), that can be easily implemented and coupled to a µm-size circuit (miniaturization is possible) and to commercial microwave components (possibility to

couple it to a coaxial transmission line). Since the proposal of A. Blais *et al.* [23] and the first realization by Schoelkopf *et al.* [25], CPW resonators have been thoroughly used in cQED architectures and constitute the majority of two-dimensional implementation, although other geometries have also been used [88, 103].

In order to avoid the coupling to a whip-antenna mode of the ground plane, the CPW is folded into a meander so that the length of the resonator is distinct from the length of the ground plane. Moreover, the meander is disposed so that its length —and therefore the resonator frequency —does not change too rapidly when the chip is bent.

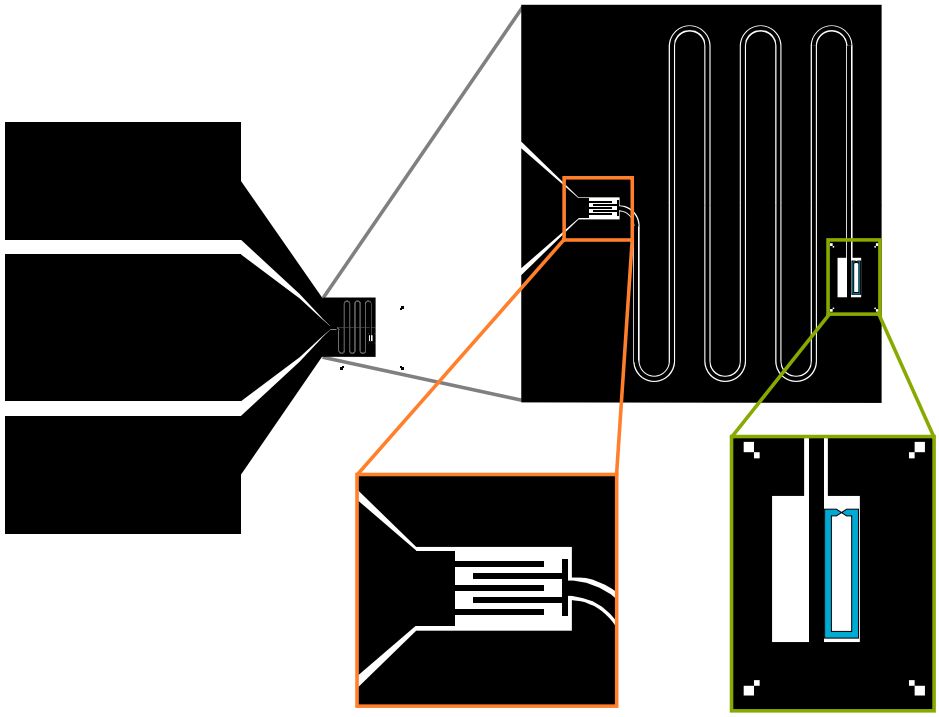

Figure 3.19: Design of the chip. Black regions are made of niobium. Top right: zoom on the meander line of the resonator. Bottom center: interdigitated capacitor. Bottom right: openings in the ground plane to fit aluminium the break-junction and the biasing loop (in blue).

The dimensions of the CPW in our design are $a = 5$ µm and $b = 8$ µm.

These dimensions have been chosen as a compromise between the reliability of the fabrication based on optical lithography, and the need to keep the impedance of the resonator low to achieve a good coupling with the Andreev dot. These dimensions result in an impedance $Z_R \approx 70\,\Omega$. The developed length of the resonator is 5.14 mm, which gives a resonance frequency of $\omega_R/2\pi \approx 10$ GHz given the dielectric constant of the substrate of $\epsilon_R = 3.2$.

The resonator is coupled to the coaxial line through a 50 Ω CPW line and a coupling capacitor (more below). Two openings in the gap are placed at the shunted end of the CPW, see Fig. 3.19. One of them is used to place the rf-SQUID loop at the position where the current is maximal in the resonator, so as to achieve a maximal coupling. The other one is there to keep the CPW symmetric.

We discuss in the following paragraphs the dimensions of the coupling capacitor needed to obtain a critical coupling of the resonator with the measurement line. We also discuss the size of the loop containing the atomic contact in order to obtain a sizeable coupling between the resonator and the Andreev qubit.

3.3.2 Fine tuning of the design

Design of the coupling capacitor

As discussed in paragraph 3.1.2, for realistic parameters a capacitance of about 3.4 fF leads to critical coupling of the resonator to its measurement line. We saw in section 1.3.3 that the best signal over noise ratio should be obtained in our experiments for an overcoupled resonator. For this reason we now to calculate the design parameters for a capacitance of 5 fF.

This capacitance is obtained using an interdigitated capacitor. Such a capacitor is shown in Fig. 3.20 with the relevant parameters. An analytical calculation of the capacitance of such a capacitor is found in Ref. [104]. A numerical calculation with a

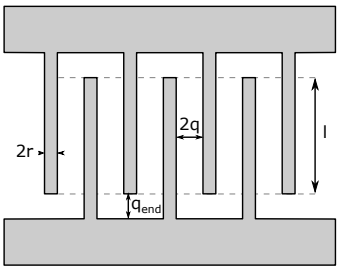

Figure 3.20: Top view of an interdigitated capacitor. The fingers have a width $2r$, a lateral separation $2q$ and an overlap length of l. The distance between the tip of a finger and the terminals is q_{end}

	As designed	Obtained on BR3
l	50 µm	48 µm
$2r$	4 µm	3 µm
$2q$	4 µm	5 µm
q_{end}	10 µm	12 µm
C	5 fF	3.9 fF

Table 3.1: Parameters used for the coupling capacitor of the resonator. The designed capaciance is 5 fF on a kapton substrate. The capacitance on chip BR3 is 3.9 fF. It was calculated from the measurement of the external quality factor of the resonator.

film thickness of 100 nm, a substrate relative dielectric constant $\epsilon_R = 3.2$, and 5 fingers, leads to the design parameters of our coupling capacitor shown Table. 3.1.

Although the design parameters should result in a 5 fF capacitance, imperfections in the fabrication lead to thinner fingers in chip BR3 (see Table 3.1). This resulted in a slightly smaller capacitance of 3.9 fF.

Estimation of the mutual inductance

The coupling between the Andreev qubit and the resonator mode depends on the mutual inductance between the resonator and the loop containing the atomic contact (see Eq.(3.29)). Considering a resonator with an impedance $Z_R = 70\ \Omega$, a resonance frequency $f_R = 10$ GHz and an Andreev transition energy f_A =8 GHz at $\delta = \pi$, a coupling factor $g = 100$ MHz is obtained for a mutual inductance $M = 27$ pH.

A first estimation of the mutual inductance can be obtained by assuming that most of the coupling comes from the center line of the CPW where the current density is the highest. The mutual inductance, between an infinite wire and a rectangular loop has an analytical form:

$$M = \frac{\mu_0}{2\pi} L \ln\left(\frac{s+w}{s}\right), \tag{3.48}$$

where μ_0 is the vacuum permeability, and L, s and w are geometrical factors shown on Fig. 3.21.

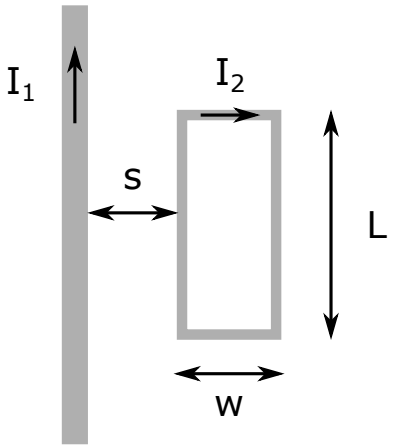

Figure 3.21: Loop coupled to a wire. The dimensions L, s and w enter in the expression of the mutual inductance (Eq. (3.48)).

In order to keep the geometrical inductance of the loop small, we limit the length of the loop to 100 µm. Moreover limitations of the fabrication process impose that s should be larger than a few micrometers. With these constraints in mind, a design for the loop is proposed: $L = 75$ µm, $w = 15$ µm, and $s = 3$ µm.

A better estimate is obtained through numerical calculations that account for the effect of the return current through the ground plane and calculate the full current distribution. Using the simulation software Sonnet (see Fig. 3.22), one obtains $M = 26$ pH for a $L = 90$ µm, $w = 22$ µm, and $s = 1$ µm. This is the geometry of BR3.

Estimation of the resonator shift at the breaking of the loop

In order to obtain single atom contacts one has to detect when the bridge breaks. In principle, this breaking should result in a sudden jump in frequency of the resonator. We now evaluate the order of magnitude of this jump using a simple electrical model shown in Fig. 3.23. The resonator is modeled as an LC-oscillator coupled inductively to an inductor L_{loop}, its

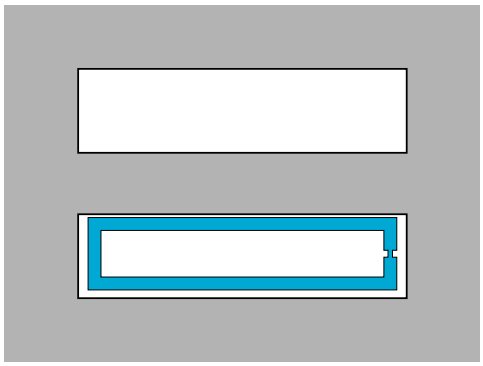

Figure 3.22: Geometrical configuration used in the Sonnet simulations. The loop has been slightly shifted in order to take into account a misalignment on the chip BR3 for which this simulation has been designed.

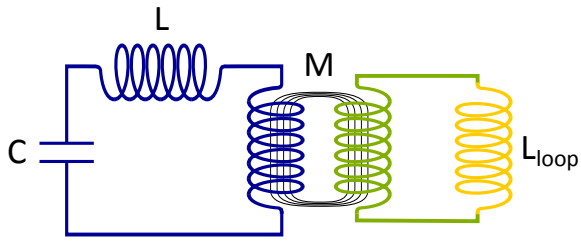

Figure 3.23: Model used to calculate the shift resulting from the breaking of the contact. The loop is modeled as a pure inductance, and the resonator as an LC-circuit. The coupling between the two is described by a mutual inductance M

resonance frequency is (assuming $\frac{M^2}{L_{loop}L} \ll 1$):

$$\frac{\omega_R}{2\pi} = \frac{\omega_0}{2\pi}\left(1 + \frac{1}{2}\frac{M^2\omega_0}{L_{loop}Z_R}\right). \tag{3.49}$$

When the contact is broken, no current circulates in the loop so that the resonance frequency is $\frac{\omega_0}{2\pi}$. Hence the frequency shift expected when the contact breaks is given by:

$$\Delta f = \frac{M^2\omega_0^2}{4\pi L_{loop}Z_R}, \tag{3.50}$$

which gives a shift $\Delta f \approx 30$ MHz for the values of inductance and mutual inductance calculated previously. This shift is much larger than the linewidth $\Delta\omega = \omega_R/Q_{tot} \approx 5$ MHz of the resonator, therefore the breaking of the contact is easily detected.

3.3.3 Fabrication

Wafer fabrication

Kapton wafers are not available commercially and thus have to be custom made. A 50 mm disk is cut out of a 0.5 mm-thick kapton sheet. One surface of the disk is then polished to allow subsequent optical and e-beam lithography. The wafer is glued to a steel flat cylinder using double-sided tape; the cylinder presses the wafer against the rotating polishing sheet of a polishing machine; friction causes the cylinder to rotate, which ensures that the polishing is isotropic. The process is repeated with polishing sheets of decreasing grain size:

- Large scratches are removed using a wet 1200-grit polishing sand paper. This step is short (less than 30 s).
- Medium-size scratches are removed using nylon sheets impregnated with 9 µm and then 6 µm diamond particles. These steps are usually between 3 and 5 minutes long. Visual control is used to determine when the step is finished.
- Mirror aspect of the wafer is obtained using velvet sheets impregnated with 3 µm and then 1 µm diamond particles. These steps are usually 5 minutes long.

Once the wafer is polished, two successive layers of polyimide PI2610 are deposited, spun at 2000 rpm during 60 s, and soft baked at 180 °C during 3 min on a hot plate. These layers further planarize the surface of the wafer and form a homogeneous medium that is going to be partially etched in order to suspend the constriction of the MCBJ. The wafer is then baked in a vacuum oven at a pressure $\approx 10^{-6}$ mbar 350 °C for 1 h. After this preparation the wafer has thickness around $400 - 450$ µm. Finally a 150 nm film of niobium is deposited at 2 nm/s on the substrate using a DC-magnetron sputtering machine.

Resonator fabrication

The resonators are patterned on this Nb layer using optical lithography. A layer of MicroChem S1813 resist is spun at 4500 rpm during 60 s and soft-baked at 110 °C on a hot plate during 1 min. A Karl-Süss MJB3 or MJB4 optical aligner is used to expose the resist. The resist is then developed in Micoposit MF319 during 50 s and rinsed in deionized water. The niobium is then dry etched in a Plassys MG200 reactive ion etching machine using a flow of 20 sccm of CF_4 and 10 sccm of Ar at a pressure of 5.10^{-2} mbar and a self-polarization voltage of 200 V (power $\approx$ 50 W). The etching is monitored by measuring the reflection of a laser-beam on a part of the niobium which is not protected by the resist. The plasma is stopped one minute after the minimum of reflectivity is reached, typically after 6 min. A chip is shown Fig. 3.24 at the end of this step.

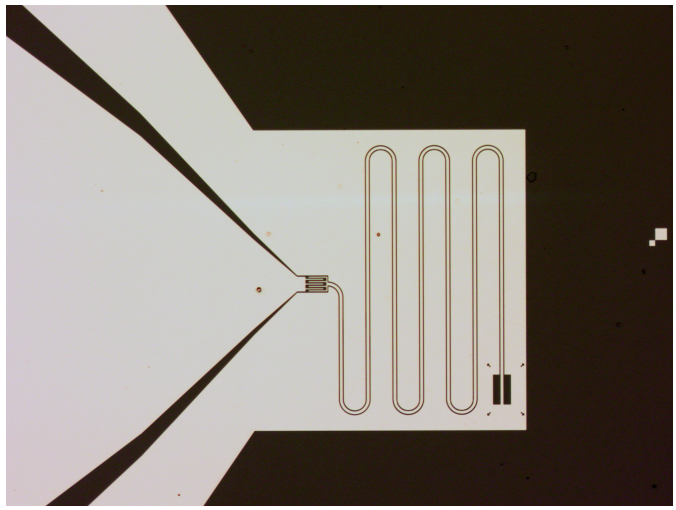

Figure 3.24: Micrograph of a niobium resonator.

Aluminum-loop patterning

The next step is to create the aluminum loop with its constriction that is needed to produce the atomic contact. The geometry is defined by electron-beam lithography. For this purpose a bi-layer of MAA-PMMA is first deposited:

- A 500 nm thick layer of MAA EL10 is spun at 2000 rpm during 1 min and baked 2 min at 170 °C on a hot plate.
- A 300 nm thick layer of PMMA A6 950K is spun at 5000 rpm during 1 min and baked 2 min at 170 °C on a hot plate.

Because the substrate is insulating, an additional metallic layer is needed on the resist to evacuate the charges during e-beam lithography. For this purpose a layer of 7 nm of aluminum is deposited on top of the resist in an electron-gun evaporator. The wafer is then cut into individual chips using office scissors or an office paper guillotine.

The loop and constriction are exposed using a Philips XL 30 scanning electron microscope. A dose of 250 $\mu C/cm^2$ is used with an acceleration voltage of 25 kV. The dose is increased by a factor 1.3 at the constriction. The top layer of aluminum is removed in 10 s in a KOH solution, the chip is then rinsed in deionized water, developed in MIBK:IPA (1:3) during 45 s and finally rinsed in IPA or ethanol during 15 s. A visual control of the development is done at this stage using an optical microscope. The deposition of 100 nm of aluminium is done in a Plassys MEB 550S electron-gun evaporator at a rate of 1 nm/s. The unwanted aluminium is removed by dissolving the resist in 60 °C acetone or preferably N-Methyl-2-pyrrolidone in order to avoid residues on the chip. Finally the constriction is suspended by dry-etching the kapton sacrificial layer. This process is done with the chip on a aluminium block that has been pre-heated to 170 °C. To ensure an isotropic etching, which is needed to suspend the constriction, a high pressure plasma (0.3 mbar) is used. It is constituted by 50 sccm of O_2 and 2 sccm of SF_6. The auto-polarization voltage is 45 V. In order to have a reproducible process with a suspension of about 2 µm, the following timing is strictly followed:

- At t=0': chip is placed in the chamber on the hot block and the chamber is pumped.

- At t=5': gas valves are opened and the flow rates set.
- At t=7': plasma is turned on
- At t=9'30": plasma is turned off.

The chip is then ready. A control with a scanning electron microscope can be performed in order to check the integrity of the constriction and the size of the suspended region.

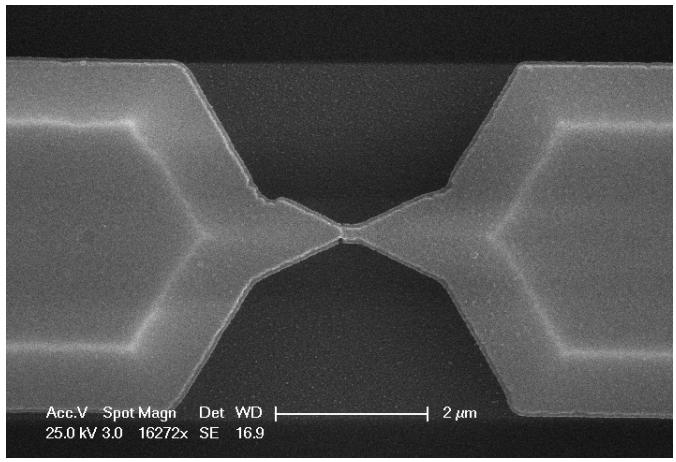

Figure 3.25: Scanning electron microscope image of a suspended bridge observed with a 25 kV acceleration voltage. The darker regions corresponds to the kapton substrate. The brighter region to the aluminium bridge. By transparency one can discriminate the suspended regions (brighter) of the bridge from the regions still in contact with the substrate.

3.4 Microwave setup

3.4.1 Cold setup

All the experiments of this thesis were carried out in an Oxford kelvinox 300 wet dilution refrigerator. The microwave setup used for the chips BR3 and VR2 is shown Fig. 3.26. The red line on the graph represents the coaxial line that carries the microwave tone used to excite the Andreev transition.

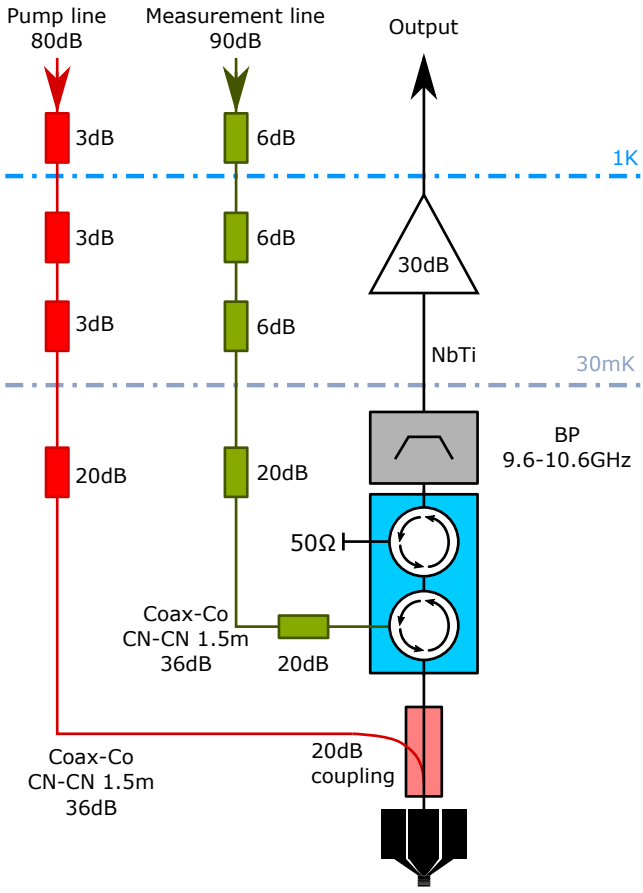

Figure 3.26: Schematics of the microwave cabling within the refrigerator.

It is heavily attenuated using lumped element XMA-attenuators, and lossy Cu-Ni cables from CoaxCo. This attenuation damps the Johnson-Nyquist noise from the room temperature components while only re-emitting noise at their own temperature (from 4 K to 25 mK). The line is connected to the coupling port of a 20dB directional coupler (Clear Microwave C20218). The green line on the graph represents the coaxial line that carries the microwave tone used to probe the resonator. It is connected to a double

circulator Quinstar QCY-100400XM20 and reaches the chip through the direct port of the directional coupler. The reflected signal goes through the double circulator followed by a Microtronics microwave filter, and reaches through superconducting lines a HEMT amplifier (Caltech CIT2-4434-020 with a noise temperature of 7 K at 10 GHz) thermalized at 1.5 K. The Microtronics filter was a custom 9.6-10.6 GHz bandpass filter for runs BR3c to VR2b and an 8-12 GHz for runs BR3a and BR3b. Its role is to filter out the microwave signal that is used to excite the Andreev transition, which could saturate the amplifier. The signal is further amplified by 80 dB at room temperature.

3.4.2 Chip holder and sample environment

The chip holder has two roles: it keeps the chip in place when it is bent and ensures a good connection to the microwave lines. For these purposes, the chip is firmly pressed against a SMA launcher, the pin of which has been milled to a half cylinder (see Fig. 3.27). The chip holder has been designed close to the pin to reduce the impedance mismatch with the coaxial line. On its other side, the chip is pressed against the pushing rod of the bending mechanism (see Sec. 3.2). The chip holder, and the bending mechanism are anchored to the mixing chamber of the dilution refrigerator and placed inside several shields. From the outermost to the innermost:

- A copper shield that acts as a Faraday cage;
- A cryoperm magnetic shield ;
- A superconducting aluminum shield for further magnetic shielding;

The last shield is coated on its inner surface with a thick microwave absorber in order to avoid standing waves inside the superconducting shield. This material has been made by mixing 15 g of part A of Stycast 1266 with 4 g of part B, 55 g of bronze powder (grain size < 50 µm) and 1 g of carbon powder.

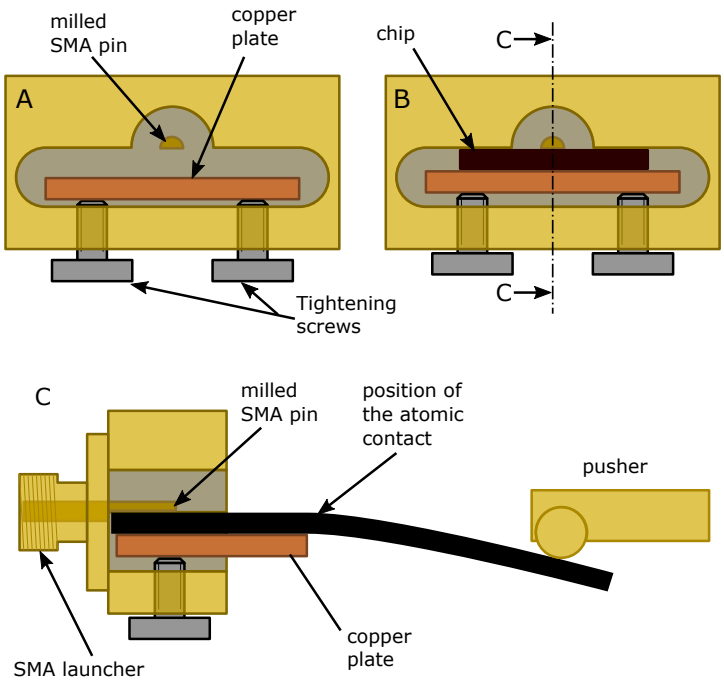

Figure 3.27: A: front view of the chip holder without chip. B: front view with a chip. C: cross-section of the chip holder and the pusher. The chip is clamped using a copper plate and screws. The length of the copper plate has been adjusted so the the maximal deformation of the chip occurs at the position of the atomic contact. The connection is done using a SMA launcher, the pin of which has been milled.

3.5 Obtaining an atomic contact

In previous experiments on superconducting atomic contacts, DC measurements were performed to monitor the size of the contacts and of their channels content [34]. To better control the electromagnetic environment, DC connections were removed in our experiments.

With the setup used during this thesis, all the information available on the size of the contact is obtained through the coupling with the resonator. This section discusses the steps followed to obtain a single-atom contact with this setup.

3.5.1 Coarse tuning

The first step to obtain an atomic contact is to look for the position of the pusher for which the contact breaks. This position is not the same for every chip because it depends on the distance on which the bridge is suspended and on the exact positioning of the chip in the chip holder.

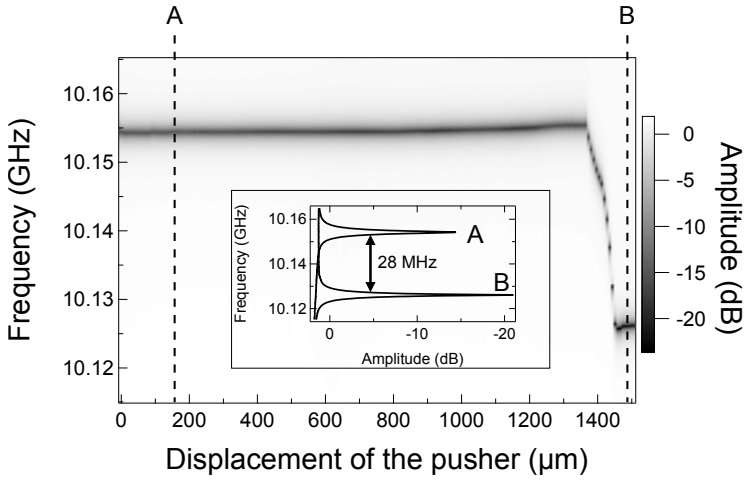

Figure 3.28: Typical evolution of the single-tone spectrum obtained when breaking the contact. The horizontal axis is the displacement of the pusher, the vertical axis the frequency of the pump probe and the color-scale is the amplitude of the reflected signal. Inset: are plotted two vertical cuts of the color-map. The one labeled A shows the resonance before breaking, the second one labeled B shows the resonance after the breaking.

As seen in the previous section, a sudden jump of the frequency of the resonator occurs when the bridge opens. In Fig. 3.28 is shown the typical evolution of the resonance frequency of the resonator[10] (black line) as a function of the displacement of the pusher. The resonance frequency is relatively stable for small bendings. It then decreases rapidly, stepwise, and finally reaches a stable value 28 MHz smaller than the initial one. At this point the contact is broken. A contact is recovered by withdrawing the

[10]The measurement method is described in details in Section 4.1.

pusher. Once the contact is reformed, a fine tuning of the position of the pusher allows to find a one-atom contact.

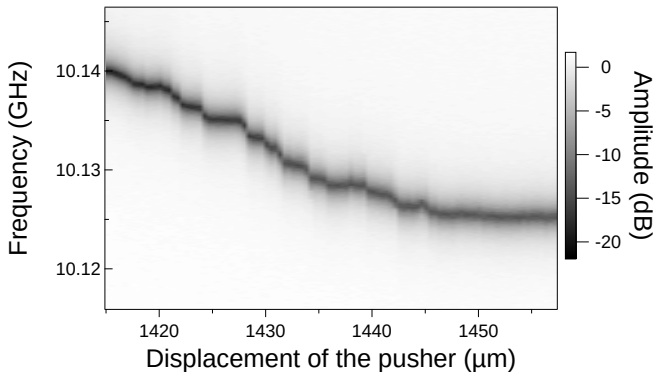

Figure 3.29: Close-up view of the evolution of the resonance frequency up to the complete opening of the bridge.

As shown in Fig. 3.29, just before breaking the frequency of the resonator evolves stepwise, corresponding to jumps between different arrangements of the atoms near the contact [34]. The final tuning requires to observe the flux modulation of the resonance frequency as explained in the next paragraph.

3.5.2 From big contacts to single-atom contacts

As the contact gets smaller, its critical current decreases and it becomes possible to phase-bias the rf-atomic SQUID. For big contacts the flux-modulation is hysteretic, see Section 2.2.3. Such a modulation is shown Fig. 3.30a and 3.30b for two scanning direction of the flux. The phase jump and the hysteretic behavior appears clearly.

For smaller contacts, the hysteresis loop is reduced and finally disappears. However, even when the modulation is non-hysteretic the contact can contain many channels and the relation between phase accross the contact and the applied flux can still be non-linear. This results in a sharp minimum of the resonance frequency at $\delta = \pi$, see Fig. 3.31.

The final steps aims at obtaining a contact with only one conduction channel well coupled to the resonator. This means that the Andreev transition frequency $2E_A/\hbar$ should be close to the resonator frequency, which sets

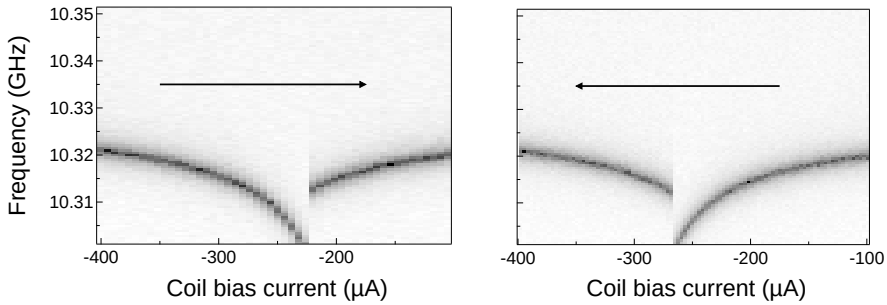

(a) (b)

Figure 3.30: Flux modulation of the resonator frequency obtained for big contacts. The left figure shows the modulation when the flux is swept rightwards while the flux is swept leftwards on the right figure. Notice how the jumps occurs at different flux biases.

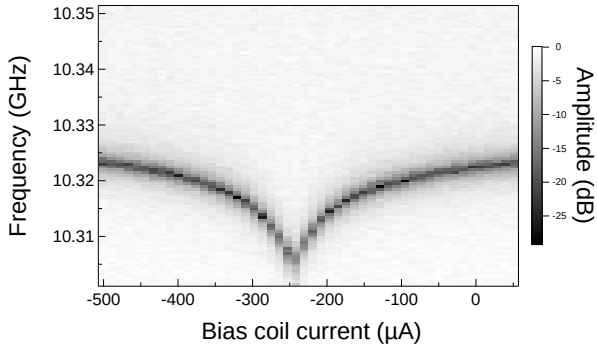

Figure 3.31: Modulation of contact for which the flux bias induces a modulation that is not hysteretic. Note how the resonator is affected far from π

a constraint on the transmission of the channel $\tau > 0.97$. An aluminum single atom contact accomodates only three channels [34], with only one with a transmission high enough to be coupled to the resonator. This the situation that is aimed to.

If the transmission of a channel is high enough so the Andreev transition frequency at $\delta = \pi$ is lower than the resonator frequency, it is possible to

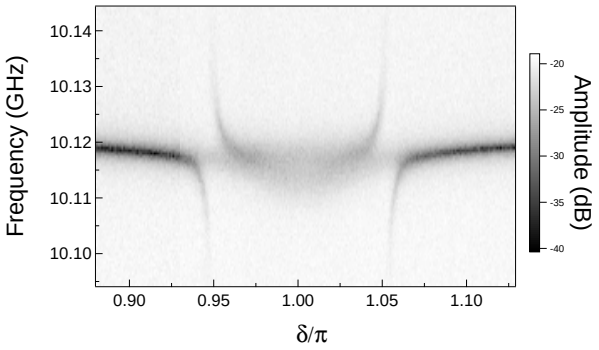

Figure 3.32: Contact with only one Andreev transition that crosses the resonator frequency. However the fading of the resonance close to $\delta = \pi$ shows the presence of at least one other channel coupled to the resonator.

observe an avoided crossing such as the one presented in Fig. 3.6. However an avoided crossing can also be observed for contacts with more than one highly transmitted channel, as in Fig. 3.32. In this figure, only one channel has a transmission large enough to produce an avoided crossing with the resonator, however an other channel is also coupled to it. The presence of this second channel is signaled by the fading of the resonance around $\delta = \pi$ (compare with Fig. 3.33. This fading is due to the parity jumps in the second channel that modulates the frequency of the resonator when the cavity shift χ is large enough. Finally, with a fine tuning one obtains a clear anticrossing with only one set of lines such as the one shown in Fig. 3.33, the resonance is well defined for all phases except at the anti-crossings. Moreover for a contact with such a high transmission, the resonance is constant except close to the anticrossing.

3.5.3 Examples of contacts

In this section we present a "familly album" of single-tone spectra such as the ones shown above, with the characteristics of the contact inferred from data taken by other means[11].

[11]For further detail see chapter 4.

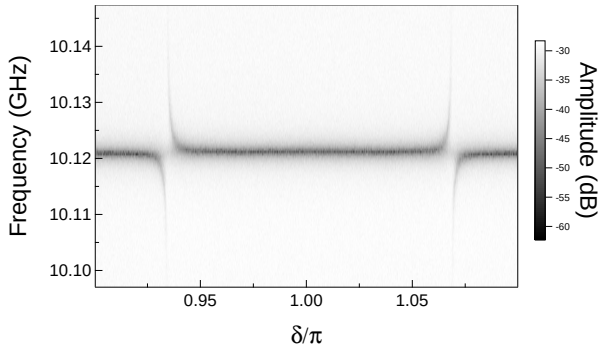

Figure 3.33: A one-atom contact with high transmission: the avoided crossing has a single set of lines that are well defined at all phases.

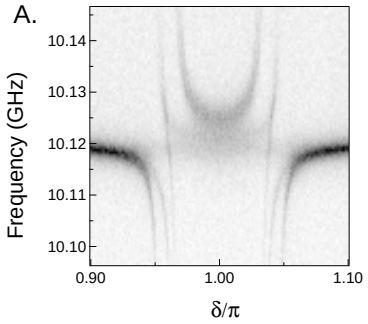

At least two channels
$\tau_1 = 0.9941$ and $\tau_2 = 0.9925$
$\omega_{A1}/2\pi = 6.9$ GHz and $\omega_{A2}/2\pi = 7.75$ GHz

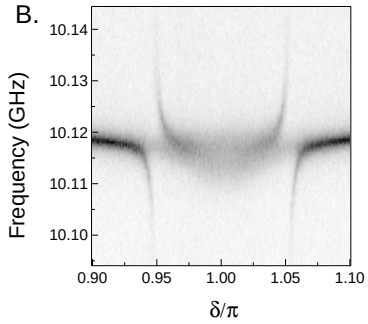

One channel crossing,
(several?) others at proximity

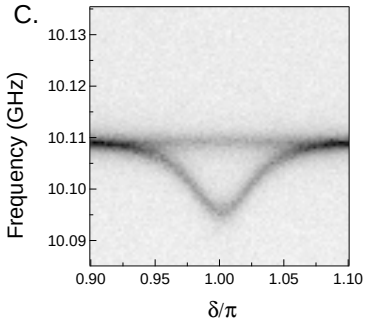

A single channel (?) with
Andreev frequency just
above the resonator

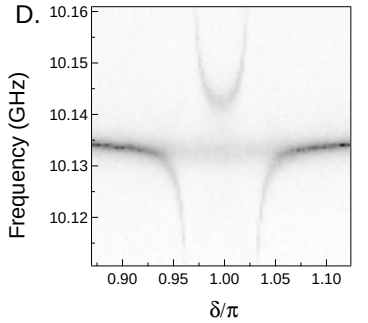

A single channel crossing
$\tau = 0.9889$
$\omega_A/2\pi = 9.5$ GHz

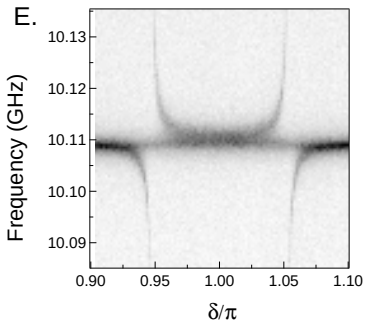

A single channel crossing
$\tau = 0.9941$
$\omega_A/2\pi = 6.9$ GHz

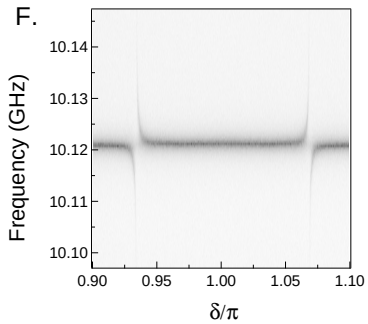

A single channel crossing
$\tau = 0.9983$
$\omega_A/2\pi = 3.66$ GHz

Chapter 4

Characterization of Andreev qubits

4.1 Detecting the coupling between the resonator and the Andreev qubit

In chapter 3 we presented the design of our chips and estimated the quality factor of the resonator as well as the coupling factor between the resonator and the qubit. In this section we present experiments that provide measurements of these two quantities and validate the proposed design.

4.1.1 Measurement setup and resonator characterization

In order to characterize the resonator and measure its coupling to the Andreev qubit, single continuous microwave tone is used to probe the system. The reflection coefficient S_{11} is measured as a function of the frequency of the microwave. This frequency is here swept close to the resonator resonance frequency of f_R.

The experimental setup for this measurement is shown in Fig. 4.1. The first port of a Vector Network Analyser (VNA) is connected to the sample

through the measurement line[1] of the refrigerator, the second port is connected to the output line of the refrigerator through a chain of two room temperature amplifiers with a 40 dB gain each.

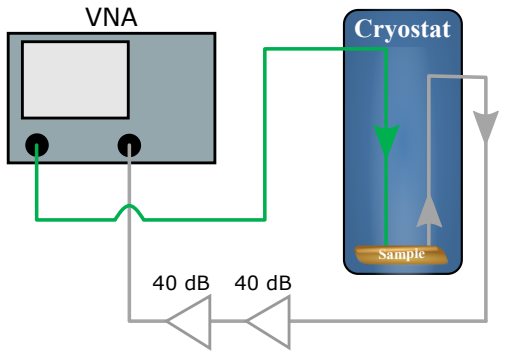

Figure 4.1: Setup used for single tone spectroscopy. A VNA (keysight PNA-L 5232A) is connected to the measurement and output lines of the refrigerator, two amplifiers (Miteq JS41-0010200-33) are used to further amplify the signal at the output of the fridge.

In order to characterize the bare resonator response, the phase across the contact must be set so that the cavity shift due to the qubit is negligible compared to the linewidth κ of the resonator: $\kappa \gg \chi = g^2/(\omega_A - \omega_R)$. We have shown in Chapter 3 that the coupling factor, g, is maximum at $\delta = \pi$. The resonator is hence characterized at a phase far from $\delta = \pi$ which also leads to large detunings. In Fig. 4.2 The reflection coefficient $S_{11}(\omega)$ is shown for $\delta = 0.9\pi$ which leads to a cavity shift of $\chi = 0.4\,\text{MHz} \ll \kappa$. Fits of the amplitude and the phase of S_{11} using Eq. 3.18 give the total quality factor $Q_{tot} = 2200$ as well as the external and internal quality factors $Q_{ext} = 4800$ and $Q_{int} = 4060$. The resonator is therefore close to the critical coupling $Q_{ext} \approx Q_{int}$ although slightly undercoupled, which scarcely reduces the SNR of the measurement as discussed in Section 3.1.3.

[1]The refrigerator lines are described in section 3.4.1

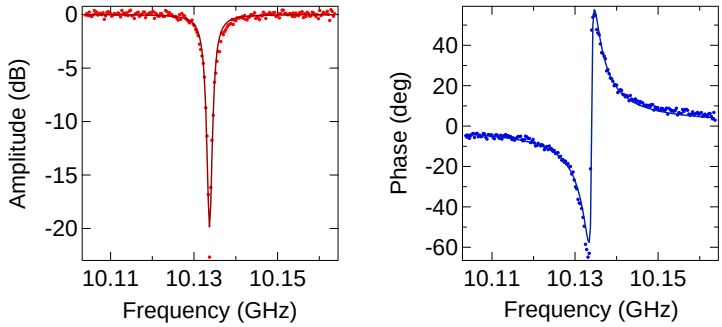

Figure 4.2: Characterization of the resonator. Symbols: Amplitude (left) and phase (right) of the reflected signal as a function of the measurement tone frequency. Solid line: fit using Eq. 3.18.

4.1.2 Measuring the coupling between the Andreev qubit and the resonator

In what follows, we present data taken on an atomic contact that had a channel with transmission $\tau > 0.99$. With such a high transmission, the transition frequency at $\delta = \pi$, $2E_a(\pi)$, is smaller than the resonator frequency f_r.

The coupling between the resonator and the qubit reveals itself by an avoided crossing between the Andreev transition and the resonator frequency (see Section 3.1.3), which is observed in Fig. 4.3. On this figure, the amplitude of the reflected signal is shown as a function of the microwave frequency and the phase difference across the contact. The avoided crossing is fitted using the Jaynes-Cummings model (Eq. 3.30), which yields a coupling factor $g(\pi)/2\pi \approx 100$ MHz, as well as a first estimation of the transmission $\tau = 0.992$.

Note that this avoided crossing presents an unusual feature: the bare resonator response at f_R is visible at all phases. As we shall discuss later, this reveals the existence of the odd state. In this state there is no coupling between the Andreev dot and the resonator, therefore the latter responds at its bare frequency independently of δ.

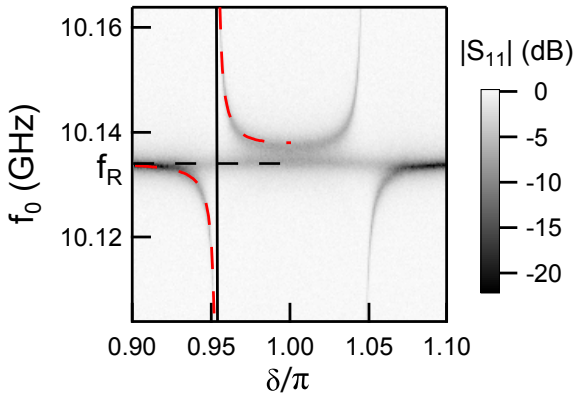

Figure 4.3: Single tone spectroscopy showing the avoided crossing of the Andreev transition with the resonator. The amplitude $|S_{11}|$ of the reflection coefficient is plotted as a function of the frequency f_0 of the measurement microwave tone and the phase difference δ across the contact. In the left half of the figure, is represented the bare frequency of the resonator f_R (black dashed line), the bare Andreev transition energy $2E_A/h$ (thick black line) and a fit using the Jaynes-Cummings Hamiltonian with $g(\delta = \pi)/2\pi = 100$ MHz (red dashed lines). The power of the microwave used for this measurement was $P_{in} = -120$ dBm at the input of the resonator. The bandwidth was BW = 10 Hz

4.2 Measuring the state of the Andreev qubit

In the previous section we confirmed experimentally that the qubit is coupled to the resonator. We now show how this coupling is used in practice to measure the state of the Andreev qubit.

4.2.1 Continuous wave measurements

The qubit spontaneously jumps between states because of parity and quantum jumps. It is possible to capture this dynamics by measuring the resonance as it was done in Fig. 4.2 but at a point in phase where the coupling is large (here $\delta = \pi$) and with a very large bandwidth. The result is shown in Fig. 4.4. Under these conditions, one measurement point is taken faster

than the characteristic lifetime of anyone of the three states of the Andreev dot. This allows to observe the dispersive shift of the resonator (see chapter 3) due to each individual state separately.

Three superimposed resonances are observed and identified using Eq. 3.35. Since we are in a situation so $2E_A < f_r$, $\chi = \frac{g^2}{\omega_A - \omega_R}$ is negative. The left-most resonance corresponds to the qubit being in its excited state while the highest one corresponds to the qubit being in its ground state. The central resonance is the bare resonator which can be observed when the Andreev dot is in one of its odd states and therefore not coupled to the resonator. The cavity shift is $\chi = 3$ MHz which gives, together with the estimated transmission, a smaller coupling factor $g(\pi) \approx 80$ MHz than the one found by fitting the avoided crossing. This difference is probably due to the imprecision of the fitting of the avoided crossing.

This figure reveals that the Andreev dot is in its odd state a significant fraction of the time.

The bandwidth necessary to observe three separated resonances is in this case 600 kHz, which sets a higher bound for the rates of quantum and parity jumps of the dot.

4.2.2 Pulsed measurements: clouds in the IQ-plane

The previous results were obtained with CW measurements: The sample is continuously irradiated by a microwave tone and the reflected signal is integrated to produce one data-point. In order to manipulate the Andreev qubit, pulsed measurements and synchronised excitation of the qubit are needed. For this purpose, we have implemented the microwave setup shown in Fig. 4.5. The setup can be divided in three parts:

- A measurement part, in green in Fig. 4.5. This microwave circuit shapes the microwave pulses used to probe the resonator.

- An excitation part, in red in Fig. 4.5. This part is used to produce microwave-pulse sequences used to manipulate the quantum state of the qubit.

- An acquisition chain, positioned on the right of Fig. 4.5. This chain demodulates, filters, and acquires the signal reflected by the resonator.

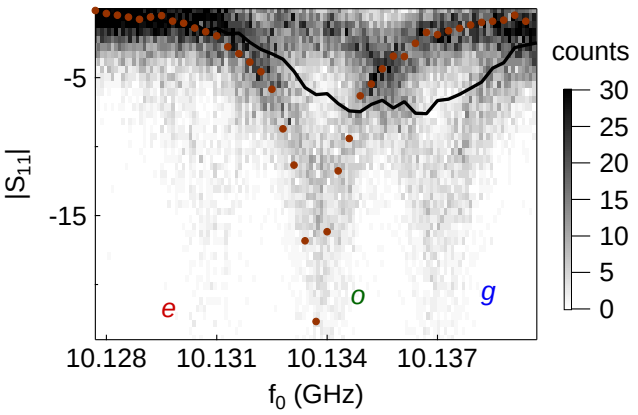

Figure 4.4: Vector network analyser (VNA) measurements of the resonator for the contact with $\tau \approx 0.992$ described previously. $|S_{11}|$ measured at $\delta = \pi$. Image in the background is a two-dimensional histogram of 32000 data points taken in a single frequency sweep with a 600 kHz bandwidth, and a larger power ($\bar{n} \approx 40$ photons in the resonator at resonance). Brown symbols are the resonance of the bare resonator measured at $\delta = 0.9\pi$ (same data as Fig. 4.2). Black line is taken at low power ($\bar{n} \approx 0.1$ photon in the resonator) and a 10 Hz acquisition bandwidth (corresponds to a vertical cut in the middle of Fig. 4.3). The central resonance corresponds to the bare resonance that is observed when the Andreev dot is in the odd state $|o\rangle$. Two replicas of the bare resonance are observed: the rightmost corresponds to the dot being in $|g\rangle$ and the leftmost to the dot being in $|e\rangle$.

The first element of the measurement chain is a microwave source that produces a continuous microwave tone at a frequency close to the resonator frequency. This tone is then splitted in two: half of the microwave signal is sent to the acquisition chain to serve as a reference signal for the homodyne detection. The other half is shaped by two mixers[2] and sent to the resonator. These mixers can be seen as voltage-controlled switches. An arbitrary function generator (AFG) generates square voltage pulses that are

[2]Two mixers are used instead of a single one in order to obtain a better on/off contrast at their output. Microwave leakage can perturb the evolution of the Andreev qubit.

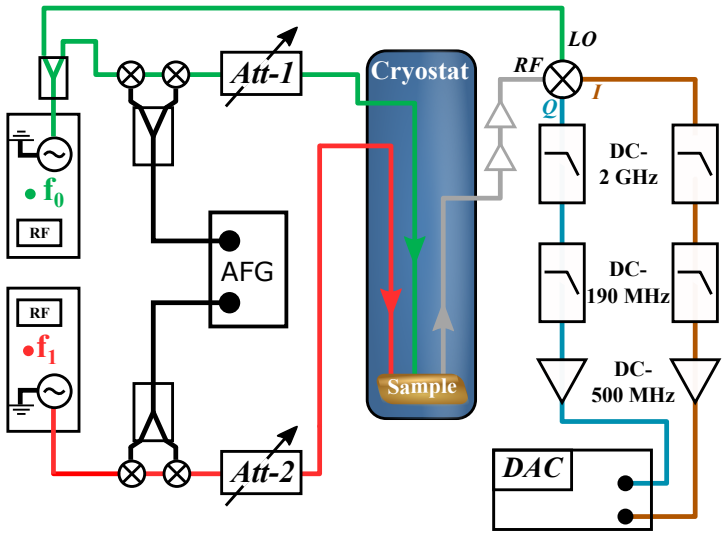

Figure 4.5: Setup used for pulsed measurements. The left part shows the excitation chain and the right part the acquisition chain. The green line is dedicated to the measurement pulse shaping; the red line to the qubit drive pulses shaping. The microwave sources are Anritsu MG3694B; the AFG is a Tektronix AFG3252; the black splitters are MiniCircuit ZFR-SC42S+; the green splitter is a Miteq 20238; the variable attenuators are Pulsar microwave AAT-23-479S; the IQ-mixer is a Hittite HMC-C042; the low pass filters are from MiniCircuits; the DC amplifiers are Femto HVA-500M-20B; the acquisition card is an Acqiris U1071A.

splitted and send to both mixers on their IF input to let the microwave pass through. Another component is placed on this measurement chain: a voltage controlled attenuator is used to finely tune the measurement power.

The acquisition chain contains the same room-temperature microwave amplifiers that were used for the single-tone experiment, followed by an IQ-mixer used as an homodyne demodulator. In this operation mode the IQ-mixer delivers at its two outputs (or quadratures) the amplitudes of the in-phase (I) and out-of-phase (Q) components of the reflected signal (applied at its RF input) with respect to the reference signal applied at its LO input. Several stages of low-pass filters and a DC-500 MHz amplifier

are placed at each output of the IQ-mixer. Each quadrature of the signal is finally digitized by a fast-ADC acquisition card (8-bits, 1Gs/s).

Figure 4.6 shows the time evolution of the signal of one quadrature when a 1 µs-long measurement pulse is applied, recorded with a 10 ns sampling time. The transient parts of the signal correspond to the photon-loading and unloading of the cavity. An exponential fit yields $\kappa = 1.7$ MHz close to the determination done using the linewidth $\kappa = f_r/(\pi Q_{tot}) = 1.5$ MHz. In the following experiments, these transient parts are not acquired. Only the signal in the time interval indicated by the green arrow is kept. It is averaged by the acquisition card to produce, together with the corresponding average on the Q quadrature, a single point in the IQ-plane.

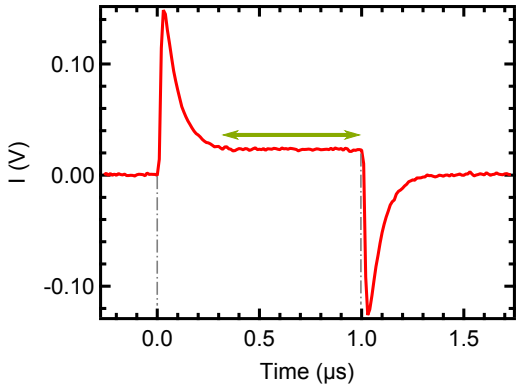

Figure 4.6: In-phase signal acquired by the acquisition card, for a 1 µs-long measurement pulse. The green arrow represents the points that are actually acquired and averaged to obtain one point in the IQ-plane. The beginning and the end of the microwave pulse are indicated by the double-dashed lines.

Clouds in the IQ-plane In Fig. 4.7 are represented in the IQ-plane the histogram of 8000 measurements obtained for the measurement tone at the bare resonator frequency. Three clusters of points (or clouds) are observed. They correspond to the three possible states of the qubit, associated with different values of the resonator frequency (discussed in the previous section). In order to identify the state associated to each cluster, we use the fact that, at the measurement frequency, the reflected amplitude is minimal

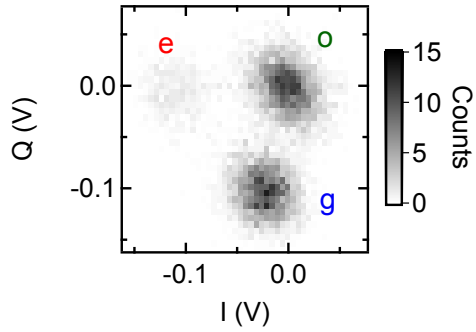

Figure 4.7: Density plots of I and Q quadratures at $\delta = \pi$ illustrate single-shot resolution of the quantum state of the dot. (a) No drive at f_1; (b) after a long driving pulse at f_1 pulse transferring population from $|g\rangle$ to $|e\rangle$.

when the odd state is occupied. Therefore the cloud corresponding to the odd state is the one centered at the origin of the plot. The cloud corresponding to the excited state has to be the less populated of the two remaining clouds. The last cloud corresponds to the qubit being in the ground state.

In the following experiments, each measurement results in an image like Fig. 4.7, which can be treated using two protocols:

- The image is analyzed in terms of populations of the three states using a Gaussian mixture model algorithm[3] that fits the three clusters and returns their position and weights. However this procedure is rather slow and not very robust to noise.

- All the points are averaged to obtain a mean value in each quadrature. This procedure is very fast and robust but requires a calibration to obtain the population of each state.

[3]The Python toolbox scikit.learn was used for this task. The "gmm" (Gaussian mixture model) function was used to fit the clusters with three 2-dimensional Gaussian "clouds" and return their positions and relative weights. The weights are then interpreted in terms of populations.

4.3 Exciting the Andreev qubit

4.3.1 Two-tone spectroscopy

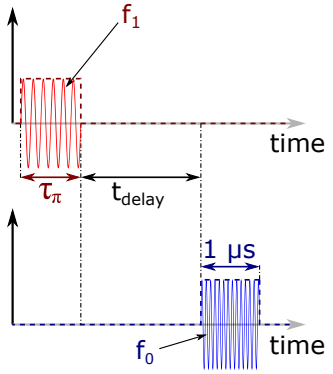

Figure 4.8: Sequence of pulses used for the two-tone spectroscopy. The red microwave pulse corresponds to the qubit driving tone, the blue pulse corresponds to the measurement pulse at $f_0 = f_r$.

Compared to the previous experiments in which no excitation of the qubit was performed, two-tone spectroscopy involves a driving microwave pulse at a frequency f_1 different from that of the measurement tone f_0. This microwave tone f_1 is used to excite the qubit when its frequency matches the Andreev transition frequency $f_1 = f_A(\delta, \tau)$. It is shaped in a 13 µs-long square pulse (see Fig. 4.8) by the excitation part of the microwave setup shown in Fig. 4.5. Then a measurement pulse is sent to the resonator in order to probe the state of the Andreev qubit using the averaging method discussed in section 4.2.2.

Figure 4.9 shows the result of a two-tone spectroscopy of the contact discussed in section 4.1. The Andreev transition appears clearly and is fitted with a very good agreement with expression Eq. (2.6) for the Andreev transition energy. Figure 4.10 shows the spectroscopy line at $\delta = \pi$ in terms of populations. It is fitted with a lorentzian function with a full-width-at-half-maximum FWHM = 16 MHz. For low power[4] this width is only

[4]In order to access the coherence time of the qubit from its spectroscopy line, one has

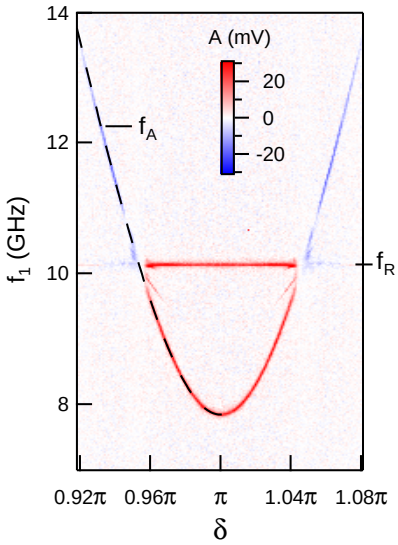

Figure 4.9: Pulsed two-tone spectroscopy: color-coded amplitude A of one quadrature of the reflected signal as a function of δ and f_1. The dashed black line shows the theoretical fit of Andreev transition frequency $f_A = 2E_A/h$ with $\tau = 0.99217$. A parasitic line, corresponding to a two-photon process $2f_1 = f_R + f_A(\tau, \delta)$, is visible just below 10 GHz. The line of the resonator is also clearly visible between the avoided crossings. This line is attributed to population inversions observed when large photon numbers are reached in the resonator. These effects are discussed in chapter 5.

given by the dephasing time $T_2^* = (\pi \text{FWHM})^{-1}$ [105]. Here, one obtains $T_2^* \approx 20$ ns.

This type of spectroscopy was performed on many different contacts. Figure 4.11 shows the result of a 2-tone spectroscopy done on different contacts with transition frequency (8.69 GHz) at $\delta = \pi$ higher or lower (2.85 GHz) than in Fig. 4.9.

Finally we remark that the coupling between the Andreev qubit and

to be in the linear response regime. This is achieved when the rabi frequency (determined by the amplitude of the driving pulse) is lower than the dephasing rate of the qubit [105].

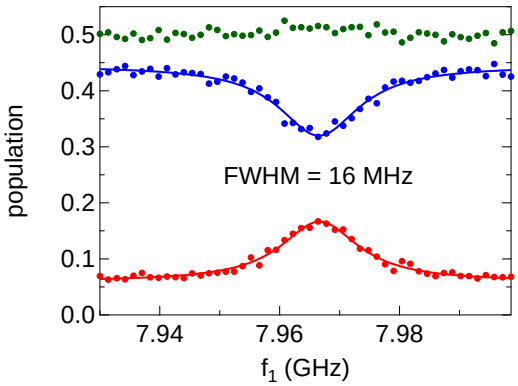

Figure 4.10: Spectroscopy at $\delta = \pi$ of the same contact as shown in Fig. 4.9. The populations are plotted as functions of the frequency f_1 of the saturating drive pulse. Blue dots represent the population of the ground state, red dots the population of the excited state and green dots the population of the odd states. Full lines are lorentzian fits. (FWHM, full width at half maximum)

the resonator makes possible multiphoton excitations of the qubit and the resonator at strong driving power. This is illustrated Fig. 4.12, where the spectrum of the same contact is shown at two different driving powers.

4.3.2 Comment on the clouds

The 2-D histogram presented in Fig. 4.7 showed the equilibrium populations of the Andreev qubit. Now that we can drive the transition between the ground and excited state of the qubit we can validate the identification of the clouds by performing the same measurement but after a driving pulse at f_A. The result of this experiment is shown in Fig. 4.13B. The 2-D histogram in absence of excitations is recalled on Fig. 4.13A for comparison.

The population transfer from $|g\rangle$ to $|e\rangle$ is clearly visible, whereas the population of the cloud corresponding to $|o\rangle$ remains unaffected.

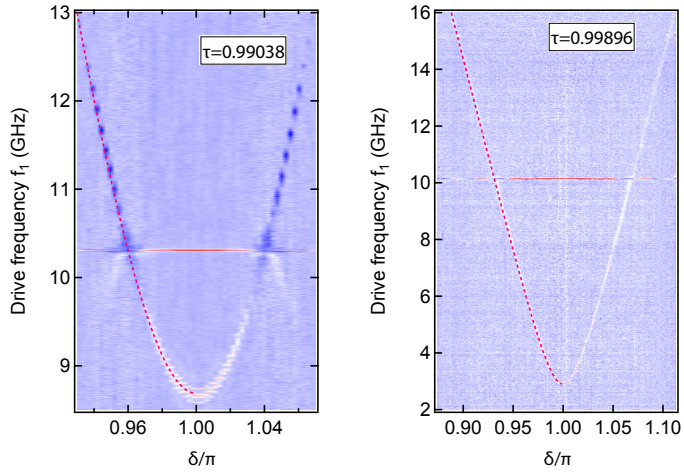

Figure 4.11: Two-tone spectroscopy of two different contacts. Left: the Andreev transition frequency is at $\delta = \pi$ at 8.69 GHz. The sidebands clearly visible close to π are discussed in Appendix D. Right: A contact with a much higher transmission ($\tau \approx 0.999$) and a transition frequency of 2.85 GHz at $\delta = \pi$.

4.4 Characterization of the Andreev qubit at the sweet spot

This section presents the coherent manipulation of the Andreev qubit. All the results presented here were obtained at $\delta = \pi$, a "sweetspot" where the qubit is sensitive to flux noise only to second order. Although this characterization was performed on many different contacts, we detail here the coherent manipulation of a single contact. The contact on which the experiments described in this section were performed (with the exception of the CPMG and the characterization of the transmission noise) was the same as the one on which the spectroscopy data of Fig. 4.9 were taken. The microwave setup used to perform the experiments presented in this section was also the same as for the two-tone spectroscopy (except for the CPMG measurements).

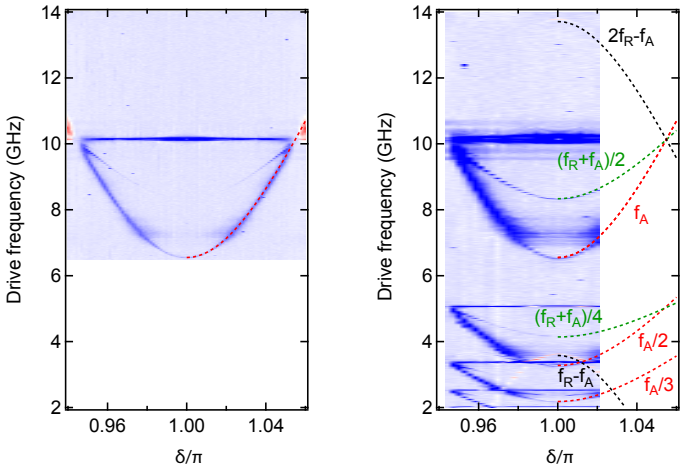

Figure 4.12: Two-tone spectroscopies of a contact with a transition frequency at $\delta = \pi$ of 4.64 GHz. Left: Lower driving power spectroscopy, a multiphoton excitation is already visible close to the resonator frequency. Right: Strong power spectroscopy performed with a larger span. The Andreev transition appears larger, and more multi-photon transitions are visible. The multi-photon transitions of the qubit alone appear at sub-multiples of the Andreev transition. Four lines are visible implying transitions of the dressed system. Two of them ($(f_A + f_R)/2$ and $(f_A + f_R)/4$) consist in a transition between $|g, n\rangle$ and $|g, n + 1\rangle$ (with n the number of photons in the resonator) with 2 or 4 photons. The other two ($(f_R - f_A)$ and $(2f_R - f_A)$) are transition from $|e, n\rangle$ to $|g, n + 1\rangle$ or $|g, n + 2\rangle$ respectively.

4.4.1 Rabi oscillations

When a two-level system is irradiated by a resonant driving field, it oscillates coherently between its ground and excited state at a frequency proportional to the drive amplitude [106]. In order to capture this oscillation, the population of the qubit is measured just after a driving pulse of variable duration t_{drive}, as sketched in Fig. 4.14.

The result of this procedure is shown in Fig. 4.15. The populations of the ground and excited states oscillate while the population of the odd state remains constant. The oscillation is damped with a characteristic time of

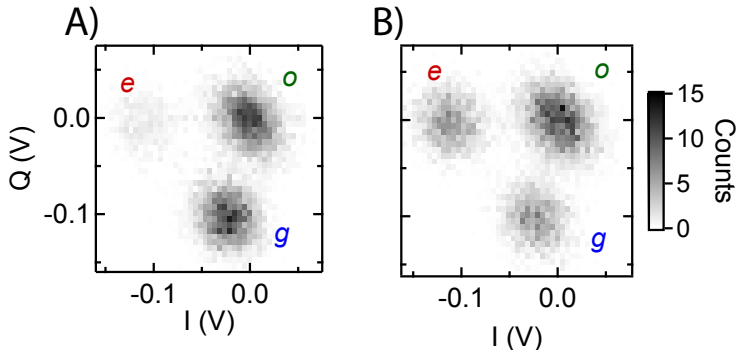

Figure 4.13: Density plots of I and Q quadratures at $\delta = \pi$ illustrate single-shot resolution of the quantum state of the dot. (a) No drive at f_1; (b) after a long driving pulse at f_1 pulse transferring population from $|g\rangle$ to $|e\rangle$.

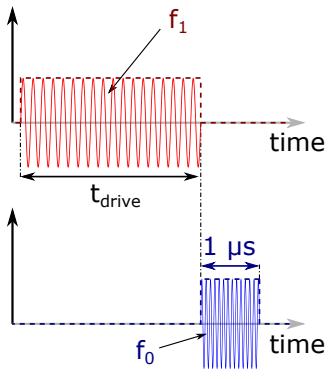

Figure 4.14: Sequence of pulses used to measure Rabi oscillations.

595 ns. This time depends both on the rate of relaxation of the excited state and on dephasing at the Rabi frequency [105].

In order to measure these rates separately, other pulse sequences are used. For this purpose, two particular pulses are defined using the Rabi oscillations. The "π-pulse" sets the qubit into its maximally excited state. Its duration for the driving power used in Fig. 4.15 is $t_{\mathrm{drive}} = 16$ ns. The "$\pi/2$-pulse" is a pulse that drives the system from its ground state to an equal weight superposition of ground and excited state. Its duration is half

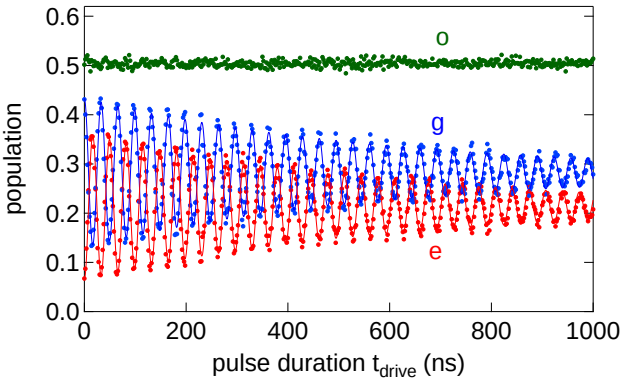

Figure 4.15: Rabi oscillations: populations as a function of the driving-pulse duration. Red dots: population of the excited state. Blue dots: population of the ground state. Green dots: population of the odd states. Thick line: Fit of the Rabi oscillation using an exponentially decaying sine function, with a frequency of ≈ 30 MHz and a decay time of 595 ns.

that of a π-pulse.

4.4.2 Lifetime of the excited state

To access the lifetime of the excited state, the qubit is driven to its maximally excited state using a π-pulse, and the state of the qubit is measured after a delay, as shown in Fig. 4.16. As the delay is increased, the population of the excited state decreases because it relaxes to the ground state. For this contact, this decay is exponential with a characteristic time $T_1 = 4$ µs, as shown in Fig. 4.17.

The corresponding rate $\Gamma_1 = 250$ kHz has to be compared with the theoretical prediction. Relaxation arises from processes in which energy is transferred from the qubit to the environment in the form of phonons, photons, or to out-of-equilibrium quasi-particles.

The relaxation rate due to the coupling to phonons is given, for $E_A \ll \Delta_{sc}$, by [14]:

$$\Gamma_{ph}(\delta,\tau) \approx \kappa_{ph} \frac{\Delta_{sc}(1-\tau)}{E_A(\delta,\tau)} \left(\frac{E_A(\delta\tau)}{k_B}\right)^3 \tag{4.1}$$

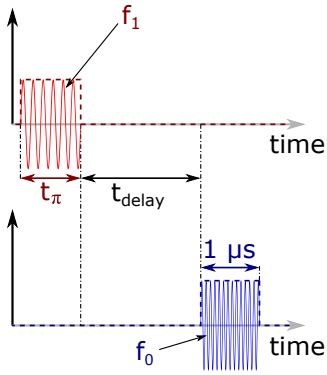

Figure 4.16: Sequence of pulses used for the T1 measurements. The qubit driving pulse is shown in red, it is resonant with the Andreev transition frequency: $f_1 = 2E_A/h$. After a delay, the measurement pulse is sent to the resonator.

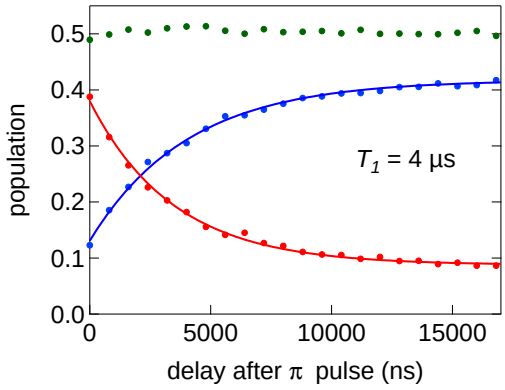

Figure 4.17: Relaxation of populations of the even states after a π-pulse. Red dots: population of the excited state. Blue dots: population of the ground state. Green dots: population of the odd states. Full lines: fit with an exponential decay, with a characteristic time of 4 µs.

where $\kappa_{ph} \approx 3\,\mathrm{MHz/K^3}$ [77]. At $\delta = \pi$, and for the contact considered here, this rate is $\Gamma_{ph}(\pi,0.992) \approx 2\,\mathrm{kHz}$, which is too small to account for the measured rates, as already observed in previous experiments (Ref. [16],

pp. 88-91).

The expected relaxation rate due to the emission of a photon into the electromagnetic environment (Purcell effect) was derived by Desposito and Levy-Yeyati [107, 16]. It is given by:

$$\Gamma_\nu = \frac{\pi\Delta_{sc}}{2\hbar}\frac{\mathrm{Re}[Z_{env}]}{R_Q}\frac{(1-\tau)(\tau\sin^2(\delta/2))^2}{(1-\tau\sin^2(\delta/2))^{3/2}}, \tag{4.2}$$

where $R_Q = \frac{h}{4e^2}$ is the resistance quantum and Z_{env} the environment impedance as seen from the atomic contact. If we consider that the contact only see the dissipative environment through the resonator, we get:

$$\mathrm{Re}[Z_{env}] = \frac{zR_Q}{\pi}\frac{Q_{tot}}{1+\left(Q_{tot}\frac{1-(\omega/\omega_0)^2}{\omega/\omega_0}\right)^2}, \tag{4.3}$$

where $z = 1.9.10^{-5}$ is given by Eq. (3.29) and is extracted from the coupling factor g obtained from the fit of the anticrossing. Using $Q_{tot} = 2200$, one obtains at $\delta = \pi$ $\Gamma_\nu \approx 60$ kHz, which is much larger than the phonon relaxation rate, yet a factor 4 too low to account for the observed relaxation rate.

The origin of the fast relaxation of the Andreev qubit is still unclear. Three explanations can be invoked for the discrepancy observed:

- A secondary relaxation channel exists through the odd states. As will be discussed in chapter 6, this channel does contribute to the relaxation but is not sufficient to account for the rates observed.

- The coupling to the phonon bath might be underestimated. The dependence of the Andreev energy to the strain of the contact through the transmission [34] might be at the source of a stronger coupling to the mechanical modes of the electrodes than the regular electron-phonon coupling.

- The actual electromagnetic environment is more complex than it was designed to be. In particular, in other microwave experiments the sample is usually placed in a tight casing that rejects all environmental modes to high frequencies. Although not impossible, it would be quite difficult to implement such strategy with the current setup in

which the sample has to be bent. In order to compensate for this absence of casing, microwave absorbent has been placed inside the magnetic shields. This absorbent could be responsible for a higher impedance seen from the contact. An other solution to circumvent this problem would be to redesign the experiment from scratch and use of a 3D microwave cavity with an embedded bending mechanism. The electromagnetic environment would then only be constituted by this simple cavity.

4.4.3 Coherence times

We now present the experiments performed to quantify the coherence properties of the Andreev qubit at $\delta = \pi$. The coherence of a qubit can be limited by two phenomena:

- Pure relaxation, with a characteristic time T_1.
- Pure dephasing, characteristic time T_ϕ, which is due to fluctuations of the Andreev transition energy. This is the subject of this section.

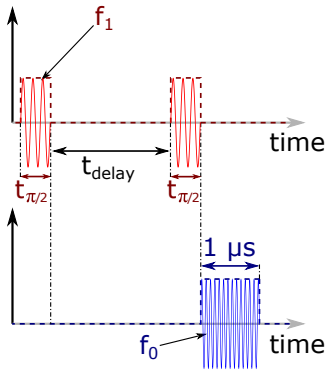

Figure 4.18: Sequence of pulses used for the T_2^* measurements. The qubit driving pulse is shown in red, it is detuned the Andreev transition frequency in order to obtain the oscillatory behaviour observed in Fig. 4.19.

The dephasing time of the qubit is obtained using a Ramsey sequence. Such a sequence consists in two $\pi/2$-pulses separated by a delay as shown

in Fig. 4.18. The state of the qubit is measured right after the second pulse. The effect of the first pulse is to drive the qubit to an equal superposition of ground and excited state. If no dephasing occurs during the delay the second pulse drives the qubit to the excited state. If dephasing occurs and the phase of the qubit is randomly distributed, the second pulse drives the qubit to a random state. What is then measured is a random mixture of ground and excited state.

When the dephasing noise is white, an exponential decay of the excited state population is observed as a function of the delay between the pulses. This decay occurs with a time scale T_2^* which is linked to the dephasing and relaxation times by [105]:

$$\frac{1}{T_2^*} = \frac{1}{2T_1} + \frac{1}{T_\phi}. \tag{4.4}$$

A Ramsey experiment is extremely sensitive to the detuning between the qubit transition energy and the driving tone. Such a detuning results in an oscillation of the populations of the excited and ground states at the detuning frequency, with the same decaying envelope as at zero detuning. It is therefore preferable to have a detuning larger than the dephasing rate so that both the detuning and the decay can be fitted accurately. Figure 4.19 shows the result of such a Ramsey experiment.

The best fit is obtained using a Gaussian envelope for the decay, which suggests a $1/f^\alpha$ noise[5] with $\alpha \geq 1$ [105] rather than a white noise that produces an exponential envelope. Moreover the characteristic time of decay $T_2^* = 38$ ns being much lower than T_1, $T_\phi \approx T_2^*$.

Two parameters in the Andreev energy can fluctuate and induce dephasing: the phase difference δ, and the transmission τ.

At the sweet spot, the main source of dephasing noise are the transmission fluctuations, which are the results of fluctuations of the electronic

[5]The decay function of a Ramsey sequence in the presence of $1/f^\alpha$ noise is given in Ref. [105] by $f_\lambda(t) = \exp\left(-t^2 D_\lambda^2 t^{\alpha-1} \int_{\omega_{ir}}^{\infty} \frac{A_\lambda}{(\omega t)^\alpha} \mathrm{sinc}^2(\omega t/2) d(\omega t)\right) \approx \exp\left(-\frac{t^2 A_\lambda D_\lambda^2}{\omega_{ir}^{\alpha-1}}\right)$, where A_λ is the noise power of a parameter λ that couples to the transition frequency, and $D_\lambda = 2\frac{\partial E_A(\tau,\pi)}{\partial \lambda}$

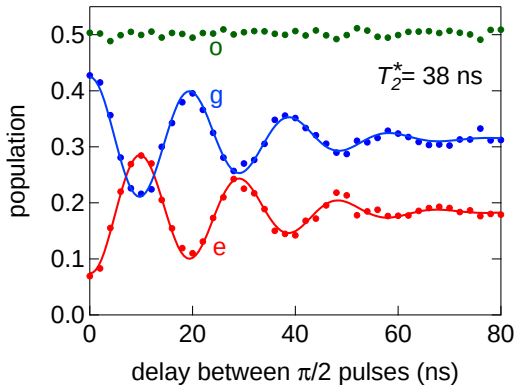

Figure 4.19: Ramsey oscillations: populations as a function of delay between the two detuned $\pi/2$-pulses. Red dots: population of the excited state. Blue dots: population of the ground state. Green dots: population of the odd states. Full lines: Fit using sine function with a gaussian decay. The detuning frequency is 51 MHz and the decay time is 38 ns

configuration close to the contact. These fluctuations may have different origins:

- Macroscopic vibrations: since the transmission depends on the strain [34] on the contact, any vibration of the mechanical setup induces fluctuation of the transmission.
- Mesoscopic vibrations: the suspended bridge of the MCBJ has eigenmodes and create fluctuations of the strain in the contact and therefore transmission fluctuations (more in Appendix D). Creep in the substrate would also lead to strain fluctuations in the bridge.
- Microscopic reconfigurations: vacancies or atoms close to the contact can jump between adjacent sites and modify the local electronic configuration and therefore the channel transmission.

Further insight on the origin of dephasing noise is obtained using a Hahn echo sequence. This sequence of pulses is made of a Ramsey sequence in the middle of which a π-pulse has been added, as shown in Fig. 4.20. The effect of this π-pulse is to filter-out the noise which has a frequency lower

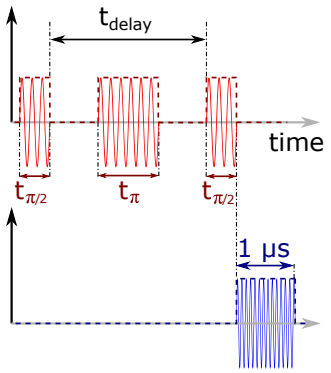

Figure 4.20: Sequence of pulses used for the T_{2E} measurements. The qubit driving pulses are shown in red, they are resonant with the Andreev transition frequency: $f_1 = 2E_A/h$.

than $1/t_{delay}$ [105, 89], where t_{delay} is the time between the two $\pi/2$-pulses. The decay time observed with this sequence is much longer than the one observed for the Ramsey sequence, see Fig. 4.21. An exponential fit gives a characteristic time T_{2E} =565 ns. The echo decay time can be related to the Ramsey decay time in presence of $1/f$ or $1/f^2$ noise. For $1/f$ noise, one obtains [105, 41]:

$$\frac{T_2^*}{T_{2E}} = \sqrt{\ln(2)/\ln(\omega_{ir}t)} \approx 0.2,$$

where ω_{ir} is a cutoff pulsation related to the time needed to take a single point (here $\omega_{ir} = 2\pi\times 2$ Hz). This ratio is not in agreement with the experimental value $\frac{T_2^*}{T_{2E}} = 0.07$. For $1/f^2$ noise, one obtains [105]:

$$\frac{(T_2^*)^2}{(T_{2E})^3} = \frac{\pi}{12\omega_{ir}} \approx 3 \text{ Hz}.$$

Again this theoretical value is not in agreement with the experimental one $\frac{(T_2^*)^2}{(T_{2E})^3} \approx 8$ kHz. This indicates that the frequency dependence of the noise does not follow the same power law below and over 1 MHz.

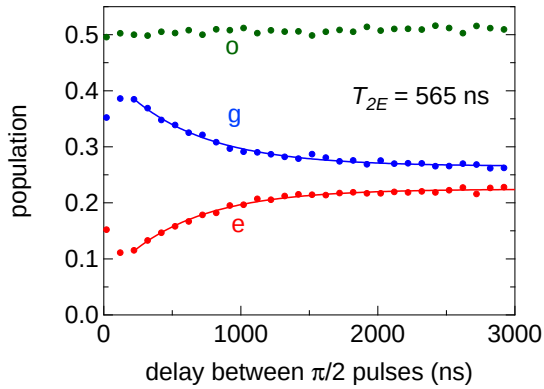

Figure 4.21: Hahn echo: populations as a function of delay between the two $\pi/2$-pulses with a π-pulse in between. Red dots: population of the excited state. Blue dots: population of the ground state. Green dots: population of the odd states. Full lines: Fit using an exponential decay with a characteristic time of 565 ns.

4.4.4 Evaluation of the noise power density using CPMG sequences

Background: The Carr-Purcell-Meiboom-Gill (CPMG) sequence is a pulse sequence designed by Carr and Purcell [108] and improved by Meiboom and Gill [109] in order to maintain the coherence of a nuclear spins ensemble by decoupling them dynamically from the noise of their environment. It was later proposed to use the filtering properties of this type of sequence to sample the noise power spectrum of the environment [110, 111]. This idea was first implemented for a superconducting qubit by Bylander *et al.* [89]. We now present the results obtained on the Andreev qubit with this technique. The CPMG sequence is an echo sequence in which the π-pulse around the x axis has been replaced by a series of π-pulses alternatively around the x-axis and the y-axis, as shown in Fig. 4.22. During a CPMG sequence the dephasing noise is integrated with a filtering window that is defined by the number N of π-pulses and the duration of the sequence. For long enough sequences, the filter function can be approximated as a delta function that samples the noise at it center frequency $\approx \frac{N}{T_{CPMG}}$ for $N \gg 1$.

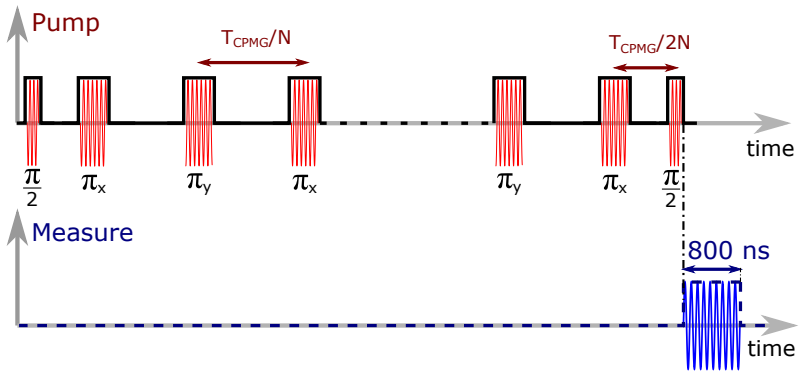

Figure 4.22: Sequence of pulses of a CPMG sequence.

This noise sampling is then used to reconstruct the noise spectrum [89].

Experimental setup: The experimental setup for the CPMG measurements is similar to the one used for previous pulsed experiments except for the pump-pulse shaping part. The two Marki mixers have been replaced by a single IQ-mixer (Marki IQ-1545). A dedicated pulse generator (Tektronix AFG3252) is used to control the output of the IQ-mixer that produces pulses that are in-phase or in quadrature with the LO signal input. An in-phase pump pulse induces a rotation of the qubit around the x-axis and a pump pulse in quadrature induces a rotation of the qubit around the y-axis. The modified setup is shown in Fig. 4.23.

A critical issue for the CPMG sequence is the calibration of the π-pulses, because the pulse errors accumulate and become sizable for large numbers of pulses. The calibration was done by fixing a pulse duration $t_\pi = 16$ ns and sweeping the pump power (hence the Rabi frequency) with the voltage-controlled attenuator labeled 'Att-2' in Fig. 4.23, in order to determine for which power a single pulse produces a rotation by π. In the absence of dephasing, an odd number of π-pulses drives the system to its excited state independently of the number of pulses[6]. The exact power that produces a

[6]In the calibration only π-pulses are used. The final state is therefore the opposite of what would be obtained with a CPMG sequence containing the same number of pulses.

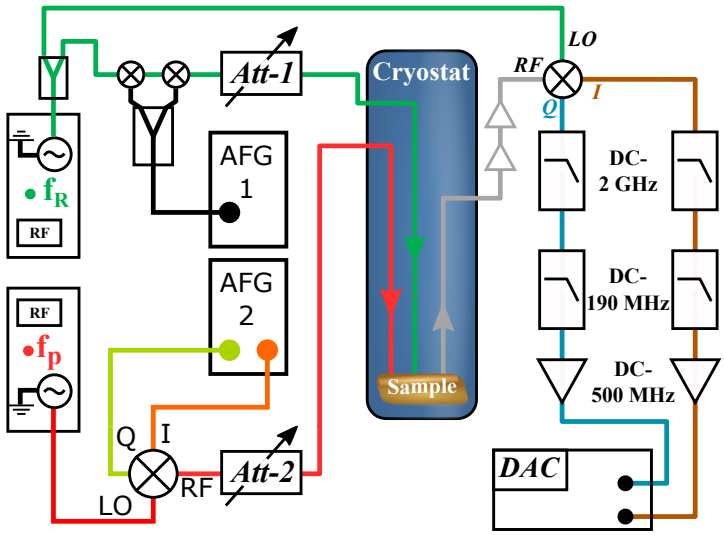

Figure 4.23: Setup used to perform the CPMG experiments. It differs from the setup previously used (Fig. 4.5) by the replacement of the two mixers on the pump line by a single IQ-mixer and the use of a dedicated arbitrary function generator to produce the rotations of the qubit around the x-axis and y-axis.

π-pulse for $t_\pi = 16$ ns is found by measuring the state of the Andreev qubit after different odd numbers of pulses, and as a function of the measurement power as shown in Fig. 4.24. A dead time of 10 ns was left between the pulses in order to take into account the imperfections of a single pulse such as ripples, in the calibration.

The measurement presented below was performed at $\delta = \pi$ for a contact with a minimum transition energy $2E_A(\tau, \pi)/h = 3.49$ GHz ($\tau = 0.9984$). The relaxation time of the excited state was $T_1 = 11$ µs and the dephasing time was $T_2^* = 30$ ns.

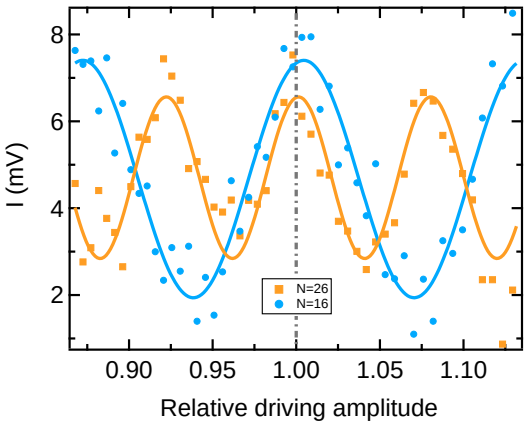

Figure 4.24: I-quadrature as a function of the driving amplitude (normalized by the power corresponding to a π-pulse in 16 ns), for 16 and 26 pulses. When the driving power is such that $\Omega_{Rabi} \times T_\pi = \pi$, the final state of the qubit does not depends on the number of pulses.

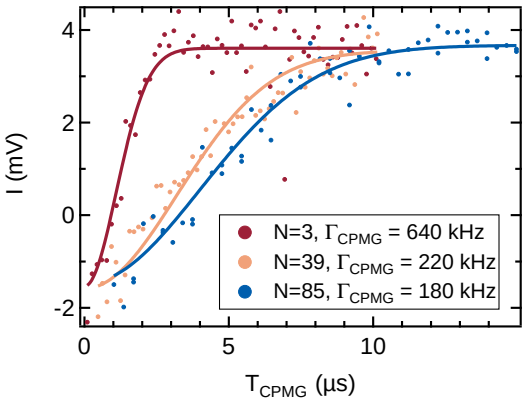

Figure 4.25: Three CPMG decays obtained for N=3, 39, and 85 pulses, respectively (dots) and the associated Gaussian fit (thick lines).

Results and interpretation: Figure 4.25 shows the result of CPMG sequences performed for odd numbers[7] of pulses from 1 to 85. The signal to

[7]Only odd numbers of pulses were used in order to always have the qubit in its ground state for no dephasing.

noise ratio is too low in this data to perform reliably the same analysis as in Bylander *et al.* [89]. Instead we treat the data assuming three different type of noise:

- White noise with a PSD $A_{\tau,\alpha=1}$. It is a very common type of noise and is expected to dominate ultimately at high frequency.
- $1/f$ noise with a PSD at 1 Hz $A_{\tau,\alpha=2}$. Again it is a very common type of noise usually attributed to two-levels fluctuators.
- $1/f^2$ noise with a PSD at 1 Hz $A_{\tau,\alpha=3}$, for reasons that will be apparent in section 4.6.

The decay of the CPMG sequences in presence of these three type of noises is given by [89]:

$$f_{N,\alpha}(t) = \exp\left(-t^{\alpha} D_{\tau}^{2} A_{\tau,\alpha} \int_{0}^{\infty} \frac{g_N(u)}{u^{\alpha-1}} du\right), \tag{4.5}$$

where $\alpha = 1,2,3$, $D_\tau = 2\frac{\partial E_A(\tau,\pi)}{\partial \tau}$ and $g_N(u)$ is a filter function associated to the CPMG sequence. It can be shown that the argument of the integral converges in zero for $N > 1$. The data is therefore fitted with three different types of decay: an exponential decay, a Gaussian decay and e decay in $e^{-(\Gamma \times t)^3}$. The PSD at 1 Hz for each type of noise is extracted from the rates $\Gamma_{\mathrm{CPMG},\alpha}$ obtained with these fits:

$$A_{\tau,\alpha} = \frac{(\Gamma_{\mathrm{CPMG},\alpha})^{\alpha}}{I_{N,\alpha} D_{\tau}^{2}}, \tag{4.6}$$

where $I_{N,\alpha}$ is integral in Eq. 4.5 which integration is performed numerically. The noise in the data is too high to properly discriminate between three types of decay. We therefore report here the PSD at 1 Hz obtained for the three noises:

- For white noise: $A_{\tau,\alpha=1} = 6.10^{-21} \pm 5.10^{-21}$ Hz^{-1}
- For $1/f$ noise: $A_{\tau,\alpha=2} = 1.5.10^{-13} \pm 4.10^{-14}$ Hz^{-1}
- For $1/f^2$ noise: $A_{\tau,\alpha=3} = 4.10^{-6} \pm 2.10^{-6}$ Hz^{-1}

Remarkably these values give a similar noise density around 10 MHz, which is the range of frequencies the CPMG sequence is sensitive to. We further comment these values in section 4.6.3.

4.4.5 Dispersion of the characteristic times

An important advantage of the experimental setup is the possibility to change *in situ* the contact and explore different transmissions. Here, we recapitulate the values of T_1, T_2^*, T_{2E} for approximately 30 different contacts, as a function of the Andreev transition energy between 3.125 GHz and 12 GHz.

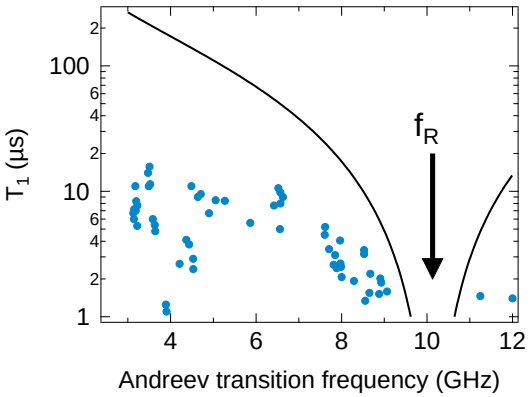

Figure 4.26: T_1 as a function of $f_A(\delta = \pi)$ measured for approximately 30 different contacts. Solid line: prediction for the Purcell limited T_1 when only considering the mode of the resonator.

Figure 4.26 shows the measured T_1 at $\delta = \pi$ as a function of the Andreev transition frequency. The arrow indicates the position of the resonator frequency f_R. At lower energies, a larger dispersion is observed as well as larger maximum relaxation times. The expected Purcell-limited T_1 calculated using Eq. (4.2) is shown as a comparison. The maximum T_1 was measured for a contact at energy $2E_A(\tau, \pi)/h = 3.51$ GHz ($\tau = 0.99843$) with $T_1 = 15.7$ µs. The shortest relaxation time measured was found for a contact having an energy $2E_A(\tau, \pi)/h = 11.25$ GHz ($\tau = 0.98388$), with $T_1 = 0.73$ µs.

Figure 4.27 shows the measured T_2^* at $\delta = \pi$ as a function of the Andreev transition frequency. On the majority of the contacts, the dephasing times were lower than 100 ns. However, for about 5 different contacts on two different samples the measured T_2^* was above 100 ns (maximum:

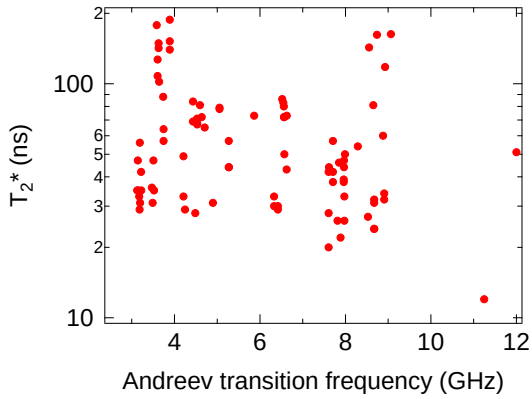

Figure 4.27: T_2^* as a function of $f_A(\delta = \pi)$ measured for approximately 30 different contacts.

$T_2^* = 188$ ns). The dispersion of the Ramsey decay times is rather large (standard deviation of 40 ns) and no clear dependence on the transmission can be observed from this data. Therefore this survey seems to point towards a contact-dependent source of decoherence that would be independent of the transmission itself.

Figure 4.28 shows the measured T_{2E} at $\delta = \pi$ as a function of the Andreev transition energy. Here also, no clear trend appears. The average value is $\langle T_{2E} \rangle = 960$ ns, with a standard deviation of 310 ns. No correlation between the transmission and T_{2E}, is observed which suggests that the higher frequency noise to which the echo sequence is sensitive is also independent of the transmission and the contact. Moreover, the absence of correlation between T_2^* and T_{2E}, see Fig. 4.29, suggests that the low frequency noise has a source different from the high frequency noise.

This systematic survey of the relaxation and coherence properties of the different contacts does not provide a clear picture of the sources of relaxation and decoherence. The relaxation times are too short and too dispersed to be attributed solely to photon relaxation in the resonator. The absence of correlation between the echo decay time and the dephasing time shows that at least two independent sources of decoherence exist, one at low frequency and the other at high ($\gtrsim 1$ MHz) frequencies.

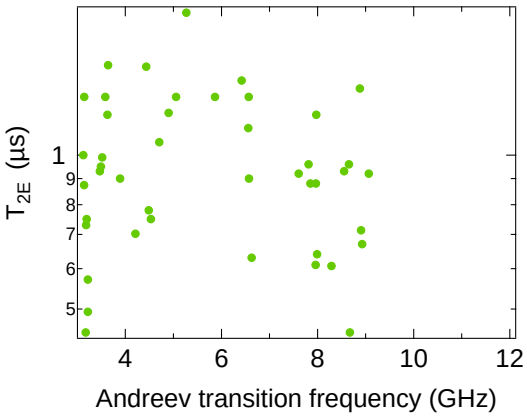

Figure 4.28: T_{2E} as a function of $f_A(\delta = \pi)$ measured for approximately 30 different contacts.

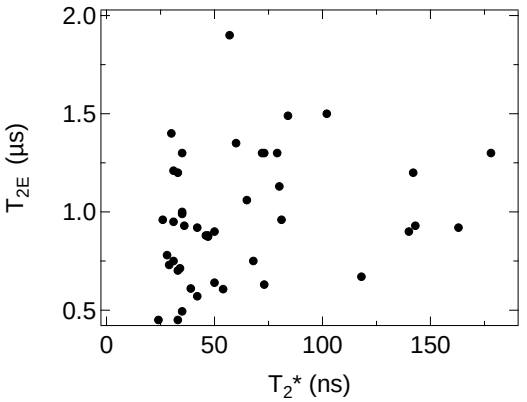

Figure 4.29: T_{2E} as a function of T_2^* for approximately 30 different contacts. No correlation between the two quantities is observed.

4.5 Phase dependence of the lifetimes and coherence times

We now present the phase dependence of the characteristic times T_1 and T_2^* on one contact.

4.5.1 Relaxation rate of the excited state

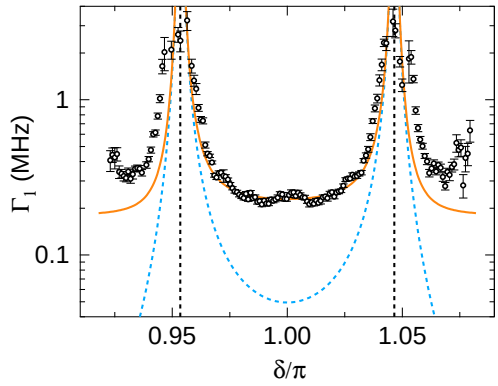

Figure 4.30: Phase dependence of relaxation rate $\Gamma_1 = 1/T_1$. Circles represent experimental data. The orange curve is the sum of the expected Purcell rate (light blue line) and an empirical phase-independent rate (180 kHz). Vertical dotted lines indicate degeneracy points $f_A = f_R$. Error bars on circles denote uncertainties of the fits.

Figure 4.30 shows the measured relaxation rate $\Gamma_1 = 1/T_1$ as a function of the phase δ. The Purcell relaxation rate calculated from the expected dissipative impedance seen by the atomic contact (dashed blue line) matches the experimental results only close to the degeneracy points where $f_A = f_R$ (vertical dotted lines) but is about five times smaller at $\delta = \pi$, as already observed for the contacts survey. Empirically, we fit the data in Fig. 4.30 using an additional phase-independent relaxation mechanism, which remains to be identified.

4.5.2 Linewidth of the spectroscopy line

Because the Andreev qubit is very sensitive to flux noise when the phase is different from π, the dephasing times T_2^* becomes rapidly too short to be measured using a Ramsey sequence. Therefore it is deduced from the linewidth of the spectroscopy line measured at a power so low that the Rabi frequency is much smaller than the decoherence rate. In this regime, the driving tone does not affect the width of the spectral line [105]. In order to make sure that the driving power is small enough[8], the spectroscopy is done for decreasing driving power until the linewidth saturates to its minimal value.

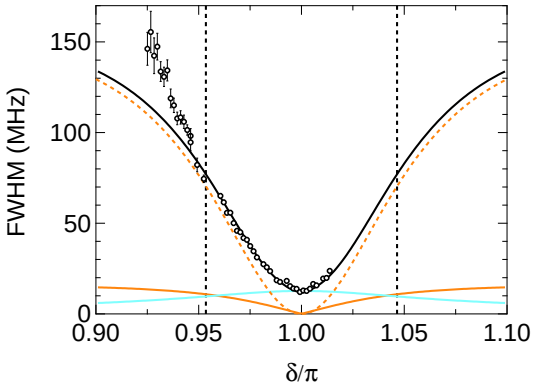

Figure 4.31: Phase dependence of the linewidth (FWHM) of the spectral line. Symbols correspond to the result of a Lorentzian fit of the experimental resonances. The brown curve is the best fit to the data, including the contributions of $1/f$ transmission noise (light blue line) and both $1/f$ (orange line) and white flux noise (orange dashed line).Vertical dotted lines indicate degeneracy points $f_A = f_R$.

Flux noise in our experiment can arise from two sources: $1/f$-noise known to have a weak dependence[9] on the size of SQUID loops [113], and

[8]The microwave power that reaches the Andreev dot varies with its frequency due to the resonator that acts as a band-pass filter.

[9]This point was clarified recently by identifying magnetic adsorbates as the primary

white noise due to leaky magnetic shielding which leads to a flux noise proportional to the SQUID loop area. Since our SQUID loop is large (1000 μm^2), white noise is expected to dominate rapidly outside the optimal point. The experimental data were thus fitted with Lorentzian functions appropriate for white noise. The FWHM obtained from this fit is shown with symbols in Fig. 4.31. In order to compare with theory three noise sources are combined to obtain the best fit:

- $1/f$ transmission noise, which is supposed to dominate close to the sweet-spot $\delta = \pi$.
- $1/f$ flux noise.
- White flux noise.

The combination of these three contributions leads to a lineshape that is a convolution of a Lorentzian and a Gaussian function. However, in order to compare with experiment, we proceeded as for the experimental data and extracted a linewidth from a fit of the calculated resonance with a Lorentzian function on a 300 MHz interval.

The amplitude of the $1/f$ transmission noise, 2.5×10^{-6} $Hz^{-1/2}$ at 1 Hz, was adjusted to fit the measurement at $\delta = \pi$. The amplitudes of the white and $1/f$ flux noise were then obtained from a best fit of the phase dependence of the linewidth. The $1/f$ noise amplitude extracted from the fit (5 $\mu\phi_0.Hz^{-1/2}$ at 1 Hz) is a typical value for superconducting devices and has a negligible effect to second order [114]. The source of the apparent white flux noise (48n$\phi_0.Hz^{-1/2}$ at 1 Hz) has not been identified.

4.6 Low frequency measurements of transmission fluctuations

In order to access the low frequency noise and confirm the presence of $1/f$ transmission noise, the low frequency variations of the Andreev energy was monitored with two different protocols that are discussed in the following paragraphs.

source of this flux noise [112].

4.6.1 Spectroscopic measurements

Method: A two-tone spectroscopy is performed at constant pump frequency as a function of the flux applied on the loop (green line in Fig. 4.32). The two spectroscopy lines are then fitted with Lorentzians in order to extract the position of their minima. As shown in Fig. 4.32, if the transmission changes, the distance in flux between the two minima changes. If the flux changes, the distance between the minima remains the same but the average position of the two lines changes. This procedure is then repeated to obtain the value of the transmission and the shift in flux as a function of time. Since the acquisition of the two spectral lines takes ≈ 80 s, this procedure only gives access to very low frequency noise.

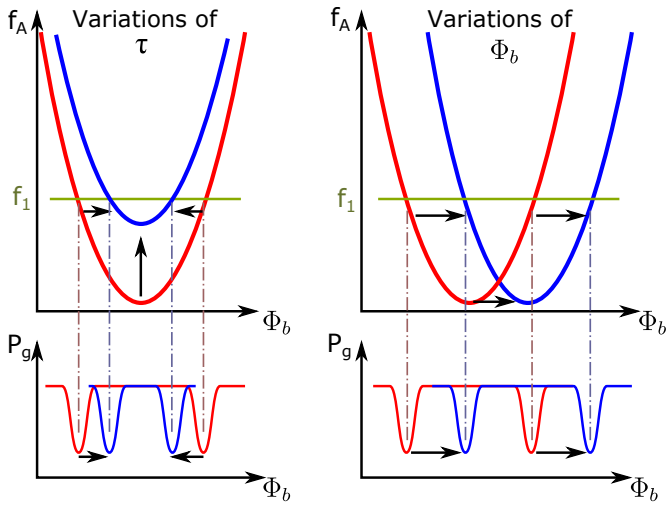

Figure 4.32: Effect of a transmission variation (left) and of a flux variation (right) on a 2-tone spectroscopy measured at constant pump frequency f_1. When τ is reduced the Andreev transition frequency increases at all phases, which pull closer in phase the two resonances measured at constant frequency. On the other hand a variation in flux translates the whole spectrum in flux. The flux variation is described here as a constant bias flux Φ_b and a parasitic flux Φ_p.

Result and discussion: The transmission and flux noise of a contact with a transmission $\tau \approx 0.9979$ ($f_A \approx 4.1$ GHz) has been monitored for 40 hours with a 2-tone spectroscopy at constant frequency f_1 =4.5 GHz. The result is shown in Fig. 4.33. The flux undergoes a continuous drift for 15 hours and then stops drifting. This drift could be due to mechanical relaxation of magnetic parts (in stainless steel or in brass) in the vicinity of the sample. The transmission on the other hand drifts in discrete jumps suggesting rearrangement of the contact configuration.

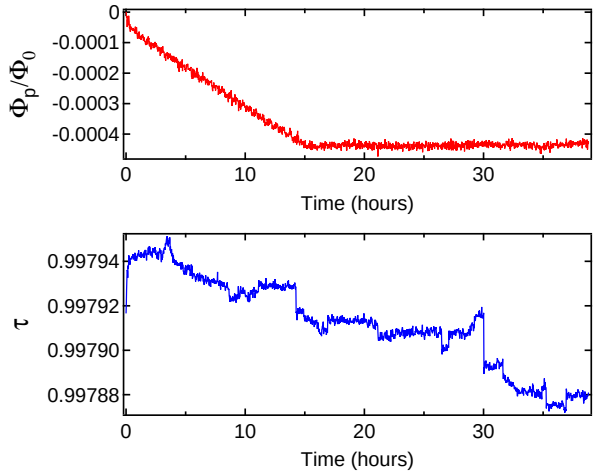

Figure 4.33: Transmission (bottom), and parasitic flux Φ_p (top) noise measured as a function of time.

The extracted transmission noise power spectrum is shown in Fig. 4.34. It is compatible with a $1/f^2$ noise with a noise power at 1 Hz $P(1\text{ Hz}) \approx 2.10^{-14}$ Hz^{-1} which is significantly smaller than the transmission noise obtained with the flux dependence of the linewidth of the Andreev transition.

4.6.2 Method using Ramsey fringes

Method: This protocol is inspired by the frequency locking used in atomic clocks [115]. In a first step, one acquires the result of Ramsey sequences with a fixed delay t_{delay} between the $\pi/2$-pulses, as a function of the frequency

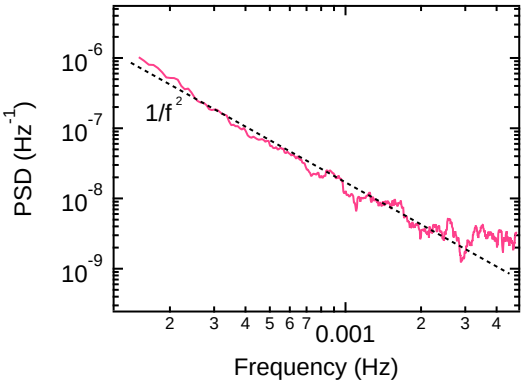

Figure 4.34: Power noise spectrum of transmission fluctuations extracted from the trace Fig. 4.33 (bottom).

detuning $f_A - f_1$. The resulting pattern is shown in Fig. 4.35 is called Ramsey fringes [115], and has a beating frequency given by $1/t_{delay}$.

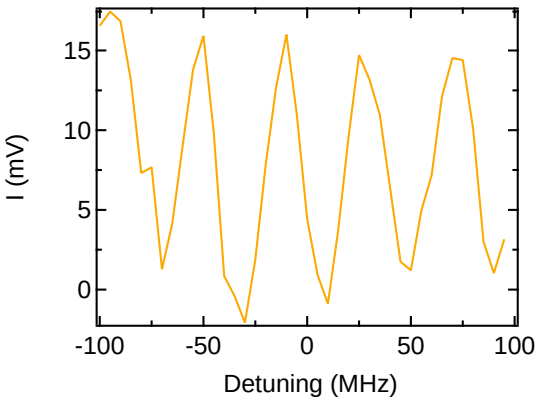

Figure 4.35: I-quadrature obtained for a Ramsey sequence with $T_{delay} = 20$ ns as a function of the detuning.

The position of the central fringe does not change with t_{delay} and corresponds to a zero detuning ($f_1 = f_A$) Ramsey sequence. Following the position in frequency of this fringe therefore gives access to the variations of f_A. In practice, the signal (I-quadrature) is measured at $f_1 = f_A + \Delta f$ and

$f_1 = f_A - \Delta f$, and a PID-controller ensures that the difference between the two measurements remains close to zero by changing the central frequency $f_A(t)$. The advantage compared to the first protocol is that it can be performed at higher repetition rate and therefore an increased bandwidth. A drawback is that it does not allow discriminating between transmission and flux noise. However, as already mentioned, the sensitivity to flux noise is quadratic at $\delta = \pi$ and is going to be neglected in the following.

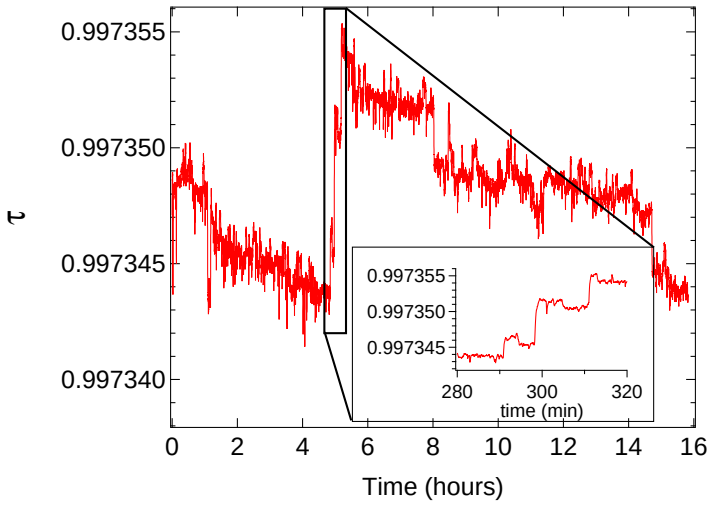

Figure 4.36: Transmission fluctuations of a single contact ($f_A \approx 4.635$ GHz) as a function of time.

Result and discussion: Figure 4.36 shows an example of the variations of the transmission over 16 hours using this method with a delay of 50 ns. The bandwidth is here 0.5 Hz but can be different from contact to contact depending on its coherence time and how the measurement setup has been optimised. Noise on the transition frequency is observed with discrete jumps. A big jump observed after 4.5 hours is actually made of several discrete jumps, as shown in the inset. Note that the frequency excursion spans over ≈10 MHz, which is smaller than the period of the Ramsey fringes and therefore rules out jumps of the PID-controller by one fringe.

The noise in transmission is obtained using $\tau = 1 - (E_A/\Delta_{sc})^2$ and

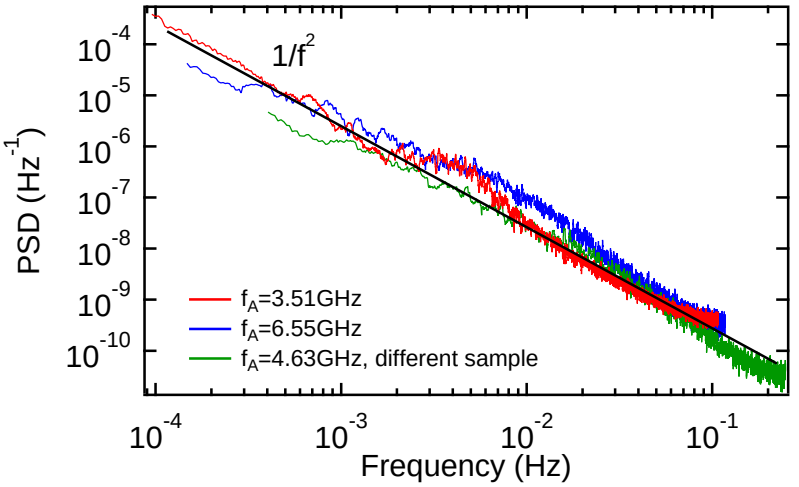

Figure 4.37: Transmission noise power spectrum obtained for three different contacts obtained on two different samples. A 20-point box average has been applied to smooth the data. A $1/f^2$ dependence is shown in black, with a power spectral density at 1 Hz of $2.10^{-12}\mathrm{Hz}^{-1}$.

taking the square of the Fourier transform to access the power spectrum. Figure 4.37 shows the power spectrum obtained for three different contacts obtained with two different samples made on different substrate (Kapton and Vespel[10]). The different datasets were obtained with different settings for the bandwidth and the duration of the Ramsey sequences, which explains the different spans. A 20-points box average was applied to the spectrum to reduce the noise. No strong differences between the spectra are observed although the characteristics of the contacts were different, as shown in Table 4.1. The slope of the spectra corresponds to a $1/f^2$ of the noise.

f_A	substrate	T_1	T_2^*	Remarks
3.51 GHz	kapton	11 µs	30 ns	Same contact that was used for CPMG study, characteristic times measured before the stability measurements
6.55 GHz	kapton	8 µs	50 ns	Characteristic times measured after the stability measurements
4.63 GHz	vespel	9 µs	80 ns	T_1 measured after the stability measurements, T_2^*measured before and after with the same result

Table 4.1: Characteristics of the contacts used to measure the data in Fig. 4.37.

4.6.3 Summing up on the transmission noise

We have presented different methods to measure the transmission noise over low and high frequency domains (see Fig. 4.38). The CPMG sequences that provide information on the high frequency noise (0.1 MHz to 100 MHz) seem compatible with white, $1/f$, and $1/f^2$ noise. On the other hand, the low frequency noise probed by following the Andreev transition frequency at $\delta = \pi$ shows a clear dependence in $1/f^2$ of the transmission fluctuations PSD[11], with a noise power of 2.10^{-12} Hz^{-1} at 1 Hz. The flux scanning method provides also information at low frequencies.

Although the results of this method do confirm a $1/f^2$ decay of the transmission noise, the noise level measured is two orders of magnitude smaller. The origin of this difference is unclear. It must however be noted

[10]Trade name of non-laminated polyimide

[11]In Ref. [40] the authors monitored the low frequency fluctuation of the transition energy of a transmon qubit and found a $1/f^2$ dependence of these fluctuations. These fluctuations were attributed to "single atomic rearrangements in the tunnel junction barrier". Single atomic rearrangements could also be the source of the transmission fluctuations in an atomic contact.

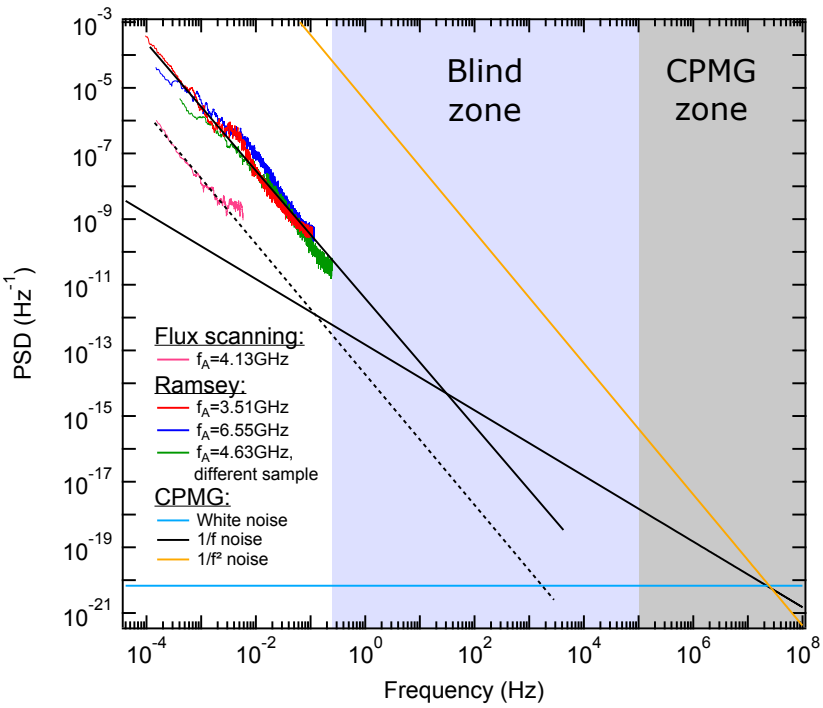

Figure 4.38: Transmission noise spectra obtained with different techniques, contacts and samples. The CPMG sequence is sensitive to noise in the 0.1 MHz to 100 MHz range, the method using Ramsey fringes in the 0.1 mHz to 0.2 Hz range, the flux scanning in the 0.15 mHz to 6 mHz range. Note that the transmission fluctuations of the same contact with $f_A(\pi)$ =6.55 GHz were captured both with Ramsey (red line) and CPMG.

that the flux scanning data and the first Ramsey data were never taken on the same contact.

These measurements being extremely time consuming (at least a full day), only few measurements of that type could be performed during this thesis. This low statistics prevents to test the correlation between the PSD measured and the Ramsey decay times.

By comparing the low and high frequency measurements see Fig. 4.38, it appears that the low and high frequency measurements reveals two different sources of noise. If the low frequency noise is clearly identified as

$1/f^2$ noise, the frequency dependence of the high frequency noise is less clear. If one assume $1/f^2$ at high frequency, the PSD at 1 Hz is 6 orders of magnitude higher than the one measured with the low frequency measurements. Therefore this hypothesis is highly improbable. White noise and $1/f$ noise seem equally plausible because, with the PSD found, both would have minor influence at low frequency where they are not observed.

The insight provided by the absence of correlation between the echo decay times and the Ramsey decay times during the systematic survey seems to be confirmed here: two different sources of noise are present, one dominant at low frequency decaying as $1/f^2$, the other dominant at high frequency with a lower noise power at 1 Hz.

In order to be conclusive on the high frequency noise, one would have to observe the intermediate frequency regime. For that, new techniques have to be developed to measure the noise spectrum in the 1 Hz to 100 kHz range, which has remained inaccessible so far.

Chapter 5

Measuring the number of photons in the resonator

5.1 Introduction

In this chapter we describe experiments that give access to the number of photons in the resonator and to the cavity pull[1] χ . They rely on the fact that, in the dispersive regime, the resonator frequency depends on the qubit state and the transition frequency of the qubit depends on the number of photons in the resonator. The resonator frequency is $f_{r,g} = f_r - \chi$ when the qubit is in $|g\rangle$, and $f_{r,e} = f_r + \chi$ when the qubit is in $|e\rangle$. The transition frequency from $|g, n\rangle$ to $|e, n\rangle$ is $f_{A,n} = f_A + 2n\chi$. The experiments consist in the spectroscopy of the Andreev transition at a given phase difference δ in presence of a tone at a frequency close to the resonator frequency. Three tones are therefore involved (see Fig. 5.1). Two are applied simultaneously: the "qubit drive" at a frequency f_1 near the Andreev frequency f_A, and the "cavity drive" at a frequency f_2 near the resonator frequency f_r. The third tone is applied immediately after and is the measurement tone. It has a frequency $f_0 \approx f_r$. The cavity drive at f_2 populates the resonator with a

[1]The cavity pull could already be determined using high measurement power, high bandwidth single-tone spectroscopy as presented in chapter 4. However the measurement power needed to perform these measurements is likely to perturb the system and provide a biased determination of χ.

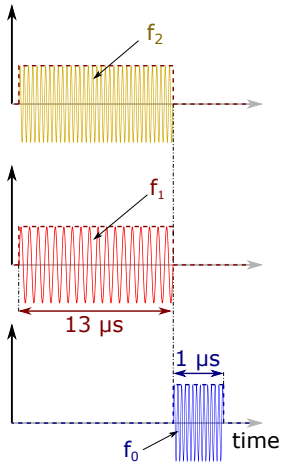

Figure 5.1: Pulse sequence used for the 3-tone spectroscopy experiments.

number of photons that depends on its frequency, its amplitude and on the qubit state. The qubit drive at f_1 drives the transition between states $|g,n\rangle$ and $|e,n\rangle$ if $f_1 = f_{A,n}$, if either of these states is populated. The length of the two pulses is long enough to reach a steady state. The tone at f_0 then probes the occupation of $|g\rangle$ and $|e\rangle$.

The quantitative description of the steady state requires a simulation of the evolution of the quantum system. A qualitative understanding can nevertheless be reached with a semi-classical description that only considers the effects of the driving pulses and relaxation in the photon number, and assumes that it is possible to populate the cavity with a perfect selectivity on the state of the qubit ($|f_{r,g} - f_{r,e}| \gg \kappa$).

We first recall the case of an isolated cavity driven by a microwave field with a power leading, in average, to an average of $\overline{n_d}$ photons in the cavity. The state of this cavity is a coherent state [116] with a probability of detecting n photons in the cavity given by $P(n) = e^{-\overline{n_d}} \frac{\overline{n_d}^n}{n!}$. For photon numbers much larger than 1, this probability is well approximated by a Gaussian function as shown in Fig. 5.2.

We now discuss the cavity with the qubit, in a situation when the cavity drive is resonant with $f_{r,g}$. It drives transitions in the resonator towards a coherent state with $\overline{n}$ photons on average, only if the qubit is in state $|g\rangle$.

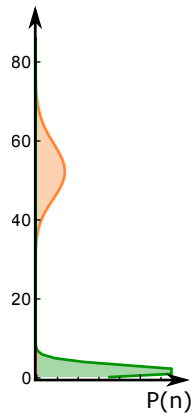

Figure 5.2: Photon number probability in a driven cavity (without qubit) for two different driving powers. Orange: the average photon number in the cavity is $\overline{n_d} = 55$. Green: the average photon number in the cavity is $\overline{n_d} = 2$.

The effect of the qubit drive depends on its frequency as follows:

- When the qubit drive is at $f_1 = f_{A,0}$, (see right hand side of Fig. 5.3), it drives Rabi oscillations between $|g,0\rangle$ and $|e,0\rangle$, which, after a time long compared to the coherence time, tends to equilibrate the populations of the two states. Combined with the effect of the cavity drive that depopulates $|g,0\rangle$, the net effect is to transfer population from $|e,0\rangle$ to $|g,n\rangle$ with $n \approx \overline{n}$. In a steady state, the population of $|e\rangle$ is reduced: the qubit is cooled down. This protocol was investigated in details in Ref. [117], where it was named DDROP for "double drive reset of population".

- When the qubit drive is at $f_1 = f_{A,\overline{n}}$, (see left-hand side of Fig. 5.3) it drives Rabi oscillations between $|g,n\rangle$ and $|e,n\rangle$, which, after a time long compared to the coherence time, tend to equilibrate the populations in the two states. Combined with the effect of the cavity relaxation that relaxes the population from $|e,\overline{n}\rangle$ towards $|e,0\rangle$, the net effect is to transfer population from $|g,\overline{n}\rangle$ to $|e,0\rangle$. In a steady

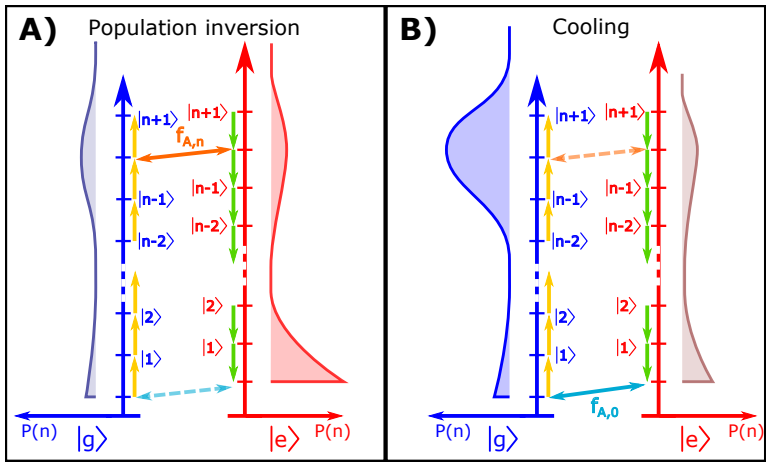

Figure 5.3: Steady state dressed cavity in presence of a cavity drive at $f_{r,g}$. The probability of a given photon number in the resonator is plotted for the qubit in $|g\rangle$ (blue line) and for the qubit in $|e\rangle$ (red line). A) the qubit drive is at $f_{A,\overline{n}}$, the qubit transition frequency for $\overline{n}$ photons in the resonator. B) the qubit driving tone is applied at its bare transition frequency $f_{A,0}$. The green arrows represent cavity relaxation. The yellow arrows represent the drive of the cavity (the relaxation of the cavity is not represented in this case for clarity). The full line transverse arrows represent the drive at $f_{A,\overline{n}}$ (orange) or $f_{A,0}$ (blue). The dashed arrows represent relaxation or thermal excitation of the qubit.

state, the population is transfered from $|g\rangle$ to $|e\rangle$, resulting in population inversion.

The values of the qubit drive f_1 at which the two opposite effects occur differ by $2\overline{n}\chi$. Reverse effects are obtained when the cavity drive $f_2 = f_{r,e}$ (see Fig. 5.4): population inversion is obtained when $f_1 = f_{A,0}$, and cooling at $f_1 = f_{A,\overline{n}}$. One therefore obtains χ from half the difference in the cavity drive frequencies f_2 at which the effects are maximal.

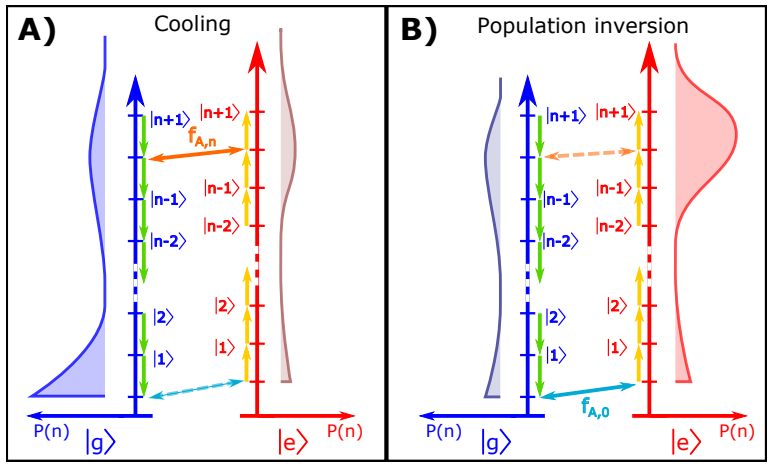

Figure 5.4: Steady-state dressed cavity in presence of a cavity drive at $f_{r,e}$. The probability of a given photon number in the resonator is plotted for the qubit in $|g\rangle$ (blue line) and for the qubit in $|e\rangle$ (red line). A) the qubit drive is at $f_{A,\overline{n}}$, the qubit transition frequency for $\overline{n}$ photons in the resonator. B) the qubit driving tone is applied at its bare transition frequency $f_{A,0}$. The green arrows represent cavity relaxation. The yellow arrows represent the drive of the cavity (the relaxation of the cavity is not represented in this case for clarity). The full line transverse arrows represent the drive at $f_{A,\overline{n}}$ (orange) or $f_{A,0}$ (blue). The dashed arrows represent relaxation or thermal excitation of the qubit.

5.2 Experimental implementation and results

5.2.1 Setup

The setup is the same as in the two-tone spectroscopy experiments except that a third microwave source has been added to drive the resonator, see Fig. 5.5. The signal from this source is combined with the pump signal at the input of the fridge lines. Since these experiments use only long pulses ($T_{pulse} \approx 13\ \mu s \gg T_1, T_2^*$), the time resolution of the pulse shape does not need to be as accurate as for coherent manipulations. Therefore, instead of using mixers, the cavity drive pulse is shaped using the gated mode of the microwave source controlled by an arbitrary function generator.

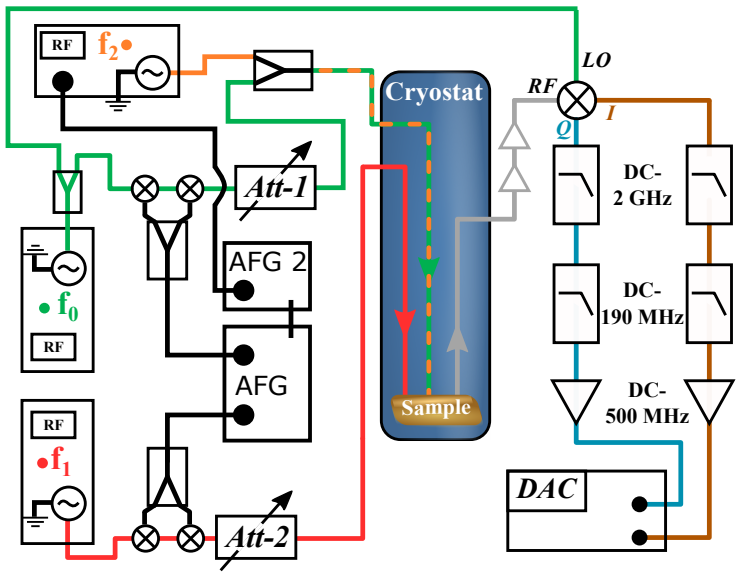

Figure 5.5: Microwave setup used for 3-tone spectroscopy experiments. The microwave tone from the source f_2 is shaped using the gated mode of the source.

We recall here the main characteristics of the resonator: the bare resonance frequency is $f_r = 10.1357$ GHz, and the total quality factor is $Q_{tot} = 2200$, corresponding to an energy relaxation rate of the cavity $\kappa = 4.7$ MHz. The characteristics of the contact that was used for these experiments are summed up in Table 5.1.

5.2.2 Experimental results and numerical simulations

3-tone spectroscopy at a fixed cavity drive frequency

Figure 5.6 compares the result of a 2-tone spectroscopy (without cavity drive) and a 3-tone spectroscopy taken at $f_2 \approx {f_{r,g}}^2.f_{r,g}$ =10.1374 GHz was

[2]In this section, odd states are disregarded, and all figures show the populations of the even states $|g\rangle$ and $|e\rangle$ only, normalized.

frequency at $\delta = \pi$	6.547 GHz
τ	0.9947
T_1	8 µs
T_2^*	72 ns
Populations at equilibrium	$P_g = 0.87$, $P_e = 0.13$

Table 5.1: Main characteristics of the contact used for the 3-tone spectroscopy experiments. The population of the ground and excited states have been re-normalized as the odd state does not interfere with the following experiments and is not accounted for in the simulations.

estimated from the high-bandwidth single-tone spectroscopy like the one presented in Fig. 4.4, which corresponds to χ =1.7 MHz.

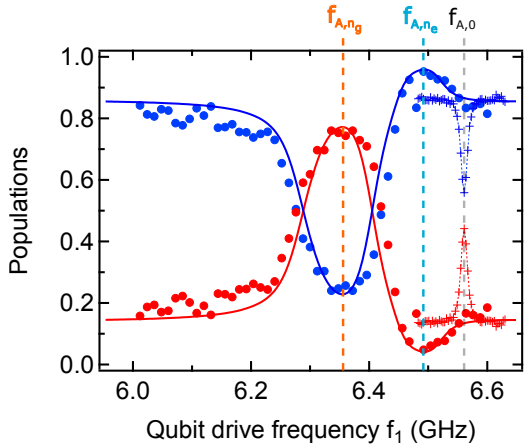

Figure 5.6: Populations of the ground (in blue) and excited states (in red) as a function of the frequency of the qubit driving tone (odd population is ignored). Markers: experimental data, with third tone at a frequency $f_2 = f_{r,g}$ (circles) and without third tone (crosses). Full lines: simulation obtained with QuTiP. The Andreev frequencies for the different photon numbers in the resonator are marked by the vertical dashed lines.

Slightly below the natural transition frequency of the qubit, at drive

frequency $f_1 \approx$ 6.49 GHz, the population of the excited state decreases. This net cooling of the qubit with respect to the equilibrium case, corresponds to the situation described on the panel B of Fig. 5.3. In Fig. 5.6, this cooling happens at f_1 smaller than $f_{A,0}$. This signals that the cavity drive also populates the resonator when the qubit is in state $|e\rangle$. This is due to the fact that the value of κ is of the same order as χ, leading to some excitation of the resonator even when the qubit is in $|e\rangle$. In the following, we note $\overline{n_g}$ and $\overline{n_e}$ the average number of photons when the qubit is in $|g\rangle$ and $|e\rangle$, respectively. Cooling occurs when $f_1 = f_{A,\overline{n_e}}$.

At $f_1 \approx$ 6.34 GHz, a population inversion is observed. This corresponds to the situation of the left-hand side of Fig. 5.3, when $f_1 = f_{A,\overline{n_g}}$.

From $f_{A,\overline{n_e}} = 6.49$ GHz and $f_{A,\overline{n_g}} = 6.35$ GHz one obtains, using $\chi = 1.7$ MHz, $\overline{n_g} = 58$ and $\overline{n_e} = 17$ at the cavity drive power used for this dataset.

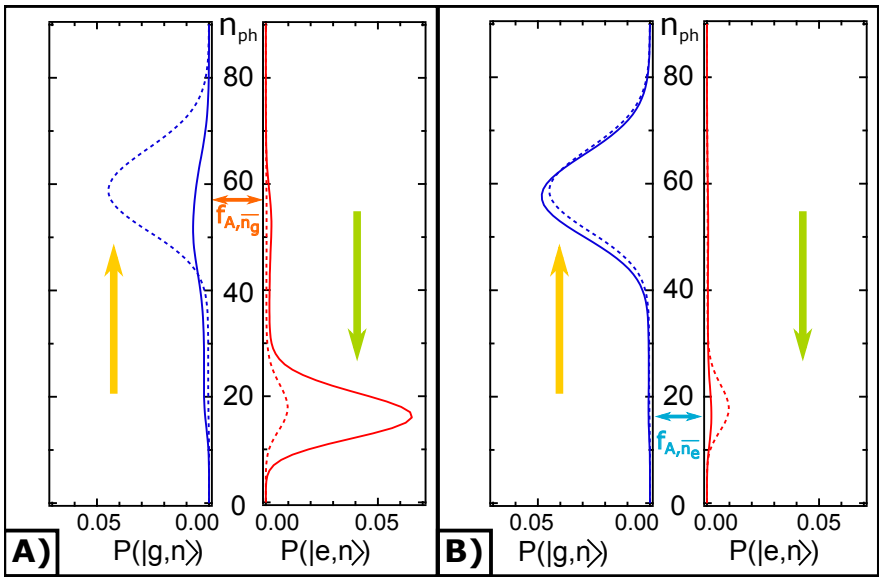

Figure 5.7: Simulated probability of the photon number in the cavity for the qubit being in $|g\rangle$ (in blue) or $|e\rangle$ (in red). Dashed lines represent the data when no qubit tone is applied (Gaussian fits yield $\overline{n_g} = 57.8$ and $\overline{n_e} = 16.7$). A) thick line: qubit drive at $f_1 = f_{A,\overline{n_g}} = 6.36$ GHz, population is inverted. B) thick line: qubit drive applied at $f_1 = f_{A,\overline{n_e}} = 6.49$ GHz, cooling occurs.

In order to quantitatively account for the data, we simulated the quantum dynamics of the system with the Python toolbox QuTip [118, 119], the Andreev dot being described with the dispersive Jaynes-Cummings Hamiltonian (see chapter 3, section 3.1.3). The code used for the simulation is presented in Appendix E. Simulation parameters are the dispersive shift χ, the amplitudes of the cavity and qubit drives, the relaxation times of the qubit and the cavity and the dephasing time of the qubit.

The result of a simulation performed with QuTiP, is also plotted on Fig. 5.6. The parameters for this simulation are presented in Table. 5.2. The agreement between simulation and data is satisfactory, although the qubit driving power is slightly larger than expected from a comparison with the Rabi oscillations period. The corresponding distributions of the photon number in the resonator when the qubit is in $|g\rangle$ or $|e\rangle$ are shown in Fig. 5.7 as full lines. The dotted lines are the photon number distributions in the absence of qubit drive, and correspond to $\overline{n_e} = 16.7$ and $\overline{n_g} = 57.8$. These values are in good agreement with those deduced from the mere position in f_1 of the maximum population inversion and maximum cooling described previously.

	Measured	Simulation
frequency at π	6.547 GHz	6.547 GHz
T_1	8 µs	8 µs
T_2^*	72 ns	72 ns
Resonator frequencies	$f_{r,o} = 10.1357$ GHz $f_{r,g} = 10.1374$ GHz $f_{r,e} = 10.1338$ GHz	$f_r = 10.1357$ GHz $f_{r,g} = 10.1374$ GHz
κ	$f_r/Q = 4.6$ MHz	idem
Qubit drive power expressed as Rabi frequency	7.3 MHz	8.3 MHz
Populations at equilibrium	$P_g = 0.87$ $P_e = 0.13$	$P_g = 0.88$ $P_e = 0.12$

Table 5.2: Parameters of the experimental system and the ones used for the simulations.

When fitting the data at a single value of the cavity drive frequency,

the numbers of photons that are obtained depend on the value of χ that had to be deduced from an independent measurement. We now show that a determination of χ is obtained when similar data are taken as a function of f_2.

Three-tone spectroscopy as a function of the cavity drive frequency

Measurements of the populations of state $|e\rangle$ as a function of both drive frequencies f_1 and f_2, for the same cavity drive power as in Fig. 5.6, are shown in the left pannel of Fig. 5.8. The right panel shows the result of the QuTip simulations using the same parameters as for the curve shown in Fig. 5.6. Agreement between theory and experiment is quantitative. Population inversion appears in red ($P_e \approx 0.8$), cooling in dark blue ($P_e \approx 0$). The qubit drive frequency f_1 at which population inversion takes place is $f_1 = f_{A,\overline{n_g}}$, whereas cooling means $f_1 = f_{A,\overline{n_e}}$. The average number of photons $\overline{n_g}$ and $\overline{n_e}$ vary with the detuning between the cavity drive f_2 and the resonator frequencies $f_{r,g}$ and $f_{r,e}$, with a maximum at zero detuning. This is seen in the data as a minimum in the frequency f_1 for cooling when $f_2 = f_{r,e}$, and a minimum in the frequency f_1 for population inversion when $f_2 = f_{r,g}$.

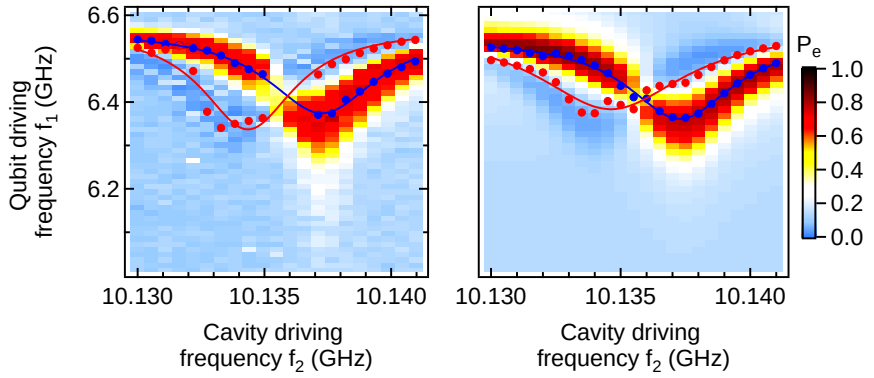

Figure 5.8: Populations of the excited state as a function of the cavity drive frequency f_2 and the qubit drive frequency f_1. Left: experimental data. Right: Simulated data.

In an attempt to read out directly from the data the value of χ, proceed as follows: For each cavity drive frequency f_2, the position of the two resonances expected at $f_1 = f_{A,\overline{n_g}}$ and $f_1 = f_{A,\overline{n_e}}$ are extracted from a fit of the data with a sum of two Gaussian functions with positive (population inversion) and negative (cooling) amplitudes. To validate the procedure, this analysis was carried out both for the experimental data and the results of QuTip, resulting in the red and blue dots in Fig. 5.8. The f_2-dependence of the f_1-position of the extracted frequencies were then fitted with Lorentzian functions that correspond to the shape of the cavity resonance at $f_{r,g}$ (blue line) or $f_{r,e}$ (red line) . The center value of these two Lorentzians are $f_{r,g} = 10.137$ GHz and $f_{r,e} = 10.134$ GHz for the experimental data and $f_{r,g} = 10.137$ GHz and $f_{r,e} = 10.135$ GHz for the simulated data. These values are to be compared with $f_{r,g} = 10.1374$ GHz and $f_{r,e} = 10.134$ GHz used to produce the simulated data: the agreement is reasonable but χ is systematically underestimated. This is because of the small contrast at cooling (less than 10% in population) and the small shift in frequency of the two effects. This procedure is not very robust at this number of photons, neither for the experimental data nor for the simulations results.

In order to determine $f_{r,g}$ and $f_{r,e}$ more precisely, we increased the power of cavity drive by 5 dB, which corresponds to a threefold increase of the photon number in the resonator. The result is shown in Fig. 5.9. As expected, larger shifts of the Andreev transition are observed. The width of the transitions also becomes larger when the cavity drive is resonant with $f_{r,e}$ or $f_{r,g}$. A striking feature of these data that was not observed at lower power is the global population inversion when the cavity drive is close to $f_{r,g}$ independently of the qubit drive frequency f_1. For completeness, we show the population of the odd states in Fig. 5.10. It shows a slight decrease of the population of the odd state when the qubit drive is resonant with $f_{A,\overline{n_g}}$. This decrease is not directly related to the populations of $|g\rangle$ and $|e\rangle$ since the population of the odd state is not affected by the population inversion observed when the $f_2 \approx f_{r,g}$. It is more likely an artifact from the determination of the populations.

The result of QuTiP simulations is shown in the right panel of Fig. 5.9. All parameters but the cavity drive power are the same as before and already presented in Table.5.2. The positions of the cooling and population inversion peaks are well reproduced by the simulation. We used the same fitting procedure as for the low power measurements. As anticipated, the

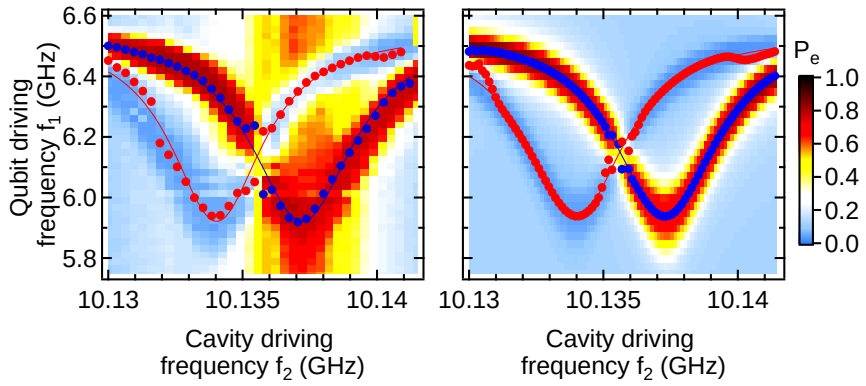

Figure 5.9: Renormalized populations of the excited state as a function of the cavity driving frequency and the qubit driving frequency for a cavity drive power three times larger as in Fig. 5.8. Left: experimental data. Right: Simulated data. The red zones of the figure correspond to population inversion and follows the photon number in $f_{r,g}$. The darker blue region corresponds to cooling of the qubit and follows the photon number in $f_{r,e}$.

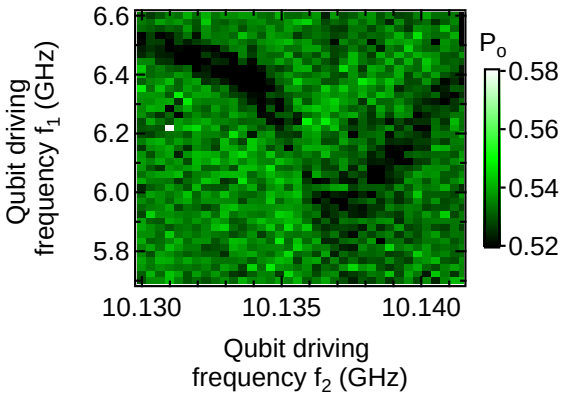

Figure 5.10: Population of the odd states in the same experiment as in Fig. 5.9. The population variations are smaller than 3% but visible.

fit is more reliable than for low power measurements, at least when the

frequencies where cooling and inversion occur are far apart (edges and center of the figure are more problematic). The frequencies $f_{r,e}$ and $f_{r,g}$ are obtained by fitting the position of the cooling peak and the population inversion peak with a Lorentzian as shown in Fig. 5.9. The results are shown in Table 5.3, and compared with the parameters of the simulation:

	Fit from experiment	Fit from simulation	Simulation parameters
$f_{r,e}$ (GHz)	$10.13403 \pm 4 \times 10^{-5}$	$10.13397 \pm 2 \times 10^{-5}$	10.1340
$f_{r,g}$ (GHz)	$10.13721 \pm 4 \times 10^{-5}$	$10.13729 \pm 6 \times 10^{-6}$	10.1374
χ (MHz)	$1.6 \pm 8 \times 10^{-2}$	1.65 ± 0.03	1.7

Table 5.3: Comparison between the actual parameters used in the simulation and the resonator frequencies obtained by fitting with experimental and simulated data (see text) .

The positions of the peaks are determined with good accuracy[3], and lead to a determination of the cavity pull χ within better than 10%.

However, there are also disagreements between experiment and simulation. The linewidth of the cooling and population inversion peaks is only well accounted for by the simulation when the cavity drive is far from $f_{r,e}$ and $f_{r,g}$, as shown in Fig. 5.11. In addition, the global population inversion observed for all values of the qubit drive f_1 at $f_2 \approx f_{r,g}$ is not reproduced by the simulations. This might be related to the breakdown of either the dispersive approximation or of the rotating wave approximation, which are both used in the simulation. Further work would be necessary to conclude on this issue.

We now focus on the photon population in the resonator for $f_2 = f_{r,e}$ (red data in Fig. 5.11). The photon population when the qubit is in $|g\rangle$ and $|e\rangle$ are shown in Fig. 5.12 for three qubit driving frequencies: $f_{A,\overline{n_e}}$ ($f_1 = 5.95$ GHz), $f_{A,\overline{n_g}}$ ($f_1 = 6.36$ GHz), and without qubit drive. The population of the resonator when the qubit is not driven are $\overline{n_g} = 55$ when the qubit is in $|g\rangle$ and $\overline{n_e} = 180$ when the qubit is in $|e\rangle$. When the qubit drive is applied at $f_{A,\overline{n_e}}$, the qubit is cooled down and the probability for the

[3]The uncertainties are the ones of the Lorentzian fit.

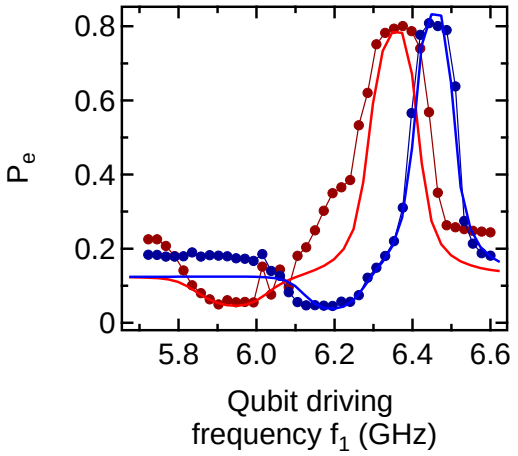

Figure 5.11: Populations of the excited state as a function of the frequency of the qubit drive for $f_2 = f_{r,e} = 10.134$ GHz (red) and $f_2 = 10.132$ GHz (blue). Markers: experimental data. Lines: QuTiP simulations. The linewidth of the cooling and population inversion peaks is well reproduced for the blue curve when $f_2 \neq f_{r,g}, f_{r,e}$. It is not the case for $f_2 = f_{r,e}$. Moreover one can observe on the baseline of both curves precursors of the global population inversion occurring at $f_2 = f_{r,g}$

resonator frequency to be $f_{r,e}$ is strongly reduced. The probability of a given photon number $P(n)$ is also broader. On the other hand, the probability for the resonator frequency to be $f_{r,g}$ increases and $P(n)$ becomes sharper around $\overline{n_g}$. A reversed behavior is observed when the qubit drive is applied at $f_{A,\overline{n_g}}$.

We now evaluate the number of photons in the resonator from the fits shown in Fig. 5.9. From these fits, we obtain χ (see Table 5.3) and determine $f_{A,\overline{n_e}}$ and $f_{A,\overline{n_g}}$ for $f_2 = f_{r,e}$. We therefore have the number of photons in the resonator when the qubit is in $|g\rangle$: $\overline{n_g} = (f_{A,0} - f_{A,\overline{n_g}})/(2\chi)$, and when the qubit is in $|e\rangle$: $\overline{n_e} = (f_{A,0} - f_{A,\overline{n_e}})/(2\chi)$. In order to estimate the accuracy of this method we compare the results obtained with this method on the simulated data to the true photon numbers that are extracted from Fig. 5.12.

The combined uncertainties on χ and $f_{A,n}$ lead to a final uncertainty

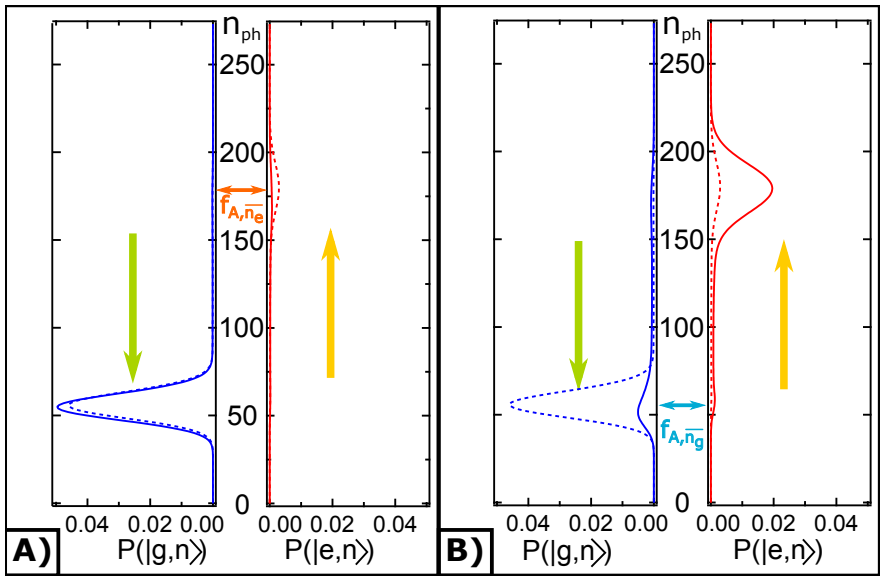

Figure 5.12: Simulated probability of the photon number in the cavity for the qubit being in $|g\rangle$ (in blue) or $|e\rangle$ (in red) for a cavity drive applied at $f_2 = f_{r,e}$. Dashed lines represent the data when no qubit tone is applied (Gaussian fits yield $\overline{n_g} = 55.3$ and $\overline{n_e} = 179.7$). A) thick line: qubit drive at $f_1 = f_{A,\overline{n_e}} = 5.95$ GHz, cooling occurs. B) thick line: qubit drive applied at $f_1 = f_{A,\overline{n_g}} = 6.36$ GHz, population is inverted. The yellow arrows signal on which state the cavity drive is applied. The green arrows signal on which state the cavity relaxation is used.

on the photon number at this cavity drive frequency of about 10% for $\overline{n_e}$ and 20% for $\overline{n_g}$. The uncertainty for $\overline{n_g}$ can be reduced by using the same procedure for $f_2 = f_{r,g}$. We note that the 5 dB increase of the cavity drive power compared to Fig. 5.8 has indeed lead to a threefold increase of the photon number in the resonator.

	Fit from experiment (Fig. 5.9)	Fit from simulation (Fig. 5.9)	From simulated P(n) (Fig. 5.12)
$f_{A,\overline{n_e}}$	5.922 GHz	5.933 GHz	5.935 GHz
$\overline{n_e}$	195	186	180
$f_{A,\overline{n_e}}$	6.337 GHz	6.349 GHz	6.36 GHz
$\overline{n_g}$	65	60	55

Table 5.4: Comparison of the photon number obtained from the fit of the experimental and simulated data to the one directly extracted from the simulations. We observe a good agreement with an error below 10%.

5.3 Conclusion on 3-tone spectroscopy

Using experimental data and numerical simulations, we have shown that 3-tone spectroscopy can be used to obtain a full calibration of the photon number in the resonator as a function of the cavity driving power. A precision of about 10% on the photon number could be achieved.

The comparison with simulations also demonstrates how far the Andreev qubit could be described with the dispersive Hamiltonian, even when the cavity drive was strong. A global population inversion between $|g\rangle$ and $|e\rangle$ when the cavity was driven strongly at $f_{r,g}$ was observed in the experiments, an unexpected effect that is not found in the simulations, which could be explained by the breakdown of the dispersive limit [120] even though the photon number is still lower than the critical number $n_{crit} \approx 500$.

Chapter 6

Quantum and parity jumps

6.1 Introduction

In this chapter we present continuous measurements of the state of the Andreev dot. Jumps between the states of the Andreev dot are observed, which can be classified in two categories: quantum and parity jumps. Quantum jumps are random jumps between the states of a quantum system. They have been observed in a few different systems [121, 122], including superconducting qubits [123]. Parity jumps are jumps in electronic parity due to the addition or the removal of a single quasiparticle to or from the system. Parity jumps between the even and odd states of an Andreev dots [44] have been already observed using switching current measurements. The rates at which these parity jumps occur are directly linked to the density of unpaired quasiparticles in the superconductor [72] which is known to be anomalously high in most superconducting devices below 100 mK [50, 51, 52, 49]. Recently Vool *et al.* have reported bursts in the quasiparticle density of a fluxonium superconducting qubit with non-Poissonian statistics [47] .

Here, we present measurements in which we continuously tracked these jumps to access the dynamics of the population of the Andreev dot. The motivation is threefold: to quantify the influence of the measurement pulses power on the dynamics of the occupation of the dot; to reach a better understanding of the lifetime of the excited state and of the influence of odd states; and to compare the (de)poisoning statistics of the Andreev dot with measurements performed by Vool *et al.* [47].

The relaxation and excitation processes of the even excited state of the Andreev dot were discussed in Chapter 4. They consist in the emission (absorption) of photons or phonons into (from) the environment. The processes leading to the trapping or un-trapping of a single quasiparticle in the Andreev dot (called "poisoning" and "unpoisoning" because in general single quasiparticles are detrimental for superconducting devices) are more complex since they require a simultaneous exchange of energy and of a quasiparticle with the environment. Figure 6.1 shows the different processes at stake. Two processes can cause the system jump from the ground state into the odd states of the Andreev dot. If a single quasiparticle is present in the continuum, it can get trapped in the dot by releasing an energy $\Delta - E_A$ to the environment (either by emitting a photon or a phonon), see Fig. 6.1A. The second process consists in breaking a Cooper pair in the ground state and adding one of the quasiparticles to the Andreev dot and the other one to the continuum. An energy $\Delta + E_A$ needs to be provided by the environment in this process, see Fig. 6.1B. Starting from the excited Andreev state, the odd state is reached either by recombining one quasiparticle in the Andreev level with one quasiparticle from the continuum (Fig. 6.1C) or exciting to the continuum one quasiparticle in the Andreev level (Fig. 6.1D). Reverse mechanisms lead to transitions from the odd state to the ground or excited state (Fig. 6.1 E,F,G,H).

The energy dependence of these rates was theoretically described in the presence of an electromagnetic mode in Refs. [72, 124]. However, only weak coupling between the Andreev states and the mode was treated. Moreover the electromagnetic mode was treated in a thermal state which is not the case of our microwave resonator during measurement.

6.2 Measurement setup

The setup for these experiments differs from the one used for the two-tone experiments (see chapter 4) only by the fact that the mixers in the measurement lines are DC-biased instead of being pulsed. The DC voltage corresponds to the pulse height in the two-tone experiments, so that the microwave power can be quantified using the photon number calibration described in the previous chapter. The measurement frequency f_0 is set at the frequency of the bare resonator, in order not to induce an asymetry in

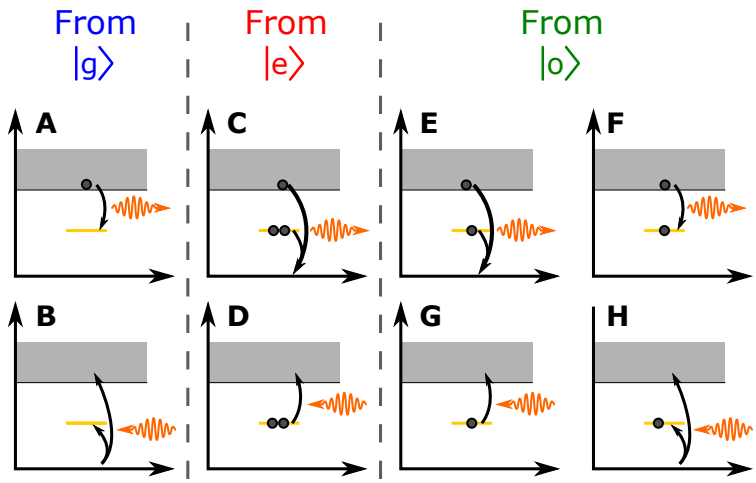

Figure 6.1: Poisoning and depoisoning processes of the Andreev dot in the excitation representation. A),B) Poisoning processes from the ground state. C),D) Poisoning processes from the even excited state. E),F),G),H) Depoisoning processes.

the average number of photons n_{ph} in the resonator when the dot is in the even states. The number of photons in the odd states is 60% larger[1].

Whereas pulsed measurements use the average value of 80 data points sampled every 10 ns, for continuous measurements segments of 1.2×10^6 data points (one every 50 ns) are recorded. The number of points is limited by the memory of the acquisition board. To further smooth the data, 5 successive points are replaced by their average all along the trace (five-points box-average). Longer traces, obtained in practice with 6 successive acquisitions, are used to achieve a better estimation of the jumping rates. A short part of a representative trace, which contains both I and Q quadratures of the reflected signal, is shown in Fig. 6.3. The data is noisy, but jumps can be distinguished. In order to extract transition rates, the full trace

[1] When the Andreev dot changes parity, the number of photons in the resonator changes at a rate of 7 MHz, which is much larger than the jumping rates. Transients can therefore be ignored.

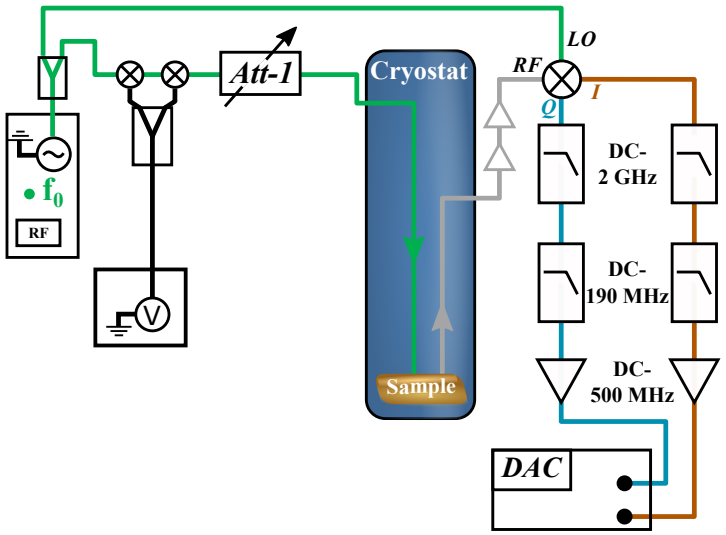

Figure 6.2: Setup used for the experiments presented in this chapter. The measurement mixers are biased at $V = 4.5$ V, which is the same voltage as at during the pulses of the AFG in the 2-tone spectroscopy. The excitation line was not used in this experiment.

is analyzed using a Hidden Markov Model (HMM) toolbox, SMART [53]. Given the number of states involved, three in our case (states $|g\rangle$, $|o\rangle$, $|e\rangle$), SMART determines the set of parameters that have the maximal likelihood to correspond to the data: values of I and Q for the three states (*i.e.:* the position of the clusters in the IQ-plane), and most importantly transition rates between all pairs of states (6 rates for 3 states), see Fig. 6.4 left. (for more details see Appendix F).

The states are identified using the following protocol. Since we are measuring at the frequency of the resonator when the dot is in the odd state, the cluster associated to $|o\rangle$ is always found as the same position. This position can be determined by pulsed measurements. On the other hand, the position of the clusters of $|g\rangle$ and $|e\rangle$ move with n_{ph} and f_A. The ground state is then identified as the one of the two remaining states having the largest population. The remaining state is the excited state. This identification is then validated by observing the position of the states given by SMART in

the IQ-plane as a function of the varying parameter (measurement power or phase) and making sure that no contradiction appears in the identification of the states.

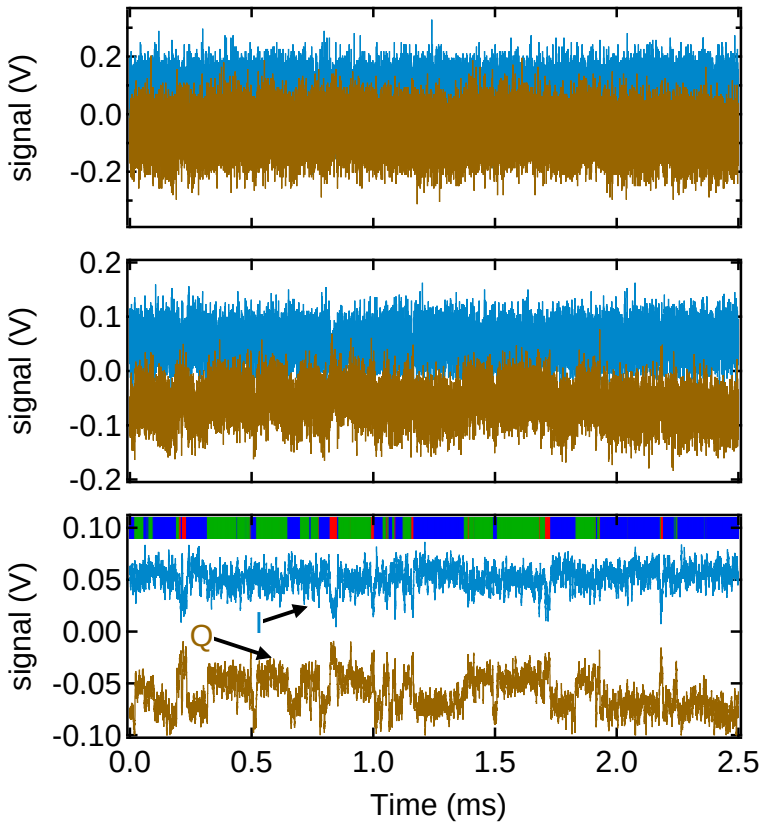

Figure 6.3: First 2.5 ms of a trace used to extract the jumping rates between the states of the Andreev dot ($\overline{n_{ph}} \approx 15$ in the even states). The data is shown for three different strength of smoothing. Top: raw data. Middle: 5-points box average. This shows the data as it is processed by SMART. Bottom: 50-points box average for readability. Both quadratures are recorded and used by the HMM algorithm, the in-phase amplitude is shown in blue and the out-of-phase quadrature in brown. The state of the Andreev dot inferred by the algorithm is shown in color-code on top of the bottom graph: blue for $|g\rangle$, green for $|o\rangle$, and red for $|e\rangle$.

Because of the spin-degeneracy, the two odd states $|o\uparrow\rangle$ and $|o\downarrow\rangle$ cannot be distinguished. In order to obtain the rates to and from each of them, one must "unfold" the diagram on the left of Fig. 6.4 with appropriate 1/2 factors (as pointed out to us by G. Catelani): the rate from $|e\rangle$ to $|o\rangle$ corresponds to the sum of the rates to $|o\downarrow\rangle$ and $|o\uparrow\rangle$, therefore $\Gamma_{e\to o\uparrow} = \Gamma_{e\to o\downarrow} = \frac{1}{2}\Gamma_{e\to o}$. In contrast, transitions from $|o\rangle$ to $|e\rangle$ correspond to transitions from either of the two states $|o\downarrow\rangle$ and $|o\uparrow\rangle$, therefore $\Gamma_{o\uparrow\to e} = \Gamma_{o\downarrow\to e} = \Gamma_{o\to e}$. Using these equations and their equivalents for transitions between $|g\rangle$ and $|o\rangle$, one obtains the diagram on the right-hand side of Fig. 6.4.

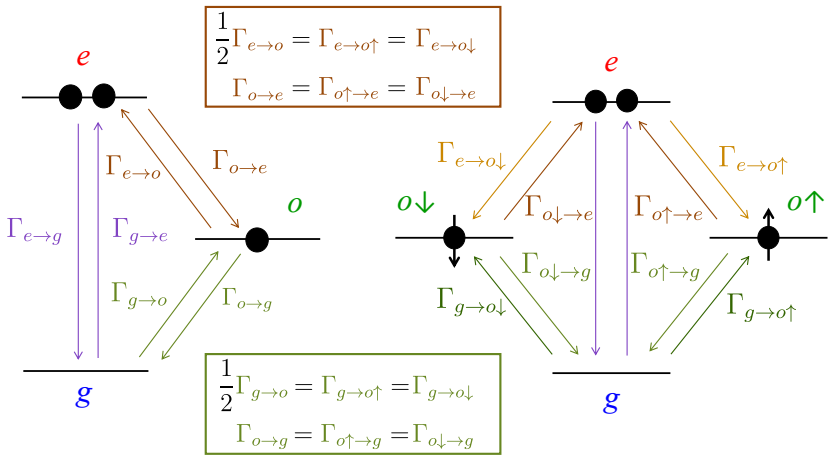

Figure 6.4: Left: States resolved by the experiment and rates obtained at the output of the HMM algorithm. Right: Rates with the lifted spin degeneracy of the odd states.

The data presented hereafter were taken on a different sample from that of chapters 4 and 5. It was fabricated on a bulk polyimide substrate (DuPont Vespel) instead of layered polyimide (DuPont Kapton). The resonator had a slightly higher resonance frequency $f_r = 10.310$ GHz, the atomic contact had an Andreev transition frequency at π of $f_A = 4.73$ GHz, and the cavity pull at $\delta = \pi$ was $\chi = 2$ MHz. The characteristics of the contact are summed up in Table 6.1.

frequency at π	4.73 GHz
τ	0.997
T_1	10 µs
T_2^*	70 ns
Populations at thermal equilibrium	$P_{\|g\rangle} = 0.5$, $P_{\|e\rangle} = 0.06$, $P_{\|o\rangle} = 0.44$

Table 6.1: Main characteristics of the contact used for the experiments presented in this chapter, obtained from pulsed experiments.

6.3 Jumping rates at $\delta = \pi$

6.3.1 Influence of the measurement power

We first present the rates obtained at $\delta = \pi$ as a function of the measurement power[2] in order to quantify the influence of the measurement tone on the rates. In chapter 5, we already showed that it influences strongly the populations of the qubit. The number of photons in the resonator n_{ph} when the dot is in an even state is estimated using the calibration described in Chapter 5.

Figure 6.5 shows the transition rates and average populations calculated by the algorithm as a function of the measurement power. Two datasets are shown, which do not exactly overlap. We explain this discrepancies by the fact that the low power dataset was taken 2 weeks after the other one. In the meantime, undocumented modifications of the microwave setup (cable modification for instance) could have lead to a slightly different calibration of the photon number. The minimal measurement power at which the signal to noise ratio is sufficient for SMART to converge corresponds to $n \approx 8$ photons.

Even at high photon numbers, all rates remain below 200 kHz, which indicates that the pulsed measurements were performed in satisfactory conditions: the duration of the measurement pulse, 1 µs, was sufficiently short for the populations not to be severly affected by the measurement.

[2]The amplitude of the measurement tone is set using a voltage-controlled attenuator, see Fig. 6.2.

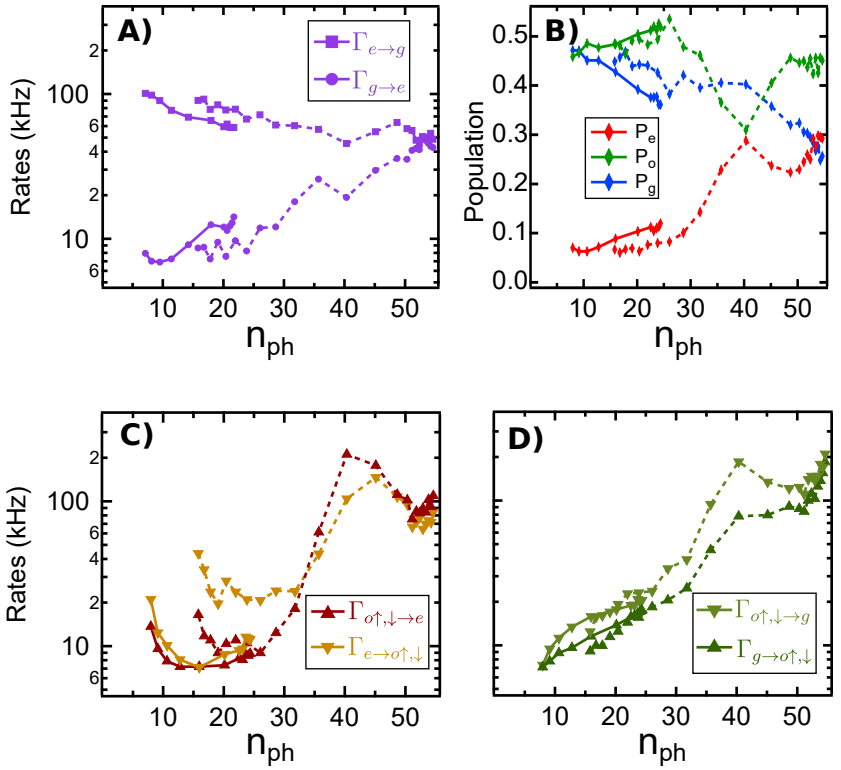

Figure 6.5: Jumping rates and populations as a function of the measurement power. Two datasets taken two weeks apart are shown. The first one explores the high-power region (dashed) the second one a low-power region (thick line). A) jumping rates between $|e\rangle$ and $|g\rangle$. B) Populations of the Andreev states. C) jumping rates between $|e\rangle$ and $|o\sigma\rangle$. D) jumping rates between $|o\sigma\rangle$ and $|g\rangle$.

The rates related to the odd states (panels C and D) are very sensitive to the measurement power. An increase by more than one order of magnitude is observed on the range explored. The $\Gamma_{o\sigma\leftrightarrow g}$ rate increase monotonously with the measurement power. On contrary, $\Gamma_{o\sigma\leftrightarrow e}$ first decreases sharply for $n_{ph} < 10$, then present a plateau between 10 and 30 photons and finaly presents a sharp increase close to 35 photons.

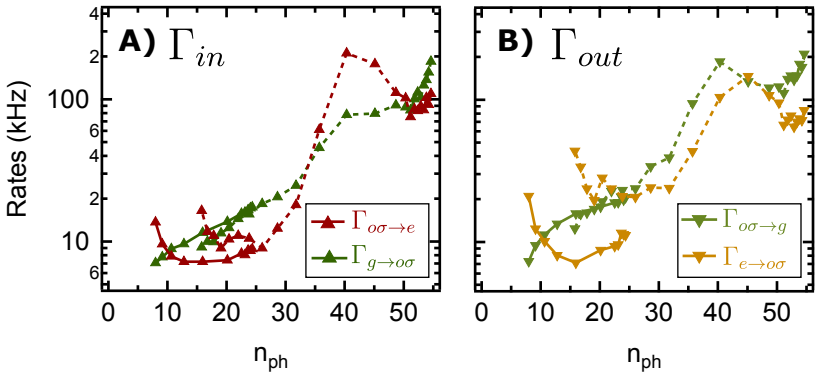

Figure 6.6: Same data as in Fig. 6.5 presented so the rates of adding (removing) Γ_{in} (Γ_{out}) a single quasiparticle to the dot can be compared more easily. A) Rates for adding a single quasiparticle to the dot from the ground state (green) and from the odd state (dark red). B) Rates for removing a single quasiparticle from the dot from the excited state (yellow) and from the odd state (green).

The steady increase of $\Gamma_{o\sigma\leftrightarrow g}$ with power could suggest that the energy injected in the system by the measurement tone produces quasiparticles in the SQUID loop. However this should also result in a steady increase of $\Gamma_{o\sigma\leftrightarrow e}$, which is not observed. Another striking feature of the data is the fact that the two rates corresponding to the trapping (respectively the untrapping) of a single quasiparticle in the Andreev dot $\Gamma_{g\to o\sigma}$ and $\Gamma_{o\sigma\to e}$ (respectively $\Gamma_{e\to o\sigma}$ and $\Gamma_{o\sigma\to g}$) are not equal as one would expect [72], see Fig. 6.6. The rates coupling the odd states to the excited state (ground state) $\Gamma_{o\sigma\leftrightarrow e}$ ($\Gamma_{o\sigma\leftrightarrow g}$) show similar variations, as seen in panel C (panel D).

The direct relaxation rate of the excited state to the ground state $\Gamma_{e\to g}$ (A) is quite stable with the photon number, while the excitation rate $\Gamma_{g\to e}$ increases, until it becomes equal to the relaxation rate for $n_{ph} \gtrsim 50$. This shows that the qubit gets heated up by the resonator.

The evolution of the populations (B) with the measurement power reflect the evolution of the rates. The population P_g of $|g\rangle$ decreases monotonously as the rate $\Gamma_{g\to e}$ increases (the qubit becomes hotter). The excited state

population P_e remains stable around 10% below $n_{ph} = 30$ as all the rates to reach this excited state remain small compared to its relaxation rate to the ground state. Above, $\Gamma_{o\sigma\to e}$ increases sharply and reaches a maximum at $n_{ph} = 40$ leading to the balance of the populations in $|o\rangle$ and $|e\rangle$. It then decreases and become close to $\Gamma_{e\to o\sigma}$ which results in an increase of the population of $|o\rangle$.

Overall, this analysis indicates that the photon population in the resonator strongly influences the transition rates between the states of the Andreev dot. Theoretical work is needed to describe these effects. In what follows, we discuss more in details the results obtained with $n_{ph} \approx 15$ (see Fig. 6.7), which is a compromise between the reliability of the data processing and the changes induced by the measurement power.

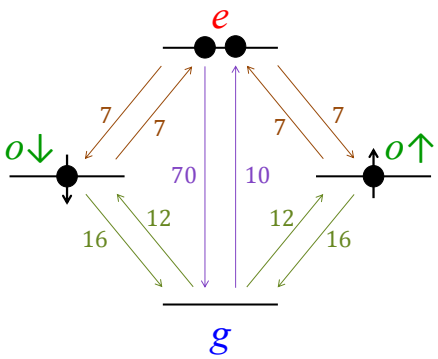

Figure 6.7: Rates measured for $n_{ph} \approx 15$ at $\delta = \pi$. The dominant rate is the direct relaxation rate of the excited state $\Gamma_{e\to g}$. The other rates are close to 10 kHz. Note that $\Gamma_{e\to o\sigma} \neq \Gamma_{o\sigma\to g}$, and $\Gamma_{g\to o\sigma} \neq \Gamma_{o\sigma\to e}$

.

6.3.2 Relation between the transition rates and T_1

The lifetime T_1 of the excited state is determined by three relaxation channels: the direct relaxation from $|e\rangle$ to $|g\rangle$, and two indirect channels through the odd states. Relaxation through the odd channels occurs at a rate $\Gamma_{1,odd}$ given by:

$$\Gamma_{1,odd} = \frac{\Gamma_{e\to o}\Gamma_{o\to g}}{\Gamma_{o\to g} + \Gamma_{e\to o}} \approx 4.9 \text{ kHz}, \tag{6.1}$$

which is much smaller than the rate of direct relaxation $\Gamma_{e\to g} = 70$ kHz. This value is itself much larger than what one estimated from Purcell relaxation (see chapter 4, section 4.4.2), calculated with the impedance of the resonator: $\Gamma_P(4.7\text{ GHz}) = 6$ Hz. The lifetime of the excited state deduced from the combination of all rates is $T_1 = 14.3$ µs, which is reasonably close to the one measured using pulsed experiments $T_1 = 10$ µs.

6.4 Energy dependence of the jumping rates

We now focus on how the jumping rates depend on the Andreev energy. The Andreev energy is tuned by controlling the phase across the contact. The energy range that was accessed in the experiments presented here is $E_A(\delta,\tau)/h$ =4.73 GHz to 11 GHz. Higher energies could not be accessed because the coupling between the Andreev dot and the resonator decreases rapidly away from $\delta = \pi$ and the SNR becomes too low to detect the jumps. The result of these measurement is shown in Fig. 6.8, along with the population of each state.

Quantum jump rates: The rates between the even states exhibit two sharp resonances at 5.5 GHz and 10 GHz. The resonance at 10 GHz corresponds to Andreev transition energies close to the resonator transition. As f_A gets close to f_R the qubit can easily absorb and emit photons (Purcell effect). The two systems are in "speaking terms". The similar resonance at 5.5 GHz is unexpected. It might be due to a parasitic resonance in the electromagnetic environment, although we could not find a reason for it.

Parity jump rates: At low energy, the parity jump rates show strong, reproducible fluctuations. They occur in the same region as the first peak in the even states rates, close to 5.5 GHz. Between 6 GHz and 8 GHz, a plateau is observed where the equality of the rates to add (remove) a single quasiparticle to the Andreev dot is essentially respected. Finally, as the Andreev transition energy gets closer to the resonator all rates increase. All these rates are well above what is predicted by theory [72]: the rates of parity jumps due to phonons are expected close to 1 kHz; the rates of parity jumps due to photons present in a single mode resonator should be negligible at energies lower than $\Delta_{sc} - hf_r$ which is here on the order of

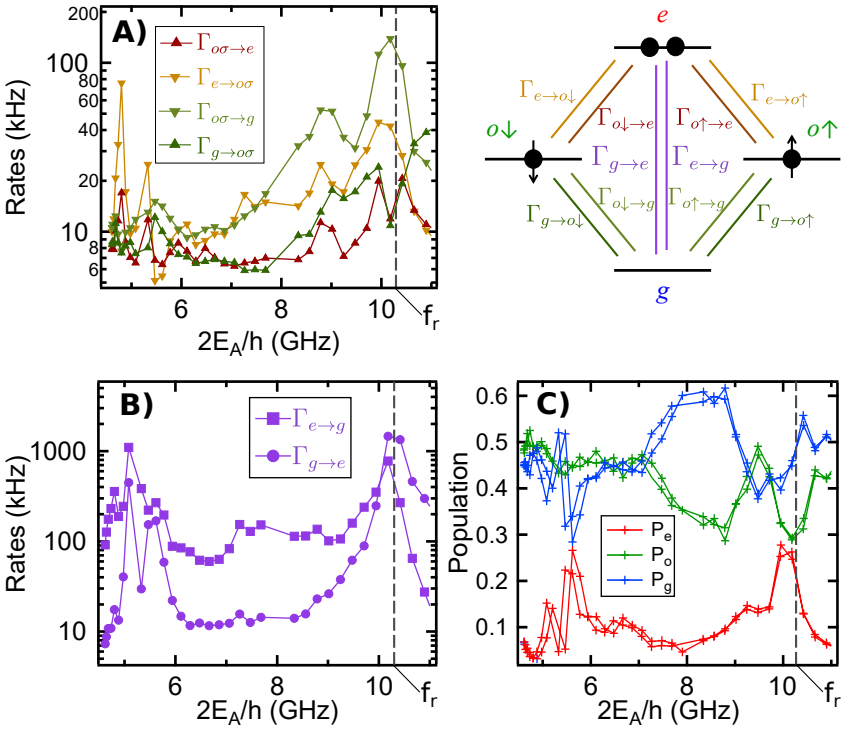

Figure 6.8: Jumping rates and populations as a function of the transition energy between the even states. A) jumping rates between the even states and the odd states. B) jumping rates between $|e\rangle$ and $|g\rangle$. C) Populations of the Andreev states.

35 GHz for the $\lambda/4$ mode of the resonator, and 15 GHz for the $3\lambda/4$ mode of the resonator.

6.5 Relaxation rate of the excited state

We now compare the relaxation rates of the even excited state Γ_1 obtained with continuous measurement and with pulsed measurements such as those discussed in chapter 4. The goal of this comparison is twofold: first, it is a consistency check; second, the continuous measurement allows to decompose

the relaxation rate into its different channels and to identify the dominating ones at each frequency.

Pulsed experiments to determine $\Gamma_1 = 1/T_1$ were here performed with a 13 µs saturating pulse, which sets the qubit in a random mixture of $|g\rangle$ and $|e\rangle$, instead of a π-pulse because Rabi oscillations are not observed at all values of the Andreev energy due to dephasing. The contrast is halfed, but the rate is the same as for a π-pulse. The relaxation is then fitted with an exponential decay.

In order to remain as close as possible to the procedure used in the pulsed experiments to determine Γ_1, the rates obtained with the continuous measurements presented above were used in the master equation to simulate a relaxation experiment. This relaxation is then fitted with an exponential decay in the same way as for the pulsed experiments. The result of this procedure is shown in Fig. 6.9

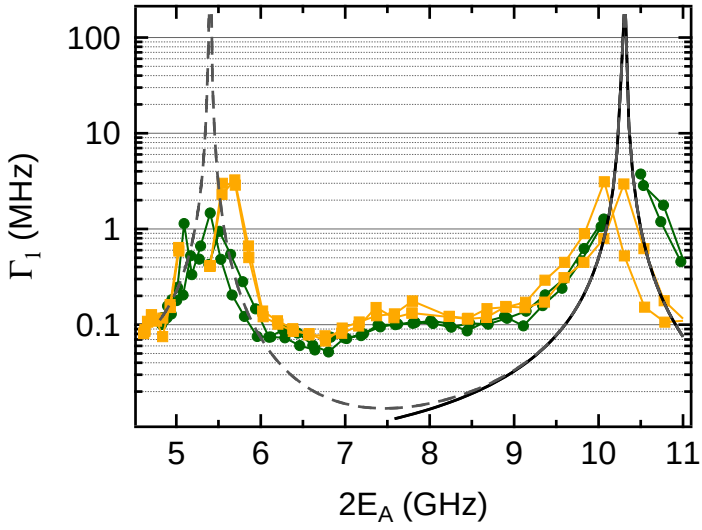

Figure 6.9: Relaxation rate of the even excited state as a function of the Andreev transition energy. Green: Γ_1 as measured using pulsed experiments. Yellow: relaxation rate determined using the continuous measurements. Black: estimation of the Purcell limited Γ_1 due to the resonator only. Dashed gray: estimation of the Purcell limited Γ_1 due to the resonator and a second electromagnetic mode at 5.4 GHz.

Two peaks in Γ_1 are observed, with a plateau in-between. The peak close to 10 GHz corresponds to transition energies close to the resonator mode. The peak close to 5.5 GHz was already observed in the rates presented in the previous section. In Fig. 6.9 is also plotted the calculated Purcell limited Γ_1 for the resonator alone and for the resonator plus a second mode at 5.4 GHz with a total quality factor $Q_{tot2} = 1300$ for a best fit. The prediction for Purcell limited Γ_1 describes qualitatively the trend observed in the experimental data for this second case, at Andreev transition energies close (less than 1 GHz) to the resonances of the environment. Between 6 GHz and 9 GHz, the relaxation rate remains close to 100 kHz which is consistent with the data presented in chapter 4. This plateau is not explained by the secondary relaxation channel through the odd states (see Fig. 6.8). However it could be due to an electromagnetic environment seen by the dot more complex than expected, which is already suggested by the resonance at 5.4 GHz. Finally, the agreement between the two techniques is good, except at the center of the resonances at 5.5 GHz and 10.3 GHz.

6.6 Statistics of the depoisoning events

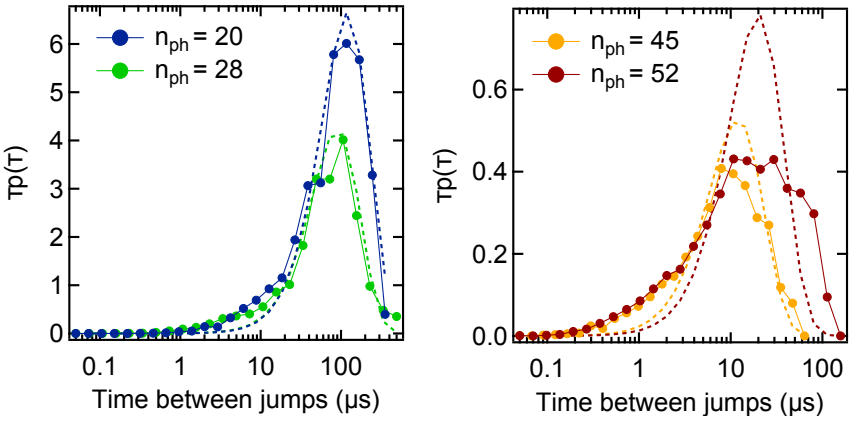

Figure 6.10: Histograms with logarithmic binning of the duration between depoisoning events τ, scaled by the duration τ. Circles: experimental data obtained from the reconstructed trace outputed by SMART. Dashed lines: fit using the Poissonian prediction.

In Ref. [47] the tunneling of single quasiparticles through the junction of a fluxonium qubit [125] was observed. This tunneling induces transitions in the fluxonium qubit which are observed using a similar procedure as the one presented in this chapter. A striking feature of these measurements was the fact that for some periods of time (of the order of a few minutes), the statistics of these tunneling events became non-Poissonian. This was shown by measuring the probability of having a time τ between two tunneling events. Here, we reproduce the same data processing on the depoisoning events, that is to say we measure the probability to stay for a duration τ in the $|o\rangle$ state. We compare this probability to a fitted Poissonian model [126] as shown in Fig. 6.10 for four different values of the measurement power.

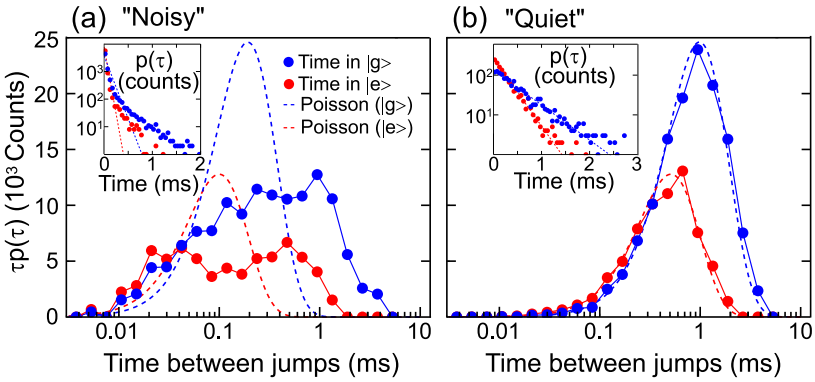

Figure 6.11: Data taken in a fluxonium qubit (from [47]): histograms with logarithmic binning of the duration between depoisoning events τ, scaled by the duration τ. Note the similar distribution in the "noisy" moments to what was found when $n_{ph} = 52$.

At low measurement power, the distribution of time between jumps is centered close to 100 µs. This is consistent with the rates presented above, which are close to 10 kHz. The Poisson model fits the data well except for a shoulder for time between jumps close to 10 µs. However, for larger measurement powers, the distribution of time between jumps diverges clearly from the Poisson distribution. Again, the distribution of duration between the depoisoning events is consistent with the rates presented in Fig. 6.5.

The distribution of the time between jumps in large n_{ph} regime is similar to what was found by Vool *et al.* in the "noisy" intervals, see Fig. 6.11. In the fluxonium experiments these noisy intervals were understood as period of time during which the quasiparticle density in the continuum was significantly increased by an intermittent source. Similarly, the non-poissonian distribution of times between jumps that we observe could be related to a large quasiparticle density created by the photons of the resonator, by a mechanism that remains to be understood. We did not analyze enough traces to tell if noisy intervals are found when n_{ph} is small.

6.7 Conclusion on continuous measurements

In this chapter we described the results of continuous monitoring of the state of the Andreev dot. With the rates extracted from these measurements, we quantified the influence of the photon population in the resonator and observed that even at low photon numbers ($n_{ph} \approx 10$) this influence is sizeable. Concerning the energy dependence of the jumping rates, we observed the influence of the resonator transition as well as a parasitic resonance. Only a few features of the data presented in this chapter are presently understood. More measurements on different contacts could provide a better insight. The addition of a quantum limited amplifier [127] would enable to measure at even lower photon number in the resonator while ruling out artifacts due to the processing algorithm.

Chapter 7

Conclusion

The main result of this thesis work is the demonstration of the coherence properties of Andreev qubits. Using atomic contacts in a circuit-QED architecture, we showed that the state of Andreev dots could be accessed in a single shot. Spectroscopy of the Andreev transition and measurements of the coherence time and lifetime of many different Andreev qubits were obtained from pulsed measurements. Our experiments, which constitute an additional example of the use of circuit QED to probe a mesoscopic system [128, 28, 129], are the realization of a 10-year-old proposal by Zazunov *et al.* [13]. We now discuss the perspectives associated to the questions that remain unsettled.

Lifetime of the excited state

Only when the Andreev frequency approaches that of the resonator (by less than 1 GHz) was the lifetime T_1 of the Andreev qubits found to be limited by the interaction with the resonator (Purcell limit). At the optimal point, corresponding to the minimum transition energy, T_1 does not exceed a few microseconds, almost an order of magnitude less than the Purcell limit. Using continuous measurements, we showed that the relaxation through the odd states does not contribute significantly to T_1. The source for excess relaxation is most probably an insufficient control over the electromagnetic environment of the qubit. In our experiments, the constraint that the substrate needs to be bent to obtain Andreev dots makes it difficult to employ

tight shields similar to those used in other superconducting qubits experiments [130]. It might be more favorable to use 3D-cavities instead of a 2D resonator [40, 41]. Such cavities offer in general a better control over the environment, but combining them with moving elements necessary for the break junction technique is an experimental challenge.

Coherence properties of the Andreev qubit

At $\delta = \pi$, the coherence times of Andreev qubits is limited by transmission noise. A large dispersion was observed on both the Ramsey (15 ns to 188 ns) and echo decay times (450 ns to 1.9 µs). Large Ramsey decay times (T_2^*) were found to be uncorrelated with large echo decay times (T_{2e}), suggesting that two independent sources of noises are at work, one at low frequency limiting the T_2^* and one at high frequency limiting the T_{2e}. The low frequency transmission noise was probed by measurements of the fluctuations of the Andreev transition frequency for long periods of time. The power spectrum of these fluctuations decays as $1/f^2$. This dependence on the frequency f is that of Brown noise, which is related to a Brownian motion, or to telegraphic noise associated to a single fluctuator. Transmission fluctuations can have (at least) three origins:

- A microscopic origin: Vacancies close to the contact, at the surface of the electrodes, can move even at milli-Kelvin temperatures (by tunneling between neighboring atomic sites), which changes the electronic configuration close to the contact and therefore the transmission coefficient τ [131]. The transmission noise generated by such displacements could be the source of the observed low frequency Brown noise;

- A mesoscopic origin: The large stress applied to the chip could result in creep of the plastic substrate. Another source of transmission fluctuations are vibrations of the suspended bridge. Evidence of the coupling between this micro-mechanical oscillator and the Andreev qubit are presented in Appendix D.

- A macroscopic origin: Vibrations of the dilution refrigerator are transmitted to the suspended bridge through the mechanical setup. Due to the size of the mechanical setup, only the low frequency noise is

decoupled from the bending of the bridge. Hence, this macroscopic noise could be at the origin of the high frequency noise observed.

Quasiparticle poisoning

The transition rates between the states of Andreev dots, extracted from the parity jumps observed in continuous measurements, revealed the strong influence of the microwave resonator and of the measurement power on the quasiparticle poisoning dynamics. The underlying physical processes remain unknown but measurements on more contacts could provide more insight. In order to perform these continuous measurements at a power low enough not to perturb the dynamics, experiments using a quantum limited amplifier (a Josephson parametric converter) [127] are in progress.

Perspectives: wires and 2D-gases

Although atomic contacts and break junctions are remarkable tools to investigate Andreev physics and have been successfully used as such during the last twenty years, this work has also shown their limits. The first limit is the relatively loose control over the transmission of these contacts: not only is it cumbersome to obtain a contact with a desired transmission (and impossible with an accuracy greater than 0.005), but the break junction technique makes the atomic contact very sensitive to its mechanical environment, which is hard to control. In addition, break junctions do not allow to obtain multi-terminals junction devices, which have been recently been predicted to give access to topological effects [132].

In order to circumvent these limitations, new weak links have to be used. Two candidates are proposed: nanowires and 2-dimensional electron gases (2DEGs). Nanowires [133] can be directly used as a Josephson weak link. Gates can be used to control electrically the transmission of semiconducting nanowires [134], with a good accuracy. The presence of stationary points in the voltage-dependence of the transmission [71] could solve the problem of transmission noise as a limitation of the coherence of Andreev qubits. Alternatively, one could use Bismuth nanowires, which have been shown to exhibit edge states with unity transmission under high magnetic fields [135]. In order to obtain multi-terminal junctions, a versatile solution would be

to proximize 2DEGs with superconducting electrodes. Electrostatic gates are then used to deplete locally the gas and create quantum point contacts [136]. After several decades of work in this direction, very recent results [137] suggest that good contacts can now be obtained to 2DEGs.

A further motivation pushes to the investigation of the weak links presented here-above: all of them also present high spin-orbit interaction. This interaction is expected to enrich the physics of Andreev bound states, by lifting the spin degeneracy of odd states [138, 139] and giving rise to topologically protected states at finite magnetic fields [140, 141].

Appendices

Appendix A

The rotating wave approximation

This appendix contains a detailed derivation of the Jaynes-Cummings Hamiltonian (Eq. 3.30), starting from Eq. (3.20):

$$H = \hbar\omega_R(\hat{N} + \frac{1}{2}) - \frac{\hbar\omega_A}{2}\sigma_z + \hbar g(a^\dagger + a)(\sigma_x + \frac{1}{\sqrt{1-\tau}\tan(\delta/2)}\sigma_z). \quad \text{(A.1)}$$

Using

$$\sigma_x = \sigma^+ + \sigma^-, \quad \text{(A.2)}$$

where $\sigma^+ = |e\rangle\langle g|$ and $\sigma^- = |g\rangle\langle e|$, and reintroducing H_A and H_R, Eq. (A.1) reads:

$$\begin{aligned} H =& H_A + H_R \\ &+ \hbar g a^\dagger(\sigma^+ + \sigma^-) + \hbar g a(\sigma^+ + \sigma^-) \\ &+ \frac{\hbar g}{\sqrt{1-\tau}\tan(\delta/2)}(a^\dagger + a)\sigma_z. \end{aligned}$$

The Hamiltonian is then written in the interaction picture, using the unitary operator:

$$U = e^{-i(H_A+H_R)t/\hbar} = \alpha e^{-i\omega_R\hat{N}t}e^{i\omega_A\sigma_z t/2}, \quad \text{(A.3)}$$

with $\alpha = e^{-i\omega_R t/2}$.

We use the Baker-Campbell-Hausdorff lemma which states for any hermitian operators U and H [22]:

$$e^{iU\lambda}He^{-iU\lambda} = H+(i\lambda)\,[U,H]+\frac{(i\lambda)^2}{2!}\,[U,[U,H]]+...+\frac{(i\lambda)^n}{n!}\,[H,[...,[U,H]\,...]] \tag{A.4}$$

The relevant commutators that appear in the calculation are:

$$\left[\hat{N},a\right] = -a \tag{A.5}$$
$$\left[\hat{N},a^\dagger\right] = a^\dagger \tag{A.6}$$
$$\left[a,a^\dagger\right] = 1 \tag{A.7}$$
$$\left[\sigma_z,\sigma^+\right] = -2\sigma^+ \tag{A.8}$$
$$\left[\sigma_z,\sigma^-\right] = 2\sigma^- \tag{A.9}$$

All operators from the resonator subspace commute with the operators from the qubit subspace. The effect of the unitary transformation on each of the operators is evaluated as follows:

$$U^\dagger aU = \alpha^* e^{-i\omega_A\sigma_z t/2}e^{i\omega_R\hat{N}t}ae^{-i\omega_R\hat{N}t}e^{i\sigma_z t}\alpha \tag{A.10}$$
$$= e^{i\omega_R\hat{N}t}ae^{-i\omega_R\hat{N}t} \tag{A.11}$$
$$= a + (i\omega_R t)\left[\hat{N},a\right] + \frac{(i\omega_R t)^2}{2!}\left[\hat{N},\left[\hat{N},a\right]\right] + ... \tag{A.12}$$
$$= a + (-i\omega_R t)a + \frac{(-i\omega_R t)^2}{2!}a + ... \tag{A.13}$$
$$= e^{-i\omega_R t}a. \tag{A.14}$$

Likewise :

$$U^\dagger a^\dagger U = e^{i\omega_R t}a^\dagger \tag{A.15}$$

and

$$U^\dagger\hat{N}U = \hat{N}. \tag{A.16}$$

Now for the qubit operators:

$$U^\dagger \sigma^+ U = e^{-i\omega_A \sigma_z t/2} \sigma^+ e^{i\omega_A \sigma_z t/2} \tag{A.17}$$

$$= \sigma^+ + (-i\omega_A t/2)(-2\sigma^+) + \frac{(-i\omega_A t/2)^2}{2!}(4\sigma^+) + ... \tag{A.18}$$

$$= (1 + i\omega_A t + (i\omega_A t)^2 + ...)\sigma^+ \tag{A.19}$$

$$= e^{i\omega_A t}\sigma^+. \tag{A.20}$$

Likewise,

$$U^\dagger \sigma^- U = e^{-i\omega_A t}\sigma^-, \tag{A.21}$$

and:

$$U^\dagger \sigma_z U = \sigma_z. \tag{A.22}$$

Therefore

$$U^\dagger (H_A + H_R) U = H_A + H_R. \tag{A.23}$$

In the coupling Hamiltonian, the unitary transformation gives phase factors:

- $a^\dagger \sigma^+ \rightarrow \ a^\dagger \sigma^+ e^{i(\omega_R + \omega_A)t}$
- $a^\dagger \sigma^- \rightarrow \ a^\dagger \sigma^- e^{i(\omega_R - \omega_A)t}$
- $a\sigma^+ \rightarrow \ a\sigma^+ e^{-i(\omega_R - \omega_A)t}$
- $a\sigma^- \rightarrow \ a\sigma^- e^{-i(\omega_R + \omega_A)t}$
- $a^\dagger \sigma_z \rightarrow \ a^\dagger \sigma_z e^{i\omega_R t}$
- $a\sigma_z \rightarrow \ a\sigma_z e^{-i\omega_R t}$

The rotating wave approximation (RWA) consists in neglecting all the fast rotating terms, assuming that $|\omega_A - \omega_R| \ll \omega_R$. One obtains the Jaynes-Cummings Hamiltonian:

$$H = \hbar\omega_R (a^\dagger a + \frac{1}{2}) - E_A \sigma_z + \hbar g (a\sigma^+ + a^\dagger \sigma^-). \tag{A.24}$$

Appendix B

The dispersive limit

The following derivation follows the indications in Blais *et al.* [23]. The Jaynes-Cummings Hamiltonian

$$H = \hbar\omega_R(a^\dagger a + \frac{1}{2}) - E_A\sigma_z + \hbar g(a\sigma^+ + a^\dagger\sigma^-) \tag{B.1}$$

$$= H_R + H_A + H_g \tag{B.2}$$

takes a simpler form when $g \ll |E_A - \hbar\omega_R|$. It is obtained by performing a unitary transformation with the operator:

$$U = e^{\frac{g}{\Delta}(a\sigma^+ - a^\dagger\sigma^-)}, \tag{B.3}$$

and developing it to second order in $\frac{g}{\Delta}$. As in Appendix A, we make use of the Baker-Campbell-Hausdorff lemma. Using the following commutation relations,

$$\left[a\sigma^+, a^\dagger a\right] = a\sigma^+ \tag{B.4}$$

$$\left[a^\dagger\sigma^-, a^\dagger a\right] = -a^\dagger\sigma^- \tag{B.5}$$

$$\left[a\sigma^+, \sigma_z\right] = 2a\sigma^+ \tag{B.6}$$

$$\left[a^\dagger\sigma^-, \sigma_z\right] = -2a^\dagger\sigma^- \tag{B.7}$$

$$\left[a^\dagger\sigma^-, a\sigma^+\right] = a^\dagger a\sigma_z + \sigma^+\sigma^- \tag{B.8}$$

one calculates to second order in $\frac{g}{\Delta}$:

$$\begin{aligned}\tilde{H}_R &= UH_RU^\dagger \\ &= H_R + \frac{\hbar g\omega_R}{\Delta}\left(\left[a\sigma^+, a^\dagger a\right] - \left[a^\dagger\sigma^-, a^\dagger a\right]\right) \\ &+ \frac{\hbar\omega_R}{2}\left(\frac{g}{\Delta}\right)^2\left[a\sigma^+ - a^\dagger\sigma^-, \left(\left[a\sigma^+, a^\dagger a\right] - \left[a^\dagger\sigma^-, a^\dagger a\right]\right)\right] \\ &= H_R + H_R^a + H_R^b\end{aligned}$$

with

$$H_R^a = \frac{\hbar g\omega_R}{\Delta}\left(a\sigma^+ + a^\dagger\sigma^-\right) \tag{B.9}$$

$$H_R^b = \frac{\hbar\omega_R}{2}\left(\frac{g}{\Delta}\right)^2\left[a\sigma^+ - a^\dagger\sigma^-, a\sigma^+ + a^\dagger\sigma^-\right]. \tag{B.10}$$

Now for the atomic part:

$$\begin{aligned}\tilde{H_A} &= UH_AU^\dagger \\ &= H_A - \frac{\hbar g\omega_A}{2\Delta}\left(\left[a\sigma^+, \sigma_z\right] - \left[a^\dagger\sigma^-, \sigma_z\right]\right) \\ &- \frac{\hbar\omega_A}{4}\left(\frac{g}{\Delta}\right)^2\left[a\sigma^+ - a^\dagger\sigma^-, \left(\left[a\sigma^+, \sigma_z\right] - \left[a^\dagger\sigma^-, \sigma_z\right]\right)\right] \\ &= H_A + H_A^a + H_A^b\end{aligned}$$

with:

$$H_A^a = -\frac{\hbar g\omega_A}{\Delta}\left(a\sigma^+ + a^\dagger\sigma^-\right) \tag{B.11}$$

$$H_A^b = -\frac{\hbar\omega_A}{2}\left(\frac{g}{\Delta}\right)^2\left[a\sigma^+ - a^\dagger\sigma^-, a\sigma^+ + a^\dagger\sigma^-\right]. \tag{B.12}$$

Finally for the coupling part:

$$\begin{aligned}\tilde{H}_g &= UH_gU^\dagger \\ &= H_g + H_g^a\end{aligned}$$

with:

$$H_g^a = \frac{\hbar g^2}{\Delta}\left[a\sigma^+ - a^\dagger\sigma^-, a\sigma^+ + a^\dagger\sigma^-\right]. \tag{B.13}$$

Since,

$$H_R^a + H_A^a = \frac{\hbar g}{\Delta}\left(a\sigma^+ + a^\dagger\sigma^-\right)(\omega_R - \omega_A) = -H_g \tag{B.14}$$

these three terms cancel. Moreover:

$$H_R^b + H_A^b = \hbar\frac{\omega_R - \omega_A}{2}\left(\frac{g}{\Delta}\right)^2\left[a\sigma^+ - a^\dagger\sigma^-, a\sigma^+ + a^\dagger\sigma^-\right] = -\frac{H_g^a}{2} \tag{B.15}$$

so that :

$$\tilde{H} - H_R - H_A = \frac{H_g^a}{2} \tag{B.16}$$

$$= \frac{\hbar g^2}{2\Delta}\left[a\sigma^+ - a^\dagger\sigma^-, a\sigma^+ + a^\dagger\sigma^-\right] \tag{B.17}$$

$$= \frac{\hbar g^2}{\Delta}\left[a^\dagger\sigma^-, a\sigma^+\right] \tag{B.18}$$

$$= \frac{\hbar g^2}{\Delta}\left(a^\dagger a\sigma_z + \sigma^+\sigma^-\right) \tag{B.19}$$

Finally, using $\sigma^+\sigma^- = \frac{1}{2}(\sigma_z + \mathbb{1})$, and removing an energy offset, one obtains:

$$\tilde{H} = \hbar\left(\omega_R + \frac{g^2}{\Delta}\sigma_z\right)a^\dagger a - \frac{\hbar}{2}\left(\omega_A - \frac{g^2}{\Delta}\right)\sigma_z \tag{B.20}$$

which is simply interpreted in terms of a shift of the resonator that depends on the state of the two-level system and a shift of the two-level system depending on the number of photons in the resonator.

Appendix C

Coupling between two conduction channels

In the Landauer-Büttiker formalism, transport between reservoirs occurs through independent transmission channels. In our experiments, due to the finite loop inductance and the relevance of the superconducting phase, the two electrodes on both sides of the atomic contact are not good "reservoirs", and the channels are not strictly independent. As shown in chapter 2, the phase across the contact, which is shared by all the channels, depends on the loop current. This current depends on the state of all the Andreev dots associated to all the channels. If the current in one channel is modified (because the Andreev dot changes state), the phase across the contact changes for all dots, leading to an effective coupling between the channels. The coupling between two Andreev dots in a few-atoms contact is evidenced in the high power spectroscopy shown in Fig. C.1 (see Fig. C.2, for the identification of the transitions). Several subharmonics of the transitions are visible as well as a splitting of the spectroscopy lines. The splitting corresponds to the fact that the phase across the contact can take several values at a given applied magnetic field, as explained above. When the applied flux corresponds to half a flux quantum, the phase across the contact is $\delta = \pi$ and the current is zero in all states, therefore this splitting vanishes. The dynamical coupling between channels labelled 1 and 2 is observed as a spectroscopy line at $f_1 = f_{A1} + f_{A2}$ (in the upper part of the figure), which corresponds to a simultaneous excitation of two Andreev qubits. Since the

current vanishes at $\delta = \pi$, this coupling disappear close to this point.

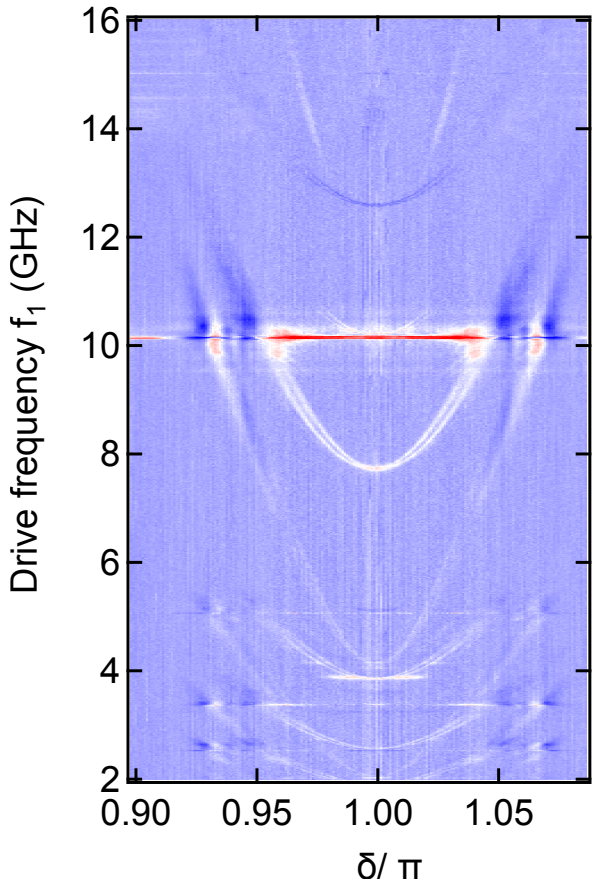

Figure C.1: High-power two-tone spectroscopy of a few-atom contact. Four Andreev transitions are visible, as well as subharmonics due to multiphoton excitations. See Fig. C.2 for the identification of the lines.

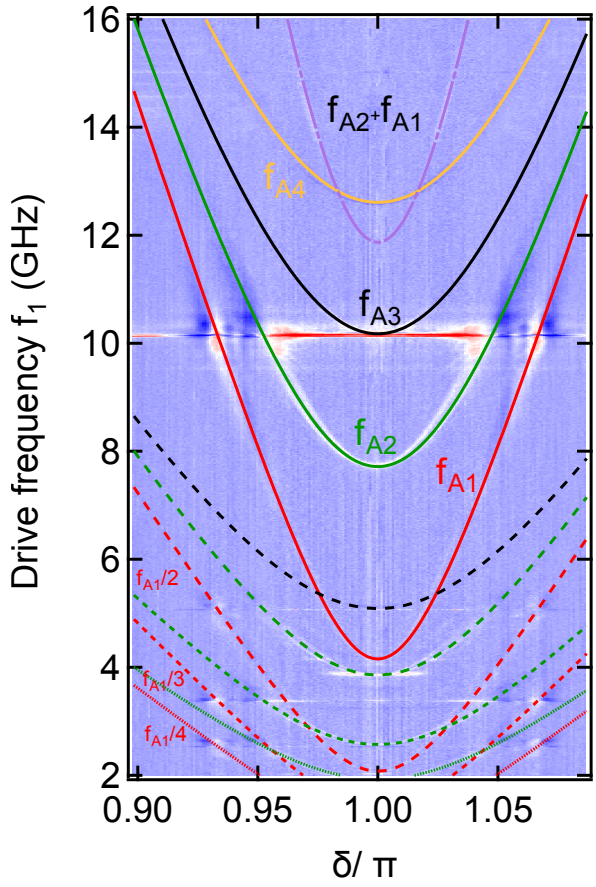

Figure C.2: Same data as in Fig. C.1, along with fits of the visible transitions. Full lines: Andreev qubit transitions, labelled f_{A1} to f_{A4}. Dashed lines: multiphoton excitations of the Andreev transitions with the same color code as for the direct excitations. The long dash corresponds to 2-photons excitations, the shorter dash to 3-photons excitations and the shortest dash to the 4-photons excitations. The dot-dash line corresponds to the combined excitation of the Andreev qubits supported by two channels which have the highest transmissions, 1 and 2.

Appendix D

Evidence for the coupling of Andreev qubits with a mechanical mode

As shown in chapter 4, transmission fluctuations are the main source of dephasing of the Andreev qubit at its optimal point. The transmission fluctuations observed in that chapter were assumed to be the result of stochastic processes and therefore incoherent. Here, we show data suggesting that the Andreev transition is also coupled to coherent modes, which could be mechanical modes associated to the suspended bridge.

In several experiments, most of them on the Vespel chip, sidebands were observed in the spectroscopy of Andreev qubits, as shown in Fig. D.1. Sidebands at $f_A \pm f_0$ signal the coupling between the qubit and another degree of freedom with frequency f_0. In the data of Fig. D.1, a single pair of sidebands is observed, corresponding to a frequency of 80 MHz.

The detuning of these sidebands varies slightly with the contact but remains close to 80 MHz. However, the strength of the coupling and the number of sidebands observed varies strongly from contact to contact. Up to three pairs of sidebands were observed, as shown in Fig. D.2a and Fig. D.2b. The detuning of the sidebands with respect to the central Andreev transition is not affected by the phase across the contact (see left panel of Fig. 4.11). This suggests that the degree of freedom responsible for the sidebands couples through the transmission of the contact and is only slightly affected by

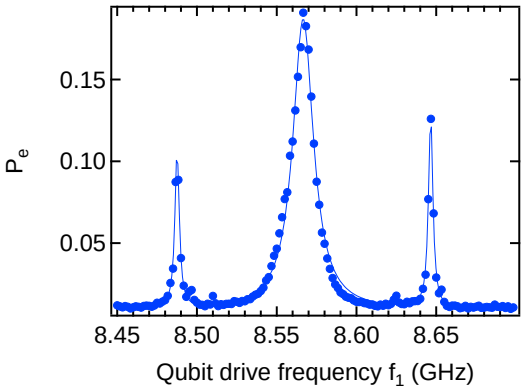

Figure D.1: Spectroscopy of an Andreev qubit at $\delta = \pi$: population of the excited state as a function of the drive frequency f_1. One pair of sidebands is visible, with a detuning of 80 MHz. Dots: experimental data. Full lines: lorentzian fits.

the contact. We interpret these data as the coupling between the Andreev transition and the bridge modes. These modes induce strain fluctuations on the atomic contact, which lead to transmission fluctuations [34]. Because the stiffness of a contact may vary with its microscopic arrangement, it affects slightly the frequencies of the bridge modes. Moreover this microscopic configuration could also be responsible of the varying sensitivity of the Andreev transition to the bridge mode.

We now derive a mechanical description of the suspended bridge supporting the contact in order to estimate the mode frequencies of the bridge. In a rough approximation, the bridge is modelled as a doubly clamped beam of constant section. Following Ref. [100], the eigenfrequencies f_n^M of the flexural modes of the beam are given by the Euler-Bernouilly theory:

$$f_n^M = \frac{1}{2\pi}\sqrt{\frac{EI_y}{\rho A}}\left(\frac{\gamma_n}{l}\right)^2, \tag{D.1}$$

where E is the Young modulus of the material constituting the beam, ρ its density, I_y is the bending moment of the beam along the bending axis, A the beam cross-section area, and l its length. The γ_n coefficients are constants

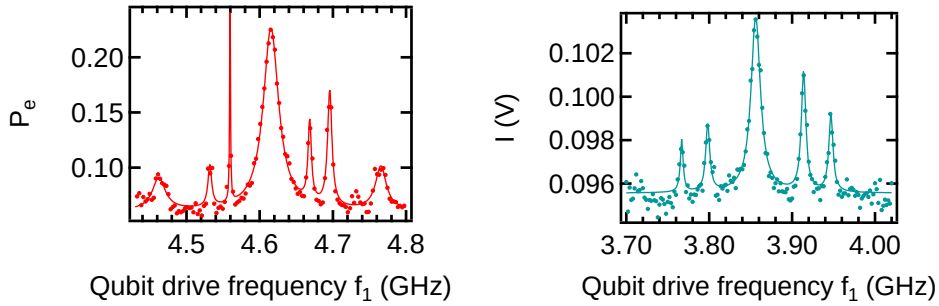

(a) (b)

Figure D.2: Spectroscopy of the Andreev transition shown for two different contacts. a) Spectroscopy line in terms of population of the excited state. 3 pairs of sidebands are clearly visible at the following detunings: 56 MHz, 84 MHz, and 150 MHz. b) Spectroscopy line measured using the average of the I quadrature. 2 pairs of sidebands are clearly observed at detunings of: 56 MHz and 90 MHz. Note the asymmetry on the height of the sidebands.

that can be calculated numerically[1] : $\gamma_1 \approx 4.73$, $\gamma_2 \approx 7.85$, $\gamma_3 \approx 11.0, ...$ The other parameters of our model are summed up in Table D.1:

E	6.9×10^{10} Pa
ρ	2.7×10^{3} kg/m^3
I_y	8.3×10^{-29} m^4
A	10^{-13} m^2
l	2.5×10^{-6} m

Table D.1

The first flexural mode of such a beam is at a frequency $f_1^M = 83$ MHz, which is of the same order of magnitude as the modes observed here. It is therefore likely that the sidebands found in the data are associated with the mechanical modes of the suspended bridge. A better modeling of the

[1] These coefficients[100] are solutions of the equation $\cos(\gamma_n)\cosh(\gamma_n) - 1 = 0$ which arises from the boundary conditions of the problem

bridge would be needed to take into account the triangular shape of the beam, the elasticity associated with the one-atom contact, and the actual boundary conditions of the system. Experimentally, further work is needed to find out for which bridge geometries the sidebands are observed, and if the suspended length of the bridge has an effect on the frequency of the sidebands.

Appendix E

Qutip code for simulating 3-tone spectroscopy

We here present as an exemple the Python code used to obtain the data shown in Fig. 5.9 in chapter 5, which makes use of the Qutip package.

```
# -*- coding: utf-8 -*-
"""
Created on Mon 11 04 2016
@author: cjanvier
"""
# importation of the toolboxes
from qutip import* # get qutip
from matplotlib.pyplot import * # get matplotlib if you want to plot something
import time, itertools # used to measure the duration of a calculation
from numpy import * # numpy for everything else


# INTRODUCTION
#
# We consider the system made of:
#   - a harmonic oscillator with frequency w0, and anihilation operator a,
#     and superrelaxation operator sqrt(kappa) a
#   - a two level system (2LS) with frequencies wge = w0 + Delta, anihilation
#     opearator sm, and superrelaxation operator sqrt(gamma1a) sm;
#
# The resonator is driven at wd=w0+delta (not to be confused with Delta)
# along a+a.dag
#
```

```
# The qubit is driven at wdq=wge - beta in sx (sigma x)
#
# All parameters are expressed in w0 units => w0=1 and (hbar =1).
#
# The goal is to obtain the steady state of the system under this double drive
# and relaxation of  both subsystems
#
# We use the dispersive, time independant Jaynes-Cummings hamiltonian.


#-------System parameters (all frequencies and rates in f0 units) --------------
f0 = 10135.7      # frequency of the bare resonator in MHz
fg=10137.4        # frequency of the resonator when the qubit i
                  # s in the ground state in MHz
fq = 6547.        # frequency of the Andreev transition in MHz


Delta0 = -(f0-fq)/f0              # Delta0=chi/f0
g0 = sqrt((f0-fg)*Delta0*f0)/f0   # Coupling parameter
betaCenter=g0**2/Delta0           # The frequency of the qubit is shifted
                                  # by chi without photons


kapaR = 0.45e-3           # cavity energy relaxation rate kappa in units of f0
gamma1 = (1/8.)/f0        # 2LS relaxation rate , T1=8µs
gamma2 = (1/0.072)/f0     # Dephasing rate of the qubit, T2*=72ns
drive0 = 1.*kapaR         # reduced drive of the cavity yielding 1 phton inside
                          # a harmonic oscillator
driveq0= 1.*gamma2        # reduced drive of the qubit
gamma_temp=0.000002       # rate of thermal excitation. Adjusted to fit the data.
#-------------------------------------------------------------------------------


#------------------------------------ Define the operators -----------------
def aOp(N): return tensor(destroy(N),qeye(2)) # a in the full hilbert space
def nOp(N): return aOp(N).dag()*aOp(N)        # n in the full hilbert space
#-------------------------------------------------------------------------------

#------------------------- operators sm, sx, sz -------------------------------
# sigma_m in the full hilbert space
def smOp(N): return tensor(qeye(N),destroy(2))
# sigmax in the full hilbert space
def sxOp(N): return tensor(qeye(N),sigmax())
 # sigmaz in the full hilbert space
def szOp(N): return tensor(qeye(N),sigmaz())
```

```
# at.a.sigmaz
def sznOp(N): return tensor(destroy(N).dag()*destroy(N),sigmaz())
#-------------------------------------------------------------------------------

#-------------- Dispersive Hamiltonian (see introduction above) ---------------
def H0(N,Delta,beta,g,delta):
    return beta/2*szOp(N) + delta*nOp(N) + g**2/Delta*sznOp(N)
#-------------------------------------------------------------------------------

#-------------------- Hamiltonian with the driving part ------------------------
def H(N,Delta,beta,g,delta,ad0,adq):
    return H0(N,Delta,beta,g,delta) + ad0/2*(aOp(N)+aOp(N).dag()) +adq/2*sxOp(N)
#-------------------------------------------------------------------------------

#--- -------------------------collapses operators -----------------------------
def c_ops(N):
    return [sqrt(gamma)*decayOp
        for gamma,decayOp in zip([kapaR,gamma1,gamma2,gamma_temp],
        [aOp(N),smOp(N),smOp(N).dag()*smOp(N),sxOp(N)]) if gamma!=0  ]
#-------------------------------------------------------------------------------
#-------------------------------------------------------------------------------

#-------------------------- Simulation parameters ------------------------------
# list of frequencies of the cavity drive to which the calculation is performed
# here the calculation is done from 10.13GHz to 10.133GHz with a step of 250kHz
deltas = arange((10130-f0),(10133-f0),0.25)/f0
# list of frequencies of the qubit drive to which the calculation is performed
# here the caclulation is done from fq to 5.647Ghz with a step of 50MHz
betas = betaCenter+arange(0,(fq-5647),50)/f0

# List of powers of the drive cavity to which the calculation is performed
drivek0s = array([7.7*1.75]) # here only one power
# List of powers of the drive qubit to which the calculation is performed
drivekqs = array([.6]) # here only one power

N0=25 # SIZE OF THE PHOTON SPACE need 64 bits to go above 120 photons
#-------------------------------------------------------------------------------


#--------------------------------- Simulation loops ----------------------------
it=0 # increment initialisation (for file naming)
doSavePofn=False # Save the Pofn only for simulations at 1 cavity drive frequ-
                 # ency. It returns N0.len(betas) percavity drive frequency
```

```
for delta in deltas:  # for each cavity drive frequency

    #-------------- (re-)initialize the list of P(n) -------------------------
    pofnListsg=zeros([len(betas),N0]) # P(n) when the qubit is in g
    pofnListse=zeros([len(betas),N0]) # P(n) when the qubit is in e
    #-------------------------------------------------------------------------

    #--------- make the file name-------------------------------------------
    pre='C:\Myfolder/simu_'
    num='%05d' %(it) # get the right number of file
    fin='.txt'  #postfix
    filename=pre+num+fin # combine everything
    #-------------------------------------------------------------------------

    for k0,kq in zip(drivek0s,drivekqs): # for each powers in qubit and drive
        popEx=[] # initialize the list used to store the population of e
        i=0 # increment initialisation (used to adress properly the lists)

        for beta in betas: # for each frequency of the qubit drive

            # calculate the steady state of the system with the
            # hamiltonian defined before and the collapse operators:
            rho_ss = steadystate(H(N0,Delta0,beta,g0,delta,k0*drive0,
            kq*driveq0), c_ops(N0), method = 'direct', use_precond = True)
            #---------------------------------------------------------------

            #--------get the diagonal elements of the density matrix: ---------
            diago=rho_ss.diag()
            #---------------------------------------------------------------

            #--get the expected value of the population of the excited state --
            pex=expect(0.5*(qeye(2)-sigmaz()),rho_ss.ptrace(1))
            #---------------------------------------------------------------

            #--- store  the value obtained at this frequency in the list-------
            popEx.append(pex)
            #---------------------------------------------------------------

            if doSavePofn==True: # if one wants to save P(n)

                #--------------- store the P(n) for this resonator frequency---
                pofn_tot=rho_ss.diag()
                # take the population of the resonator when qubit is in g
                pofnListsg[i,0:N0]=pofn_tot[0:2*N0:2]
                # take the population of the resonator when qubit is in e
```

```
                pofnListse[i,0:N0]=pofn_tot[1:2*N0:2]
                #-------------------------------------------------------------

                #------------ more naming -----------------
                numb='%05d' %(i+1)
                inter='Pofn'
                pofname=pre+num+inter+numb+fin
                #-----------------------------------------

                #Save P(n)
                savetxt(pofname, c_[pofnListsg[i,0:N0], pofnListse[i,0:N0]],
                delimiter='\t', newline='\n')

            i+=1 # increment i

    it+=1
    # save the excited state population for each cavity drive frequency.
    savetxt(filename,c_[(fq-betas*f0)/1000,popEx], delimiter='\t', newline='\n')
#-------------------------------------------------------------------------------
```

Appendix F

Processing of the continuous measurement traces

F.1 Hidden Markov Models

In order to process the data from the continuous measurements presented in chapter 6, we used an algorithm [53] relying on hidden Markov models (HMM) [142]. The goal of this appendix is to present a brief introduction in HMM inspired by Refs. [142, 143].

A HMM describes the dynamics of a system like the Andreev dot as a Markov process. The key hypothesis of a Markov process is that there is no memory in the system: the rate of jumping to a given state at a given time is only determined by the state in which the system is. As a consequence, the system dynamics is governed by a given set of probabilities to jump from one to another, see Fig. F.1.

The term "hidden" in Hidden Markov Models refers to situations where the system is observed through a second random process. As an example, in Fig. F.1, we consider a 3-states Markov model with 5 observable states. The system can jump between the states S1, S2, and S3 with probabilities $a_{i,j}$. If the system is in state S1, the observation will either be V1 or V2 with probabilities $b_1(V1)$ or $b_1(V2)$ respectively. In our experimental situation, the states are discrete (g, e and o), but the observable is a paire of continuous ones: the voltages on the I and Q quadratures, with a normal distribution due to noise.

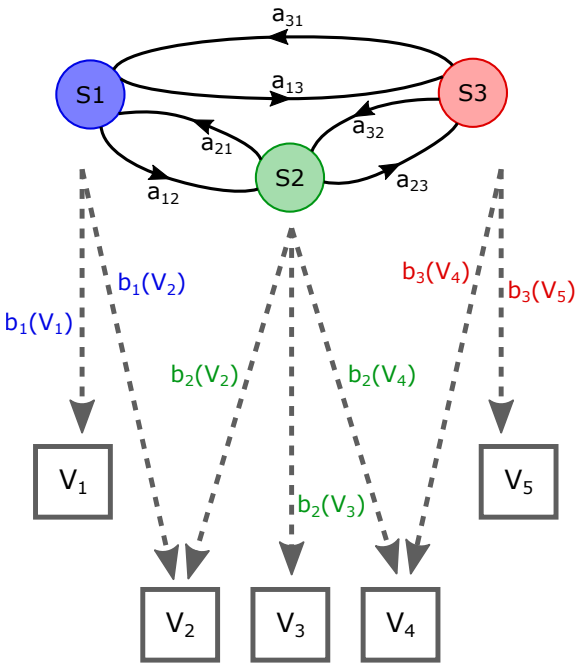

Figure F.1: Exemple of a hidden Markov model. Three states are available to the system: S1, S2, S3. Five observables are available: V1, V2, V3, V4 and V5. Note that one variable can correspond to several states, for exemple V2 can be observed if the system is in S1 or S2.

In the language of HMM, the observable variables are called 'alphabet', and the model is defined by the number of states, the probabilities linking them, the probabilities linking them to the alphabet and an initial state. An observation is the list of values taken by the observable variables in time. Using conditional probabilities it is possible to compute the most likely state of a system given an observation and a model, but it is also possible from an observation and knowing the number of states to estimate the most probable model according to the observation. It is this last point that is relevant for us. It makes use of the Baum-Welsch algorithm [142].

We now describe the Baum-Welsch algorithm in the case of a discrete alphabet of K values for more simplicity. We assume that we have a Markov process with $N = 3$ states and that the state of the process is described by

a discrete random variable X_t. We define the transition matrix:

$$A = \{a_{ij}\} = P(X_t = j | X_{t-1} = i). \tag{F.1}$$

The matrix element a_{ij} is therefore the probability for the system to jump to the state j at time t if it was at time $t-1$ in the state i. The observations are described by a second discrete random variable Y_t. We define the $K \times N$ observation matrix:

$$B = \{b_j(y_t)\} = P(Y_t = y_t | X_t = j). \tag{F.2}$$

Each element of this matrix is the probability of observing the value y_t of Y_t if the system is in state j. Finally we define the initial state by a $1 \times N$ vector with coefficients:

$$\pi_i = P(X_1 = i). \tag{F.3}$$

The goal of the algorithm is to calculate the model $\theta = \{A, B, \pi\}$ that maximizes the probability $P(\theta|O)$ where $O = \{y_1, ..., y_T\}$ is the set of T observations of Y_t, $O = \{Y_t\}$. The algorithm starts with an initial model θ_0, which can be chosen randomly or estimated with the prior knowledge on the system. The algorithm then computes two estimators that will then be used to update the model. The forward estimator is defined by $\alpha_i(t) = P(Y_1 = y_1, ..., Y_t = y_t, X_t = i|\theta_0)$, that is to say the probability to have the series of observation $\{y_1, ..., y_t\}$ and that the system is in state i, given the model θ_0. This estimator can be calculated iteratively using the data:

$$\alpha_j(t+1) = b_j(y_{t+1}) \sum_{i=1}^{N} \alpha_i(t) a_{ij}, \tag{F.4}$$

and $\alpha_i(1) = \pi_i b_i(y_1)$. The second estimator calculates the same probability but going backward in the data, $\beta_i(t) = P(Y_{t+1} = y_{t+1}, ..., Y_T = y_T, X_{t+1} = i|\theta_0)$, that is to say the probability to have the series of observation $\{y_{t+1}, ..., y_T\}$ and that the system is in state i, given the model θ_0. This estimator can be calculated iteratively using the data:

$$\beta_j(t) = b_j(y_{t+1}) \sum_{i=1}^{N} \beta_i(t+1) a_{ij}, \tag{F.5}$$

and $\beta_j(T) = 1$.

It is now possible to re-estimate the parameters of the model. For his purpose two temporary variables are used. The first one is the probability of the system of being in state i at a time t given all the observations and the model $\gamma_i(t) = P(X_t = i|O, \theta_0)$. It is calculated from β and α using Bayes' theorem:

$$\gamma_i(t) = \frac{\alpha_i(t)\beta_i(t)}{\sum_{j=1}^{N} \alpha_j(t)\beta_j(t)}. \tag{F.6}$$

Likewise we define $\xi_{i,j}(t) = P(X_t = i, X_{t+1} = j|O, \theta_0)$, which is the probability of the state being in state i at a time t and in state j at a time $t+1$ given the observations O and θ_0. Then the new model θ^* is given by:

- $\pi_i^* = P(X_1 = i|O, \theta_0) = \gamma_i(1)$
- $a_{ij}^* = \frac{\sum_{t=1}^{T-1} \xi_{ij}(t)}{\sum_{t=1}^{T-1} \gamma_i(t)}$
- $b_i^*(v_k) = \frac{\sum_{t=1, y_t=v_k}^{T} \gamma_i(t)}{\sum_{t=1}^{T} \gamma_i(t)}$

This model can then be used as the new input model for the algorithm. The model is therefore calculated iteratively until a convergence criterion is reached.

F.2 SMART

In the case of our data the Markov model has a three states. The observables are the measured voltage on I and Q which are continuous observables with Gaussian distributions. The SMART toolbox [53], which is written in MATLAB, performs the Baum-Welch algorithm described above for this model. The workflow of the data processing is presented in Fig. F.2.

The data is first smoothed to reduce the noise, and undersampled to remove correlation between points which would lead to the breakdown of the Markov model hypothesis. The data is then directly processed by the SMART toolbox using the "TrainPostDec" function. This function takes a set of parameters such as the number of states (3), the number of channels (here 2: I and Q), the distribution of the noise in the observables, and a convergence threshold. This function returns the matrix A and the reconstructed state of the system as a function of time, the position and size of

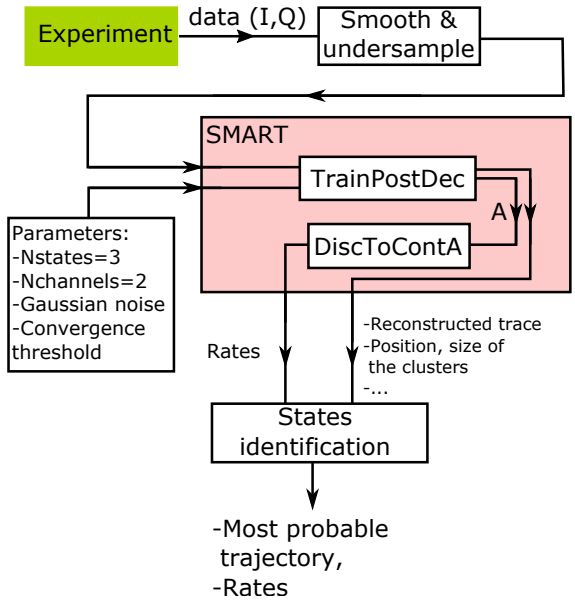

Figure F.2: Workflow of the data processing of the continuous monitoring of the Andreev dot. All steps presented here are done in Matlab.

the clusters, etc. In order to obtain the rates we use the function "DiscToContA" of the toolbox. Finally, the states are identified using the protocol described in the main text.

Appendix G

Synthèse en français

G.1 Le degré de liberté interne des jonctions Josephson

Bien que limités à des applications de niches, les circuits supraconducteurs sont aujourd'hui utilisés dans domaines variés allant de l'astrophysique à la médecine. Le développement de nouveaux types de circuits permettra peut-être à l'avenir d'obtenir des supercalculateurs ayant des consommations énergétiques plus faibles en utilisant la technologie RSFQ [1], et même de créer un ordinateur quantique [2]. Tous ces circuits, à l'exception des détecteurs à inductance cinétique [4], ainsi que des détecteurs de photons uniques supraconducteurs [5], reposent sur l'utilisation de l'effet Josephson.

La première description théorique de cet effet a été proposée par Brian Josephson en 1962 [6]. Cette théorie prédit qu'un courant non-dissipatif de paires de Cooper peut circuler à travers une jonction constituée d'une barrière isolante entre deux supraconducteurs, lorsque cette dernière est soumise à une différence de phase. Par ailleurs si une tension est appliquée aux bornes de cette jonction le supercourant oscille dans le temps. Admirablement, la richesse de cet effet tient dans deux équations, les équations Josephson.

Si la théorie de Josephson a été établie pour des jonctions tunnel, elle se généralise à toutes les jonctions constituées d'un lien faible entre deux électrodes supraconductrices. Ce lien faible peut être de nature variée :

nanofil métallique ou semi-conducteur, couche magnétique, *etc.* à la condition qu'il soit suffisamment court pour que les électrons conservent leur cohérence quantique lors de leur passage à travers ce lien faible. La théorie mésoscopique de l'effet Josephson [7, 8] a permis d'unifier la description de l'effet Josephson en traitant tous les liens faibles comme une assemblée de canaux de transport. Cette théorie montre que l'effet Josephson est plus riche que ce que laisse penser la théorie de Josephson. En effet, dans le cadre de cette description le courant Josephson est porté par deux états de quasiparticules localisés au niveau du lien faible. Ces "états d'Andreev" ont une énergie plus faible que l'énergie de gap des électrodes et qui dépend de la différence de phase appliquée sur la jonction et de la probabilité de transmission des électrons à travers le lien faible. Dans le cas simple où le lien faible est constitué d'un seul canal de conduction de longueur faible comparée à la longueur de cohérence supraconductrice, les états d'Andreev se réduisent à un système à deux niveaux. Le lien entre ces états et le supercourant dans les jonctions Josephson a été étudié en détail en utilisant des contacts à un seul atome entre deux supraconducteurs [9, 10, 11, 12].

Le doublet d'Andreev constitue un degré de liberté interne commun à tous les liens faibles Josephson, qui pourrait être utilisé comme un nouveau type de bit quantique supraconducteur [13, 14, 15]. Il a été sondé par spectroscopie dans les contacts atomiques [16], et les nanotubes de carbone [17, 18]. Enfin, des mesures de la susceptibilité à haute fréquence d'anneaux supraconducteurs contenant un lien faible en métal normal ont mis en évidence la dynamique de ces états [19, 20].

Le but de cette thèse a été d'observer et de quantifier les propriétés de cohérence quantique du doublet d'Andreev. Pour y parvenir, il nous a fallu combiner la technique des jonctions à cassure contrôlées mécaniquement (MCBJ) [21], avec les techniques issues de l'électrodynamique quantique des circuits (cQED) [23]. Les technique des MCBJ nous a permis d'obtenir des lien faibles courts ne contenant que quelques canaux de conduction. Les techniques de cQED nous ont, quant à elles, permis d'isoler le doublet d'Andreev ainsi que de mesurer et de manipuler son état quantique.

G.2 Du doublet d'Andreev au qubit d'Andreev

Lorsqu'une différence de phase est appliquée aux bornes d'un lien faible Josephson, la supraconductivité est frustrée localement. En réaction, des niveaux d'énergie localisés apparaissent au sein du gap supraconducteur. Lorsque le lien faible est constitué d'un unique canal de conduction court, un unique niveau apparaît dans le spectre d'excitation à une énergie $E_A < \Delta_{sc}$, l'énergie d'Andreev :

$$E_A = \Delta_{sc}\sqrt{1 - \tau \sin^2(\delta/2)}, \tag{G.1}$$

où τ est la probabilité de transmission d'un électron à travers le canal de conduction lorsqu'il est dans l'état normal. Δ_{sc} est l'énergie de gap du supraconducteur, et δ la différence de phase aux bornes du lien faible. Puisque ce niveau d'énergie se situe à l'intérieur du gap du supraconducteur, il ne peut pas se propager au sein des électrodes qui contactent le lien faible : ce niveau d'énergie est donc bien localisé. Par analogie avec les circuits semi-conducteurs où les électrons sont confinés à l'aide de barrières électrostatiques au sein de "boîtes quantiques", le lien faible peut ici être vu comme une " boîte d'Andreev " ("Andreev dot", [31]). Cette image permet de rendre compte de la physique aux énergies plus basses que celle du gap des électrodes, mais il faut noter que les états ayant des énergies supérieures au gap sont délocalisés à travers le lien faible. Le gradient de la phase ne localise que les états situés sous le gap.

Le niveau d'énergie d'Andreev de la boite d'Andreev peut être occupé par 0, 1, ou 2 quasi-particules, ce qui correspond en prenant en compte le spin, à 4 états, voir Fig. G.1:

- L'état fondamental $|g\rangle$ sans quasi-particule dans le niveau d'Andreev;
- Deux "états impairs" $|o\uparrow\rangle$ et $|o\downarrow\rangle$ avec une seule quasi-particule, de spin vers le haut ou vers le bas, dans le niveau d'Andreev;
- L'état excité pair (ou simplement état excité dans la suite de ce texte) $|e\rangle$ avec deux quasi-particules de spin opposés dans le niveau d'Andreev.

Zazunov *et al.* [13] ont proposé d'utiliser le système à deux niveaux constitué des deux états pairs $|g\rangle$ et $|e\rangle$ comme base pour un nouveau type

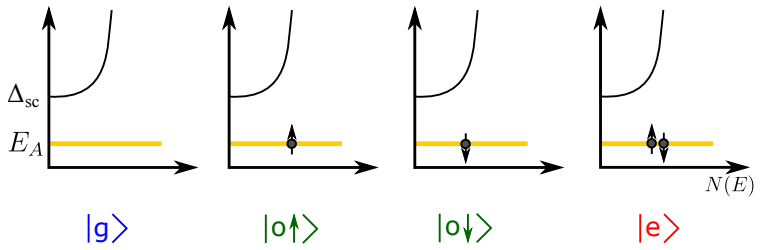

Figure G.1: Spectre d'excitation à basse énergie d'une boite d'Andreev pour un lien faible court contenant un seul canal de conduction. Les états pairs sont représentés en bleu ($|g\rangle$) et en rouge ($|e\rangle$) et correspondent à l'état d'une seule paire de Cooper localisée au niveau du lien faible. Ces états constituent le " qubit d'Andreev ". Les deux états impairs, en vert, correspondent à une situation ou une seule quasi-particule occupe la boite. Par ailleurs, la densité d'états au dessus du gap est aussi affectée [32].

de qubit supraconducteur. Ce qubit se différencie des autres qubits supraconducteurs par deux aspects :

- Il s'agit d'un qubit basé sur une excitation microscopique. Les autres qubits supraconducteurs reposent sur des modes électromagnétiques de circuits contenant une ou plusieurs jonctions Josephson;
- Il s'agit d'un véritable système à deux niveaux. Les autres qubits supraconducteurs se comportent comme des oscillateurs anharmoniques: la jonction Josephson introduit la non-linéarité qui crée l'anharmonicité. Dans ces systèmes l'anharmonicité permet de réduire l'oscillateur à un système à deux niveaux, mais les niveaux supérieurs peuvent néanmoins être adressés. Dans le cas du qubit d'Andreev, la première excitation après celle du qubit consiste à exciter une quasi-particule dans le continuum et se fait à une énergie proche de l'énergie de gap.

G.3 Réalisation d'une boîte d'Andreev

Pour cette thèse, le modèle présenté ci-dessus a été implémenté à l'aide de contacts atomiques obtenus entre deux électrodes supraconductrices en

aluminium. Il a été prouvé expérimentalement [34] que ce type de contacts ne contient que quelques canaux de conduction avec des transmissions pouvant dépasser 0.99. Plusieurs techniques existent pour obtenir de tels contacts [35, 36]. Pour les travaux présentés ici, les contacts atomiques ont été obtenus à l'aide de jonctions à cassures microfabriquées et contrôlées mécaniquement [37, 38, 21]. Ces jonctions utilisent un pont suspendu microfabriqué sur un substrat flexible (voir Fig. G.2). Lorsque le substrat est plié, le pont s'allonge et fini par casser. Un réglage fin du pliage du substrat permet d'obtenir un contact à un seul atome. Par ailleurs il a été montré qu'une variation de contrainte sur le contact entraîne une variation de la transmission de ce dernier [34]. Cet effet est utilisé affin d'obtenir de multiples qubits d'Andreev avec des énergies de transition différentes.

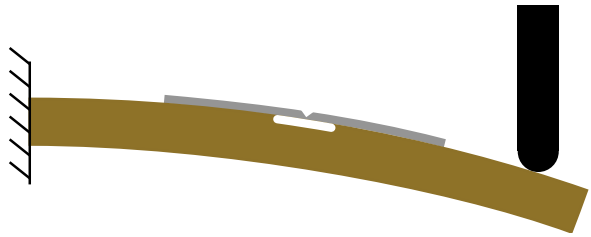

Figure G.2: Vue de côté d'une jonction à cassure contrôlée mécaniquement. Le substrat de l'échantillon (en marron) est fermement fixé à gauche, et en contact avec un pousseur à droite. Le pousseur peut monter et descendre afin d'ajuster le pliage du substrat. Sur le substrat le pont suspendu avec sa constriction. Lorsque le substrat est plié, le pont s'allonge, et l'élongation se concentre au niveau de la constriction. Le pont fini par casser mais peut être reformé (si réalisé sous vide) pour un réglage fin de la transmission.

G.4 Une architecture de cQED pour mesurer une boîte d'Andreev

L'électrodynamique quantique des circuits (cQED) est aujourd'hui largement utilisée pour mesurer et manipuler l'état de qubits supraconducteurs. L'architecture typique de ces circuits consiste en un qubit couplé à un résonateur micro-onde. La fréquence de résonance du résonateur dépend alors

de l'état du qubit. Ces variations de fréquence sont facilement détectées en mesurant la réponse du résonateur à fréquence fixe en amplitude et en phase. La description théorique de cette architecture a été fournie par Blais *et al.* [23] pour les qubits supraconducteurs et adaptée aux boites d'Andreev par Romero *et al.* [39]. Ce dernier a considéré le cas d'un résonateur demi-onde couplé galvaniquement au qubit. Pour nos expériences, en revanche, nous avons opté pour un résonateur quart-d'onde couplé inductivement au qubit d'Andreev. L'ensemble du circuit est réalisé sur un substrat plastique (Kapton) pour être compatible avec la technique de la MCBJ. Une micrographie est présentée Fig. G.3.

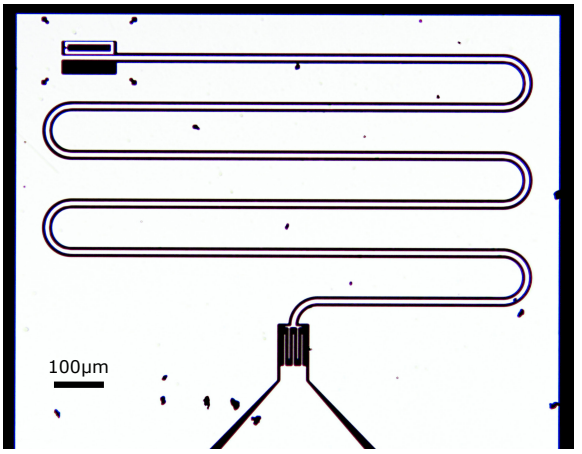

Figure G.3: Micrographie de l'un des échantillons utilisés dans ce travail. Les régions sombres sont isolantes, les régions claires supraconductrices. Le résonateur est constitué d'une ligne de transmission supraconductrice (Nb) en méandre qui forme un résonateur quart-d'onde au bout duquel est placé une boucle supraconductrice (Al) contenant la jonction à cassure (en haut à gauche). Le résonateur est couplé à la ligne de mesure par une capacité interdigitée (en bas au centre).

Le couplage entre le résonateur et le qubit est caractérisé à l'aide d'une spectroscopie à un ton, c'est à dire utilisant un seul signal micro-onde pour l'excitation du qubit et la mesure du résonateur. Le coefficient de réflexion du résonateur est mesuré en fonction de la différence de phase supraconductrice δ aux bornes du lien faible. Lorsque la fréquence de transition du qubit

devient résonante avec celle du résonateur un anticroisement est observé, voir Fig. G.4. Le fit de cet anticroisement permet d'obtenir la valeur du couplage entre le résonateur et le qubit, qui est ici de 80 MHz. La signature du résonateur non-couplé est aussi visible au milieu de cet anticroisement: ceci constitue la première indiction que la boîte d'Andreev est souvent dans son état impair qui n'est pas couplé au résonateur.

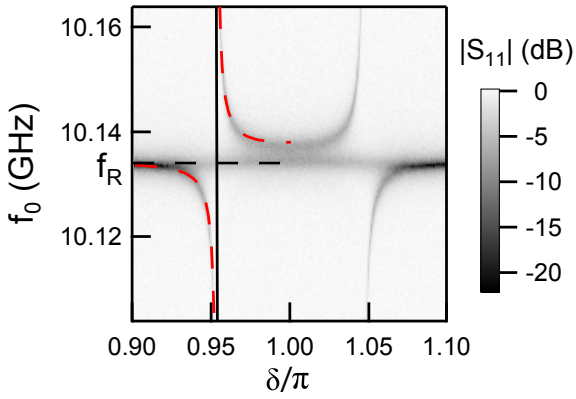

Figure G.4: Amplitude du coefficient de réflexion S_{11} du résonateur en fonction de la différence de phase δ aux bornes du contact atomique et de la fréquence du signal micro-onde utilisé pour sonder le résonateur. La fréquence de transition du qubit d'Andreev isolé est représentée par une ligne noire qui apparaît verticale à cette échelle. L'anticroisement est fitté et est représenté avec une ligne pointillée rouge. La fréquence du résonateur seul est aussi observée à toutes les phases ce qui indique que la boîte d'Andreev est souvent dans son état impair.

Lorsque le qubit est désaccordé avec le résonateur, son état peut être déduit grâce au déplacement en fréquence du résonateur. En pratique, on envoie vers le résonateur des pulses micro-onde à la fréquence du résonateur isolé. Les amplitudes des composantes en phase (I) et en quadrature (Q) du signal réfléchi sont ensuite mesurés et peuvent être représentées pour chaque pulse par un point dans le plan (I,Q). Un histogramme de ces points réalisé pour $\approx 10^4$ pulses est présenté Fig. G.5. On observe que les points se rassemblent en trois groupes qui peuvent être associés à chacun des états

occupés par la boîte d'Andreev. Le fait que ces groupes soient nettement

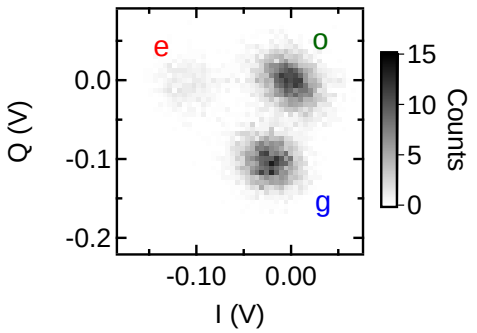

Figure G.5: Histogramme dans le plan (I,Q) du signal réfléchi par le résonateur. Les données se regroupent en trois "nuages" bien séparés qui peuvent être attribués à chacun des états de la boîte d'Andreev.

séparés est remarquable car ce résultat a été obtenu sans amplificateur limité quantiquement ce qui est généralement le cas dans les expériences de qubits supraconducteurs. Le nombre de points dans chaque groupe normalisé par le nombre de mesures donne la population de chaque état. On observe notamment que l'état impair est occupé environ la moitié du temps.

Ce type de mesure pulsée est ensuite utilisé afin de réaliser la spectroscopie de la transition d'Andreev. La figure G.6 présente l'amplitude du signal réfléchi par le résonateur en fonction de la différence de phase aux bornes du lien faible ainsi que de la fréquence d'un pulse d'excitation envoyé vers le résonateur juste avant le pulse de mesure. La transition d'Andreev est clairement observée et sa dépendance en phase est en accord quantitatif avec la prédiction théorique : $f_A = 2E_A/h$, avec E_A donnée par Eq. G.1. À $\delta = \pi$, la raie spectroscopique a une largeur de 16 MHz, ce qui est plus fin de deux ordres de grandeur comparé aux résultats précédemment rapportés [16].

G.5 Caractériser la cohérence du qubit d'Andreev

La principale contribution de cette thèse est la démonstration expérimentale de la cohérence du qubit d'Andreev. Figure G.7 montre les résultats obtenus sur l'un des qubits d'Andreev que nous avons pu mesurer. Des

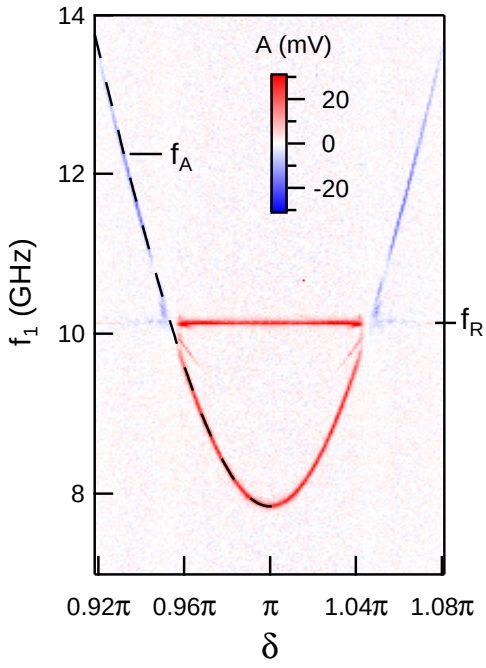

Figure G.6: Spectroscopie deux-tons de la transition d'Andreev. La ligne pointillée est un fit utilisant Eq. G.1 avec une transmission $\tau = 0.99217$.

oscillations de Rabi (panneau A) sont observées en mesurant les populations des différents états de la boîte après un pulse d'excitation de longueur variable. L'observation de ces oscillations a constitué la première signature de la cohérence quantique du qubit. La décroissance de ces oscillations est liée au temps de vie de l'état excité T_1, ainsi qu'au temps caractéristique de déphasage du qubit T_2^*. Afin de quantifier précisément chaque contribution, d'autres expériences sont nécessaires. Le temps de vie est mesuré à l'aide d'un pulse d'excitation appelé pulse π dont la durée est choisie afin d'inverser les populations de $|g\rangle$ et $|e\rangle$. Les populations sont mesurées après un délai variable. On observe une décroissance exponentielle de la population de l'état excité en fonction de ce délai, avec un temps caractéristique $T_1 \approx 1.3$ µs, pour le qubit présenté figure G.7. Le temps de déphasage est quant à lui mesuré à l'aide d'une séquence de Ramsey qui est constituée de deux pulses $\pi/2$ (des demi-pulses π) séparés par un délai variable.

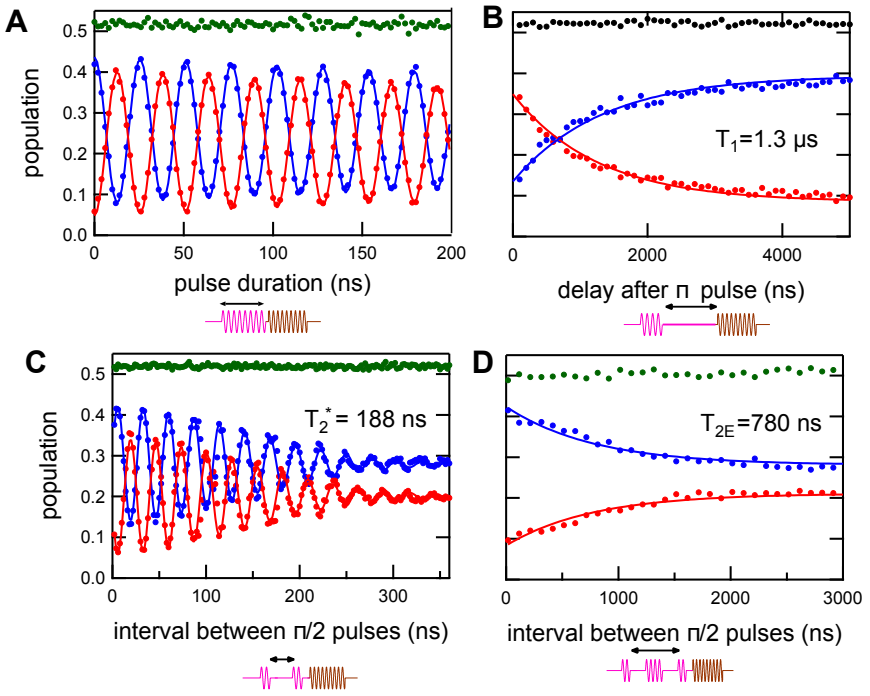

Figure G.7: Caractérisation d'un qubit d'Andreev obtenu avec un contact atomique avec une transmission $\tau = 0.99806$. Les points verts représentent la population des états impairs, les points bleus la population de l'état fondamental et les points rouges la population de l'état excité de la boîte. La séquence de pulses associée à chaque expérience est représentée sous chaque figure avec le pulse d'excitation en magenta et le pulse de mesure en marron. (A) Oscillations de Rabi; (B) Relaxation de l'état excité; (C) Franges de Ramsey (noter la décroissance gaussienne des oscillations); (D) Écho de Hahn. Ce jeu de données montre le plus long temps de déphasage (temps Ramsey) qui ait été observé pendant cette thèse.

On observe alors des oscillations avec une enveloppe gaussienne ayant un temps caractéristique T_2^* qui varie de 10 ns à 200 ns (ici 188 ns). Afin de

mieux caractériser le bruit à l'origine du déphasage du qubit d'Andreev on utilise une séquence dite "d'écho de Hahn" qui consiste en une séquence de Ramsey au milieu de laquelle est placé un pulse π. Cette séquence a pour propriété de filtrer le bruit dont la fréquence est inférieure à $1/T_E$ où T_E est l'intervalle de temps entre les deux pulses $\pi/2$. On observe une décroissance exponentielle avec un temps caractéristique nettement plus grand que pour la séquence de Ramsey, ce temps est ici de 780 ns. On en déduit que le bruit à l'origine du déphasage du qubit d'Andreev a une fréquence caractéristique plus basse que ≈ 2 MHz. Ce bruit est principalement dû aux fluctuations de transmission du lien faible et est discutée en détail dans le chapitre 4.

G.6 Sonder le résonateur grâce au qubit d'Andreev

Un paramètre important pour estimer la "force" de la mesure de l'état de la boîte d'Andreev par le résonateur est le nombre de photons présents dans ce dernier durant la mesure [42]. Ce nombre peut être estimé en connaissant la puissance du signal à l'entrée de la chaîne micro-onde ainsi que l'atténuation de cette micro-onde jusqu'au résonateur. L'estimation de cette atténuation peut cependant s'avérer délicate et peu fiable. Afin de remédier à cela, des méthodes de calibration *in situ* utilisant le couplage entre le résonateur et le qubit ont été développées [43]. Cependant ces expériences requièrent de longs temps de cohérence pour le qubit. Dans les travaux présentés ici nous avons montré que le nombre de photons dans le résonateur peut être estimé à l'aide d'une spectroscopie réalisée en présence d'un deuxième signal micro-onde à une fréquence proche de celle du résonateur pendant l'excitation du qubit. La raie de la transition d'Andreev est fortement affectée par la puissance et la fréquence de ce deuxième signal, comme montré figure G.8. En régime permanent, un refroidissement ou une inversion de population du qubit peuvent être observés. En comparant ces résultats à des simulations il nous a été possible de remonter au nombre de photon moyen dans le résonateur, voir chapitre 5.

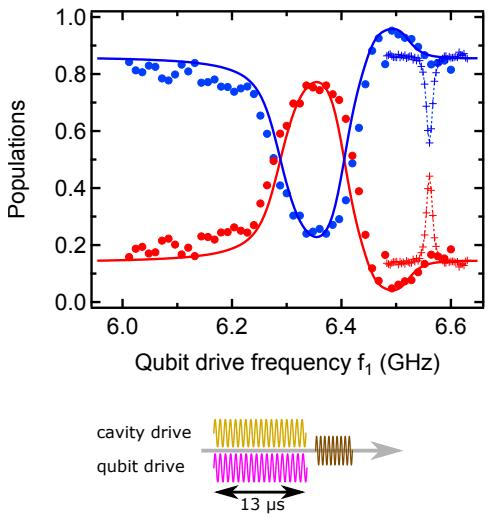

Figure G.8: Spectroscopie trois-tons en présence d'un signal d'excitation à le fréquence du résonateur lorsque le qubit est dans son état fondamental. Les données expérimentales sont représentées par des points et les résultats des simulations par des lignes. Les points bleus (rouges) représentent la population normalisée de l'état fondamental (excité) quand l'état impair n'est pas pris en compte. Le qubit est refroidi quand le signal d'excitation du qubit est proche de la fréquence de transition naturelle du qubit (croix); à une fréquence plus basse qui dépend du nombre de photons dans le résonateur, la population du qubit est inversée.

G.7 Observation de sauts quantiques et de sauts de parités dans une boîte d'Andreev

La dynamique des quasi-particules dans une boîte d'Andreev a déjà été étudiée dans de précédents travaux utilisant des mesures de courant de switching dans un contact atomique [44]. Cependant, l'état excité de la boîte d'Andreev n'avait alors pas pu être observé. Par ailleurs l'influence de quasi-particules a déjà pu être observé dans différents systèmes supraconducteurs [45, 46, 47, 48, 49]. Enfin il a été observé que la densité de quasi-particules sature sous 100 mK dans l'aluminium [50, 51, 52].

Le dernier volet de cette thèse présente une série d'expériences au cours

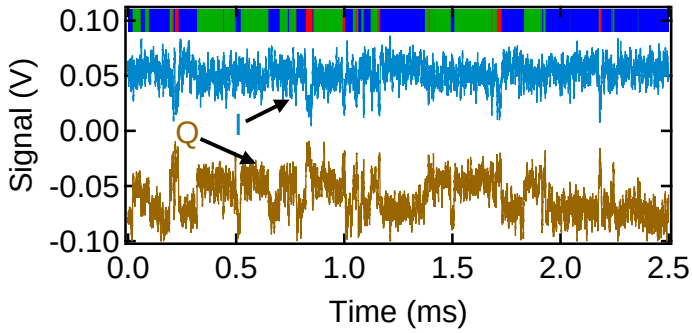

Figure G.9: Évolution des amplitudes en phase et en quadrature du signal réfléchi par le résonateur pendant une durée de 2.5 ms. Des sauts sont observés et analysés en utilisant un algorithme utilisant la théorie des modèles de Markov cachés. La barre en haut du graphe représente en code de couleur l'état de la boîte en fonction du temps, tel qu'il a été calculé par l'algorithme.

desquelles l'état de la boîte d'Andreev a été mesuré en continu grâce au résonateur. Des sauts quantiques ainsi que des sauts de parités dus au piégeage et dépiégeage de quasi-particules uniques dans la boîte ont pu être identifiés dans le signal réfléchi par le résonateur. Ce signal a été analysé en utilisant une technique basée sur les probabilités conditionnelles connue sous le nom de modèle de Markov caché (HMM) [53, 54]. Figure G.9 montre le résultat de ces mesures continues ainsi que l'évolution de l'état de la boîte telle que calculée par l'algorithme de HMM. Les taux extraits de cette reconstruction permettent d'obtenir des informations sur l'influence de la puissance du signal de mesure et de la différence de phase δ sur la dynamique d'une boîte d'Andreev.

Appendix H

Publications

The following pages present the preprint of the two papers published during this thesis by the author. The published versions are available in:

- Superconducting atomic contacts inductively coupled to a microwave resonator, Journal of Physics: Condensed Matter, Vol. **26**, Number 47, p. 474208 (2014).
- Coherent manipulation of Andreev states in superconducting atomic contacts, Science, Vol. **349**, Issue 6253, p. 1199 (2015).

Superconducting Atomic Contacts inductively coupled to a microwave resonator

C. Janvier[1], L. Tosi[2], Ç. Ö. Girit[1], M. F. Goffman[1], H. Pothier[1], C. Urbina[1].

[1]Quantronics Group, Service de Physique de l'État Condensé (CNRS, URA 2464), IRAMIS, CEA-Saclay, 91191 Gif-sur-Yvette, France

[2]Centro Atómico Bariloche and Instituto Balseiro, Comisión Nacional de Energía Atómica (CNEA), 8400 Bariloche, Argentina

E-mail: cristian.urbina@cea.fr

Abstract. We describe and characterize a microwave setup to probe the Andreev levels of a superconducting atomic contact. The contact is part of a superconducting loop inductively coupled to a superconducting coplanar resonator. By monitoring the resonator reflection coefficient close to its resonance frequency as a function of both flux through the loop and frequency of a second tone we perform spectroscopy of the transition between two Andreev levels of highly transmitting channels of the contact. The results indicate how to perform coherent manipulation of these states.

Keywords: break junctions, atomic contacts, superconductivity, Josephson effect, Andreev states.

1. Introduction

Atomic-size contacts between metallic electrodes are routinely obtained using either scanning tunneling microscopes or break-junctions [1]. From the electrical transport point of view, atomic contacts are simple systems. First, as for any good metal, electron-electron interactions are strongly screened. Second, because their transverse dimensions are of the order of the Fermi wavelength (typically 0.2 nm) they accommodate only a small number of conduction channels. Moreover, as the transmission probability τ_i for electrons through each conduction channel can be adjusted and measured in-situ [2], atomic contacts provide a test-bed to explore mesoscopic electronic transport [3, 4, 5]. In particular, when the metal is a superconductor atomic-contacts constitute elementary Josephson weak-links that allow probing the foundations of the Josephson effect [6].

Josephson supercurrents [7] will flow through any barrier weakly coupling two superconductors, including a tunnel junction, a constriction, a molecule, or a normal metal [8]. Microscopically, weak links differ in their local quasiparticle excitation spectrum. For a non-interacting system, this spectrum is determined by the length of the weak link, compared to the superconducting coherence length, and its configuration of conduction channels as characterized by the set of transmission probabilities $\{\tau_i\}$. The excitation spectrum of a short single-channel weak link of arbitrary transmission τ contains, besides the continuum of states at energies larger than the superconducting gap Δ, a sub-gap spin-degenerate level, known as the Andreev doublet (Figure 1). Its energy $E_A = \Delta\sqrt{1 - \tau \sin^2(\delta/2)}$ [9, 10] is a $2\pi-$periodic function of the superconducting phase difference δ across the weak link. It is precisely this phase dependence that gives rise to the Josephson supercurrent. In the widespread case of Josephson tunnel junctions, for which all $\tau_i \ll 1$, $E_{Ai} \sim \Delta$ and the lowest-lying excitations conserving electron parity have a threshold energy only slightly lower than 2Δ. By absorbing energy $\gtrsim 2\Delta$ a pair can be broken and two quasiparticles created at essentially the gap energy Δ, like in a bulk superconductor.

Two different spectroscopy experiments have recently probed this excitation spectrum for superconducting atomic contacts containing channels of high transmisssion. The first experiment [11, 12] spotlighted the lowest energy excitation that conserves electron parity, the "Andreev transition" of energy $2E_A$, which leaves two quasiparticles in the Andreev level (red double arrow in Figure 1a). The second experiment [13] revealed a second type of excitation, with minimum energy $E_A + \Delta$. In this case, a localized Andreev pair is broken into one quasiparticle in the Andreev level and one in the continuum (green arrows in Figure 1a) [14, 15, 16], thus leaving the system in an "odd" state. These odd states had been previously detected through the spontaneous trapping of a single out-of-equilibrium quasiparticle in the Andreev doublet [17]. This ensemble of results firmly support the description of the Josephson effect in terms of Andreev bound states.

If parity is conserved, the ground state and the even excited state constitute a two-level system [18] that has been proposed as the basis for a new class of

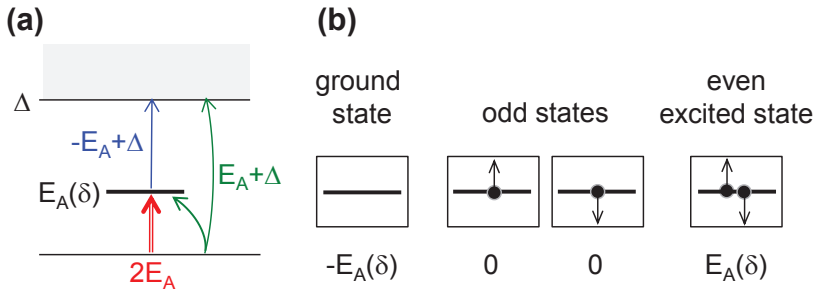

Figure 1. **(a)** The single particle excitation spectrum for each channel of a short Josephson weak link consists of a doubly-degenerate Andreev level at energy $E_A(\delta)$, and a continuum of states at energies larger than the superconducting gap Δ. Arrows indicate transitions that can be induced by microwave absorption. The four possible occupations of the Andreev level are shown in **(b)**: they correspond to the ground state (Andreev level empty), the two odd states (a single quasiparticle in the Andreev level), and the excited pair state (doubly occupied Andreev level), with energies $-E_A$, 0 and E_A respectively.

superconducting qubits [19, 20, 21, 22]. What is particularly interesting and novel is that in contrast with all other superconducting qubits based on Josephson junction circuits [23] an Andreev qubit is a microscopic two-level system akin to spin qubits in semiconducting quantum dots. Also, if one considers the odd states, despite the absence of actual barriers the system can be viewed as a superconducting "quantum dot" allowing manipulation of the spin degree of freedom of a single quasiparticle [24, 25, 26]. The coherence properties of Andreev doublets [20, 22] are still to be addressed experimentally. The relaxation time of the excited state and the dephasing time of quantum superpositions of the two states have to be measured, understood, and if possible, controlled.

Both relaxation and dephasing mechanisms contribute in principle to the linewidth of the Andreev transition. In order to achieve coherent manipulation of these Andreev states one would need much narrower lines than those observed in the aforementioned experiments, where they were typically larger than 500MHz. This was most probably due to large superconducting phase fluctuations imposed by the dissipative measurement lines that were necessary to measure the current-voltage characteristics of the contacts, a key piece of information from which the $\{\tau_i\}$ are extracted. Here, to isolate efficiently the contact from external perturbations, we follow a strategy that has been implemented successfully for superconducting qubits [27, 28]. The idea is to include an atomic contact in a small superconducting loop to form an rf-SQUID inductively coupled to the electromagnetic field of a coplanar microwave resonator. The latter should act as a narrow-band filter to allow probing the Andreev transition at $2E_A$ without excessive broadening. A similar setup was analyzed theoretically in [29], although here we have in addition avoided any galvanic connection of the SQUID loop with the rest of the circuit in order to minimize the probability of trapping out-of-

equilibrium quasiparticles in the contact [17]. By varying the flux threading the SQUID loop the Andreev transition frequency can be brought into resonance with the resonator mode. This will result in hybridization of the Andreev levels and the cavity mode (see Figure 2). The goal of the experiment presented here is to perform spectroscopy of the Andreev levels of the contact as a first step towards coherent manipulation of the two-level system.

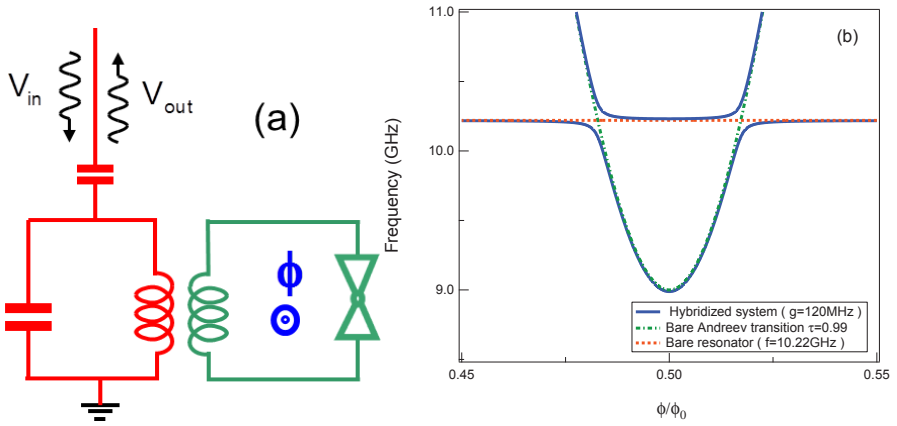

Figure 2. **(a)** An atomic rf-SQUID (in green) inductively coupled to a microwave resonator, represented here by a LC circuit (in red). The double triangle symbol represents the atomic contact. The spectrum of the combined system is probed through microwave reflectometry by weakly coupling the resonator to the external setup through a small capacitor. **(b)** example of the expected spectrum (blue full lines) as a function of the magnetic flux threading the SQUID loop. The resonance frequency of the bare resonator (red dashed line) is here 10.1 GHz; the Andreev frequency (green dashed line) corresponds to a channel with $\tau = 0.991$; and the SQUID-resonator coupling energy is $h \times (120\,\mathrm{MHz})$. The anti-crossing results from the hybridization of the two quantum systems.

2. Experimental Methods

2.1. Sample fabrication

The samples are fabricated on a flexible 500 µm-thick Kapton substrate ($\epsilon_r \simeq 3.2$, $\tan\delta \sim 1 \times 10^{-4}$ at 30 mK), 50 mm in diameter. In a first step, a series of $\lambda/4$ Nb resonators is fabricated. The substrate is then cut into 7 mm × 16 mm chips which are individually processed afterward to fabricate the atomic SQUID.

2.1.1. The microwave resonator A 200 nm thick Nb layer sputtered over the whole substrate is patterned via optical lithography, and then structured using reactive ion etching into a series of quarter-wave ($\lambda/4$) resonators in a coplanar waveguide

geometry (see Figure 3). The total length of the 36 µm wide inner conductor is 5 mm. The gap between the inner conductor and the ground plane is 18 µm. The impedance of the coplanar waveguide is $Z_r \sim 80\,\Omega$. The resonator is coupled through an interdigitated capacitor $C \sim 5$ fF to a 50 Ω line to measure its reflection coefficient $S_{11} \equiv 20 \log\left(V_{out}/V_{in}\right)$. For the 5 fF coupling capacitor the external losses should dominate over the internal ones (arising essentially from dielectric losses in the kapton substrate) leading to a global quality factor on the order of 1000.

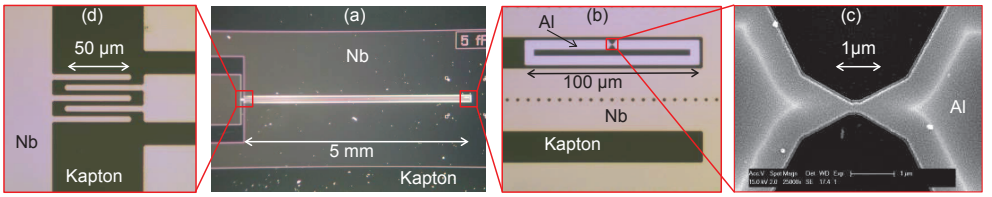

Figure 3. **(a)** Microphotograph of a coplanar quarter-wave Nb resonator. **(b)** Zoom on the shorted-end of the microwave Nb resonator (light gray). The 36 µm-wide center line contains some small holes intended as pinning centers for eventual vortices trapped in the superconducting film. The aluminum loop (white), with a suspended microbridge in one arm, is placed within the 18 µm gap (black). **(c)** Scanning electron microscope image of suspended microbridge with a 300 nm-wide constriction. The bright v-shaped ridges on both sides correspond to the border of the underlying polyimide layer which was etched to free the bridge over ~ 2 µm. **(d)** interdigitated coupling capacitor of the resonator.

2.1.2. The atomic rf-SQUID. Using electron beam lithography we fabricate a 100 nm-thick aluminum superconducting loop containing in one arm a micro-bridge, suspended over approximately 2 µm by reactive ion etching of a sacrificial polyimide layer (Figure 3). The bridge has a 300 nm constriction at the center. The width and the inner dimensions of the loop are 5 µm and 4 µm×90 µm, respectively, which lead to a geometrical inductance of around 100 pH , much smaller than the Josephson inductance of a typical atomic contact (a few nH). A magnetic flux ϕ through the loop is then used to impose a superconducting phase difference $\delta \cong 2\pi\phi/\phi_0$ across the contact, where $\phi_0 = h/2e$ is the flux quantum. This allows adjusting the phase-dependent energy of the Andreev levels.

2.2. Setup

Figure 4 shows the break-junction setup. The ensemble is attached to the mixing chamber of a dilution refrigerator. A precision screw (not shown), driven by a room temperature dc motor, controls the vertical displacement of a spindle. A copper slab attached to the spindle pushes the free end of the sample, which is firmly clamped on the opposite side against a microwave SMA launcher. The elongation of the upper face of the substrate as it bends leads eventually to the bridge rupturing. Afterward, the

distance between the two resulting electrodes varies by a few tens of picometers for every micrometer of vertical displacement of the pusher. The temperature of the ensemble is below 100 mK, and the cryogenic vacuum ensures that there is no contamination of the freshly exposed electrodes. The electrodes are gently brought back together, reforming the bridge and creating an atomic-size contact. Contacts can be made repeatedly in order to vary the number of channels and/or the transmission probabilities. An important feature of the microfabricated break junctions [30] is that a given contact can be maintained for weeks with changes in transmission below one part in a thousand.

The sample holder is enclosed in a set of three cylindrical shields (Al, Cryoperm and Cu, innermost to outermost) attached to the mixing chamber of a dilution refrigerator. All shields are capped at both ends. The inside diameter of the Al shield is 76 mm. The intermediate Cryoperm shield diverts the ambient magnetic field to reduce flux fluctuations through the SQUID loop as well as to minimize the number of vortices trapped in the Nb superconducting film. The inner walls of the Al shield are covered with a 3 mm thick layer of epoxy loaded with bronze and carbon powder to damp cavity resonances and adsorb spurious infrared radiation [31, 32]. A small superconducting coil, placed 2 mm above the sample inside a copper shield, allows controlling the flux through the loop.

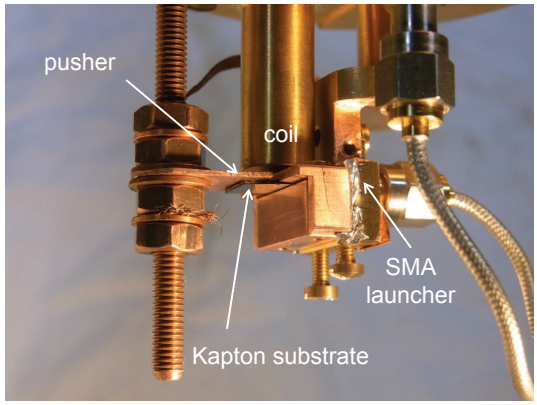

Figure 4. Break junction setup: a Kapton substrate is attached to SMA launcher (right side). The threaded spindle on the left side actuates the pusher vertically on the free end of the substrate with micrometer precision. The central cylindrical copper shield hosts a small superconducting coil that controls the flux through the SQUID loop. The whole system is enclosed in a set of three shields and anchored to the mixing chamber of a dilution refrigerator.

A single coaxial line enters this set of shields and connects to the SMA launcher. The overall microwave setup is sketched in Figure 5. There are two 8-12GHz circulators (Pamtech XTE0812KCSD) and one $0.1 - 18$ GHz directional-coupler (Clear Microwaves C20218) placed at the same temperature (25 mK) as the sample but outside

the shields. A first microwave tone, injected at one circulator, probes the response of the resonator at a frequency close to ν_0. The reflected signal from the resonator goes through the two circulators into a cryogenic amplifier (0.5-11 GHz LNA #265D from Caltech, gain 28 dB) placed at 1K. To minimize losses in the return signal a superconducting coaxial cable (Coax-Co SC-086-50-NbTi-NbTi) is used between the second circulator and the cryogenic amplifier. The output line from the cryogenic amplifier to room temperature is a CuNi coax, with a silver cladded inner conductor (CoaX-Co SC-086/50-SCN-CN). The two circulators prevent noise from the amplifier reaching the sample. A second tone at frequency ν_1 can be injected through the directional-coupler (-20dB coupling) to drive the transition between the Andreev levels at the atomic contact. Each line has a series of attenuators placed at different stages of the refrigerator to prevent external noise from reaching the sample. The total attenuation of each of the two input lines (including losses in the cables) is 90dB.

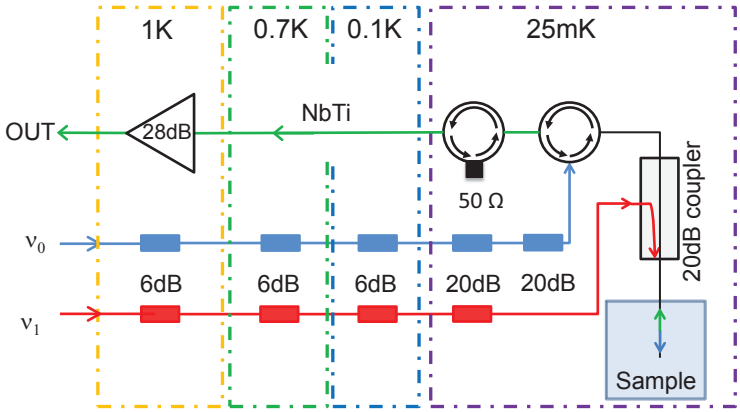

Figure 5. Microwave setup: A first tone of frequency ν_0 is used to probe the resonator. The two circulators divert the reflected signal towards a 28dB amplifier placed at 1K. A second tone of frequency ν_1 is used to drive the Andreev transition of the atomic contact.

3. Results

3.1. One-tone spectroscopy

After an additional 78dB room temperature amplification of the reflected signal, the reflection coefficient is directly measured using a vector network analyzer. As shown in Figure 6, three resonances appear in S_{11} below 10K in the range $8 - 10$ GHz. Below the superconducting transition of aluminum, only the two lowest frequency lines (#1 and #2) depend on temperature and bending of the substrate, and are thus associated with on-chip modes. The coplanar mode resonance is the one at $\nu_R \sim 10.24$ GHz, with a quality factor $Q \sim 300$. This is three times lower than expected. The measurements

clearly indicate an undercoupled regime with only 40° phase shift at resonance instead of the full 360°. We interpret this result as arising from the coupling of the coplanar resonator mode with a parasitic mode of the on-chip ground plane which is itself heavily damped by radiation to the enclosing dissipative cavity ‡.

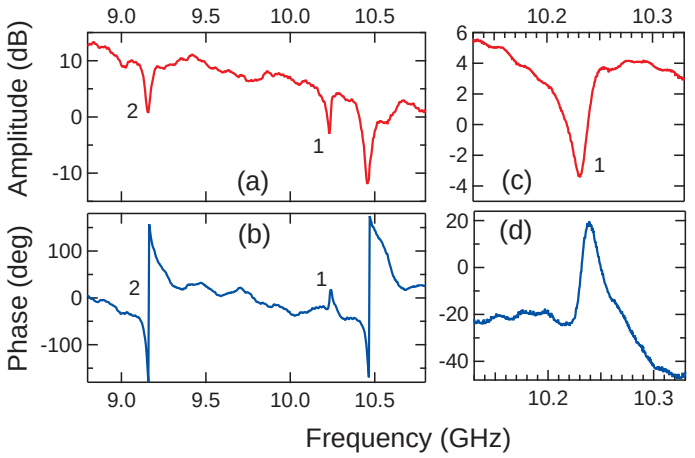

Figure 6. Amplitude (a) and phase (b) of reflection coefficient of resonator as a function of frequency, measured at 30 mK. The coplanar mode resonance is the one at $\nu_R \sim 10.24$GHz (labeled #1). There are two parasitic resonances, at 9.16 GHz and 10.45 GHz. Only resonances #1 and #2 change with temperature below 1K and when bending the substrate and are thus associated to on-chip modes. (c) and (d): zooms around coplanar mode resonance.

Despite the low quality factor, it is still possible to probe the atomic SQUID. Figure 7a shows the evolution of the resonance frequency of the resonator as the substrate is slowly bent at low temperature. As the coplanar resonator elongates, its resonance frequency decreases with the pusher vertical position at a rate of approximately 50 kHz/µm. The sharp frequency drop observed around a vertical deflection of 400 µm signals the last stage of rupture of the break junction. The frequency shift is in agreement with the change in inductance expected when opening the SQUID loop. As the vertical displacement of the pusher is actually not measured in-situ, but

‡ Because the sample must bent, the two outer electrodes of the coplanar resonator are actually grounded only at one end. As a result the ground plane behaves as an antenna. After carrying out the measurements we understood, through detailed electromagnetic simulations, that for the actual geometry of the resonator the quarter-wavelength mode had a similar resonance frequency than the antenna mode of the ground plane. The two modes hybridize and the resonator mode is also affected by radiation damping. Hybridization could be avoided by redesigning the resonator as a meander line (thus making the length of the ground plane electrode much smaller than the length of the resonator).

deduced from the measured number of turns of the motor and the pitch of the screw, the backlash of the mechanical driving setup leads to a hysteresis of around 25 µm between opening and closing directions. However, the position at which the abrupt frequency shift occurs is reproducible within a few microns for successive openings. In the region of this frequency drop the contact has atomic dimensions and its Josephson inductance becomes much larger than the geometrical inductance of the loop. In this limit, the resonator frequency evolves periodically with the magnetic flux threading the Al loop, as shown in Figure 7b. If the substrate is bent further, the loop opens completely and the flux modulation disappears.

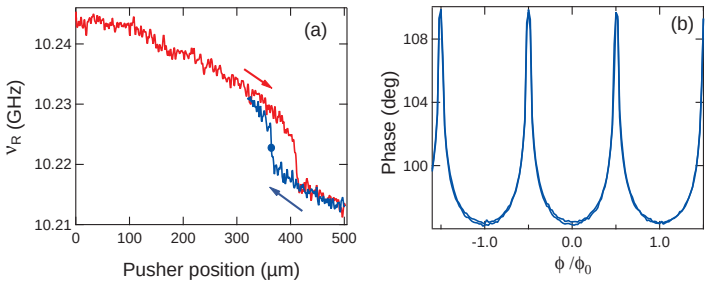

Figure 7. (a) Resonance frequency of resonator ν_R as a function of pusher position. Red (blue) curve correspond to the opening (closing) of the microbridge. (b) Phase of reflection signal as a function of the flux threading the SQUID loop (in reduced units) at the pusher position signaled by the blue dot in right panel. The modulation disappears when the microbridge is broken.

Figure 8 displays a spectrum of the reflection coefficient S_{11} as a function of the probe frequency and the flux threading the loop. An anti-crossing between the resonator and an Andreev transition in the contact is clearly observed. As shown, the shape of the spectrum can be described, at least qualitatively, by considering a single channel of transmission ($\tau \sim 0.995$) coupled ($g \sim 120\,\mathrm{MHz}$) to the coplanar resonator harmonic oscillator [29].

3.2. Two-tone spectroscopy

The spectrum can be explored over a much wider frequency range by using a two-tone technique. In this case the resonator is constantly probed at a fixed frequency ν_0 close to its resonance ν_R, while sweeping the frequency ν_1 of a second tone that is applied through the directional coupler (see Figure 5). The amplitude of this second tone is chopped at an audio frequency ν_a. The reflected signal at ν_0 is homodyne detected yielding the two quadratures I and Q which are then measured by lock-in amplifiers at ν_a (see Figure 9).

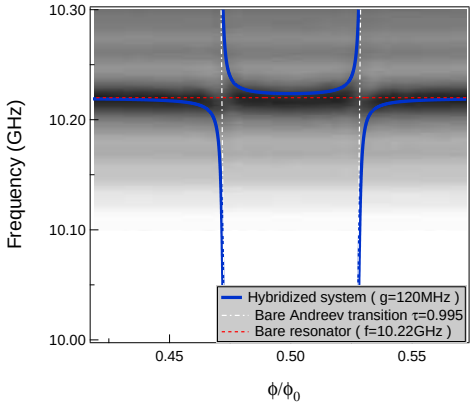

Figure 8. One-tone spectrum as a function of probe frequency (vertical axis) and phase across contact (horizontal). The gray level encodes the amplitude of the reflection coefficient. The dotted lines correspond to the bare frequencies for the resonator (red) and the Andreev transition of a single-channel of transmission $\tau \sim 0.995$ (white). The blue line is the prediction for the coupled system (coupling constant $g \sim 120\,\mathrm{MHz}$).

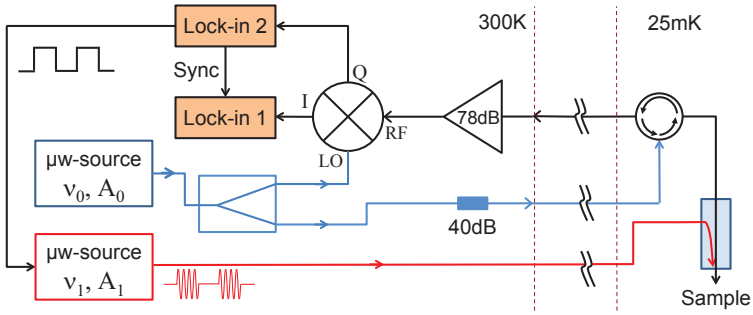

Figure 9. Room temperature setup for the two-tone spectroscopy: The pump signal at ν_1 is chopped at audio frequency. The reflected signal at ν_0 coming out of the cryostat is amplified and homodyne detected in a IQ mixer. The two phases are detected by the two lock-ins at the audio frequency at which the pump signal at ν_1 is chopped.

The spectra of the reflected signal as a function of the flux through the loop (horizontal axis) and the frequency ν_1 of the second tone (vertical axis) is shown in Figure 10 for two different contacts. Also shown in the figure are vertical cuts of each of the spectra at half flux quantum ($\delta = \pi$), which are fitted using two lorentzian peaks, all with linewidths below 60 MHz. By fitting the spectra using the analytical expression for the Andreev transition frequency $2E_A/h$, one can extract the gap Δ of the aluminum film and the transmission of the channels. Despite the apparently similar shapes of the multiple lines, the spectra do not correspond to contacts with several channels of slightly different transmissions, as shown by the continuous lines in 10(b). Instead, the

appearance of several peaks is attributed to the high microwave power injected in order to acquire sufficient signal.

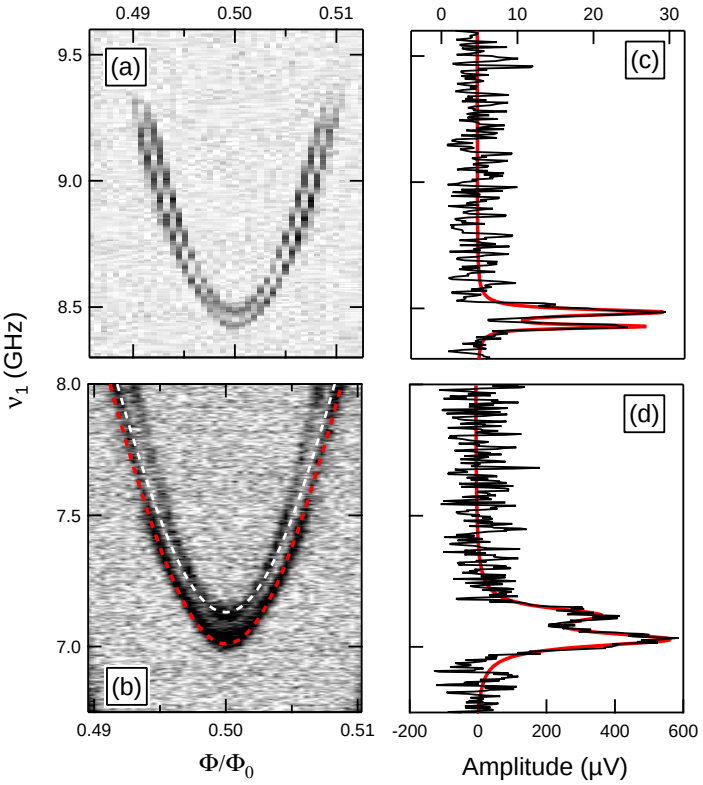

Figure 10. **(a)** and **(b)**: Greyscale coded amplitude of the reflected signal at ν_0, as a function of flux through the SQUID loop (horizontal) and frequency ν_1 of second tone (vertical) for two different contacts. Fits like red dashed line in (b) using the analytical expression for the Andreev transition frequency $2E_A/h$ determine the channel transmissions ($\tau = 0.9906$ in (a) and $\tau = 0.9934$ in (b)). The white dashed line in (b) illustrates the fact that the additional features of the spectrum cannot be attributed to Andreev transitions of other channels with slightly different transmission coefficients. **(c)** Measured amplitude (black) of reflected signal at a flux $\phi = 0.5\phi_0$ for contact of panel (a). Red line: fit of measured data using two lorentzians of widths 17 MHz and 28 MHz. **(d)** Measured amplitude (black) of reflected signal at a flux $\phi = 0.5\phi_0$ for contact of panel (b). Red line: fit of measured data using two lorentzians of widths 61 MHz and 65 MHz.

4. Conclusions

We have presented the first evidence for the efficient inductive coupling of a superconducting atomic contact to the electromagnetic field of a coplanar resonator. Using a two-tone setup, we have performed spectroscopy of the Andreev levels in the contact over several gigahertz. The observed linewidths are one order of magnitude smaller than in previous experiments and provide a lower bound of 10 ns for the coherence of the Andreev states. Although this is still too short for coherent manipulation of the Andreev doublet, we have identified a parasitic heavily damped resonance that loads the coplanar mode in the present design. A redesign of the resonator geometry to avoid this spurious resonance is expected to improve the lifetime by an order of magnitude. Pulsed pump and probe experiments should then allow performing Rabi oscillations of the state of the Andreev system.

Acknowledgments

We gratefully acknowledge technical support by P. Senat and P. F. Orfila, and the expert input and assistance of P. Bertet, D. Estève, P. Joyez and D. Vion. We have also greatly benefited from discussions with L. Bretheau, A. Levy Yeyati and J. M. Martinis. Financial support by ANR contracts DOCFLUC and MASH, C'Nano, the People Programme (Marie Curie Actions) of the European Union's Seventh Framework Programme (FP7/2007-2013) under REA grant agreement n° PIIF-GA-2011-298415, and ECOS-SUD (France-Argentina) n°A11E04 is acknowledged.

References

[1] N. Agraït, A. Levy Yeyati, and J. M. van Ruitenbeek, Physics Reports (2003), 81.

[2] E. Scheer, P. Joyez, D. Esteve, C. Urbina, and M. H. Devoret, Phys. Rev. Lett. **78**, 3535 (1997).

[3] Yu. Nazarov and Ya. M. Blanter, "Quantum transport : introduction to nanoscience", Cambridge University Press (2009).

[4] R. Cron, M. F. Goffman, D. Esteve and C. Urbina, Phys. Rev. Lett. **86**, 4104 (2001).

[5] R. Cron, E. Vecino, M.H. Devoret, D. Esteve, P. Joyez, A. Levy Yeyati, A. Martin-Rodero and C. Urbina, Proceedings of the XXXVIth Rencontres de Moriond « Electronic Correlations: From Meso- to Nano-physics », Les Arcs, (2001).

[6] L. Bretheau, Ç. Ö. Girit, L. Tosi, M. Goffman, P. Joyez, H. Pothier, D. Esteve, and C. Urbina, C. R. Physique **13**, 89 (2012).

[7] B. D. Josephson, Phys. Lett. (1962), 251.

[8] A. A. Golubov, M. Yu. Kupriyanov, and E. Il'ichev Rev. Mod. Phys. **76**, 411 (2004)

[9] A. Furusaki and M. Tsukada, Physica B: Condensed Matter (1990), 967–968.

[10] C. W. J. Beenakker and H. van Houten, Phys. Rev. Lett. **66**, (1991), 3056.

[11] L. Bretheau, Ç. Ö. Girit, H. Pothier, D. Esteve and C. Urbina, Nature **499**, 312 (2013).

[12] L. Bretheau, PhD thesis (2013), available on-line at http://hal.archives-ouvertes.fr/tel-00772851/.

[13] L. Bretheau, Ç. Ö. Girit, C. Urbina, D. Esteve and H. Pothier, Phys. Rev. X **3**, 041034 (2013).

[14] F. S. Bergeret, P. Virtanen, T. T. Heikkilä, and J. C. Cuevas, Phys. Rev. Lett. **105**, 117001 (2010).

[15] F. S. Bergeret, P. Virtanen, A. Ozaeta, T. T. Heikkilä, and J. C. Cuevas, Phys. Rev. B **84**, 054504 (2011).

[16] F. Kos, S. E. Nigg, and L. I. Glazman, Phys. Rev. B **87**, 174521 (2013).

[17] M. Zgirski, L. Bretheau, Q. Le Masne, H. Pothier, D. Esteve, and C. Urbina, Phys. Rev. Lett. **106**, 257003 (2011).

[18] D. A. Ivanov and M. V. Feigel'man, Phys. Rev. B **59**, 8444 (1999).

[19] J. Lantz, V. Shumeiko, Bratus, E. and Wendin, G., Physica C: Superconductivity (2002), 315.

[20] M. A. Desposito and A. Levy Yeyati, Phys. Rev. B **64**, 140511 (2001).

[21] A. Zazunov, V. S. Shumeiko, E. N. Bratus', J. Lantz, and G. Wendin, Phys. Rev. Lett. **90**, 087003 (2003).

[22] A. Zazunov, V. S. Shumeiko, G. Wendin, and E. N. Bratus, Phys. Rev. B **71**, 214505 (2005).

[23] G. Wendin and V. S. Shumeiko, Low Temp. Phys. **33**, 724 (2007).

[24] N. M. Chtchelkatchev and Yu.V. Nazarov, Phys. Rev. Lett. **90**, 226806 (2003).

[25] J. Michelsen, V. S. Shumeiko, and G. Wendin, Phys. Rev. B **77**, 184506 (2008).

[26] C. Padurariu and Yu. V. Nazarov, EPL **100**, 57006 (2012).

[27] A. Blais, Ren-Shou Huang, A. Wallraff, S. M. Girvin, and R. J. Schoelkopf , Phys. Rev. A **69**, 062320 (2004).

[28] A. Blais, J. Gambetta,1A. Wallraff, D. I. Schuster, S. M. Girvin, M. H. Devoret, and R. J. Schoelkopf, Phys. Rev. A **75**, 032329 (2007).

[29] G. Romero, I. Lizuain, V. S. Shumeiko, E. Solano, and F. S. Bergeret, Phys. Rev. B **85**, 180506 (2012).

[30] J.M. Van Ruitenbeek, A. Alvarez, I. Pineyro, C. Grahmann, P. Joyez, M. Devoret, D. Esteve and C. Urbina, Rev. Sci. Instrum. **67**, 108 (1996).

[31] R. Barends, J. Wenner, M. Lenander, Y. Chen, R. C. Bialczak, J. Kelly, E. Lucero, P. O'Malley, M. Mariantoni, D. Sank, H. Wang, T. C. White, Y. Yin, J. Zhao, A. N. Cleland, J. M. Martinis, and J. J. A. Baselmans, Appl. Phys. Lett. **99**, 113507 (2011).

[32] A. D. Córcoles, J. M. Chow, J. M. Gambetta, C. Rigetti, J. R. Rozen, G. A. Keefe, M. B. Rothwell, M. B. Ketchen and M. Steffen, Appl. Phys. Lett. **99**, 181906 (2011).

Coherent manipulation of Andreev states in superconducting atomic contacts

C. Janvier[1], L. Tosi[1,2], L. Bretheau[1†], Ç. Ö. Girit[1††], M. Stern[1], P. Bertet[1], P. Joyez[1], D. Vion[1], D. Esteve[1], M. F. Goffman[1], H. Pothier[1], C. Urbina[1*].

[1] Quantronics Group, Service de Physique de l'État Condensé (CNRS UMR 3680), IRAMIS, CEA-Saclay, 91191 Gif-sur-Yvette, France

[2] Centro Atómico Bariloche and Instituto Balseiro, Comisión Nacional de Energía Atómica (CNEA), 8400 Bariloche, Argentina

[†]Present address: Department of Physics, Massachusetts Institute of Technology, Cambridge, Massachusetts 02215, USA

[††]Present address: CNRS USR 3573, Collège de France, 11 place Marcelin Berthelot, 75005 Paris, France

*Correspondence to: cristian.urbina@cea.fr

Abstract:

Coherent control of quantum states has been demonstrated in a variety of superconducting devices. In all these devices, the variables that are manipulated are collective electromagnetic degrees of freedom: charge, superconducting phase, or flux. Here, we demonstrate the coherent manipulation of a quantum system based on Andreev bound states, which are microscopic quasiparticle states inherent to superconducting weak links. Using a circuit quantum electrodynamics setup we perform single-shot readout of this "Andreev qubit". We determine its excited state lifetime and coherence time to be in the microsecond range. Quantum jumps and parity switchings are observed in continuous measurements. In addition to possible quantum information applications, such Andreev qubits are a testbed for the physics of single elementary excitations in superconductors.

The ground state of a uniform superconductor is a many-body coherent state. Microscopic excitations of this superconducting condensate, which can be created for example by the absorption of photons of high enough energy, are delocalized and incoherent because they have energies in a continuum of states. Localized states arise in situations where the superconducting gap Δ or the superconducting phase undergo strong spatial variations: examples include Shiba states around magnetic impurities (*1*), Andreev states in vortices *(2)* or in weak links between two superconductors (*3*). Because they have discrete energies within the gap, Andreev states are expected to be amenable to coherent manipulation *(4,5,6,7,8)*. In the simplest weak link, a single conduction channel shorter than the superconducting coherence length ξ, there are only two Andreev levels $\pm E_A(\tau,\delta) = \pm\Delta\sqrt{1-\tau\sin^2(\delta/2)}$, governed by the transmission probability τ of electrons through the channel and the phase difference δ between the two superconducting condensates (*3*). Despite the absence of actual barriers, quasiparticles (bogoliubons) occupying these Andreev levels are localized over a distance $\sim\xi$ around the weak link by the gradient of the superconducting phase, and the system can be considered an "Andreev quantum dot" *(5,6)*. Figure 1 shows the energies $E_i(\delta)$ of the different states of this dot. In the spin-singlet ground state $|g\rangle$ only the negative energy Andreev level is occupied and $E_g = -E_A$. If a single quasiparticle is added, the dot reaches a spin-degenerate odd-parity state $|o\rangle$ with $E_o = 0$ *(9-12)*. Adding a second quasiparticle of opposite spin to the dot in state $|o\rangle$ brings it to a spin-singlet even-parity excited state $|e\rangle$ with $E_e = +E_A$ *(13,14)*. The $|e\rangle$ state can also be reached directly from $|g\rangle$ by absorption of a photon of energy $2E_A$. Here we demonstrate experimentally the manipulation of coherent superpositions of states $|g\rangle$ and $|e\rangle$, even if parasitic transitions to $|o\rangle$ are also observed.

Atomic-size contacts are suitable systems to address the Andreev physics because they accommodate a small number of short conduction channels (*15*). We create them using the microfabricated break-junction technique *(16)*. Figure 2 presents the sample used in the experiment. An aluminum loop with a narrow suspended constriction (Fig. 2C) is fabricated on a polyimide flexible substrate mounted on a bending mechanism cooled down to $\sim 30\,\mathrm{mK}$ *(17)*. The substrate is first bent until the bridge breaks. Subsequent fine-tuning of the bending allows creating different atomic contacts and adjusting the transmission probability of their channels. The magnetic flux ϕ threading the loop controls the phase drop $\delta = 2\pi\phi/\phi_0$ across the contact and thereby the Andreev transition frequency $f_A(\tau,\delta) = 2E_A/h$ (ϕ_0 is the flux quantum, *h* Plank's constant). To excite and probe the Andreev dot, the loop is inductively coupled to a niobium quarter-wavelength microwave resonator (*17*) (Fig. 2B) in a circuit quantum electrodynamics architecture *(18,19)*. The resonator is probed by reflectometry at frequency f_0 close to its bare resonance frequency $f_R \simeq 10.134\,\mathrm{GHz}$. The actual resonator frequency is different for each one of the three Andreev dot states: in the odd state, the resonance frequency is unaltered while the two even states lead to opposite shifts around f_R (*20*). The Andreev transition $|g\rangle \rightarrow |e\rangle$ is driven using a second tone of frequency f_1. Details of the setup are shown in figures S1 and S2 (*20*).

Here we present data obtained on a representative atomic contact containing only one high transmission channel. Data from other contacts is shown in figures S6-S8. First, a two-tone spectroscopy is performed by applying a 13 µs driving pulse of variable frequency, immediately followed by a 1 µs-long measurement pulse $\left(f_0 \simeq 10.1337\,\mathrm{GHz}\right)$ probing the resonator with an amplitude corresponding to an average number of photons $\bar{n} \simeq 30$ (see Fig. 3A). Apart from the signal at $f_1 \simeq f_0$, the spectrum displays a resonance corresponding

to the Andreev transition. The spectrum is periodic in flux, with period ϕ_0, which allows calibrating the value of δ across the contact (Fig. S3). Fits of the measured lines for different contacts with the analytical form of $f_A(\tau,\delta)$ provide the transmission probability τ of highly transmitting channels with up to five significant digits, as well as the superconducting gap $\Delta/h = 44.3$ GHz of the aluminum electrodes.

The coupling between the resonator and the Andreev dot is evident from the avoided crossing between the two modes observed in single-tone continuous-wave spectroscopy (Fig. 3B). Fitting the data with the predictions of a Jaynes-Cummings model *(19,20)*, yields the coupling strength $g/2\pi = 74\,\mathrm{MHz}$ at the two degeneracy points where $f_A = f_R$. Remarkably, the resonance of the bare resonator is also visible for all values of the phase, signaling that on the time scale of the measurement the Andreev dot is frequently in the odd state $|o\rangle$ (*10,12,21*).

Figure 3C shows the histograms of the reflected signal quadratures *I,Q* for a sequence of 8000 measurement pulses taken at $\delta = \pi$, without and with a π driving pulse. The results gather in three separate clouds of points demonstrating that a single measurement pulse allows discriminating the dot state. The normalized number of points in each cloud is a direct measurement of the populations of the three states. The two panels of Fig 3C show the population transfer between the two even states induced by the driving pulse. Continuous measurement of the state of the Andreev dot in absence of drive, reveals the quantum jumps (*22*) between the two even states and the changes of parity corresponding to the trapping and untrapping of quasiparticles in the dot (Fig. 3D). The analysis (*23*) of this real-time trace yields a parity switching rate of $\sim 50\,\mathrm{kHz}$ (*20*).

The coherent manipulation at $\delta = \pi$ of the two-level system formed by $|g\rangle$ and $|e\rangle$ is illustrated in Fig. 4. Figure 4A shows the Rabi oscillations between $|g\rangle$ and $|e\rangle$ obtained by varying the duration of a driving pulse at frequency $f_1 = f_A(\tau,\pi)$ (Movie S1). Figure 4B shows how the populations of $|g\rangle$ and $|e\rangle$ change when the driving pulse frequency f_1 is swept across the Andreev frequency $f_A(\tau,\pi)$. After a π-pulse the populations relax exponentially back to equilibrium with a relaxation time $T_1(\delta = \pi) \simeq 4\,\mu s$ (Fig. 4D). The Gaussian decay by 1/e of detuned Ramsey fringes (Fig. 4F) provides a measurement of the coherence time $T_2^*(\delta = \pi) \simeq 38\,ns$. This short coherence time is mainly due to low-frequency (<MHz) fluctuations of the Andreev energy $E_A(\tau,\delta)$, as shown by the much longer decay time $T_2(\delta = \pi) \simeq 565\,ns \gg T_2^*$ of a Hahn echo (Fig. 4G). Measurements at $\delta = \pi$ on other contacts with the same sample, with transmissions corresponding to a minimal Andreev frequency $3\,GHz < f_A(\tau,\pi) < 8\,GHz$, give T_1 mostly around 4 μs (up to 8.5 μs), T_2^* around 40 ns (up to 180 ns) and T_2 around 1 μs (up to 1.8 μs), but no clear dependence of the characteristic times on τ is observed (Fig. S7 and S8).

Figure 4E shows the measured relaxation rate $\Gamma_1 = 1/T_1$ as a function of the phase δ. The expected Purcell relaxation rate arising from the dissipative impedance seen by the atomic contact (dotted line in Fig. 4E) matches the experimental results only close to the degeneracy points where $f_A = f_R$, but is about five times smaller at $\delta = \pi$. Based on existing models we estimate that relaxation rates due to quasiparticles *(24-28)* and to phonons *(7,8,21)* are negligible. Empirically, we fit the data at $\delta = \pi$ by considering an additional phase-independent relaxation mechanism, which remains to be identified.

The linewidth of the spectroscopy line, which is a measure of the decoherence rate, shows a minimum at $\delta = \pi$ (Fig. 4C). The Gaussian decay of the Ramsey oscillations points to *1/f* transmission fluctuations as the main source of decoherence at $\delta = \pi$, where the system is insensitive to first order to flux noise *(28)*. Fluctuations of τ can arise from vibrations in the mechanical setup and from motion of atoms close to the contact. Figure 4C also shows the linewidths calculated assuming *1/f* transmission noise and both white and *1/f* flux noise (*20*). The amplitude of the *1/f* transmission noise, $2.5\times10^{-6}\,\mathrm{Hz}^{-1/2}$ at 1 Hz, was adjusted to fit the measurement at $\delta = \pi$. The amplitudes of the white and 1/f flux noise were then obtained from a best fit of the linewidth phase dependence. The extracted *1/f* noise amplitude ($5\mu\phi_0\,\mathrm{Hz}^{-1/2}$ at 1 Hz) is a typical value for superconducting devices and has a negligible effect to second order (*29*). The source of the apparent white flux noise $\left(48\,\mathrm{n}\phi_0\,\mathrm{Hz}^{-1/2}\right)$ is not yet identified.

The Andreev quantum dot has been proposed as a new kind of superconducting qubit *(5,6)*, which differs markedly from existing ones (*30*). In qubits based on charge, flux, or phase (*30*) the states encoding quantum information correspond to collective electromagnetic modes, while in Andreev qubits they correspond to microscopic degrees of freedom of the superconducting condensate. Our results are a proof of concept of this new type of qubit. Further work is needed to understand fully the sources of decoherence and to couple several qubits in multi-channel contacts (*5,8*). The Andreev quantum dot, with its parity sensitivity, is also a powerful tool to investigate quasiparticle-related limitations on the performance of superconducting qubits (*28,31,32*) and detectors (*33*). Furthermore, our experimental strategy could be used to explore hybrid superconducting devices in the regime where Andreev states evolve into Majorana states (*33,35,36*).

Acknowledgments: We have benefited from technical assistance by P. Sénat and P.-F. Orfila and discussions with G. Catelani, V. Shumeiko and A. Levy Yeyati. We acknowledge financial support by contract ANR-12-BS04-0016-MASH. Ç.Ö.G. was supported by the People Programme (Marie Curie Actions) of the European Union's Seventh Framework Programme (FP7/2007-2013) under REA grant agreement no. PIIF-GA-2011-298415, and L.T. by ECOS-SUD (France-Argentina) grant N° A11E04 and a scholarship from CONICET (Argentina).

Authors' contributions: C.J., M.F.G., H.P. and C.U. took part to all aspects of this work. L.T., L.B., Ç.Ö.G. and D.E. participated in the design of the experiment. M.S. and D.V. helped in setting up the microwave setup. L.T. and D.V. participated in running the experiment. All authors participated in interpreting the data and writing the manuscript.

References and Notes:

1. K. J. Franke, G. Schulze, and J. I. Pascual, Competition of Superconducting Phenomena and Kondo Screening at the Nanoscale. *Science* **332**, 940–944 (2011).
2. C. Caroli, P. G. de Gennes, and J. Matricon, Bound Fermion states on a vortex line in a type II superconductor. *Phys. Lett.* **9**, 307 (1964).
3. C. W. J. Beenakker and H. van Houten, Josephson current through a superconducting quantum point contact shorter than the coherence length. *Phys. Rev. Lett.* **66**, 3056 (1991).
4. M. A. Despósito and A. Levy Yeyati, Controlled dephasing of Andreev states in superconducting quantum point contacts. *Phys. Rev. B* **64**, 140511(R) (2001).
5. A. Zazunov, V. S. Shumeiko, E. N. Bratus', J. Lantz, & G. Wendin, Andreev Level Qubit. *Phys. Rev. Lett.* **90**, 087003 (2003).
6. Nikolai M. Chtchelkatchev and Yu. V. Nazarov, Andreev Quantum Dots for Spin Manipulation. *Phys. Rev. Lett.* **90**, 226806 (2003).
7. A. Zazunov, V. S. Shumeiko, G.Wendin, and E. N. Bratus', Dynamics and phonon-induced decoherence of Andreev level qubit. *Phys. Rev. B* **71**, 214505 (2005).
8. C. Padurariu and Yu. V. Nazarov, Spin blockade qubit in a superconducting junction. *Europhys. Lett.* **100**, 57006 (2012).
9. J.-D. Pillet *et al.*, Andreev bound states in supercurrent-carrying carbon nanotubes revealed. *Nature Phys.* **6**, 965 (2010).
10. M. Zgirski *et al.*, Evidence for Long-Lived Quasiparticles Trapped in Superconducting Point Contacts. *Phys. Rev. Lett.* **106**, 257003 (2011).
11. E. M. Levenson-Falk, F. Kos, R. Vijay, L. Glazman, and I. Siddiqi, Single-Quasiparticle Trapping in Aluminum Nanobridge Josephson Junctions. *Phys. Rev. Lett.* **112**, 047002 (2014).

12. A. Zazunov, A. Brunetti, A. Levy Yeyati, and R. Egger, Quasiparticle trapping, Andreev level population dynamics, and charge imbalance in superconducting weak links. *Phys. Rev. B* **90**, 104508 (2014).
13. L. Bretheau, Ç. Ö. Girit, H. Pothier, D. Esteve, & C. Urbina, Exciting Andreev pairs in a superconducting atomic contact. *Nature* **499**, 312 (2013).
14. L. Bretheau, Ç. Ö. Girit, C. Urbina, D. Esteve, and H. Pothier, Supercurrent Spectroscopy of Andreev States. *Phys. Rev. X* **3**, 041034 (2013).
15. E. Scheer, P. Joyez, D. Esteve, C. Urbina, and M. H. Devoret, Conduction Channel Transmissions of Atomic-Size Aluminum Contacts. *Phys. Rev. Lett.* **78**, 3535 (1997).
16. J. M. van Ruitenbeek *et al.*, Adjustable nanofabricated atomic size contacts. *Rev. Sci. Instrum.* **67**, 108 (1996).
17. C. Janvier *et al.*, Superconducting atomic contacts inductively coupled to a microwave resonator. *J. Phys.: Condens. Matter* **26**, 474208 (2014).
18. A. Wallraff *et al.*, Strong coupling of a single photon to a superconducting qubit using circuit quantum electrodynamics. *Nature* **431**, 162 (2004).
19. G. Romero, I. Lizuain, V. S. Shumeiko, E. Solano and F. S. Bergeret, Circuit quantum electrodynamics with a superconducting quantum point contact. *Phys. Rev. B* **85**, 180506 (2012).
20. Materials and methods are available as supplementary materials at the end of this file.
21. D. G. Olivares *et al.*, Dynamics of quasiparticle trapping in Andreev levels. *Phys. Rev. B* **89**, 104504 (2014).
22. R. Vijay, D. H. Slichter, and I. Siddiqi, Observation of Quantum Jumps in a Superconducting Artificial Atom. *Phys. Rev. Lett.* **106**, 110502 (2011).
23. M. Greenfeld, D.S. Pavlichin, H. Mabuchi, and D. Herschlag, Single Molecule Analysis Research Tool (SMART): An Integrated Approach for Analyzing Single Molecule Data. *PLoS ONE* **7**, e30024 (2012).
24. J. M. Martinis, M. Ansmann, and J. Aumentado, Energy Decay in Superconducting Josephson-Junction Qubits from Nonequilibrium Quasiparticle Excitations. *Phys. Rev. Lett.* **103**, 097002 (2009).
25. G. Catelani, R. J. Schoelkopf, M. H. Devoret, & L. I. Glazman, Relaxation and frequency shifts induced by quasiparticles in superconducting qubits. *Phys. Rev. B* **84**, 064517 (2011).
26. F. Kos, S. E. Nigg, and L. I. Glazman, Frequency-dependent admittance of a short superconducting weak link. *Phys. Rev. B* **87**, 174521 (2013).
27. I. M. Pop *et al.*, Coherent suppression of electromagnetic dissipation due to superconducting quasiparticles. *Nature* **508**, 369 (2014).
28. Chen Wang *et al.*, Measurement and Control of Quasiparticle Dynamics in a Superconducting Qubit. *Nature Communications* **5**, 5836 (2014).
29. Yu. Makhlin and A. Shnirman, Dephasing of Solid-State Qubits at Optimal Points, *Phys. Rev. Lett.* **92**, 178301 (2004).
30. John Clarke and Frank K. Wilhelm, Superconducting quantum bits. *Nature* **453**, 1031 (2008).
31. U. Vool *et al.*, Non-Poissonian Quantum Jumps of a Fluxonium Qubit due to Quasiparticle Excitations. *Phys. Rev. Lett.* **113**, 247001 (2014).
32. D. Ristè *et al.*, Millisecond charge-parity fluctuations and induced decoherence in a superconducting qubit. *Nature Communications* **4**, 1913 (2013).
33. P. J. de Visser *et al.*, Number Fluctuations of Sparse Quasiparticles in a Superconductor. *Phys. Rev. Lett.* **106**, 167004 (2011).

34. Chang, W., Manucharyan, V. E., Jespersen, T. S., Nygård, J. & Marcus, C. M. Tunneling spectroscopy of quasiparticle bound states in a spinful Josephson junction. *Phys. Rev. Lett.* **110**, 217005 (2013).
35. V. Mourik *et al.*, Signatures of Majorana fermions in hybrid superconductor-semiconductor nanowire devices. *Science* **336**, 1003 (2012).
36. D. Chevallier, P. Simon, and C. Bena, From Andreev bound states to Majorana fermions in topological wires on superconducting substrates: A story of mutation, *Phys. Rev. B* **88**, 165401 (2013).

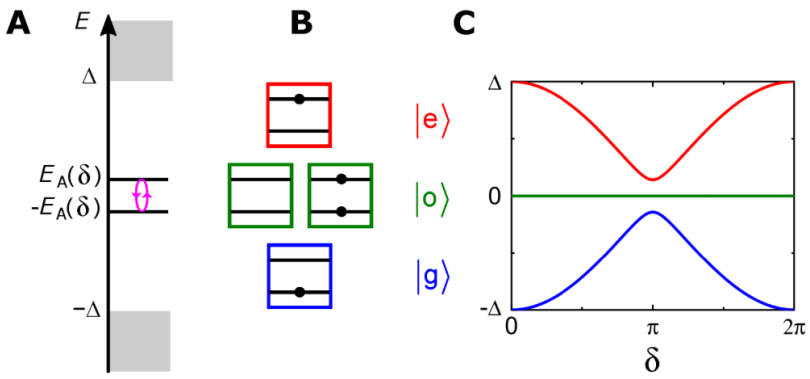

Fig.1 Single channel Andreev quantum dot. (**A**) Energy levels: Two discrete Andreev bound levels detach symmetrically from the upper and lower continua of states (light grey regions for $|E| > \Delta$). Photons of energy $2E_A$ can induce transitions between the two Andreev levels (magenta arrows). (**B**) Andreev levels occupation in the four possible quantum states of the Andreev dot. Only the lower Andreev level is occupied in the ground state $|g\rangle$ (blue box). In the excited state $|e\rangle$ (red box) only the upper Andreev bound level is occupied. In the doubly degenerate odd state $|o\rangle$ both Andreev levels are either occupied or empty. (**C**) Energy of the four Andreev dot states for a channel of transmission probability $\tau = 0.98$, as a function of the phase difference δ across the weak link.

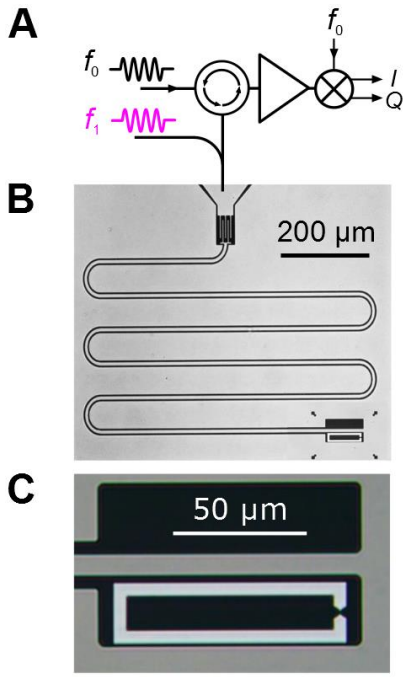

Fig.2. **Measurement setup of a superconducting atomic contact in a microwave resonator.** (**A**): Simplified 2-tone microwave setup. The measurement (frequency f_0) and drive (frequency f_1) signals are coupled to the resonator through the same port. After amplification the reflected signal at f_0 is homodyne detected by an IQ mixer and its two quadratures (I and Q) are digitized. (**B**): Optical micrograph of the $\lambda/4$ niobium coplanar meander resonator with an interdigitated capacitor $C \simeq 3\text{fF}$ at the coupling port. At the shorted end an aluminum loop is inductively coupled to the resonator field. The resonator has resonance frequency $f_R \simeq 10.134\text{GHz}$, with total quality factor $Q = 2200$, close to critical coupling (see Fig S4). (**C**): Detailed view of the aluminum loop. Upon bending the substrate the loop breaks at the narrow constriction to create an atomic contact.

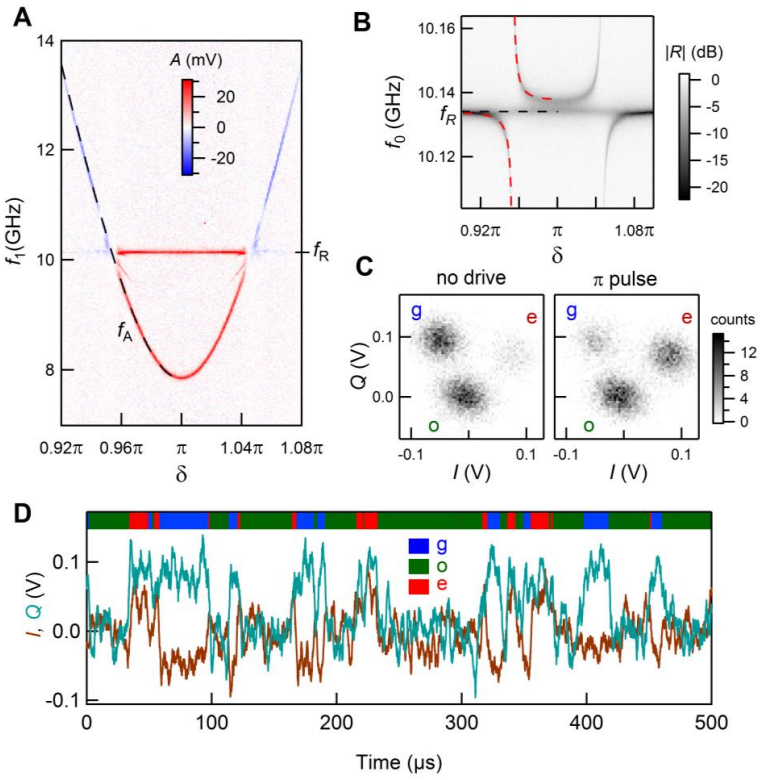

Fig. 3. Spectroscopy and quantum jumps. (**A**) Pulsed two-tone spectroscopy: color coded amplitude *A* of one quadrature of reflected signal as a function of δ and f_1. Dashed black line: theoretical fit of Andreev transition frequency $f_A = 2E_A/h$ with $\tau = 0.99217$. A parasitic line, corresponding to a two photon process ($2f_1 = f_R + f_A(\tau,\delta)$), is visible just below 10 GHz. (**B**) Single-tone continuous-wave spectroscopy using a vector network analyzer (average number of photons in resonator $\bar{n} \simeq 0.1$): resonator reflection amplitude $|R|$ as a function of δ and f_0. Red dashed curves: fits of the anti-crossings *(20)*. Data aligned with black dashed line correspond to the Andreev dot in state $|o\rangle$. (**C**) Histograms of *I*, *Q* quadratures at $\delta = \pi$ illustrate single-shot resolution of the quantum state of the dot. Left panel: no drive at f_1. Right panel: π–pulse transfering population from $|g\rangle$ to $|e\rangle$. (**D**)

Continuous measurement at $\delta = \pi$, with $\bar{n} \simeq 100$ and no driving signal. Brown (cyan) time trace corresponds to I (Q) quadrature. The color (blue, green, red) of the horizontal bar represents an estimate of the state (g, o, e) found using a hidden Markov Model toolbox (*23*).

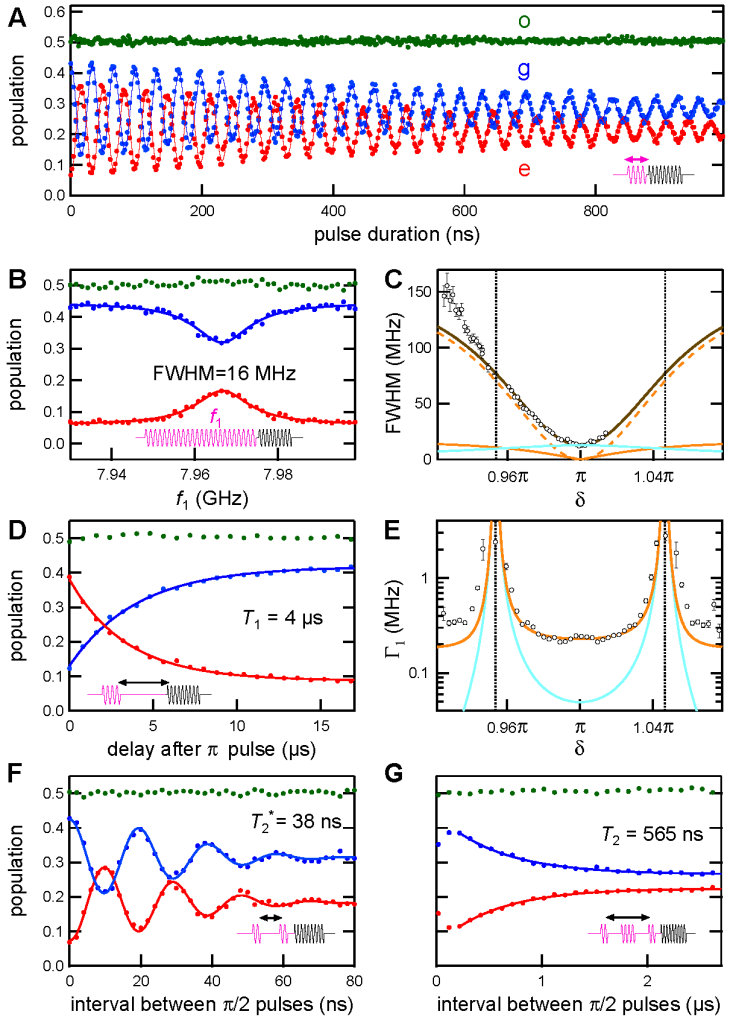

Fig. 4. Coherent manipulation of Andreev quantum dot states at $\delta = \pi$. Color dots show measured populations: ground (blue), excited (red) and odd (green) states. Lines are theoretical fits**.** Sketches of pulse sequences for each type of measurement are shown in each panel (magenta: drive; black: measurement). (**A**) Rabi oscillations: populations as a function

of the driving pulse duration. (**B**) Spectroscopy: populations as a function of driving pulse frequency f_1. (**C**) Phase dependence of linewidth (FWHM) of the spectral line. Dots: as extracted from a lorentzian fit of the experimental resonances (*20*). Black curve is best fit to the data, including the contributions of 1/f transmission noise (cyan line), and both 1/f (orange line) and white flux noise (orange dashed-line). Vertical dotted lines indicate phases for which $f_A = f_R$. (**D**) Relaxation of populations after a π driving pulse. (**E**) Phase dependence of relaxation rate $\Gamma_1 = 1/T_1$. Dots: experimental data. Continuous curve is the sum of the expected Purcell rate (dotted line) and an empirical phase independent rate (180 kHz). (**F**) Ramsey fringes: populations as a function of delay between the two $\pi/2$-pulses detuned at $f_1 = f_A(\tau,\pi) + 51\text{MHz}$. (**G**) Hahn echo: populations as a function of delay between the two $\pi/2$-pulses with a π-pulse in between.

Supplementary Materials

Materials and Methods

Theoretical description of the system

The Hamiltonian of the system can be written as $H = H_A + H_R + H_{AR}$, where the first term, the Andreev Hamiltonian, describes the atomic contact; the second one describes the electromagnetic resonator; and the third one accounts for the coupling between them. The Andreev Hamiltonian in the Andreev basis (*5*) is given by

$$H_A(\delta) = -E_A(\delta)\hat{\sigma}_z$$

where $\hat{\sigma}_z$ is a Pauli matrix acting in the $|g\rangle, |e\rangle$ space. The electromagnetic resonator is treated as a discrete single-mode oscillator described by

$$H_R = \hbar\omega_R(a^\dagger a + 1/2)$$

where $a^\dagger(a)$ are the creation (annihilation) photon operators. The term describing the coupling between the atomic contact and the resonator (up to first order) is given by

$$H_{AR} = M\,\hat{I}_R\,\hat{I}_A(\delta)$$

where M is the loop-resonator mutual inductance, $\hat{I}_R = \sqrt{\hbar\omega_0/2L}\left(a^\dagger + a\right)$ is the transmission line current operator at the position of the atomic contact loop and $\hat{I}_A(\delta)$ is the Andreev current operator

$$\hat{I}_A(\delta) = I_A(\delta,\tau)\left[\hat{\sigma}_z + \sqrt{1-\tau}\tan(\delta/2)\hat{\sigma}_x\right]$$

with $I_A(\delta,\tau) = -\varphi_0^{-1}\partial E_A(\delta,\tau)/\partial\delta$. As a result, in the region close to the degeneracy $hf_R = 2E_A$, where the rotating-wave approximation holds, the coupling Hamiltonian can be reduced to a Jaynes-Cummings model *(3)*

$$H_{AR} = \hbar g(\delta)\left(a\hat{\sigma}^+ + a^\dagger\hat{\sigma}^-\right)$$

where $\sigma^+ = |e\rangle\langle g|$ and $\sigma^- = |g\rangle\langle e|$. The phase dependent coupling energy $\hbar g(\delta)$ is given by

$$\hbar g(\delta) = \sqrt{z}\frac{\Delta}{2}\frac{E_A(\pi)}{E_A(\delta)}\tau\sin^2(\delta/2)$$

with $z = (M/L)^2\pi Z_0/R_Q$ a constant coupling parameter. Fitting the anti-crossing depicted in Fig. 3B we obtain $g(\pi)/2\pi = 95.6\ \text{MHz}$ and $z = 1.9\,10^{-5}$.

Relaxation rate through the resonator (Purcell effect)

Following Desposito and Yeyati (*4*) the relaxation rate due to the coupling to the environment can be estimated by using the expression

$$\Gamma_1 = \frac{\pi \Delta}{2\hbar} \frac{\mathrm{Re}\left[Z_{env}(\omega = 2E_A(\delta)\right]}{R_Q} \frac{(1-\tau)\left(\tau \sin^2\left(\delta/2\right)\right)^2}{\left(1-\tau \sin^2\left(\delta/2\right)\right)^{3/2}}.$$

In the phase region were T_1 was measured, the real part of the impedance seen from the atomic contact can be approximated by

$$\mathrm{Re}\left[Z_{env}\left(\omega\right)\right] = \frac{z R_Q}{\pi} \frac{Q}{1+\left(Q \frac{1-\left(\omega/\omega_0\right)^2}{\omega/\omega_0}\right)^2}$$

where Q and ω_0 are the total quality factor and the resonant frequency of the resonator far from the anti-crossing.

Fit of the resonances

In Fig. 4C, we compare with theory the measured linewidth of the Andreev resonance as a function of the phase. The experimental data were fitted with Lorentzian functions appropriate for white noise. However, for *1/f* noise theory predicts Gaussian resonances. The combination of the contributions of the three considered noise sources (*1/f* transmission noise, white and *1/f* flux noise) leads to a lineshape which is a convolution of a Lorentzian and a Gaussian function. In order to compare with experiment, we proceeded as for the experimental data and fitted the calculated resonance with a Lorentzian function on a 300 MHz interval, to extract a linewidth.

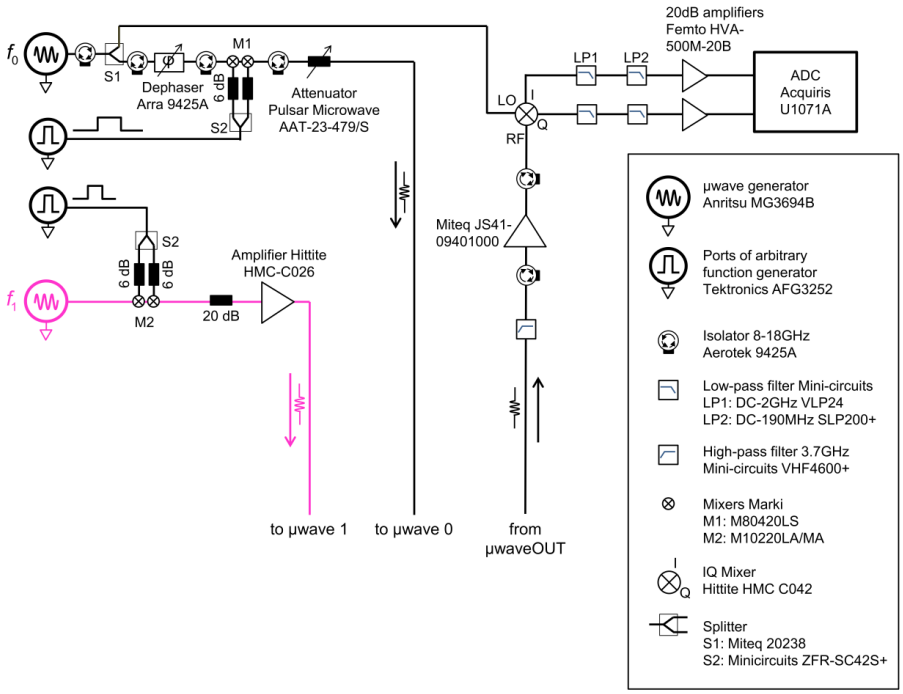

Fig. S1: Microwave setup at room temperature. There are two lines to inject driving ("µwave1") and measurement ("µwave0") pulses, and one line ("µwaveOUT") that carries the reflected signal at the measurement frequency. Microwave pulses are shaped by mixing continuous waves from the microwave sources with DC pulses from a 2-port arbitrary function generator. The latter and the acquisition board (ADC) are synchronized and triggered by an arbitrary waveform generator (Agilent AWG 33250, not represented). In order to improve the ON-OFF contrast of the microwave pulses, a second AWG (not represented) is used to pulse the f_1 microwave source itself**.**

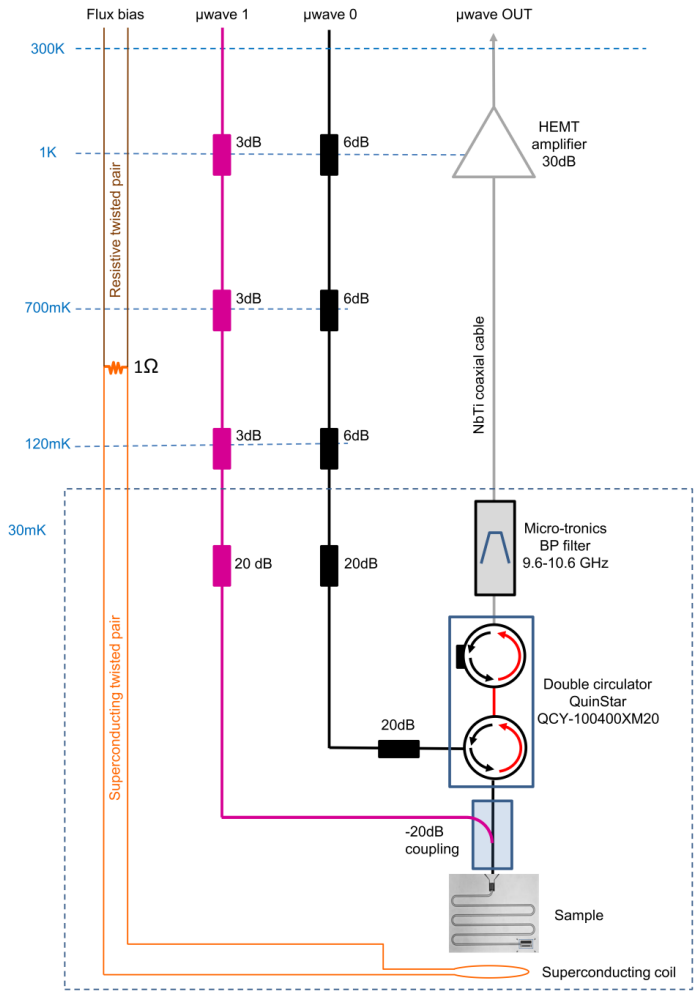

Fig. S2: Low temperature wiring. The three lines "µwave1", "µwave0" and "µwaveOUT" correspond to those of Fig. S1. The sample is enclosed in four shields: the inner one is made out of epoxy loaded with brass and carbon powder, the 2nd one out of aluminum, the 3rd one out of Cryoperm, the 4th one out of copper. The sample and the shields are thermally anchored to the mixing chamber of base temperature 30 mK. The cryogenic microwave amplifier is a commercial HEMT (CITCRYO1-12A-1 from Caltech) with nominal gain 32 dB and noise temperature 7 K at 10 GHz. A DC magnetic field is applied perpendicular to the chip using a small superconducting coil placed a few mm above the aluminum loop containing the atomic contact. Biasing is performed using a voltage source (iTest BILT BE2102) in series with a 200 kΩ resistor. Filtering is provided partly by a 1 Ω resistor placed at 0.7 K in parallel with the coil.

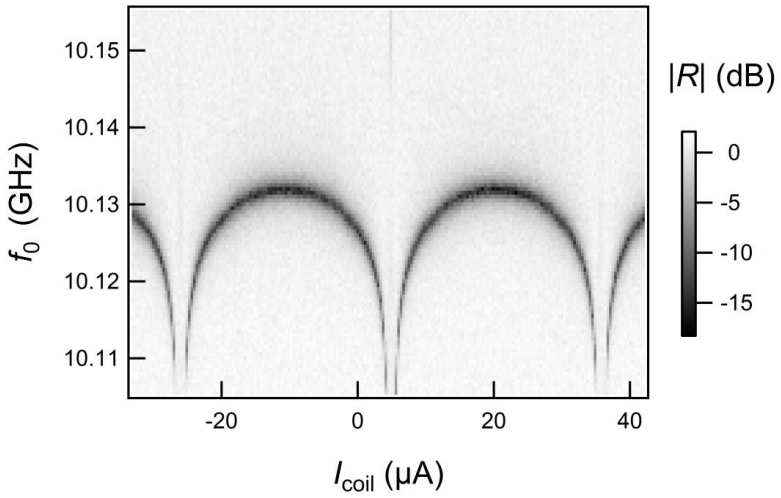

Fig. S3: Periodicity of VNA measurements with flux. Modulus $|R|$ of reflected signal as a function of the current $|I_{coil}|$ through the superconducting coil for a contact with several channels. The period allows calibrating the current associated with one flux quantum in the aluminum loop, i.e. with a 2π change in the phase δ across the contact. The currents at which the resonance frequency (dark) presents broad maxima correspond to $\delta = 0$ modulo 2π.

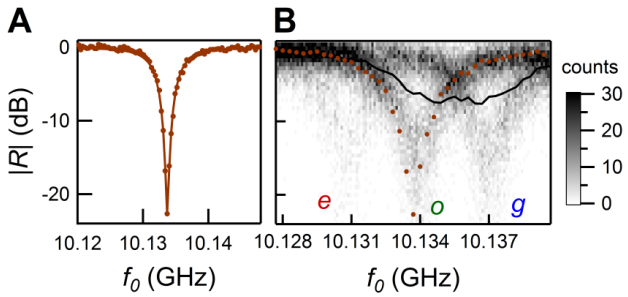

Fig. S4: Vector network analyser (VNA) measurements of the resonator for the contact with $\tau = 0.99217$ described in the manuscript. **(A)** Amplitude $|R|$ of reflexion coefficient as a function of the probe frequency f_0 when the resonator and the Andreev doublet are far detuned ($\delta = 0.9\pi$, $f_A \simeq 15.9\,\mathrm{GHz}$), corresponding to a vertical cut on the left edge of Fig. 3B**.** Symbols: measurement acquired at low power, corresponding to $\bar{n} \simeq 0.1$ photons in the resonator and a $10\,\mathrm{Hz}$ acquisition bandwidth. Solid line: fit using $|\mathrm{R}|^2 = 1 - \dfrac{1-q^{-1}}{Qx^2 + q/4}$ with $x = f_0 / f_R - 1$ and $q = Q_{ext}/Q$. The dip signals the resonance frequency $f_R \simeq 10.134\,\mathrm{GHz}$, with total quality factor $Q = 2200$ and external quality factor $Q_{ext} = 4800$ associated with the coupling capacitor. (**B**) $|R|$ measured at $\delta = \pi$. Black curve is taken at low power ($\bar{n} \simeq 0.1$ photons in resonator) and a $10\,\mathrm{Hz}$ acquisition bandwidth (corresponds to a cut in the middle of Fig. 3B). Image in the background is a two-dimensional histogram of 32000 data points taken in a single frequency sweep with a $600\,\mathrm{kHz}$ bandwidth, and a larger power ($\bar{n} \simeq 40$ at resonance). We observe three replicas of the resonance as measured at $\delta = 0.9\pi$ (brown symbols, same data as (A)). The central one corresponds to odd state $|o\rangle$**,** the rightmost to $|g\rangle$ and the leftmost (barely visible) to $|e\rangle$**.**

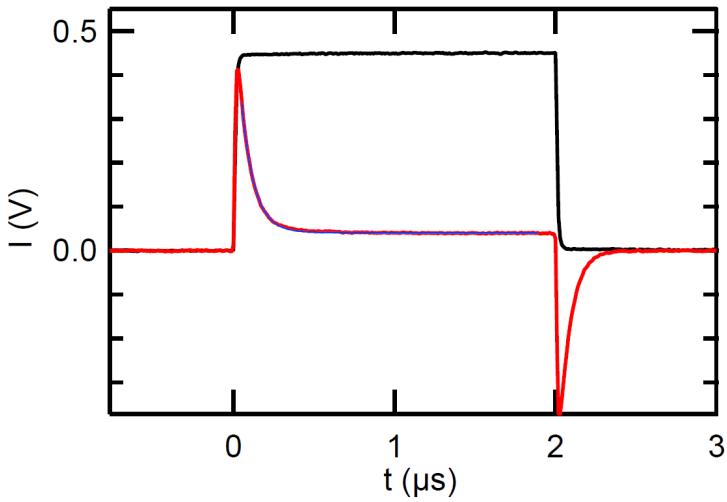

Fig. S5: Time-resolved response of the resonator to a 2 μs-long probe pulse. Black: 0.1 GHz-detuned pulse: complete reflection. Red: pulse at resonance frequency. After a loading time $2/\kappa$ of the cavity, wave exiting the cavity interferes destructively with reflected wave. The negative signal after t=2μs corresponds to photons exiting the cavity after the end of the pulse. Blue: exponential fit, with decay time $2/\kappa = 69$ ns. Total quality factor of the cavity is $Q = \omega/\kappa = 2200$ in agreement with fit of cavity resonance (see Fig. S4**A**).

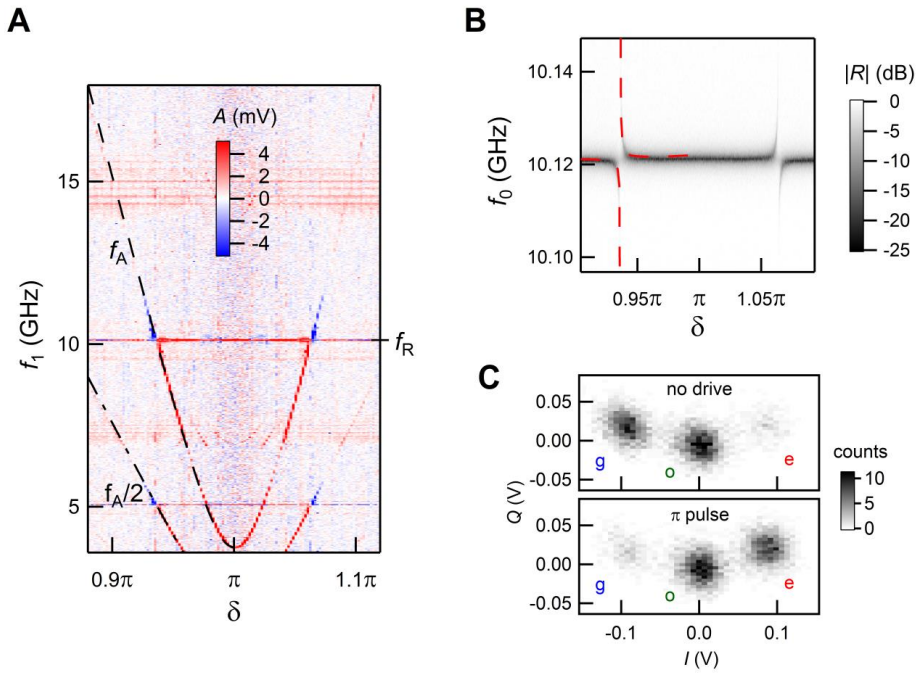

Fig. S6: Data for an atomic contact different from the one in the main text. **(A)** Pulsed two-tone spectroscopy: color coded amplitude *A* of one quadrature of reflected signal as a function of δ and f_1. Dashed black line: theoretical fit of Andreev transition frequency $f_A = 2E_A/h$ with $\tau = 0.99806$. Two-photon processes (dash-dotted line labelled $f_A/2$) are observed because a higher excitation power than the one used for Fig. 3. **(B)** Single-tone continuous-wave spectroscopy using a vector network analyzer ($\bar{n} \simeq 0.1$): resonator reflection amplitude $|R|$ as a function of δ and f_0. Red dashed curves: fits of the anti-crossings using $g(\pi)/2\pi = 72$ MHz. Compared to Fig. 3, this data was taken on a different cool-down of the sample, and the bare resonator frequency was 10.121 GHz. **(C)** Density plots of *I*, *Q* quadratures at $\delta = \pi$ illustrate single-shot resolution of the quantum state of the dot. Top panel: no drive at f_1. Bottom panel: π–pulse results in a population transfer from $|g\rangle$ to $|e\rangle$.

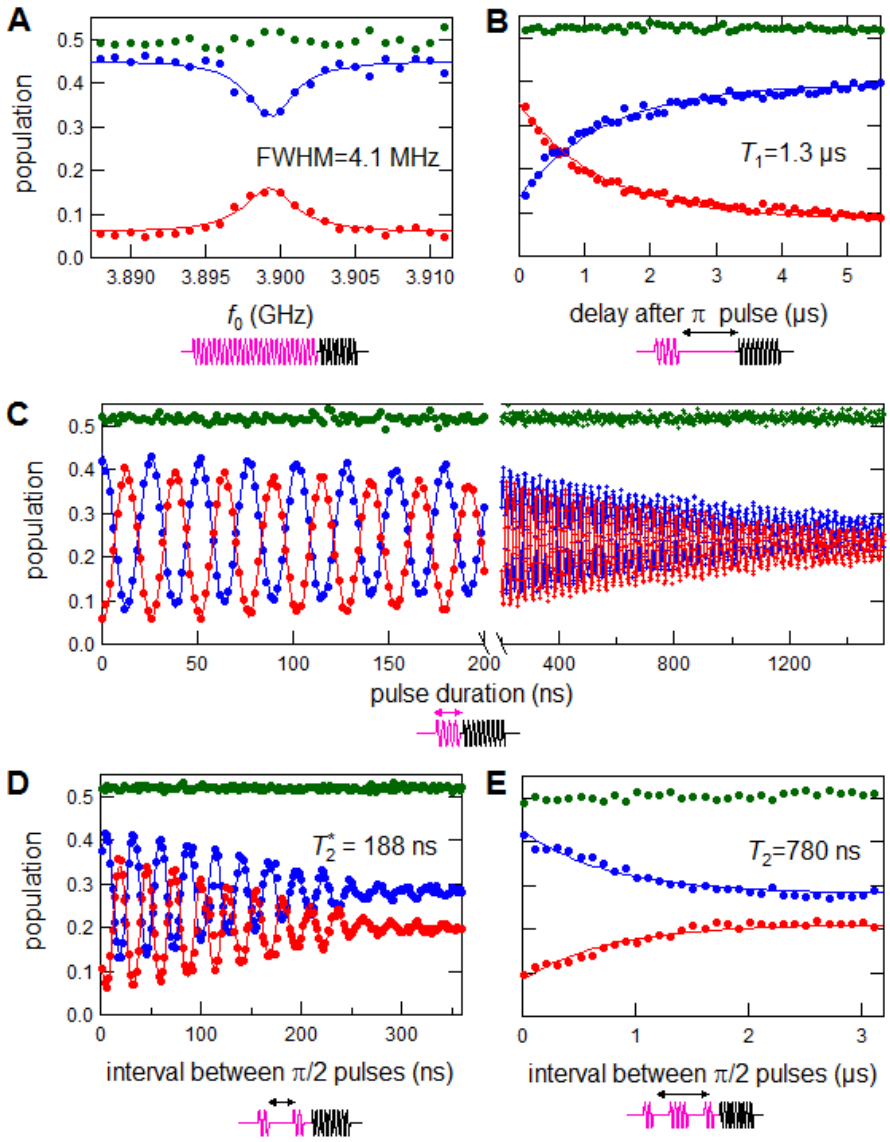

Fig. S7: Data for same contact as in Fig. S6, to be compared with Fig. 4. **(A)** Spectroscopy. **(B)** relaxation after a π-pulse. **(C)** Rabi oscillations (note break and change in scale of x-axis). **(D)** Ramsey fringes with 50 MHz detuning. **(E)** Hahn echo.

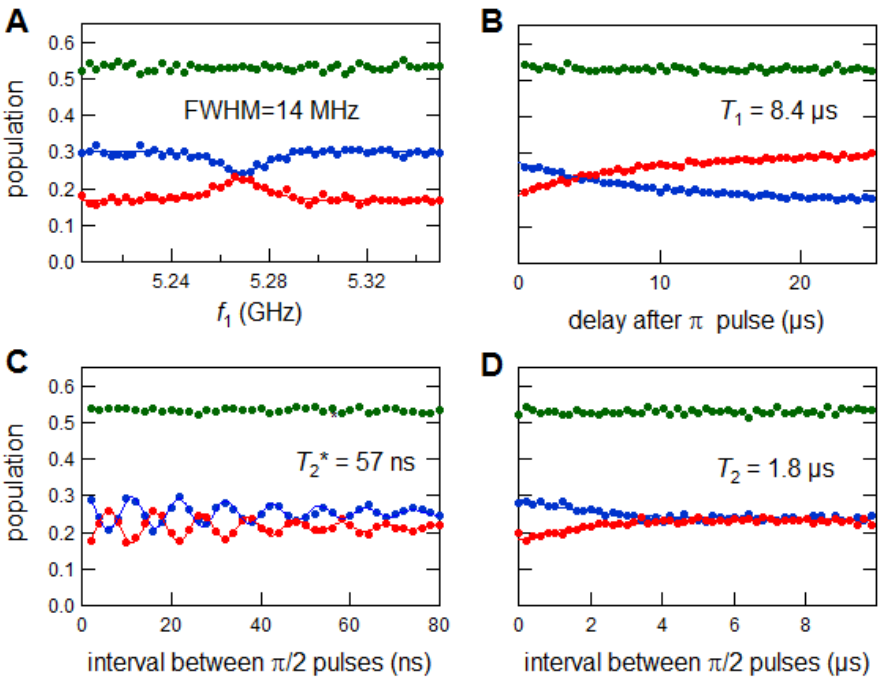

Fig. S8: Data for contact with channel transmission $\tau = 0.99647$, to be compared with Fig. 4. **(A)** Spectroscopy. **(B)** relaxation after a π-pulse. **(C)** Ramsey fringes with 95 MHz detuning. **(D)** Hahn echo.

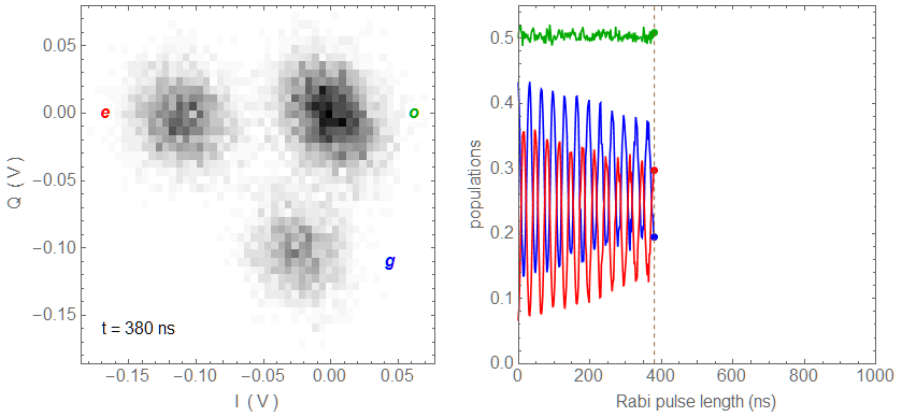

Fig. S9 (snapshot from Movie S1): (Left) Density plot of *I* and *Q* quadratures for a 380 ns-long Rabi pulse. (Right) Evolution of the populations of states $|g\rangle$ (blue), $|e\rangle$ (red) and $|o\rangle$ (green) for Rabi pulse lengths up to 380 ns.

Movie S1: (animated Gif image, available on the Science website) Rabi oscillations seen in the *I*,*Q* plane, and corresponding evolution of the populations: the populations of the ground state ($|g\rangle$) and the excited state ($|e\rangle$) swap, whereas the population of the odd state ($|o\rangle$) remains constant. Data correspond to Fig. 3C of paper, with a rotation in the *I*,*Q* plane.

Bibliography

[1] Holmes, D. S., Ripple, A. L. & Manheimer, M. A. Energy-efficient superconducting computing - power budgets and requirements. *IEEE Trans. Appl. Supercond.* **23**, 1701610 (2013). 1, 185

[2] Devoret, M. H. & Schoelkopf, R. J. Superconducting circuits for quantum information: an outlook. *Science* **339**, 1169 (2013). 1, 185

[3] Houck, A. A., Türeci, H. E. & Koch, J. On-chip quantum simulation with superconducting circuits. *Nat. Phys.* **8**, 292 (2012). 1

[4] Zmuidzinas, J. Superconducting microresonators: physics and applications. *Annu. Rev. Condens. Matter Phys.* **3**, 169 (2012). 1, 185

[5] Gol'tsman, G. N. *et al.* Picosecond superconducting single-photon optical detector. *Appl. Phys. Lett.* **79**, 705 (2001). 1, 185

[6] Josephson, B. Possible new effects in superconductive tunnelling. *Phys. Lett.* **1**, 251 (1962). 1, 185

[7] Andreev, A. F. The thermal conductivity of the intermediate state in superconductors. *Sov. Phys. JETP* **19**, 1228 (1964). 2, 186

[8] Beenakker, C. W. J. & Van Houten, H. Josephson current through a superconducting quantum point contact shorter than the coherence length. *Phys. Rev. Lett.* **66**, 3056 (1991). 2, 15, 17, 19, 186

[9] Cron, R. *Atomic contacts: a test-bed for mesoscopic physics*. Ph.D. thesis, Université Pierre et Marie Curie - Paris VI (2001). URL https://tel.archives-ouvertes.fr/tel-00001329v1. 2, 186

[10] Chauvin, M. *Josephson effect in atomic contacts*. Ph.D. thesis, Université Pierre et Marie Curie - Paris VI (2005). URL https://tel.archives-ouvertes.fr/tel-00107465v2. 2, 23, 186

[11] Huard, B. *Interactions between electrons, mesoscopic Josephson effect and asymmetric current fluctuations*. Ph.D. thesis, Université Pierre et Marie Curie - Paris VI (2006). URL https://tel.

archives-ouvertes.fr/tel-00119371v1. 2, 22, 186

[12] Le Masne, Q. *Asymmetric current fluctuations and Andreev states probed with a Josephson junction.* Ph.D. thesis, Université Pierre et Marie Curie - Paris VI (2009). URL https://tel.archives-ouvertes.fr/tel-00482483v1. 2, 186

[13] Zazunov, A., Shumeiko, V. S., Bratus, E. N., Lantz, J. & Wendin, G. Andreev level qubit. *Phys. Rev. Lett.* **90**, 087003 (2003). 2, 3, 18, 30, 41, 151, 186, 187

[14] Zazunov, A., Shumeiko, V. S., Wendin, G. & Bratus;, E. N. Dynamics and phonon-induced decoherence of Andreev level qubit. *Phys. Rev. B* **71**, 214505 (2005). 2, 26, 27, 41, 92, 186

[15] Padurariu, C. & Nazarov, Y. V. Spin blockade qubit in a superconducting junction. *Europhys. Lett.* **100**, 57006 (2012). 2, 186

[16] Bretheau, L. *Localized excitations in superconducting atomic contacts: probing the Andreev doublet.* Ph.D. thesis, Ecole Polytechnique X (2013). URL https://tel.archives-ouvertes.fr/pastel-00862029v1. 2, 8, 16, 25, 93, 94, 186, 192

[17] Pillet, J.-D. *Tunneling spectroscopy of the Andreev Bound States in a Carbon Nanotube.* Ph.D. thesis, Université Pierre et Marie Curie - Paris VI (2011). URL https://tel.archives-ouvertes.fr/tel-00833472v1. 2, 22, 24, 186

[18] Lee, E. J. H. *et al.* Spin-resolved Andreev levels and parity crossings in hybrid superconductor-semiconductor nanostructures. *Nat. Nanotechnol.* **9**, 79 (2014). 2, 186

[19] Chiodi, F. *et al.* Probing the dynamics of Andreev states in a coherent Normal/Superconducting ring. *Sci. Rep.* **1** (2011). 2, 186

[20] Dassonneville, B., Ferrier, M., Guéron, S. & Bouchiat, H. Dissipation and supercurrent fluctuations in a diffusive normal-metal-superconductor ring. *Phys. Rev. Lett.* **110**, 217001 (2013). 2, 24, 186

[21] Agraït, N., Yeyati, A. L. & van Ruitenbeek, J. M. Quantum properties of atomic-sized conductors. *Phys. Rep.* **377** (2003). 2, 4, 51, 52, 186, 189

[22] Haroche, S. & Raimond, J.-M. *Exploring the quantum: atoms, cavities, and photons* (Oxford University Press, Exploring the quantum: atoms, cavities, and photons, 2010). 2, 158

[23] Blais, A., Huang, R.-S., Wallraff, A., Girvin, S. M. & Schoelkopf, R. J. Cavity quantum electrodynamics for superconducting electrical circuits: An architecture for quantum computation. *Phys. Rev. A* **69**, 62320 (2004). 2, 5, 34, 40, 43, 45, 59, 161, 186, 190

[24] Chiorescu, I. *et al.* Coherent dynamics of a flux qubit coupled to a harmonic oscillator. *Nature* **431**, 159 (2004). 2

[25] Wallraff, A. *et al.* Strong coupling of a single photon to a superconducting qubit using circuit quantum electrodynamics. *Nature* **431**, 162 (2004). 2, 30, 59

[26] Kubo, Y. *et al.* Strong coupling of a spin ensemble to a superconducting resonator. *Phys. Rev. Lett.* **105**, 140502 (2010). 2

[27] Petersson, K. D. *et al.* Circuit quantum electrodynamics with a spin qubit. *Nature* **490**, 380 (2012). 2

[28] Viennot, J. J., Dartiailh, M. C., Cottet, A. & Kontos, T. Coherent coupling of a single spin to microwave cavity photons. *Science* **349**, 408 (2015). 2, 34, 151

[29] Frey, T. *et al.* Dipole coupling of a double quantum dot to a microwave eesonator. *Phys. Rev. Lett.* **108**, 046807 (2012). 2

[30] Bochmann, J., Vainsencher, A., Awschalom, D. D. & Cleland, A. N. Nanomechanical coupling between microwave and optical photons. *Nat. Phys.* **9**, 712 (2013). 2

[31] Chtchelkatchev, N. M. & Nazarov, Y. V. Andreev quantum dots for spin manipulation. *Phys. Rev. Lett.* **90**, 226806 (2003). 3, 15, 187

[32] Lantz, J., Shumeiko, V. S., Bratus, E. & Wendin, G. Flux qubit with a quantum point contact. *Phys. C Supercond. its Appl.* **368**, 315 (2002). 4, 188

[33] Devoret, M., Wallraff, A. & Martinis, J. Superconducting qubits: A short review. *arXiv* (2004). 3

[34] Scheer, E., Joyez, P., Esteve, D., Urbina, C. & Devoret, M. Conduction channel transmissions of atomic-size aluminum contacts. *Phys. Rev. Lett.* **78**, 3535 (1997). 4, 5, 22, 70, 72, 73, 94, 97, 170, 189

[35] Gimzewski, J. K. & Möller, R. Transition from the tunneling regime to point contact studied using scanning tunneling microscopy. *Phys. Rev. B* **36**, 1284 (1987). 4, 189

[36] Trouwborst, M. L., Van Der Molen, S. J. & Van Wees, B. J. The role of Joule heating in the formation of nanogaps by electromigration. *J. Appl. Phys.* **99**, 114316 (2006). 4, 189

[37] Zhou, C., Muller, C. J., Deshpande, M. R., Sleight, J. W. & Reed, M. A. Microfabrication of a mechanically controllable break junction in silicon. *Appl. Phys. Lett.* **67**, 1160 (1995). 4, 52, 189

[38] van Ruitenbeek, J. M. *et al.* Adjustable nanofabricated atomic size contacts. *Rev. Sci. Instrum.* **67**, 108 (1996). 4, 52, 189

[39] Romero, G., Lizuain, I., Shumeiko, V. S., Solano, E. & Bergeret, F. S. Circuit quantum electrodynamics with a superconducting quantum point contact. *Phys. Rev. B* **85**, 180506 (2012). 5, 40, 190

[40] Paik, H. *et al.* Observation of high coherence in Josephson junction qubits measured in a three-dimensional circuit QED architecture. *Phys. Rev. Lett.* **107**, 240501 (2011). 9, 31, 115, 152

[41] Stern, M. *et al.* Flux qubits with long coherence times for hybrid quantum circuits. *Phys. Rev. Lett.* **113**, 123601 (2014). 9, 30, 31, 98, 152

[42] Gambetta, J. *et al.* Quantum trajectory approach to circuit QED: Quantum jumps and the Zeno effect. *Phys. Rev. A* **77**, 012112 (2008). 11, 48, 195

[43] Schuster, D. I. *et al.* Resolving photon number states in a superconducting circuit. *Nature* **445**, 515 (2007). 11, 195

[44] Zgirski, M. *et al.* Evidence for long-lived quasiparticles trapped in superconducting point contacts. *Phys. Rev. Lett.* **106**, 257003 (2011). 11, 26, 27, 135, 196

[45] Naaman, O. & Aumentado, J. Time-domain measurements of quasiparticle tunneling rates in a single-Cooper-pair transistor. *Phys. Rev. B* **73**, 172504 (2006). 11, 196

[46] Stone, K. J. *et al.* Real time quasiparticle tunneling measurements on an illuminated quantum capacitance detector. *Appl. Phys. Lett.* **100**, 263509 (2012). 11, 196

[47] Vool, U. *et al.* Non-poissonian quantum jumps of a fluxonium qubit due to quasiparticle excitations. *Phys. Rev. Lett.* **113**, 247001 (2014). 11, 135, 149, 196

[48] Martinis, J. M., Ansmann, M. & Aumentado, J. Energy decay in superconducting Josephson-junction qubits from nonequilibrium quasiparticle excitations. *Phys. Rev. Lett.* **103**, 097002 (2009). 11, 196

[49] Pop, I. M. *et al.* Coherent suppression of electromagnetic dissipation due to superconducting quasiparticles. *Nature* **508**, 369 (2014). 11, 135, 196

[50] Joyez, P., Lafarge, P., Filipe, A., Esteve, D. & Devoret, M. H. Observation of parity-induced suppression of Josephson tunneling in the superconducting single electron transistor. *Phys. Rev. Lett.* **72**, 2458 (1994). 11, 135, 196

[51] Shaw, M. D., Lutchyn, R. M., Delsing, P. & Echternach, P. M. Kinetics of nonequilibrium quasiparticle tunneling in superconducting charge qubits. *Phys. Rev. B* **78**, 024503 (2008). 11, 135, 196

[52] Wenner, J. *et al.* Excitation of superconducting qubits from hot nonequilibrium quasiparticles. *Phys. Rev. Lett.* **110**, 150502 (2013). 11, 135, 196

[53] Greenfeld, M., Pavlichin, D. S., Mabuchi, H. & Herschlag, D. Single molecule analysis research tool (SMART): An integrated approach for analyzing single molecule data. *PLoS One* **7**, e30024 (2012). 12, 138, 179, 182, 197

[54] Gammelmark, S., Molmer, K., Alt, W., Kampschulte, T. & Meschede, D. Hidden Markov model of atomic quantum jump dynamics in an optically probed cavity. *Phys. Rev. A* **89**, 043839 (2014). 12, 197

[55] Koops, M. C., van Duyneveldt, G. V. & de Bruyn Ouboter, R. Direct observation of the current-phase relation of an adjustable superconducting point contact. *Phys. Rev. Lett.* **77**, 2542 (1996). 20

[56] Della Rocca, M. L. *et al.* Measurement of the current-phase relation of superconducting atomic contacts. *Phys. Rev. Lett.* **99**, 127005 (2007). 21

[57] Basset, J. *et al.* Joint measurement of current-phase relations and transport properties of hybrid junctions using a three junctions superconducting quantum interference device. *J. Appl. Phys.* **116**, 024311 (2014). 21

[58] Delagrange, R. *et al.* 0-pi quantum transition in a carbon nanotube Josephson junction: universal phase dependence and orbital degeneracy. *Phys. Rev. B* **93**, 195437 (2016). 21

[59] Murani, A., Deblock, R., Guéron, S. & Bouchiat, H. CPR in Bi nanowires. *Priv. Commun.* (2016). 21

[60] Yokoyama, T., Eto, M. & Nazarov, Y. V. Anomalous Josephson effect induced by spin-orbit interaction and Zeeman effect in semiconductor nanowires. *Phys. Rev. B* **89**, 195407 (2014). 21

[61] Klapwijk, T., Blonder, G. & Tinkham, M. Explanation of subharmonic energy gap structure. *Phys. B* **109 &110**, 1657 (1982). 22

[62] Landau, L. D. A theory of energy transer II. *Phys.Z. Sowjetunion* **2**, 46 (1932). 22

[63] Zener, C. Non-adiabatic crossing of energy levels. *Proc. R. Soc A.* **137**, 696 (1932). 22

[64] Chauvin, M. *et al.* Crossover from Josephson to multiple Andreev reflection currents in atomic contacts. *Phys. Rev. Lett.* **99**, 067008 (2007). 22

[65] Lee, E. J. H. *et al.* Zero-bias anomaly in a nanowire quantum dot coupled to superconductors. *Phys. Rev. Lett.* **109**, 186802 (2012). 22

[66] Dirks, T. *et al.* Transport through Andreev bound states in a graphene quantum dot. *Nat. Phys.* **7**, 25 (2010). 22

[67] Deacon, R. S. *et al.* Tunneling spectroscopy of Andreev energy levels in a quantum dot coupled to a superconductor. *Phys. Rev. Lett.* **104**, 076805 (2010). 22

[68] Bretheau, L., Girit, Ç. Ö., Pothier, H., Esteve, D. & Urbina, C. Exciting Andreev pairs in a superconducting atomic contact. *Nature* **499**, 312 (2013). 23

[69] Edstam, J. & Olsson, H. K. Josephson broadband spectroscopy to 1 THz. *Appl. Phys. Lett.* **64**, 2733 (1994). 23

[70] Devoret, M. H. *et al.* Effect of the Electromagnetic Environment on the Coulomb Blockade in Ultrasmall Tunnel Junctions. *Phys. Rev. Lett.* **64**, 4559 (1990). 23

[71] Geresdi, A. Private communication (2016). 24, 153

[72] Olivares, D. G. *et al.* Dynamics of quasiparticle trapping in Andreev levels. *Phys. Rev. B* **89**, 104504 (2014). 26, 135, 136, 143, 145

[73] Levenson-Falk, E. M., Kos, F., Vijay, R., Glazman, L. & Siddiqi, I. Single-quasiparticle trapping in aluminum nanobridge Josephson junctions. *Phys. Rev. Lett.* **112**, 047002 (2014). 26

[74] Higginbotham, A. P. *et al.* Parity lifetime of bound states in a proximitized semiconductor nanowire. *Nat. Phys.* **11**, 1017 (2015). 26

[75] Golubov, A. A., Kupriyanov, M. Y. & Il'ichev, E. The current-phase relation in Josephson junctions. *Rev. Mod. Phys.* **76**, 411 (2004). 27

[76] Tinkham, M. *Introduction to superconductivity: second edition* (Dover Publications, New York, 2004). 27, 29

[77] Anthore, A. *Decoherence mechanisms in mesoscopic conductors.* Ph.D. thesis, Université Pierre et Marie Curie - Paris VI (2003). URL https://tel.archives-ouvertes.fr/tel-00003518v1. 28, 93

[78] Martinis, J. M., Nam, S., Aumentado, J. & Urbina, C. Rabi oscillations in a large Josephson-junction qubit. *Phys. Rev. Lett.* **89**, 117901 (2002). 30

[79] Nakamura, Y., Pashkin, Y. A. & Tsai, J. S. Coherent control of macroscopic quantum states in a single-Cooper-pair box. *Nature* **398**, 786 (1999). 30

[80] Vion, D. *et al.* Manipulating the quantum state of an electrical circuit. *Science* **296**, 886 (2002). 30, 31

[81] Mooij, J. E., Orlando, T. P., Levitov, L. & Tian, L. Josephson persistent-current qubit. *Science* **285**, 1036 (1999). 30, 31

[82] Chiorescu, I., Nakamura, Y., Harmans, C. J. P. M. & Mooij, J. E. Coherent quantum dynamics of a superconducting flux qubit. *Science* **299**, 1869 (2003). 30, 31

[83] Koch, J. *et al.* Charge-insensitive qubit design derived from the Cooper pair box. *Phys. Rev. A* **76**, 042319 (2007). 31

[84] Rigetti, C. *et al.* Superconducting qubit in a waveguide cavity with a coherence time approaching 0.1 ms. *Phys. Rev. B* **86**, 100506 (2012). 31

[85] Jeffrey, E. *et al.* Fast accurate state measurement with superconducting qubits. *Phys. Rev. Lett.* **112**, 190504 (2014). 31, 47

[86] De Lange, G. *et al.* Realization of microwave quantum circuits using hybrid superconducting-semiconducting nanowire Josephson elements. *Phys. Rev. Lett.* **115**, 127002 (2015). 31

[87] Larsen, T. W. *et al.* Semiconductor-nanowire-based superconducting qubit. *Phys. Rev. Lett.* **115**, 127001 (2015). 31

[88] Kelly, J. *et al.* State preservation by repetitive error detection in a superconducting quantum circuit. *Nature* **519**, 66 (2015). 34, 59

[89] Bylander, J. *et al.* Noise spectroscopy through dynamical decoupling with a superconducting flux qubit. *Nat. Phys.* **7**, 565 (2011). 34, 98, 99, 100, 103

[90] Deléglise, S. *et al.* Reconstruction of non-classical cavity field states with snapshots of their decoherence. *Nature* **455**, 510 (2008). 34

[91] Pozar, D. M. *Microwave Engineering* (Wiley, New York, 2004), 3 edn. 34, 38

[92] Megrant, A. *et al.* Planar superconducting resonators with internal quality factors above one million. *Appl. Phys. Lett.* **100**, 113510 (2012). 36

[93] Matthaei, G., Young, L. & Jones, E. *Microwave filters, impedance-matching networks, and coupling structures* (Artech House, Dedham, 1980). 37

[94] Jaynes, E. T. & Cummings, F. W. Comparison of quantum and semiclassical radiation theories with application to the beam maser. *Proc. IEEE* **51**, 89 (1963). 40

[95] Omelyanchouk, A. N., Shevchenko, S. N., Greenberg, Y. S., Astafiev, O. & Il'ichev, E. Quantum behavior of a flux qubit coupled to a resonator. *Low Temp. Phys.* **36**, 893 (2010). 41

[96] Schmitt, V. *et al.* Multiplexed readout of transmon qubits with Josephson bifurcation amplifiers. *Phys. Rev. A* **90**, 062333 (2014). 47

[97] Palacios-Laloy, A. *Superconducting qubit in a resonator : test of the Leggett-Garg inequality and single-shot readout.* Ph.D. thesis, Université Paris 6 (2010). URL https://tel.archives-ouvertes.fr/tel-00815078v1. 48

[98] Moreland, J. & Ekin, J. W. Electron tunneling experiments using Nb-Sn "break" junctions. *J. Appl. Phys.* **58**, 3888 (1985). 51

[99] Bretheau, L. *et al.* Superconducting quantum point contacts. *Comptes Rendus Phys.* **13**, 89 (2012). 52

[100] Cleland, A. N. *Foundations of Nanomechanics* (Springer, Berlin Heidelberg, 2003). 53, 170, 171

[101] DuPont. Summary of properties for Kapton polyimide films. Tech. Rep. (2014). URL http://www.dupont.com/content/dam/dupont/products-and-services/membranes-and-films/polyimde-films/documents/DEC-Kapton-summary-of-properties.pdf. 55

[102] Simons, R. *Coplanar waveguide circuits, components, and systems*, vol. 7 (2001). 58

[103] Sandberg, M. *et al.* Radiation-suppressed superconducting quantum bit in a planar geometry. *Appl. Phys. Lett.* **102** (2013). 59

[104] Gevorgian, S. S., Martinsson, T., Linnér, P. L. J. & Kollberg, E. L. CAD models for multilayered substrate interdigital capacitors. *IEEE Trans. Microw. Theory Tech.* **44**, 896 (1996). 60

[105] Ithier, G. *et al.* Decoherence in a superconducting quantum bit circuit. *Phys. Rev. B* **72**, 134519 (2005). 87, 91, 96, 98, 108

[106] Cohen-Tannoudji, C., Diu, B. & Laloë, F. *Quantum mechanics Vol.1*. Quantum mechanics (Wiley, New York, 1977). 90

[107] Despósito, M. A. & Levy Yeyati, A. Controlled dephasing of Andreev states in superconducting quantum point contacts. *Phys. Rev. B* **64**, 140511 (2001). 94

[108] Carr, H. Y. & Purcell, E. M. Effects of diffusion on free precession in nuclear magnetic resonance experiments. *Phys. Rev.* **94**, 630 (1954). 99

[109] Meiboom, S. & Gill, D. Modified spin-echo method for measuring nuclear relaxation times. *Rev. Sci. Instrum.* **29**, 688 (1958). 99

[110] Cywiński, Ł., Lutchyn, R. M., Nave, C. P. & Das Sarma, S. How to enhance dephasing time in superconducting qubits. *Phys. Rev. B* **77**, 174509 (2008). 99

[111] Lasic, S., Stepisnik, J. & Mohoric, A. Displacement power spectrum measurement by CPMG in constant gradient. *J. Magn. Reson.* **182**, 208 (2006). 99

[112] Kumar, P. *et al.* Origin and suppression of 1/f magnetic flux noise. *Arxiv* (2016). 109

[113] Koch, R. H. *et al.* Flicker (1/f) noise in tunnel junction dc SQUIDS. *J. Low Temp. Phys.* **51**, 207 (1983). 108

[114] Makhlin, Y. & Shnirman, A. Dephasing of solid-state qubits at optimal points. *Phys. Rev. Lett.* **92**, 178301 (2004). 109

[115] Wynands, R. & Weyers, S. Atomic fountain clocks. *Metrologia* **42**, S64 (2005). 111, 112

[116] Glauber, R. J. Coherent and incoherent states of the radiation field. *Phys. Rev.* **131**, 2766 (1963). 120

[117] Geerlings, K. *et al.* Demonstrating a driven reset protocol for a superconducting qubit. *Phys. Rev. Lett.* **110**, 120501 (2013). 121

[118] Johansson, J. R., Nation, P. D. & Nori, F. QuTiP: An open-source Python framework for the dynamics of open quantum systems. *Comput. Phys. Commun.* **183**, 1760 (2012). 127

[119] Johansson, J. R., Nation, P. D. & Nori, F. QuTiP 2: A Python framework for the dynamics of open quantum systems. *Comput. Phys. Commun.* **184**, 1234 (2013). 127

[120] Boissonneault, M., Gambetta, J. M. & Blais, A. Dispersive regime of circuit QED: Photon-dependent qubit dephasing and relaxation rates. *Phys. Rev. A* **79**, 013819 (2009). 134

[121] Nagourney, W., Sandberg, J. & Dehmelt, H. Shelved optical electron amplifier: Observation of quantum jumps. *Phys. Rev. Lett.* **56**, 2797 (1986). 135

[122] Delteil, A., Gao, W. B., Fallahi, P., Miguel-Sanchez, J. & Imamoglu, A. Observation of quantum jumps of a single quantum dot spin using submicrosecond single-shot optical readout. *Phys. Rev. Lett.* **112**, 116802 (2014). 135

[123] Vijay, R., Slichter, D. H. & Siddiqi, I. Observation of quantum jumps in a superconducting artificial atom. *Phys. Rev. Lett.* **106**, 110502 (2011). 135

[124] Zazunov, A., Brunetti, A., Yeyati, A. L. & Egger, R. Quasiparticle trapping, Andreev level population dynamics, and charge imbalance in superconducting weak links. *Phys. Rev. B* **90**, 104508 (2014). 136

[125] Zhu, G., Ferguson, D. G., Manucharyan, V. E. & Koch, J. Circuit QED with fluxonium qubits: Theory of the dispersive regime. *Phys. Rev. B* **87**, 024510 (2013). 149

[126] Vool, U. *et al.* Suplementary material: Non-poissonian quantum jumps of a fluxonium qubit due to quasiparticle excitations. *Phys. Rev. Lett.* **113** (2014). 149

[127] Roch, N. *et al.* Widely tunable, nondegenerate three-wave mixing microwave device operating near the quantum limit. *Phys. Rev. Lett.* **108**, 147701 (2012). 150, 153

[128] Delbecq, M. R. *et al.* Photon-mediated interaction between distant quantum dot circuits. *Nat. Commun.* **4**, 1400 (2013). 151

[129] Ranjan, V. *et al.* Clean carbon nanotubes coupled to superconducting impedance-matching circuits. *Nat. Commun.* **6**, 7165 (2015). 151

[130] Dewes, A. *Demonstrating quantum speed-up with a two-transmon quantum processor*. Ph.D. thesis, Université Pierre et Marie Curie - Paris VI (2012). URL https://tel.archives-ouvertes.fr/tel-00857654v1. 152

[131] Dappe, Y., Urbina, C., Janvier, C., Pothier, H. & Goffman, M. Transmission fluctuations in an atomic junction : an atomistic study. *Unpublished* (2016). 152

[132] Riwar, R.-P., Houzet, M., Meyer, J. S. & Nazarov, Y. V. Multi-terminal Josephson junctions as topological materials. *Nat. Commun.* **7** (2015). 153

[133] Chang, W. *et al.* Hard gap in epitaxial semiconductor-superconductor nanowires. *Nat. Nanotechnol.* **10**, 232 (2015). 153

[134] Albrecht, S. M. *et al.* Exponential protection of zero modes in majorana islands. *Nature* **531**, 206 (2016). 153

[135] Li, C. *et al.* Magnetic field resistant quantum interferences in Josephson junctions based on bismuth nanowires. *Phys. Rev. B* **90**, 245427 (2014). 153

[136] Van Wees, B. J. *et al.* Quantized conductance of point contacts in a two-dimensional electron gas. *Phys. Rev. Lett.* **60**, 848 (1988). 154

[137] Kjaergaard, M. *et al.* Transparent semiconductor-superconductor interface and induced Gap in an epitaxial heterostructure Josephson junction. *Arxiv* (2016). 154

[138] Béri, B., Bardarson, J. H. & Beenakker, C. W. J. Splitting of Andreev levels in a Josephson junction by spin-orbit coupling. *Phys. Rev. B* **77**, 045311 (2008). 154

[139] Reynoso, A. A., Usaj, G., Balseiro, C. A., Feinberg, D. & Avignon, M. Spin-orbit-induced chirality of Andreev states in Josephson junctions. *Phys. Rev. B* **86**, 214519 (2012). 154

[140] Fu, L. & Kane, C. L. Superconducting proximity effect and majorana fermions at the surface of a topological insulator. *Phys. Rev. Lett.* **100**, 096407 (2008). 154

[141] Lutchyn, R. M., Sau, J. D. & Das Sarma, S. Majorana fermions and a topological phase transition in semiconductor-superconductor heterostructures. *Phys. Rev. Lett.* **105**, 077001 (2010). 154

[142] Rabiner, L. & Juang, B. An introduction to hidden Markov models. *IEEE ASSP Mag.* **3**, 4 (1986). 179, 180

[143] Dugad, R. & Desai, U. B. A tutorial on hidden Markov models. doi:10.1.1.27.3772. Tech. Rep. (1996). 179

Index

ÉCOLE DOCTORALE
Physique en Île-de-France (EDPIF)

Comprendre le monde, construire l'avenir

Titre : Manipulation cohérente des états d'Andreev dans un contact atomique

Mots clés : Physique, mécanique quantique, supraconductivité, physique mésoscopique

Résumé :

Des états électroniques localisés apparaissent dans les liens faibles entre électrodes supraconductrices : les états d'Andreev. Les expériences présentées dans cette thèse explorent les propriétés de cohérence quantique de ces états, en utilisant comme liens faibles des contacts à un atome entre des électrodes d'aluminium. Les contacts atomiques sont intégrés dans une cavité microonde qui permet à la fois de les isoler et de les sonder.

Dans une première série d'expériences, il est montré qu'on peut utiliser les états d'Andreev pour définir un bit quantique, le « qubit d'Andreev », qu'on contrôle à l'aide d'impulsions micro-onde. Les mesures des temps de vie de cohérence de ce qubit sont analysées en détail.

Dans une deuxième série d'expérience, l'interaction entre le qubit d'Andreev et le résonateur micro-onde est utilisée pour quantifier le nombre de photons présents dans le résonateur en fonction de la puissance d'impulsions microonde à sa fréquence propre.

Enfin, des sauts quantiques et des sauts de parité sont observés dans des mesures continues de l'état du qubit d'Andreev.

Title: Coherent manipulation of Andreev bound states in an atomic contact

Keywords: Physics, quantum mechanics, superconductivity, mesoscopic physics

Abstract:

Localized electronic states, called Andreev bound states, appear in weak-links placed between superconducting electrodes. The experiments presented in this thesis explore the coherence properties of these states. Single atom contacts between aluminum electrodes are used as weak links. In order to isolate and probe these states, the atomic contacts are integrated in a microwave cavity.

In a first series of experiments, it is shown that Andreev states can be used to define a quantum bit, "the Andreev qubit", which is controlled using microwave pulses. Measurements of the lifetime and coherence time of this qubit are thoroughly analyzed.

In a second series of experiments, the interaction between the Andreev qubit and the microwave cavity are used to determine the number of photons present in the cavity as a function of the power of microwave pulses at its eigenfrequency.

Finally, quantum and parity jumps are observed in continuous measurements of the state of the Andreev dot.

Université Paris-Saclay
Espace Technologique / Immeuble Discovery
Route de l'Orme aux Merisiers RD 128 / 91190 Saint-Aubin, France